HYDRODYNAMICS OF JET IMPACT IN A COLLAPSING BUBBLE

by

ANTONY PEARSON

A thesis submitted to
The University of Birmingham
for the degree of
Doctor of Philosophy

School of Mathematics and Statistics
The University of Birmingham
August 2002

ACKNOWLEDGEMENTS

I would like to begin by thanking my supervisors, Prof. John Blake and Dr. Steve Otto for their advice and guidance throughout the course of this work. In particular, the assistance with numerical aspects of the work by SRO and the ideas and insight of JRB were essential in producing the thesis. I am also grateful to their patience in reading early drafts of my work.

I also wish to thank my parents and close family for their support and encouragement throughout the course of my studies here in Birmingham. I also acknowledge the academic and social support of a number of close friends during this time.

Further thanks are due to Prof. John Blake, Prof. Larry Crum, Dr. Olgert Lindau and Prof. Yukio Tomita for their permission to reproduce a number of experimental photographs from their work. The presence of such striking imagery enhances discussions throughout the thesis.

Finally, the financial support of the EPSRC is acknowledged, whose studentship has made this work possible.

SYNOPSIS

An improved and highly accurate boundary integral scheme is employed to calculate the necessarily non-spherical motion of bubbles near both rigid and free boundaries (which are examined singly and combined to provide a shallow layer of fluid): where suitable examples exist, bubble shapes are compared against experiments. With regard to several physical phenomena, the motion of bubbles generated at different start times is also examined. Physical quantities such as pressure and velocity fields around the bubble, energies associated with the bubble motion, and the kinetic energy and Kelvin impulse of the liquid jet are examined to provide insight into the physics of the problem.

CONTENTS

LIST OF FIGURES

LIST OF TABLES

Chapter 1

INTRODUCTION

The typical diameters of laser-induced cavitation bubbles and those formed by underwater explosions differ by four orders of magnitude.[1] In many respects, however, the behaviour of these vastly different entities is very similar as their motions may be characterised by different parameter régimes of the same physical problem; wherein inertia is the dominant feature. In the short length-scale régime of cavitation, the bubbles are wholly unaffected by buoyancy and surface tension may begin to play a rôle; certainly, in the case of micrometre sized bubbles which may be formed in applications such as sonochemistry, the consideration of surface tension effects is essential. However, it is unnecessary to consider the explosion bubbles at the other extreme in order to witness the effects of buoyancy on a bubble. These effects may clearly be observed on centimetre sized bubbles, for example those generated in reduced pressure cavitation experiments (e.g. Gibson 1968).

As alluded to above, whatever the length and time-scales of bubble motion, the underlying physics hold much in common. Hence the consideration of two seeming different but extremely interesting physical problems may be combined into a single study. Laser-induced cavitation bubble research still deals with the much studied problem of a bubble near a rigid boundary, though in recent times in connection with Single Cavitation Bubble Luminescence (SCBL), the generation of light from the violent collapse of a single millimetre sized bubble. More recent studies also deal with the motion of these bubbles near to flexible boundaries which are formed from tissue phantoms. Such studies have many applications in the field of medicine where, for example, cavitation may occur

[1] Typical laser-induced cavitation bubbles are around 2–3mm in diameter, whilst the gaseous remnants of the detonation of an underwater explosive device may form a bubble of around 10–20m in diameter.

within the body in such diverse modern medical procedures as laser surgery and Extra-corporeal Shock Wave Lithotripsy (ESWL), a treatment for kidney stones. In a similar fashion, the study of submerged bubbles of up to 20 metres in diameter may still be applied to underwater explosions, though recent applications include the modelling of air bubbles formed by underwater airguns[2], which are used to provide a source signal in the process of marine seismic surveying. A more complete discussion of these applications may be found in the remainder of this chapter.

In this work we employ a boundary integral technique to study the motion of bubbles near both rigid and free boundaries. Such techniques have been used with great success by a number of research groups since the early 1980's as our overview in Section 1.3 and technical review of Chapter 3 demonstrate. By enhancing the basic methods of solution exploited in previous work and looking at previously unexamined physical quantities, further insight into these physical problems is obtained.

Before we detail a more complete plan of the thesis it is important we provide an account of previous work in the field of bubble dynamics. We choose to present this in three sections: an overview of the history of the subject; recent experimental work, the motivations and applications; and current analytical and computational techniques. Following these discussions, we outline the work contained in the thesis.

1.1 Historical Overview: Theory and Experiment

Cavitation was first observed experimentally over a century ago in water flowing through constricted tubes by Reynolds (1894). A transient cavity (one which has no gas content and therefore has no means of arresting a total collapse) is formed when the local fluid pressure falls below the vapour pressure of the liquid. As the pressure in the fluid changes or the bubble migrates to a region of higher pressure, the cavity will collapse, often in a violent manner. Any form of asymmetry in the system such as buoyancy or the influence of a nearby boundary will cause this collapse to occur asymmetrically, often leading to the formation of a high-speed liquid jet which is one cause of the physical damage

[2]Airgun bubbles are not so large as underwater explosion bubbles and are typically one metre in diameter. Buoyancy still plays an important rôle in their behaviour.

Figure 1.1: An air bubble near an oscillating rigid boundary. Photograph taken from the 1998 Acoustical Society of America calendar and reproduced courtesy of Prof. Larry Crum. See text for other references.

associated with cavitation. Figure 1.1 shows the celebrated photograph by Prof. Larry Crum, wherein a liquid jet may be clearly seen to be threading the bubble. This is reproduced here from the 1998 Acoustical Society of America calendar, but has also been used for illustrative purposes in many papers; for example those by Prosperetti (1984), Suslick (1989) and Blake, Keen, Tong & Wilson (1999).[3]

In the Winter of 1894, trials of Sir Charles Parsons' steam turbine powered ship *Turbinia* proved disappointing with 'propeller slip nearly 50%' accounting for the lack of speed. Parsons correctly suspected these problems lie with the formation of 'vacuous cavities' behind the propeller blades. The practical implications of this effect were revealed by engineers Thornycroft and Barnaby. The solution in this case was to increase the number and size of propeller blades attached to the steam turbine and operate them at lower speed. Extensive experiments were carried out on model propellers in a

[3]In fact this is not an observation of the violent collapse of a bubble as some authors suggest. The behaviour is in fact produced by inserting a small gas bubble into a container of liquid, which is then placed onto an oscillating platform (a paint stirrer). The oscillations cause a slow-speed jet to thread the bubble. Numerical calculations and more discussion of this phenomenon may be found in the paper by Blake, Keen, Tong & Wilson (1999).

testing tank devised by Parsons, in which it was possible to photograph cavitation and make quantitative measurements of the effects. For a more complete overview of the development of *Turbinia* the reader is referred to the booklet by Osler (1981).

The first theoretical investigation into cavitation may be attributed to Besant (1859) who considers the collapse of a void upon the instantaneous annihilation of a spherical portion of fluid within an infinite fluid domain. This work was later simplified and extended to consider the pressure within the body of the fluid by Rayleigh (1917). In this work, the bubble contents (non-condensible liquid vapour) are assumed to exert a constant pressure, p_v, throughout the lifetime of the bubble and the effects of liquid compressibility, surface tension and fluid viscosity ignored; as are any factors which may induce asymmetry. Under such assumptions, Rayleigh showed the radius of the bubble, $R(t)$ obeyed the equation

$$R\ddot{R} + \frac{3}{2}\dot{R}^2 = \frac{p - p_\infty}{\rho}, \tag{1.1.1}$$

where a dot denotes a time derivative, p is the liquid pressure at the surface of the bubble, p_∞ is the far-field fluid pressure and ρ is the fluid density. With the omission of surface tension, $p = p_v$, and hence the motion is governed by the initial velocity at the surface of the bubble. It was also shown by Rayleigh that extremely high pressures can develop within the fluid near to the surface of the bubble during the collapse phase. Although this model is very simplistic, it provides a good approximation for the early expansion phase not too close to a boundary when the bubble remains spherical, and is used later to provide an initial condition for vapour bubble calculations.

This work was extended by Lamb (1923) who considered the bubble to contain an ideal and adiabatic gas[4] so the pressure of the bubble varies as

$$p = p_0 \left(\frac{V_0}{V}\right)^\kappa, \tag{1.1.2}$$

with p denoting the pressure, V the volume (with a subscript zero denoting the initial value of a quantity) and κ the ratio of specific heats[5], taken to be constant for any given

[4] An adiabatic gas is one in which volume and pressure changes take place without heat transfer between the gas and its surroundings. This is characterised by the equation $pV^\kappa = C$, a constant.

[5] The value of which can be determined experimentally, but is often well known. For example, the value of κ for air is 1.4. For gaseous remnants of TNT, $\kappa = 1.25$. We note the standard notation for this quantity, γ is reserved for later use.

case. This allowed a much more accurate representation of an explosion bubble which contains the gaseous remnants of detonation. Again the motion of the bubble was shown to obey equation (1.1.1) with the surface pressure given by (1.1.2). At the same time Ramsauer (1923) was engaged in early experimental work. Using a system of electrodes placed at regular distances from an explosive charge, it was possible to record the radius-time curve for the expansion phase of the bubble motion. A good agreement was found with simple theory, which predicted the variation of maximum bubble radius with depth.

Further impetus for work on explosion bubbles was brought about by the advent of World War II. The theoretical work of this period was based on modelling the explosion bubble as spherical, and assuming the surrounding fluid was inviscid, incompressible and the flow induced by the bubble motion was irrotational. These assumptions are still applied today in order to reduce the complexity of numerical calculations; though direct numerical simulations are becoming possible with modern computer facilities. Key improvements over previous studies were the additional considerations of effects due to buoyancy and the influence of nearby rigid and free boundaries. Much of this work may be attributed first to Herring (1941). Numerical studies of the effects of buoyancy were undertaken by Taylor (1942). The major limiting factor of these studies was, to the order calculated by Herring, the action of the effects due to both buoyancy and nearby boundaries was to displace the bubble rather than deform it from its spherical shape.

It was also during this period in which the first investigations into the stability of the spherically shaped bubble took place. Following the detonation of a deeply submerged charge, a mixture of gas and water, rather than a connected bubble reach the surface. This observation motivated Penney & Price (1942) to consider the stability of an initially spherical bubble rising due to buoyancy. Performing a linear analysis by expanding the surface potential and radial coordinate in terms of spherical harmonics, they were able to examine the effects of small perturbations to the spherical shape. These results showed the expansion phase to be stable to perturbations, but upon collapse, any initial perturbation in shape would grow. Later studies on the stability of bubbles undergoing growth and collapse were performed by, for example, Chapman & Plesset (1972), Prosperetti & Seminara (1978), Hall & Seminara (1980) and Hao & Prosperetti (1999), and in many

works referenced therein.

Throughout this period, there were also extensive experimental programmes, the key feature of these being the use of high-speed photography which gave researchers accurate records of both the bubble shape and its migration, along with the possibility of recording the much more interesting collapse phase of the motion. For examples of such work, the reader is referred to the works of Taylor & Davies (1943) and Bryant (1944). These studies indicate a good agreement with theoretical work during the expansion and early collapse phase. During the later stages of collapse however, there was a failure to account for the non-spherical shapes observed and also to accurately predict the upward migration of the bubble. Further differences were also found between the theory and the experimental work of Swift & Decius (1947) where up to three oscillations of a bubble produced by a deep explosion were observed. The simple theory predicted an increase in each successive maximum radius achieved, conflicting with the experimentally observed decrease. A discussion of possible energy loss mechanisms which may account for this behaviour was presented by Herring (1949) in a revision to his 1941 paper. These included radiation of acoustic energy, turbulence and heat transfer. Herring concluded the primary loss mechanism was through acoustic radiation, yet it could not account for the total energy losses observed in experiments.

For further and complete details on wartime explosion bubble research, the reader is referred to the book of Cole (1948). A more recent review may be found in the work of Holt (1977); although this shows little progress in the intervening period. Some theoretical work of note may be attributed to Keller and his co-workers (Keller & Kolodner 1956, Epstein & Keller 1972, Keller & Miksis 1980), who treat the surrounding water as a compressible fluid, and consider the effect this has on a number of successive oscillations of a bubble of mixed content. This is done by assuming the velocity potential of the water satisfies the wave equation. As expected, it was found both the maximum radius and period of oscillation decreased with each oscillation, a feature associated with the dissipation of energy through the transmission of pressure waves.

Much of the work following World War II in the field of bubble dynamics has concentrated on the study, both experimentally and theoretically, of cavitation bubble dy-

namics, which had received little attention since the work of Rayleigh in 1917. Since this time, considerable effort has gone into the refinement of experimental apparatus and techniques. Key early studies include the work of Naude & Ellis (1961) who generated transient cavities using a spark discharge technique, and recorded bubble motion using high-speed photography. Later the landmark study of Benjamin & Ellis (1966) used a kinetic-impulse method to again generate cavities in the vicinity of a rigid boundary. This work demonstrated the non-spherical nature of the bubble collapse, exhibiting a greater surface velocity on the surface of the bubble furthermost from the boundary. This was ultimately seen to form a high-speed liquid jet, a key cause of cavitation erosion damage. Alongside the excellent experimental work in this paper, Benjamin & Ellis also introduced the concept of the Kelvin impulse to the field of bubble dynamics, a discussion of which follows in Section 1.3.

Whilst the kinetic-impulse method of generation most closely mimics the formation of cavities by placing the liquid under tension, it requires the accurate insertion of a gaseous impurity to seed the formation of a bubble. Due to this the spark-discharge technique found favour with experimentalists and was further refined over the following years. The merits of the spark-discharge technique are discussed alongside current experimental techniques in the following section.

1.2 Recent Experimental Work, Motivations and Applications

In the closing paragraphs of the previous section, two early experimental studies of cavitation bubble dynamics were discussed. Of these, the work of Benjamin & Ellis (1966) remains an isolated application of the kinetic-impulse method of generation, due to the difficulties involved with the insertion of a seed microbubble. The spark-discharge technique employed in the earlier study of Naude & Ellis (1961) proved to be a much more favourable technique, however, due to the reproducible nature of the results. This technique was further refined and used until the mid-1980's by many research groups. Examples of the success of this technique include the papers by Chahine (1977, 1982), Chahine

& Bovis (1980), Gibson & Blake (1980) and Blake & Gibson (1981, 1987). In many of these studies, the liquid container is held at a reduced pressure of the order of one-tenth of an atmosphere. This allows the generation of bubbles with maximum radii $\sim$ 10mm and lifetimes $\sim$ 10ms; these were more easily observed and recorded with the high-speed cameras available at that time. With the increase in volume, buoyancy effects become important and in some cases are eliminated through the use of free-fall apparatus (Gibson & Blake 1980). In other cases such as the paper by Chahine & Bovis (1980) buoyancy effects have an influence on the motion, but are not commented upon.

The main flaw of the spark-generation method is that the high-voltage electrodes intrude into the flow field and unavoidably interfere with the subsequent motion of the bubble. This is particularly relevant during the collapse phase when the bubble geometry becomes highly convoluted. One typical example of this may be seen in Figure 1.2 which shows the generation of a vapour cavity near to a free surface. The electrodes are seen to penetrate the bubble very shortly after generation and also become very close to the high-speed liquid jet which forms at the top of the bubble; though the effects on the motion are, in this case, likely to be minimal.

Such invasive techniques have now been superseded by the use of laser technology, where a series of lenses are used to split then refocus a pulse of laser-light to produce a burst of energy in precisely the required location. The near instantaneous input of energy into the system causes vapourisation and the formation of plasma within the liquid. This is clearly evident where charge-coupled devices such as many of the latest high-speed cameras are used to record the bubble motion. See, for example, Shaw, Jin, Gentry & Emmony (1999), or Figure 1.3 reproduced from Lindau (2001). The associated thermal effects, which are also an intrinsic feature of the spark-generation method, are the main flaw of this technique. In some cases the initial sphericity of the bubble produced may also be questioned, with observations suggesting the bubble produced is slightly ellipsoidal (again, note Figure 1.3). Any such discrepancies, however small, may have an important influence during collapse. Theoretical consideration of such bubbles is given in Hooton (1995).

Along with the improvements in bubble generation, there have also been significant

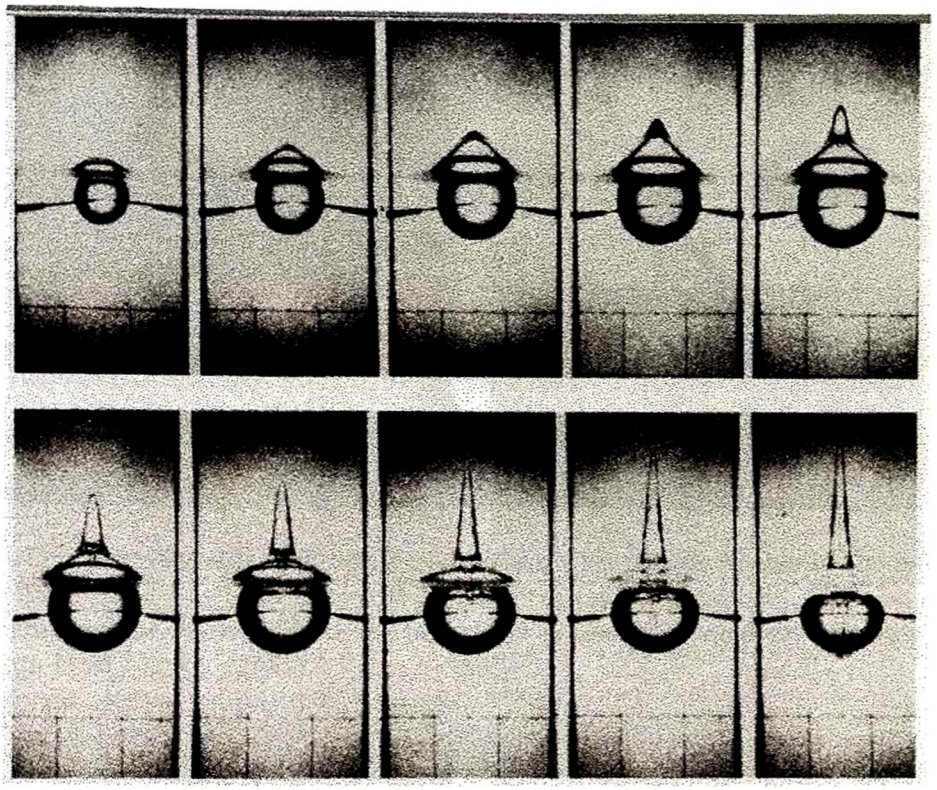

Figure 1.2: The motion of a vapour cavity generated near a free surface using the spark-discharge method. The high-voltage electrodes are clearly visible as dark lines mid-way down each frame. The bubble is generated at a standoff distance of $\gamma = -0.56$. This is defined in (1.2.1) on page 11. Reproduced with permission from Blake & Gibson (1981).

advances in the visualisation and recording of bubble motion. The most favourable observations of bubble motion are obtained when the fluid domain is backlit with diffuse lighting, whilst a non-diffused lighting is often used to visualise the motion of boundaries, where appropriate. With high-speed cameras now capable of 100 million frames per second (see, for example, Lindau 1998, 2001) and above, there also exists the possibility of examining the generation and evolution of shock waves during the collapse phase. Many of these recent advances may be attributed to Lauterborn and co-workers (Lauterborn & Bolle 1975, Lauterborn 1982, Lauterborn & Vogel 1984). A review which covers many of these advances is given in the paper by Lauterborn & Hentschel (1985).

All of the work referenced in the previous paragraph concerns the motion of laser-induced cavitation bubbles near a rigid boundary, but are not the sum total of research on the topic: The problem has been extensively investigated by many research groups

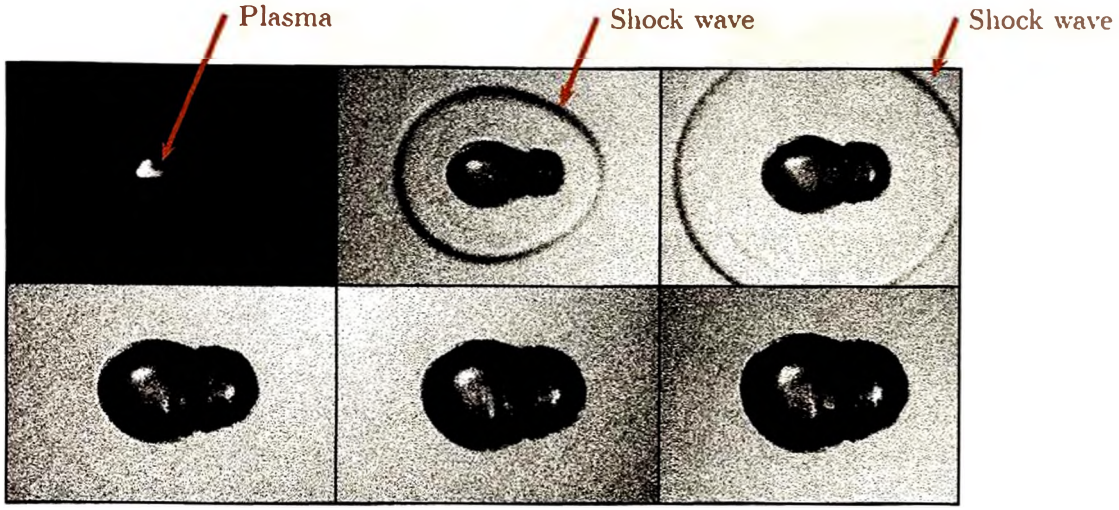

Figure 1.3: The initial stages of bubble formation with plasma visible in the first frame and the initial shock wave in frames two and three (see annotations). We also note the non-spherical shape of the bubble in these early stages of expansion. Reproduced with permission from Lindau (2001).

and many purely experimental and jointly theoretical papers have been written, though here we concentrate on the experimental aspects of these papers, leaving discussion of important theoretical work until the following section. Work by Tong, Schiffers, Shaw, Blake & Emmony (1999) and Blake, Tong, Keen & Tomita (1999) considers the rôle of splashing during the collapse phase of bubble motion. A liquid splash is formed during collapse close to a rigid boundary when liquid within the jet impacts and is thrown outward along the boundary. As fluid rushes in due to the continued collapse of the bubble, the opposing flows meet and a 'splash' of liquid is thrown up inside the bubble, yielding highly convoluted toroidal geometries. See Figure 1.4 reproduced from Lindau (2001).

A number of dimensionless parameters are important in governing the physical behaviour of the bubble and it is convenient to introduce two of these here as they greatly affect motion and hence the behaviour of the splash and will be used repeatedly throughout this work. Arguably the most critical parameter is the standoff distance; the dimensionless distance between bubble and boundary scaled with respect to the maximum radius the equivalent spherical bubble would attain in an infinite body of fluid. Thus

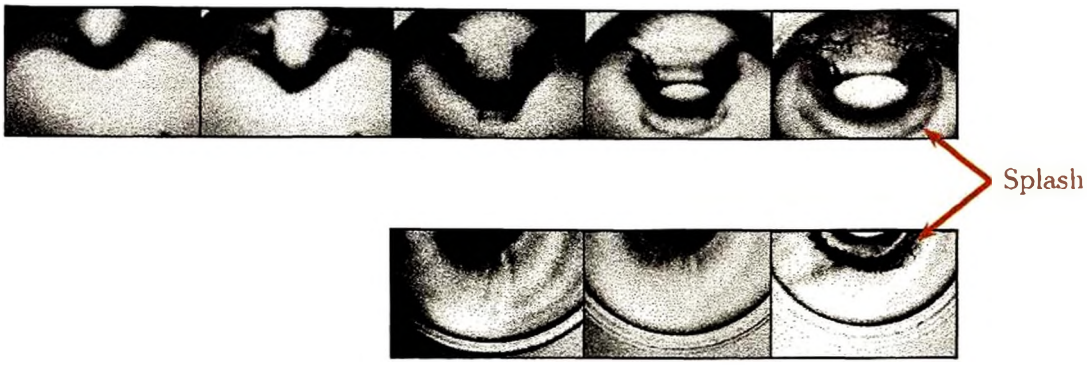

Figure 1.4: The collapse of a laser-induced cavitation bubble generated at a standoff distance of $\gamma = 0.6$ above a rigid boundary, showing the formation of a liquid splash between the bubble and boundary. Reproduce with permission from Lindau (2001).

this is defined as

$$\gamma = \frac{h}{R_{\mathrm{m}}}, \tag{1.2.1}$$

where h is the dimensional displacement from the boundary and R_{m} the maximum radius of the equivalent spherical bubble. Also of vital importance to the behaviour of the bubble is what is termed the strength parameter (Best 1991) or compression ratio (Blake & Keen 2000). This is a measure of the initial pressure within the bubble and is defined as

$$\alpha = \frac{p_0}{\Delta p}, \tag{1.2.2}$$

where p_0 is the initial pressure and Δp is the difference between the hydrostatic pressure and the vapour pressure of the bubble. More dimensionless parameters are required to fully define the problems we consider and these are introduced in due course.

Other experimental works of note include the paper by Blake, Robinson, Shima & Tomita (1993) which considers the motion of two cavitation bubbles near to a rigid boundary. High-speed photographs of laser-generated bubbles of both similar and different sizes are presented and compared with calculations. Very recent work of excellent quality was performed by Lindau (see Lindau 2001, Lindau & Lauterborn 2003), who performs a range of experiments with laser-generated bubbles near to a rigid boundary in connection with SCBL, the formation of counter jets and shock-wave generation during the collapse of the bubble. Herein, we consider the incompressible régime of the flow and so the admittance of shocks is outside the scope of this work. In order to fully capture

any shocks would require a highly accurate and computationally expensive numerical code. The generation of three shocks may be clearly seen at differing times and locations throughout the collapse phase in Figure 1.5 (reproduced from Lindau & Lauterborn 2003), illustrating the complexity of the fully compressible problem. One other extremely interesting feature of this work is the unique angle at which some high-speed photograph series are presented, being viewed from an elevation of 45° above the rigid boundary. This makes it possible to examine the radial symmetry of the bubble and gain an insight into the three-dimensional nature of the problem. Such figures are included in Chapter 3 to ratify our calculations.

Compared to the often studied rigid-boundary problem, relatively little experimental work on bubble motion near a free surface has been performed. One early study of some success is that of Blake & Gibson (1981) who, as mentioned above, used a spark-discharge method to generate transient cavities in a reduced-pressure environment. This work provided evidence of the high-speed liquid jet formed and directed away from the free surface, whereupon a counter jet is formed during the collapse phase. For bubbles generated close to the boundary this is a pronounced narrow spike of liquid. For bubbles initiated at a greater distance, a broader jet and free-surface spike are observed. A feature also evident in bubbles induced close to the free surface is the entrainment of the bubble within the raised surface; with a thin layer of liquid separating this from the surface of the bubble. Recent work by Robinson, Blake, Kodama, Shima & Tomita (2001)[6] and Tomita & Kodama (2001) examines both the behaviour of a single cavitation bubble and of two cavitation bubbles of varying relative size formed in a vertical column beneath a free surface. In this work, laser-generation techniques are utilised. High-speed photography is used to capture the bubble and surface motion, and with the increased frame-rates available, experiments are performed on smaller bubbles at atmospheric pressure rendering buoyancy effects negligible. Whilst the bubble nearest the infinite free surface continues to form a liquid jet in a direction away from the surface, the width of this jet is affected by the presence and size of the second bubble, whose behaviour depends very much both on its size relative to the bubble above it, and on the dimensionless distance between the

[6]Figures reproduced for inclusion in this paper may be found in Chapter 4.

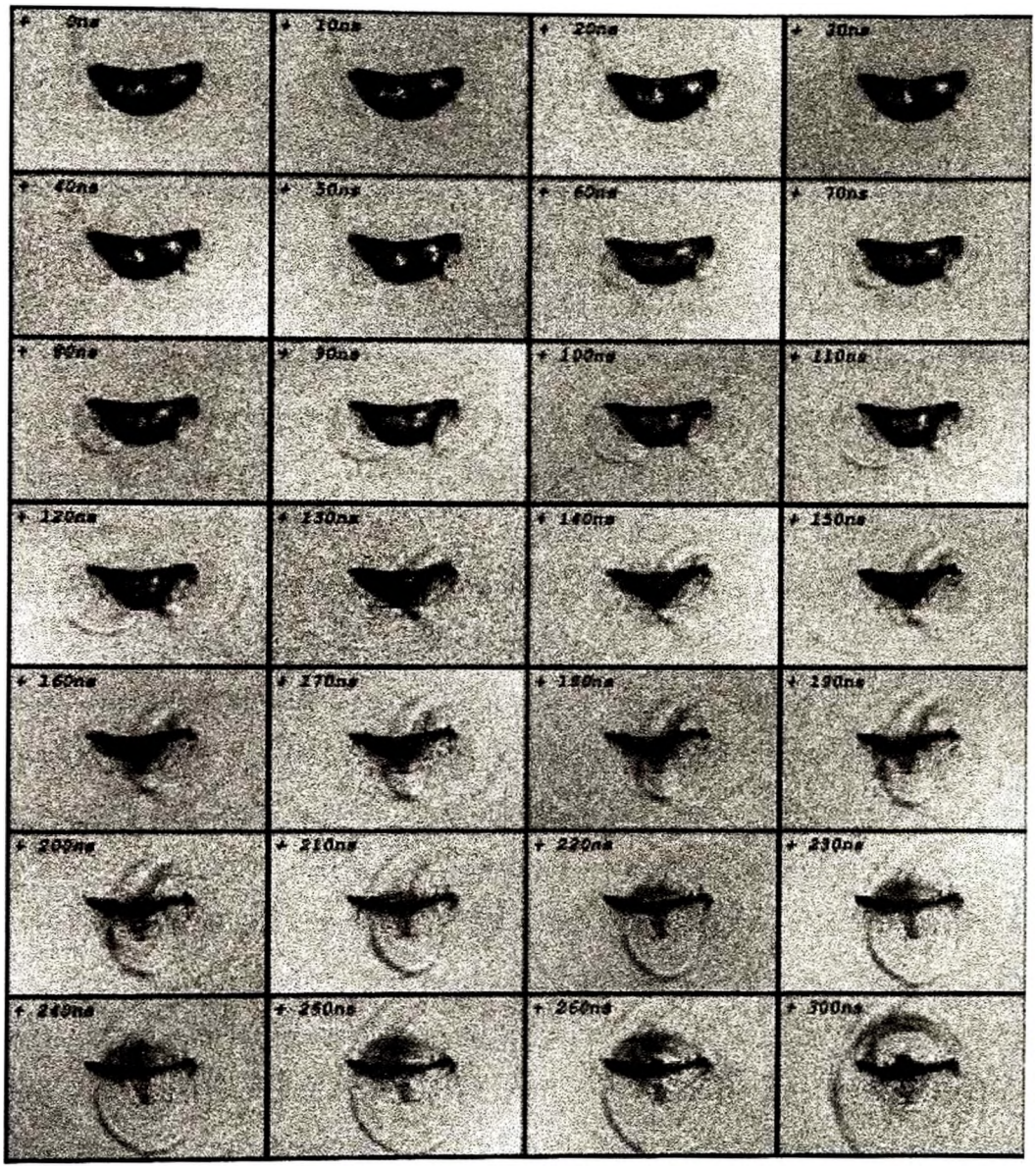

Figure 1.5: High-speed photograph series showing the generation of three shock waves during the collapse of a laser-induced cavitation bubble. The figures in the top-left corner of each frame are the time in nanoseconds following the formation of the first shock. Reproduced with permission from Lindau & Lauterborn (2003).

bubbles.[7]

As was mentioned at the start of this chapter, several recent studies deal with the motion of laser-induced cavitation bubbles near to flexible boundaries formed from tissue phantoms. These studies provide insight into the processes which may occur within the body during medical procedures such as ESWL and laser surgery, wherein cavitation phenomena may occur. Before we outline these most recent studies it is helpful to cover previous work concerning bubbles near to boundaries formed from other flexible materials so we may appropriately credit noted phenomena.

An early investigation into the dynamics of a vapour bubble near an elastic surface was performed by Gibson (1968) who observed that under certain conditions, both the liquid jet formed during collapse and the bubble migration were directed away from the boundary. As the jet impact and high-pressure regions formed during the collapse of a bubble near a rigid boundary were known to cause erosion damage; the use of compliant coatings was considered as a means of preventing this damage. Gibson & Blake (1980, 1982) and Blake & Gibson (1987), investigated the behaviour of spark-generated bubbles in the vicinity of a number of compliant surfaces. These include natural and vulcanised rubber of varying thicknesses and composite surfaces consisting of a foam-rubber layer sandwiched between a rigid perspex plate and a natural rubber layer. In some cases, a radial jet was formed leading to hour-glass shaped bubbles and bubble splitting, much like those observed in calculations of a bubble in a stagnation-point flow (Blake, Taib & Doherty 1986) or near the null impulse state (Brujan, Pearson & Blake 2002). With a boundary of greater mass, behaviour was observed to be similar to that near a rigid boundary. Whilst for lighter boundaries, migration and jet formation away from the boundary was noted, resembling bubble motion near a free surface. Physically, we should expect complex behaviour as energy may be transferred from the fluid during the expansion phase, then returned by the action of an elastic restoring force, with behaviour very much depending on the response time of the boundary in comparison to the characteristic period of the bubble.

Work by Shima, Tomita, Gibson & Blake (1989) investigated the characteristic be-

[7]Here the typical length-scale used is the equivalent maximum radius of the larger of the two bubbles.

haviour of bubble motion near composite surfaces consisting of two elastic materials. Again, like the earlier work of Gibson & Blake, this was formed from rubber foam and sheeting affixed to a rigid boundary. It was found bubble migration could be controlled by altering both the stiffness and inertial properties of the boundary. The dimensionless distance between bubble and boundary was also found to play a rôle in the behaviour during collapse.

More recent work on bubble motion near an inertial boundary was performed by Shaw, Jin, Gentry & Emmony (1999), who generated bubbles near an elastic membrane which was loosely held at each end, thus creating no significant tension in the boundary. It was found during expansion, the membrane was displaced by the growth of the bubble, as expected. However, upon collapse more unusual behaviour was observed with, in some cases, the formation of mushroom-shaped bubbles prior to total collapse.

Prior to our discussion of the recent studies which consider motion near flexible, tissue-like boundaries, it is helpful we outline the importance of these studies with consideration to modern medical procedures. The two illustrative cases we use herein are those of ESWL and laser surgery, though other techniques such as therapeutic ultrasound are equally worthy of consideration.

Since the early Eighties, the use of Extracorporeal Shock Wave Lithotripsy has all but replaced surgical methods for the treatment of kidney stones. In this procedure, shock waves are focused onto the location of the stone inside the body. For many years following the initial development of these lithotripter machines, the only physical process thought to account for the destruction of the stone was the high tensile stress produced at the tissue–stone interface. More recently, evidence of the occurrence of cavitation caused by the tensile phase of the shock has been found. In the preliminary studies of Coleman, Saunders, Crum & Dyson (1987), thin aluminium foil and sheets of copper, aluminium and lead of up to 1mm in thickness were placed at the focus of a lithotripter machine and subjected to a number of applications of a shock wave. Cavitation was found to occur over a relatively large volume, not just at the focus. Indeed, many newer machines are not so efficient as their older counterparts. This may be due to the improved engineering of the reflector where tighter focusing of the shock wave means there is less

scope for the generation of cavitation nuclei around the stone. The early ignorance of the importance of cavitation in destroying the stone is evident. In the book by Chaussy (1986) which reviews the development of lithotripter machines, no mention is made of cavitation. Other authors mention the possibility, but dismiss the rôle it plays, and give no consideration to the matter. In the studies by Coleman *et al.*, visual inspection of the area surrounding the focus also revealed the presence of not only transient cavities, but also of stable cavitation nuclei formed by rectified diffusion, with such bubbles persisting for several acoustic cycles.

The other key occurrence of cavitation effects in a medical sense which we consider here is in the application of laser surgery techniques. Here these are discussed in the context of laser eye-surgery. During intraocular surgery, a short pulse of laser light is focused into the eye, causing plasma formation. Within the volume of this plasma, evaporation of the tissue or liquid occurs. This rapid temperature rise and subsequent expansion forms a shock wave, leaving behind a cavity within the fluid. Under typical clinical conditions this cavity reaches a maximum radius $\sim$ 1mm. Such is the rapidity of expansion the bubble will exceed its equilibrium radius, then due to ambient pressure will collapse within 1ms. In some situations this will cause temperature and pressure within the fluid to rise to values near those initially caused by the laser pulse, causing a second acoustic wave to emanate into the fluid. Such a cycle may repeat several times before the energy is dissipated. Further details on this technique may be found in the paper by Vogel (1997). There is clearly much scope for the damage of human tissue in such a procedure, which is often unwanted, although in the case of tissue ablation, such effects may be a welcome addition for the removal of tissue.

Work by Kodama & Tomita (2000) considers the collapse of a cavitation bubble near a gelatin surface with Young's modulus in the range 0.043–0.304MPa (depending on the water content of the gelatin sample). This mimics a wide range of human tissues, for example the thoracic aorta (0.3–0.94MPa) or the human cornea (0.3–5MPa). It was found in general, the bubbles had a tendency to migrate away from the boundary, and were not seen to develop liquid jets. However, in the study of bubbles attached to the boundary, it was observed that shock-wave interaction resulted in the formation of a high-speed liquid

jet directed toward the boundary, impiercing several millimetres into the gelatin. Such a characteristic may be important in both lithotripsy where the formation of gas bubbles which persist through many shock applications are observed, and in laser surgery where the violent collapse of a bubble may cause the generation of a shock wave.

A much more complex response to the boundary properties, and in particular the standoff distance was observed by Brujan, Nahen, Schmidt & Vogel (2001a, 2001b), who studied the behaviour of laser-induced cavities near to a polyacrylamide (PAA) gel. As in the work of Kodama & Tomita the rheological properties of the gel may be adjusted by varying the water content of the sample. In the first of these papers, a detailed examination of the variation of the standoff, γ is undertaken. For values of γ of the order of one, bubble migration and jet formation away from the boundary are observed. For intermediate values of γ, the formation of mushroom shaped bubbles upon collapse, bubble splitting and a liquid jet directed towards the boundary may all be observed. Small values of γ are characterised by jet formation in the PAA gel and the tearing of material from the boundary. In the second paper Brujan *et al.* vary the elastic modulus of the PAA sample, again yielding a complex behaviour. For an intermediate elastic modulus, the pattern of behaviour detailed above is observed, whilst for stiffer boundaries the predominant feature is of jetting and migration toward the boundary, as is commonly observed near a rigid boundary. In softer samples, the behaviour is much like that of a bubble in an infinite fluid, except during the collapse, when material is torn from the boundary. These excellent series of results give a good indication of several mechanisms responsible for erosion and enhanced tissue ablation in the context of cavitation, namely jet penetration into, and material ejection out of the boundary, coupled with high stresses thereon.

We close this section by returning to the topic of underwater explosions. Whilst not strictly an experimental study in the normal sense, Figure 1.6 shows the destructive results of a live-firing test by the Australian Navy of a Mark 48 torpedo. Information from the Navy website confirms the nature of the explosion: The torpedo detonates beneath the target ship, first fracturing the back of the ship due to the explosive shock

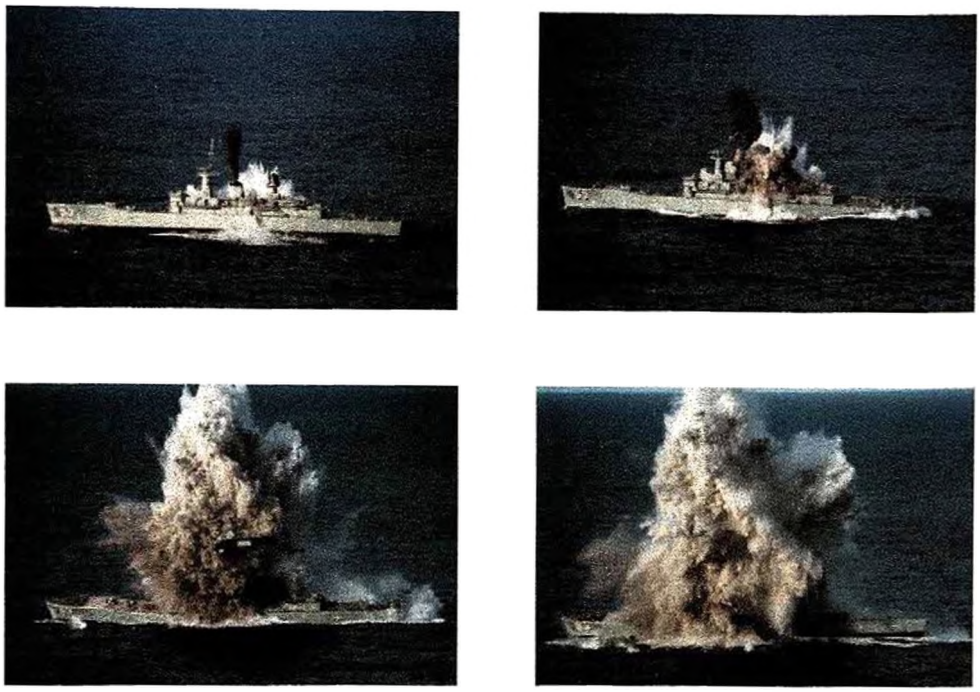

Figure 1.6: The sinking of *HMAS Torrens* by Mark 48 torpedo during a live firing exercise. Images taken from the Royal Australian Navy website.

wave and the first expansion of the bubble formed.[8] Oscillations of the bubble cause further stresses on the hull prior to the liquid jet impacting on the hull of the ship, violently ripping through the superstructure of the vessel. Such was the violence of the jet impact, the assembled press assumed the ship had been rigged with explosives to ensure the 'successful' sinking of the ship by the torpedo.

Before concluding this section, we pause to introduce a parameter which is central to the study of bubbles of a centimetre or more in diameter; that which governs buoyancy. The buoyancy parameter δ is defined by

$$\delta^2 = \frac{\rho g R_{\mathrm{m}}}{\Delta p}, \tag{1.2.3}$$

where ρ is the density of the fluid, g is acceleration due to gravity, and R_{m} and Δp are as defined earlier. A fuller discussion of the dimensionless parameters introduced in this section may be found in the following chapter.

The field of bubble dynamics is one area of fluid mechanics in which we have a wealth of experimental data against which we may compare our theoretical work. Unlike many

[8]The diameter of the bubble is given as approximately 18 metres.

other branches of applied mathematics, these experiments are often performed in advance of the theoretical work, with many studies being motivated by experimental observation. In the next section, we consider recent theoretical and computational studies in this area; including the theoretical side of joint experimental–theoretical work.

1.3 Current Analytical and Computational Techniques

A comprehensive review which covers much of the work on 'Bubble Dynamics and Cavitation' up to the mid-1970's was authored by Plesset & Prosperetti (1977) and must be regarded as the key starting point for information on research prior to this time. The coverage of spherical bubble dynamics, in particular, is truly startling in its depth and diversity. In the years following this review, the volume and variety of quality research in the field of bubble dynamics is immense. Worthwhile summaries include those by: Blake & Gibson (1987), which covers bubble motion near planar boundaries, and Feng & Leal (1997), which may be regarded as a follow-up to the review of Plesset & Prosperetti; though these are far from exhaustive. For more thorough coverage, the reader may be well advised to examine the proceedings of the IUTAM meetings at Caltech (July 1981) and Birmingham (September 1993) edited by van Wijngaarden (1982) and Blake, Boulton-Stone & Thomas (1994) respectively. In this section, much of the work mentioned provides an important foundation for current and ongoing studies or is of related interest, yet barely scratches the surface of the wealth of information available in this field.

Of the joint theoretical and experimental studies, perhaps the earliest paper which contains techniques which are still applicable to non-spherical bubble dynamics is that of Benjamin & Ellis (1966) whose experimental efforts were mentioned earlier. This work also introduced the concept of the Kelvin impulse to the field of bubble dynamics, allowing a feasible explanation of the deformation from sphericity during the collapse phase to be made. The Kelvin impulse has the dimensions of momentum and is related to the concept of impulse in particle mechanics. A mathematical definition of the Kelvin impulse may be found in Section 2.7.

The Kelvin impulse was later studied by Blake (1988), who formulated expressions for

the potential and impulse due to a source–dipole combination near a number of boundary types, including rigid and free boundaries, a two-fluid interface and a number of flexible surfaces. Such techniques may readily be applied to more complex boundary types for which a governing linearised differential equation may be found. The Kelvin impulse was used by Blake, Taib & Doherty (1986, 1987) to partition the γ–δ (standoff–buoyancy) parameter space of buoyant bubbles near rigid and free boundaries to indicate the direction of jet formation and bubble migration. This simple theory provides an excellent agreement with both numerical calculations and experiments as to the global behaviour of the bubble. Later work by Best & Blake (1994) produced a general expression for the Kelvin impulse of a transient cavity suitable for the calculation of the final impulse near a general body shape. This permitted the calculation of a 'zone of attraction' around an axisymmetric body of revolution.

A key study of spherical bubble dynamics in a weakly compressible liquid is presented in the papers by Prosperetti & Lezzi (1986) and Lezzi & Prosperetti (1987) using singular-perturbation methods. In the first of these papers expansions to first-order in the bubble-wall Mach number are made, with the second-order expansions being considered in the second paper. In the first-order case, it is found a one-parameter family of equations exists; members of which include equations previously obtained by Herring (1941) and Keller (e.g. Keller & Miksis 1980). Application of these techniques to non-spherical bubbles is one of the topics of ongoing study by our research group.

More quantitative studies have been made in recent years due to the widespread availability of computers and their subsequent advances in speed. These have included full numerical solutions to Laplace's equation, which describes the flow field under the assumptions the fluid is inviscid and incompressible, and the motion induced is irrotational. An early example of such a study is that of Plesset & Chapman (1971), who employ a marker-in-cell technique to compute the motion of a vapour cavity near to a rigid boundary. The characteristic jet directed towards the rigid boundary was observed and the motion followed until this jet impacted on the opposing side of the bubble, forming a toroidal bubble and altering the fluid topology.

An approximate method valid for 95% of the lifetime of a bubble was formulated by

Kucera & Blake (1990) using a source–dipole combination, along with their images in the boundary. The results produced by this method for bubble growth and collapse near a rigid boundary are compared with results from an earlier boundary integral study, and are found to compare well for standoff distances down to about two (maximum bubble radii). The true beauty of this method lies in the simplicity in which unusual geometries may be treated. Results are presented for: arrays of bubbles; bubbles in a corner, near to a semi-infinite rigid boundary and contained within a pipe. Due to the simplistic modelling of the bubbles, this method fails upon formation of the high-speed liquid jet, which usually occurs within the final 5% of the bubble's lifetime. More recent calculations using these techniques, and concerning buoyant bubbles produced by underwater airguns were made by Cox (2001).

In the following paragraphs, we concentrate on boundary integral (BI) studies as this is the method we will later employ for our calculations. As the name suggests, application of Green's theorem allows us to formulate the problem entirely on the boundaries of the fluid domain and hence reduce the dimensions of the problem by one, so making a great saving in computational cost. In doing this we obtain a Fredholm integral equation of the first-kind, which may be solved using direct methods. Further savings are also made in most studies by the assumption of an axisymmetric flow field. A number of improved techniques are also gleaned from calculations on the inviscid behaviour of drops though discussion of these is left until Chapter 3, where the relevance may be instantly appreciated.

The earliest applications of the boundary integral method (BIM) to the field of bubble dynamics may be attributed to: Lenoir (1976), who considers the collapse of an initially spherical bubble near to both a rigid boundary and an infinite free surface; and Guerri, Lucca & Prosperetti (1981), who consider the collapse of a spherical bubble near a rigid boundary. The main failing of these works is the omission of any consideration of the expansion phase of the bubble. Even for bubbles formed several maximum bubble radii from the boundary the expansion phase will be non-spherical, and no matter how small the differences in surface geometry or velocity from those of a spherical bubble, these differences will play a key rôle during the unstable collapse phase of the bubble.

Work by Blake, Taib & Doherty (1986, 1987) considers both the growth and collapse of a transient vapour cavity near both rigid and free boundaries. Despite the primitive piecewise linear representation of the bubble surface and potential thereon; this work provided a benchmark for future calculations. It is only when regions of very high curvature form; such as in the bullet-shaped bubbles formed near the null Kelvin impulse state or on bubbles close to a rigid boundary where sharp corners form, that the code was unable to cope. Extended details on the numerical scheme employed and on many basic aspects of the BIM may be found in Taib (1985). This should be regarded as the key starting point for boundary integral calculations in the field of bubble dynamics.

This numerical scheme was later improved by Kucera (see Best & Kucera 1992), with the surface geometry and potential thereon being represented by a series of cubic spline elements; though the unknown normal velocity is still assumed to vary linearly for ease of solution. This scheme was used with great success by Best to study the dynamics of underwater explosion bubbles. In his studies, Best (1991) also considers some physical aspects of the topology change from a singly-connected to doubly-connected fluid domain upon jet impact, resulting in a modified boundary integral equation valid for the motion of a toroidal bubble. The numerical scheme employed introduces a cut in the fluid domain in order to render it simply-connected once more. In this work the cut is tracked as a material surface and evolved in time with the flow. Results presented compare favourably with available experimental observations. Later work by Best (1994) introduces a 'dynamic cut relocation algorithm' whereby the cut is remapped at each time step to a simple disc. This negates the need to track the geometry of the cut. In doing this, accuracy is improved and large computational savings are made.

Further BI studies utilising this technique include the work by Tong, Schiffers, Shaw, Blake & Emmony (1999) wherein calculations of bubble motion near to a planar rigid boundary are compared against experiments in order to examine the phenomena of the liquid splash thrown up inside the bubble. Calculations by Blake, Robinson, Shima & Tomita (1993) and Robinson, Blake, Kodama, Shima & Tomita (2001) consider the interactions of two cavitation bubbles near rigid and free boundaries. Such studies are a first step to understanding the behaviour of bubble interactions in bubble clouds such as

those formed in cavitation and multi-bubble sonoluminescence experiments. These studies show an excellent agreement between the calculations and experiments presented. The problem of the bursting of a bubble at the surface of a bioreactor is considered by Boulton-Stone & Blake (1993). Therein the effects of viscosity are examined. This necessitates the inclusion of viscous boundary layers at the surface of the bubble and boundaries. A later study by Boulton-Stone (1995) also investigated the effects of surfactants on this process.

Many solid boundaries occurring in physical problems are not flat planar boundaries, for example the blade of a propeller or the interior of a flask (sonoluminescence). To aid understanding of such cases, Tomita, Blake & Robinson (1998) consider motion near to concave and convex curved rigid boundaries both experimentally and theoretically using a BIM. These results show higher speed liquid jets than may be observed in bubbles near a planar rigid boundary. It was concluded that surface roughness may enhance cavitation erosion at a boundary.

Recent work by Blake, Boulton-Stone & Tong (1995) utilises a fully three-dimensional code to study the collapse of an explosion bubble rising due to buoyancy next to a vertical rigid wall, again comparing well with experimental observations. Further three-dimensional studies of bubble motion near a free surface have been performed by Zhang, Yeo, Khoo & Chong (1998); with great success.

Current research in our group includes the addition of heat and mass transfer effects at the surface of the bubble. Here the techniques developed by Storey & Szeri (2000, 2001) for spherical bubbles are included in a BI code based on the studies described above. Preliminary reports on these techniques (Szeri, Storey, Pearson & Blake 2002) are encouraging.

Despite the great success of the BIM, there are also a number of other successful and emerging techniques which have been applied to the study of cavitation and explosion bubble dynamics. These are briefly discussed below.

One such technique is the level-set method used by Sussman & Smereka (1997) to study a series of axisymmetric free boundary problems. Here the interface is taken as the zero level set of a continuous function and the motion of the fluid and gas (or two fluids)

is described by the solution of the incompressible Navier-Stokes equations on a fixed grid; thus allowing consideration of viscous flows. Due to the need to solve the governing equations throughout the fluid domain, Sussman & Smereka placed limitations on the grid resolution they used. The results presented for drop impacts and rising bubbles did, however, compare well with those of previous researchers. Many variations in the basic level-set method devised by Osher & Sethian (1988) exist; an overview of which may be found in Osher & Fedkiw (2000). Alongside the review, a number of recent results calculated using this method are presented. In particular those of the shock-induced collapse of a helium bubble and the impact of a solid object in water are astonishingly detailed.

Popinet & Zaleski (2000) utilise a hybrid fixed-grid – front-tracking scheme to undertake a numerical study of the effects of viscosity on bubble collapse. Whilst the additional consideration of viscosity makes quantitative differences, the qualitative features of bubble collapse remain similar for a large range of Reynolds numbers. One recently emerging technique is the interestingly named 'Ghost Fluid Method'; which was developed to capture boundary conditions at a contact discontinuity in the inviscid Euler equations. Thus the numerical smearing, which is inherent where continuity is forced at an interface, is overcome.

Having given a brief insight of research in the field of bubble dynamics covering (predominantly) the last century, the following section outlines the plan for the current body of work.

1.4 Plan of the Current Work

In the current work, we employ a highly accurate boundary integral scheme which offers a number of improvements over the previous benchmark studies of Best (1991, 1994). Of these, the changes to a fourth-order time stepping scheme (afforded to us by increases in computer power over the past decade) and the use of improved smoothing algorithms are key in gleaning improved accuracy from the current formulation. Further improvements which were discovered in the final months of research and hence too late to be included in the main body of work are included in Appendix A. These remove the need for smoothing

in cases where curvature of the surface is not too high.

Utilising our improved numerical scheme, we consider the motion of vapour and gas bubbles near infinite rigid and free boundaries both prior to and following liquid jet impact. Justification for our calculations is provided numerically, through the calculation of energies associated with the motion of the bubble; and by comparison with a range of experiments ranging from spark-generated vapour bubbles formed near an infinite free surface, to laser-induced cavitation bubbles formed near a rigid boundary and viewed at an elevated angle above the boundary, all with great success. Further, to ratify the multi-bubble aspect of our work, experimental images of two bubbles near a free surface are considered.

In order to provide further physical insight into the motions considered, a number of physical quantities are calculated, including pressure and velocity fields in the fluid around the bubble, the energies associated with the motion of the bubble, and the kinetic energy and Kelvin impulse associated with the liquid jet. Many of these, especially quantities associated with the jet require complex and sometimes novel methods of calculation in order that they are correctly determined.

In Chapter 2 we provide a formulation of the problems we consider. Justifications are made for the omission of several physical factors and for other assumptions made. The concept of the Kelvin impulse is introduced and the quantity defined.

In Chapter 3, we introduce the boundary integral scheme and detail the numerical method for a single bubble in an infinite fluid or, through the use of an appropriate image system, in the presence of an infinite rigid boundary. Techniques are also presented for the calculation of instantaneous pressure and velocity fields and for quantities associated with the liquid jet. Results are presented over a wide range of dimensionless parameters, and physical quantities arising from the motion of the bubble thoroughly investigated. Finally, justification of our calculation comes in the form of both the examination of numerical energy calculations and from comparison with experiments.

In Chapter 4 we outline extensions to the basic boundary integral scheme of the preceding chapter which permit the addition of further bubbles and an infinite free surface. Motion of both a single bubble (including the toroidal phase of motion) and two bubbles

near a free surface are considered alongside experimental work. The motion of a bubble in a shallow layer of fluid is considered through the addition of a rigid boundary to the system.

In Chapter 5 we further extend out numerical scheme to allow for the introduction of bubbles at different start times. This relies on the calculation of the fluid potential within the body of the fluid, which is here necessarily integrated in to the main body of code to permit further evolution of the flow.

Finally in Chapter 6, we draw conclusions and give final discussions on the results presented through the main body of this work. Recent advances which further improve our numerical scheme are discussed alongside suggested improvements through which it may be possible to remove the requirement for smoothing from boundary integral studies of this type. Further topics for research are also suggested.

Chapter 2

MATHEMATICAL FORMULATION

2.1 The Flow Field

We consider the motion of one or more bubbles in some fluid domain and denote the volume occupied by the fluid as Ω, using the notation $\partial\Omega$ to refer to its boundary or boundaries. The surface of the bubble (a subset of $\partial\Omega$) will be denoted by S; with an arabic subscript differentiating between bubbles where two or more are considered. Other surfaces types such as a rigid boundary or infinite free surface are distinguished by use of the notation Σ, so $\partial\Omega = S \cup \Sigma$. Where both a rigid boundary and a free surface are present, a subscript RB or FS is used to denote the surface type. We note that when considering the motion of the bubble in an infinite fluid domain, $S \equiv \partial\Omega$. We choose the normal to $\partial\Omega$, say $\boldsymbol{n}$, to be directed out of the fluid, so on S, the normal is directed into the bubble. We also allow for the presence of a uniform gravitational field of magnitude g, which we take to be directed in the negative z-direction with respect to Cartesian coordinates (x, y, z). A schematic of the flow field may be found in Figure 2.1.

We assume the fluid may be adequately described as incompressible and hence conservation of mass yields

$$\nabla \cdot \boldsymbol{u} = 0, \tag{2.1.1}$$

where $\boldsymbol{u}$ is the fluid velocity. If we further consider the flow due to the motion of the bubble(s) to be irrotational, we may introduce a velocity potential ϕ, such that

$$\boldsymbol{u} = \nabla\phi, \tag{2.1.2}$$

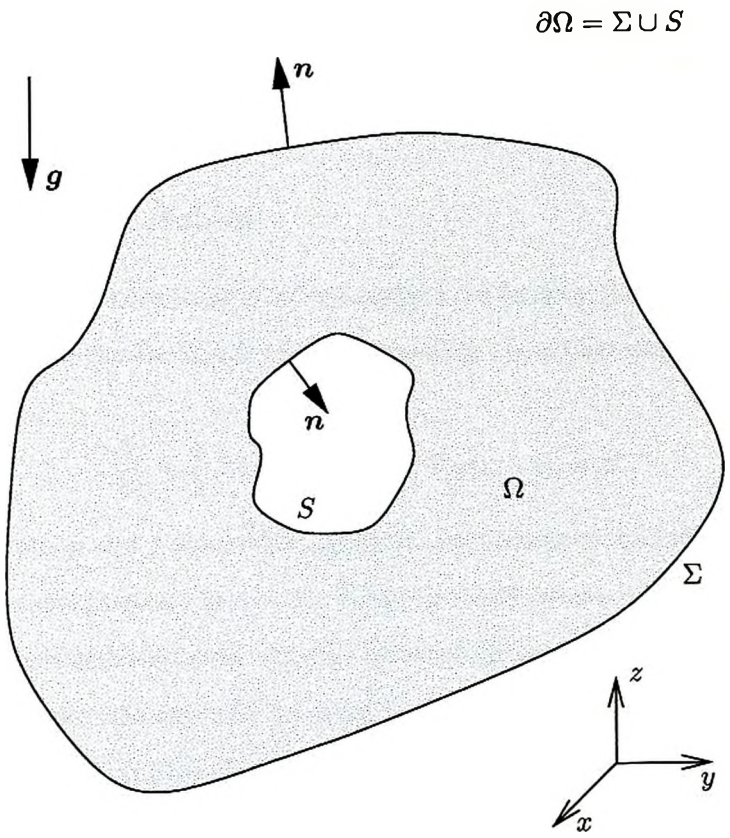

Figure 2.1: Schematic of the flow field and coordinate system.

where ϕ satisfies Laplace's equation

$$\nabla^2\phi = 0, \tag{2.1.3}$$

in the body of the fluid.

2.2 Boundary Conditions

We must also employ an appropriate set of boundary conditions on $\partial\Omega$. In this work, we consider the effects of both rigid and free boundaries, the relevant features of which are detailed below. However first we discuss the bubble.

2.2.1 Surface of the Bubble

In order to determine a condition at a free surface, we employ the integrated form of the momentum equation, the Bernoulli pressure equation. In a Cartesian coordinate system, this takes the form

$$\frac{\partial\phi}{\partial t} + \frac{1}{2}|\nabla\phi|^2 + \frac{p - p_\infty}{\rho} + g(z - z_0) = 0. \tag{2.2.1}$$

Here t denotes time, p and ρ denote the pressure and density of the fluid respectively, and p_∞ is the hydrostatic pressure at $z = z_0$. In the far-field, where no motion occurs, ϕ and its derivatives are identically zero. At the free surface, we apply a continuity condition on the normal stress, whereby the pressure in the fluid differs from a known external pressure due to the effects of surface tension and viscosity which may be calculated over the interface. Substituting this known value into equation (2.2.1) yields a non-linear boundary condition over the free surface. On the surface of the bubble, this stress balance is determined by the description of the bubble contents and the use of viscosity and surface tension in the model. These features are detailed later in this chapter.

2.2.2 Rigid Boundary

At a rigid boundary, there is no flow through the surface and hence the normal velocity there is zero, which in terms of our velocity potential is

$$\frac{\partial\phi}{\partial n} = 0, \tag{2.2.2}$$

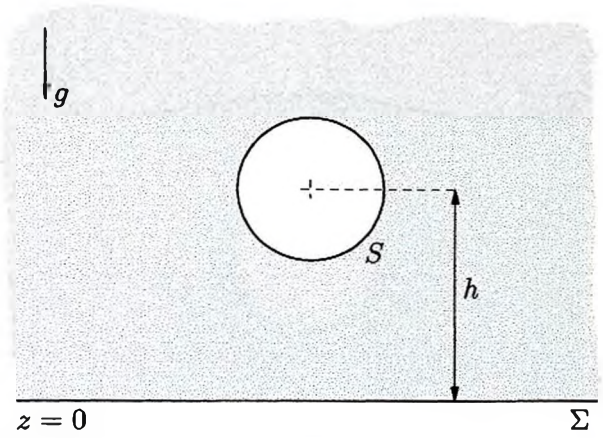

Figure 2.2: Schematic showing a bubble near a rigid boundary. The bubble is generated at a dimensional distance h from the boundary.

where $\partial/\partial n$ signifies a normal derivative. We note this may be calculated by taking the scalar product of the normal to $\partial\Omega$ with the gradient there (i.e. $\boldsymbol{n} \cdot \nabla\phi$). In our work, the rigid boundary is taken to lie in the plane $z = 0$ and dealt with by means of an image system, thus reducing the complexity of the calculations. See Figure 2.2 for a schematic of the system.

2.2.3 Infinite Free Surface

On some infinite free surface Σ, such as the surface of the ocean, we take the pressure there to equal atmospheric pressure and write the elevation of the surface as $\eta(x, y, t)$, and hence equation (2.2.1) yields the dynamic boundary condition

$$\frac{\partial\phi}{\partial t} + \frac{1}{2}|\nabla\phi|^2 + g\eta = 0. \tag{2.2.3}$$

The kinematic boundary condition is given by

$$\frac{\mathrm{D}}{\mathrm{D}t}(z - \eta) = 0, \tag{2.2.4}$$

which effectively states that any fluid particle on the free surface will remain there.

2.2.4 Shallow Fluid Layer

As may be seen in the schematic representation of this problem in Figure 2.4, the shallow layer is bounded by a rigid boundary beneath the bubble and a free surface above.

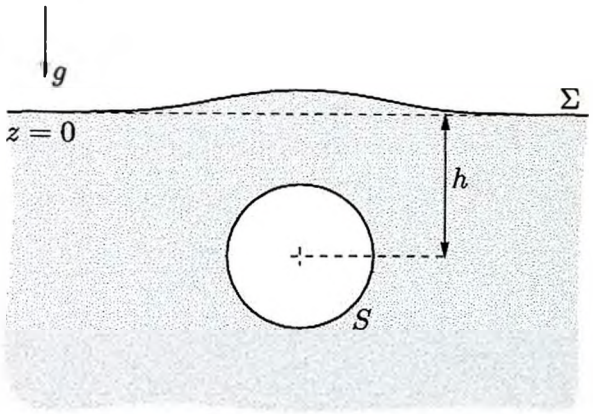

Figure 2.3: Schematic showing a bubble near an infinite free surface. The bubble is generated at a dimensional distance h from the boundary.

Whilst these infinite boundaries can be tens of maximum bubble radii apart, the most interesting behaviour is observed in cases where these boundaries are much closer. Hence the terminology 'shallow fluid layer' is favoured over 'finite depth of fluid' or other similar wording for brevity; though any depth of fluid may be treated equally well. Hence no additional boundary conditions need be introduced. We note the convention of taking the rigid boundary at $z = 0$ holds precedence over the free surface in order to simplify integrations involving images in the rigid boundary. The free surface is hence initially located in the plane $z = d$.

2.3 Contents of the Bubble

Here we employ a simple description of the contents of the bubble, assuming both the pressure and temperature are constant throughout the volume at any given instant and that no flow occurs within the bubble. Whilst these assumptions are not ideal, they allow us to make a good approximation very easily. The bubble contents fall into two categories, liquid vapour and gas, one or both of which may be present in any given situation. Below we outline the features pertinent to each, and note the pressure in a bubble of mixed content is simply the sum of the pressure due to liquid vapour and that due to gas.

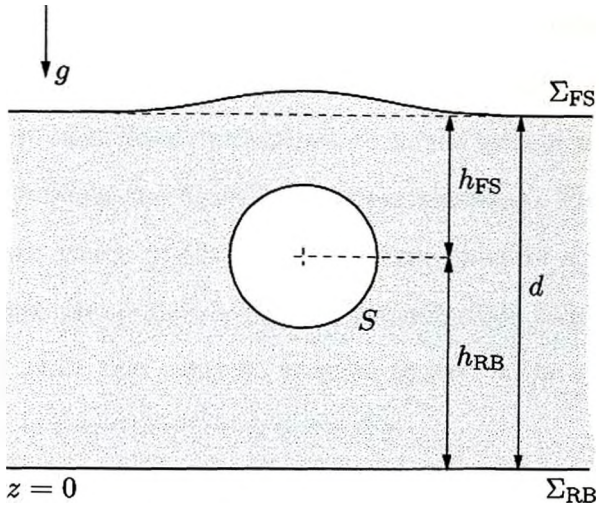

Figure 2.4: Schematic showing a bubble in a shallow layer of fluid of dimensional depth d. The distance from the initial centroid of the bubble to the free surface is denoted by h_{FS} and the distance from the bubble to the rigid boundary by h_{RB}.

2.3.1 Liquid Vapour

Since the work of Lord Rayleigh (1917), studies of cavitation bubble dynamics have assumed the bubble contains only liquid vapour. By further assuming the mass transfer across the surface of the bubble is fast enough[1], we may consider the pressure exerted by the vapour to be constant, say p_v, throughout the lifetime of the bubble.

2.3.2 Gaseous Content

In order to deal with the gaseous contents of an explosion bubble or stable cavitation nucleus which has acquired a gaseous content by, for example, rectified diffusion, we appeal to the work of Lamb (1923). We assume the gas may be considered ideal, and on the time-scales we use to consider the motion, the heat transfer across the surface of the bubble is negligible, so we may consider the process to be adiabatic. Hence we may write the pressure exerted by the gaseous contents of the bubble as

$$p_g = p_0 \left(\frac{V_0}{V} \right)^{\kappa}, \tag{2.3.1}$$

[1]The effects of heat and mass transfer on the motion of a spherical bubble are considered by Storey & Szeri (2000, 2001); and on non-spherical bubble motion in the preliminary work of Szeri, Storey, Pearson & Blake (2002).

where p_0 and V_0 denote the initial pressure and volume of the bubble, V the instantaneous volume of the bubble, and κ is the polytropic index. The value of the polytropic index varies from unity where heat flows unhindered, to γ (the ratio of specific heats) when no heat transfer occurs between the bubble and it surroundings. Physically there is often some limited heat flow, which yields an intermediate value of κ, however this is often found to vary with time. Henceforth we choose our polytropic index, κ to equal the ratio of specific heats, but retain this notation in order to reserve the symbol γ. We note the ratio of specific heats is determined experimentally.

2.4 Non-Dimensionalisation

We choose to non-dimensionalise length with respect to the maximum bubble radius, R_m and scale the pressure, p by $(p - p_\mathrm{v})/\Delta p$, where $\Delta p = p_\infty - p_\mathrm{v}$. In order to determine a time-scale, we appeal to the work of Rayleigh (1917), who obtains an expression for the time of total collapse[2] from a given initial radius. This may be expressed in terms of an incomplete Beta function[3] as

$$t_\mathrm{c} = 6R_\mathrm{m}B_a\left(\frac{5}{6},\frac{3}{2}\right)\sqrt{\frac{3\rho}{2\Delta p}}, \tag{2.4.1}$$

where $a = (R_0/R_\mathrm{m})^3$. Hence the motion occurs on a time-scale proportional to $R_\mathrm{m}\sqrt{\rho/\Delta p}$. Armed with scales for length and time, we choose a potential scale of $R_\mathrm{m}\sqrt{\Delta p/\rho}$. Hence we may non-dimensionalise Bernoulli's equation (2.2.1) to yield

$$\frac{\partial\phi}{\partial t} + \frac{1}{2}|\nabla\phi|^2 + \alpha\left(\frac{V_0}{V}\right)^\kappa - 1 + \delta^2(z-\gamma) = 0, \tag{2.4.2}$$

where all variables are now dimensionless, and we have obtained the dimensionless parameters δ, α and γ, which we recall are

$$\delta = \sqrt{\frac{\rho g R_\mathrm{m}}{\Delta p}}, \tag{2.4.3}$$

$$\alpha = \frac{p_0}{\Delta p}, \tag{2.4.4}$$

[2]This is done by integrating the Rayleigh equation, $R\ddot{R} + \frac{3}{2}\dot{R}^2 + \Delta p/\rho = 0$, twice.

[3]The incomplete Beta function is defined as $B_x(a,b) = \int_0^x t^{a-1}(1-t)^{b-1}\,\mathrm{d}t$. For further details, see Abramowitz & Stegun (1965).

and

$$\gamma = \frac{h}{R_{\mathrm{m}}}. \tag{2.4.5}$$

Physically δ may be thought of as being the ratio of the bubble half-life to the time which it takes to rise one maximum bubble radius from rest due to the action of buoyancy; and is consequently referred to as the buoyancy parameter. Similarly α arises in the consideration of gas bubbles and is a measure of the initial gas pressure within the bubble. As such the parameter is often termed the strength parameter (Best 1991) or compression ratio (Blake & Keen 2000). For the consideration of vapour bubbles, $\alpha = 0$. The final parameter, γ is the standoff distance, the dimensionless distance between bubble and boundary.

2.5 Initial Conditions

In order we may properly prescribe our problem, we must now consider a suitable set of initial conditions with which to start our calculations. We begin by outlining conditions for vapour bubble calculations, where the internal pressure is taken to be constant and the motion is governed by an initial velocity imposed on the surface of the bubble. In Section 2.5.2 we consider initial conditions for a gas bubble whose motion is due to the initially high (or low) pressures within the bubble. Finally we recall conditions for an infinite free surface.

2.5.1 Vapour Bubbles

We begin by recalling the equation due to Rayleigh (1917), which governs the radial motion of a spherical vapour cavity

$$R\ddot{R} + \tfrac{3}{2}\dot{R}^2 + \frac{\Delta p}{\rho} = 0. \tag{2.5.1}$$

During the earliest moments of the lifetime of a cavitation bubble, it may be reasonably assumed the spherical bubble approximation remains valid, since during this time the bubble is small and will therefore experience negligible forces due to buoyancy and the presence of boundaries in the system.

Hence we may assume an initial radius, say R_0 at time t_0, to be determined by the solution of (2.5.1), which may then yield an initial potential over the surface of the bubble as

$$\phi_0 = -R_0\dot{R}_0. \tag{2.5.2}$$

This is readily obtainable from the literature (Gibson & Blake 1980; Blake, Taib & Doherty 1986) as

$$\phi_0 = -R_0\sqrt{\frac{2\Delta p}{3\rho}\left[\left(\frac{R_m}{R_0}\right)^3 - 1\right]}, \tag{2.5.3}$$

with corresponding initial time

$$t_0 = 3R_0B_a\left(\tfrac{5}{6},\tfrac{3}{2}\right)\sqrt{\frac{3\rho}{2\Delta p}}, \tag{2.5.4}$$

where $a = (R_0/R_m)^3$. Here the value of $\dot{R}_0$ has been obtained via integration of equation (2.5.1), yielding the initial potential over the surface of the bubble in the absence of boundaries. We note the constant multiplying equation (2.5.4) is half that of (2.4.1) which takes into account both the growth and collapse of a cavity.

Rigid Boundary

In many studies, the initial Rayleigh potential given by equation (2.5.3) is also used as an initial condition for bubble motion near a rigid boundary or other interface type, but is not entirely accurate. In order to adjust this potential to account for the presence of the rigid boundary, we use the method suggested by Blake, Taib & Doherty (1986). Here the image source is added to the potential to yield the initial potential

$$\phi_0 = \phi_0^R\left[1 + \frac{R_0}{\sqrt{r^2 + (z+\gamma)^2}}\right], \tag{2.5.5}$$

where ϕ_0^R is the initial Rayleigh potential given by equation (2.5.3), (r, z) are the coordinates on the bubble surface and γ is the standoff distance. We note here this adjustment changes only slightly the initial potential, and as such will make a negligible change to the stable growth phase of the bubble motion. In comparing results with and without the correction, no visible difference is observed.

Free Surface

For the case of the bubble near a free surface, the image sink term was added by Blake, Taib & Doherty (1987) to yield the initial potential

$$\phi_0 = \phi_0^R \left[1 - \frac{R_0}{\sqrt{r^2 + (z+\gamma)^2}} \right]. \tag{2.5.6}$$

2.5.2 Gas Bubbles

Here we consider the initial state of a bubble which has some gaseous content, such as is the case with an underwater explosion bubble or a laser-induced cavitation bubble. In these cases, the motion is driven by the internal gas pressure, in addition to any initial velocity we impose on the bubble. In order to allow for the case of a deeply-submerged buoyant bubble beneath a free surface, it is necessary to take into account the difference in atmospheric pressure and hydrostatic pressure at the bubble inception depth in order to correctly calculate the initial radius. However, any variation of effects due to buoyancy and nearby boundaries over the surface of the bubble are ignored. Hence we consider the early motion to be governed by the non-dimensional equation

$$R\ddot{R} + \frac{3}{2}\dot{R}^2 = \alpha \left(\frac{R_0}{R} \right)^{3\kappa} - 1 - \delta^2 \gamma, \tag{2.5.7}$$

where we note the final term of this modified Rayleigh-Plesset equation should be omitted where the pressure at the inception depth is used as the reference pressure. This is primarily the case where no free surface is present.

For all but the very smallest scale oscillations, we may integrate backwards in time to yield a new initial radius and pressure which corresponds to a zero initial velocity. Since (for most motions) the time-scale over which we must integrate is much smaller than the period of oscillation, we may adequately assume the motion to be driven from rest by the internal pressure of the bubble. Hence we choose the initial potential over the surface of a gas bubble to be

$$\phi_0 = 0. \tag{2.5.8}$$

We further choose the initial radius of the bubble, R_0, to be such that the maximum radius to which the bubble grows in an infinite fluid is R_m. Integrating equation (2.5.7)

yields an equation for the bubble radius, R of the form

$$\dot{R}^2 = \frac{2\alpha R_0^{3\kappa}}{3(\kappa-1)}\left(\frac{R_m^{3-3\kappa}}{R^3} - \frac{1}{R^{3\kappa}}\right) + \frac{2}{3}\left(\frac{R_m^3}{R^3} - 1\right) + \frac{2\delta^2\gamma}{3}\left(\frac{R_m^3}{R^3} - 1\right), \tag{2.5.9}$$

where we have taken $\dot{R} = 0$ at $R = R_m$. Utilising the fact that $\dot{R} = 0$ at $R = R_0$, we obtain an equation for R_0 which is solved using Newton's method. In the above, we note that: a dot denotes a time derivative, α the compression ratio, δ the buoyancy parameter, γ the standoff distance and κ is the ratio of specific heats. We note the required maximum bubble radius is usually taken to be unity, though other values may be required in multi-bubble systems.

It is convenient to comment at this point on a pseudo-equilibrium radius. This is effectively the radius of a spherical bubble wherein the internal pressure balances the external hydrostatic pressure for a given set of dimensionless parameters. Setting $\dot{R} = \ddot{R} = 0$ in equation (2.5.7) and rearranging yields the equilibrium radius

$$R_{eq} = \left(\frac{\alpha}{1+\delta^2\gamma}\right)^{\frac{1}{3\kappa}} R_0. \tag{2.5.10}$$

2.5.3 Infinite Free Surface

On an infinite free surface we choose the initial potential there to be

$$\phi_0 = 0. \tag{2.5.11}$$

For a gas bubble, this choice is fine since we consider the fluid to be initially at rest with the motion being driven by a high excess pressure within the bubble whereon the surface potential is zero; hence the initial potential is zero throughout the fluid.

For a vapour bubble, this choice requires further justification since, in this case, the pressure within the bubble is considered constant and the motion is driven by an initial velocity imposed on the surface of the bubble. We begin by noting that the potential due to the small, initially spherical bubble is $\phi = -R^2\dot{R}/r$, at a distance r from the centroid. Hence the contribution of the initial potential at the free surface is given by $\phi_0 = -R_0^2\dot{R}_0/\gamma$, where γ is the initial dimensionless displacement of the bubble from the free surface. We note from (2.5.3) that $\dot{R}_0 \sim R_0^{-3/2}$, and hence

$$\phi_0 \sim \frac{R_0^{1/2}}{\gamma}. \tag{2.5.12}$$

Thus our choice of $\phi_0 = 0$ is an accurate approximation provided we choose an initial radius such that $R_0 \ll \gamma^2$. Computationally the choice of such a small initial radius for this to hold for, say, $\gamma = 0.56$ would introduce errors into our calculations and hence we choose an initial radius of $R_0 = 0.1$ with corresponding initial time $t_0 = 0.0015495$. In order to show that our choice of initial potential on the free surface is still valid, we consider the kinetic energy of the liquid due to a spherical bubble, given by

$$E = 4\pi\rho R^3 \dot{R}^2. \tag{2.5.13}$$

If we consider R of the form $R \sim t^\alpha$, we require $\alpha = 2/5$ so that the energy of the system is independent of time (the famous Taylor two-fifths law: see for example Batchelor 1996, Brenner & Stone 2000). Neglecting gravity[4] in the free surface dynamic condition (2.2.3) yields

$$\frac{\partial \phi}{\partial t} + \frac{1}{2}|\nabla\phi|^2 = 0, \tag{2.5.14}$$

which we may integrate with respect to time from $t = t_\epsilon$ to $t = t_0$ noting that $|\nabla\phi| = R^2\dot{R}/\gamma^2 \sim t^{1/5}/\gamma^2$. This yields

$$\phi(t_0) - \phi(t_\epsilon) \sim \int_{t_\epsilon}^{t_0} \frac{t^{2/5}}{\gamma^4}\,\mathrm{d}t. \tag{2.5.15}$$

If we choose t_ϵ such that $\phi(t_\epsilon) \sim 0$ and write $\phi(t_0) = \phi_0$, then

$$\phi_0 \sim \left[\frac{t^{7/5}}{\gamma^4}\right]_{t_\epsilon}^{t_0} < \frac{t_0^{7/5}}{\gamma^4}. \tag{2.5.16}$$

Hence our choice of initial potential $\phi_0 = 0$ on the free surface is acceptable provided $t_0^{7/5} \ll \gamma^4$, a condition met in all examples considered in this study.

2.6 Validity of Assumptions

In formulating the model, we have chosen to omit a number of physical aspects from the problem, including the viscosity and compressibility of the fluid and surface tension at the bubble–fluid interface. Whilst we do accept these mechanisms make a very real contribution to the physics of the problem, we show below that a reasonable approximation can still be made in their absence.

[4]Typically, spark generated vapour bubbles have maximum radii $\sim$ millimetres, and so buoyancy effects are unimportant.

We determined earlier a time-scale based on the collapse time of a Rayleigh cavity of $R_{\rm m}\sqrt{\rho/\Delta p}$ and length-scale $R_{\rm m}$. It is therefore appropriate we utilise these to generate a Reynolds number, Re for the radial motion,

$$\mathrm{Re} = \frac{R_{\rm m}\sqrt{\rho\Delta p}}{\mu}, \tag{2.6.1}$$

which physically represents the ratio of inertial terms to viscous terms. In order to ascertain the magnitude of this parameter, we consider the spark-generated bubbles in the work of Blake & Gibson (1981), generated in a reduced pressure environment in water. Here $R_{\rm m} \sim 10^{-2}$m, $\Delta p \sim 10^4$Pa and water is characterised by $\rho \sim 10^3$kg/m^3, $\mu \sim 10^{-1}$kg m/s yielding a Reynolds number Re $\sim 10^4$. A similar figure is also obtained for the laser-generated cavities of Vogel, Engelhardt, Behnle & Parlitz (1996), whose results were obtained at atmospheric pressure. In the context of underwater explosion bubbles near to the sea surface, Reynolds numbers of the order of 10^6 are obtained.

We may also define a Reynolds number due to translational motion under the action of buoyancy forces to ascertain the rôle viscosity plays in this motion. In order to do this, we consider the final velocity of a bubble rising from rest to a distance $R_{\rm m}$ above its initial location. Hence we consider an energy balance between the initial gravitational potential energy of the water to be displaced and the final kinetic energy of the bubble due to its added mass, hence

$$mgR_{\rm m} = \tfrac{1}{2}m_{\rm a}U^2, \tag{2.6.2}$$

which yields

$$U = 2\sqrt{gR_{\rm m}}. \tag{2.6.3}$$

Here m is the mass of the fluid, $m_{\rm a}$ the added mass of the bubble and U is the bubble velocity after rising one maximum bubble radius. The added mass due to a sphere is readily calculated in the case of a bubble as half the mass of the fluid it replaces. (See, for example, Lighthill 1990.) Hence a Reynolds number $\mathrm{Re} = UL/\nu$ is given by

$$\mathrm{Re} = \frac{2\rho\sqrt{gR_{\rm m}^3}}{\mu}, \tag{2.6.4}$$

which becomes

$$\mathrm{Re} \sim 10^7 R_{\rm m}^{\frac{3}{2}}. \tag{2.6.5}$$

Hence we may reason that for large explosion bubbles, viscosity plays very little part in the translational motion of the bubble. Whilst for a smaller cavitation nuclei, where this number is small, very little translational motion will occur due to the small buoyancy forces on the bubble and hence this consideration is not required.

Further, we comment on the diffusion of vorticity. The characteristic thickness of the boundary-layer at the surface of the bubble, where the vorticity diffuses may be given by

$$\delta^* = \mathrm{O}\Big((\nu t)^{\frac{1}{2}}\Big), \tag{2.6.6}$$

where we note that in this context, δ^* refers to the boundary layer thickness. Comparing this with the characteristic length-scale, the maximum bubble radius, we obtain

$$\frac{\delta^*}{R_{\mathrm{m}}} = \frac{(\nu t)^{\frac{1}{2}}}{R_{\mathrm{m}}} = \mathrm{Re}^{-\frac{1}{2}}. \tag{2.6.7}$$

As calculated above, these Reynolds numbers are large and hence over one cycle, the boundary layer is very thin. Hence we may reasonably neglect any consideration of energy loss through diffusion of vorticity.

In order to ascertain the importance of surface tension effects most easily, we consider a modified form of Rayleigh's equation due to Poritsky (1952) which is given by Best (1991) in the dimensionless form

$$R\ddot{R} + \tfrac{3}{2}\dot{R}^2 + \frac{4}{\mathrm{Re}}\dot{R}R + \frac{2}{We}\frac{1}{R} = p_g - 1, \tag{2.6.8}$$

with

$$We = \frac{R_{\mathrm{m}}\Delta p}{\sigma}. \tag{2.6.9}$$

For an air–water interface, $\sigma = 7.28 \times 10^{-2}\mathrm{N/m}$. This yields a value of $We \sim 10^3$ and hence surface tension will not make a contribution unless $R \sim 10^{-3}$, i.e. when the bubble falls to about one-thousandth of its maximum radius.

If we proceed to consider the effects of surface tension for the general motion of a non-spherical bubble, the term $2/R$ above is replaced by the term $\nabla \cdot \boldsymbol{n}$, the local surface curvature. Only during jet formation in very small scale experiments will a region of sufficiently high curvature arise so as to play a significant rôle. This is commented upon later in the light of some computational results.

It is also worthwhile at this stage to discuss the assumption of liquid incompressibility. Water, for example, has a small but finite compressibility, as indicated by the relatively large speed of sound $\sim$ 1500m/s. Only when the fluid velocity approaches that of the speed of sound would we expect these effects to be noticeable. Even during asymmetric collapse, when a high-speed liquid jet threads the bubble, surface velocities reach only about 100m/s (Lauterborn & Bolle 1975). Hence for much of the bubble's lifetime it is reasonable to neglect fluid compressibility. However a typical speed of sound for gas $\sim$ 300m/s, and so jet motion may appreciably affect the gas dynamics within the bubble during the final stages of collapse. We comment here that besides the aforementioned jet impact, compressibility will also play a rôle during initiation when shocks propagate into the fluid, and during rebound of a gas bubble when the volume passes through its minimum value.

2.7 The Kelvin Impulse

In the final section of this chapter, we introduce the concept of the Kelvin impulse and outline its application to the field of bubble dynamics. Following definition of the quantity, we proceed to outline its use in the remainder of this work and provide sources for further reading on the topic.

The Kelvin impulse has proved to be an extremely useful concept in the area of unsteady fluid mechanics. Its particular value in the field of bubble dynamics was first realised by Benjamin & Ellis (1966) in their work on cavitation. The Kelvin impulse has the dimensions of momentum and is related to the concept of impulse in particle mechanics, and as noted by Benjamin & Ellis:

> *"...the impulse associated with a moving bubble presents much the same intuitive physical picture as the momentum of a rigid projectile in free space, and hence the feasibility of impact effects in the process of cavitation damage is immediately appreciated."*

We note here care must be taken in relating the Kelvin impulse to instantaneous changes in the fluid momentum, which will depend on the far-field conditions applied. In general

the choice of conditions at infinity are immaterial as these will have no influence on the motion of the body under consideration. And hence Benjamin & Ellis recommend that:

> *"...one should always reason in terms of the Kelvin impulse, not in terms of the fluid momentum..."*

For a rigid body, Kelvin established that

$$\frac{\mathrm{d}\boldsymbol{I}}{\mathrm{d}t} = \boldsymbol{F}. \tag{2.7.1}$$

where $\boldsymbol{I}$ is known as the Kelvin impulse and $\boldsymbol{F}$ is some external force applied to the body in question. It was noted by Lamb (1932) this argument remains valid for deformable bodies, or equivalently, rotationally motive masses of fluid. Despite these observations, it was not until the aforementioned work of Benjamin & Ellis (1966) that the technique was applied to bubble dynamics.

Physically, the Kelvin impulse may be thought of as an instantaneous 'wrench' required to generate motion from rest and is defined as

$$\boldsymbol{I} = \rho \int_S \phi \boldsymbol{n} \, \mathrm{d}S, \tag{2.7.2}$$

a thorough derivation of which may be found in the paper by Blake (1988).

Work by Blake & Cerone (1982) and Blake (1988) used the principle of the Kelvin impulse to determine the gross behaviour of bubble motion near a number of boundary types including the rigid and free boundaries covered in this work. By using a source–dipole combination and system of images to model the potential, it was possible to determine analytically an expression for the force, $\boldsymbol{F}$ and hence impulse due to these boundaries.

Perhaps the most useful aspect of the Kelvin impulse is the ease with which it allows researchers to partition the parameter space associated with the standoff distance, γ and buoyancy, δ into separate regions where gross bubble motion and jet formation is directed either towards or away-from the boundary in question. The resulting partition is often referred to as the 'null impulse line', near which there is negligible gross bubble motion. However, due to the competing effects of buoyancy and the Bjerknes force of

attraction (rigid boundary) or repulsion (free surface), the actual motion of the bubble if often extremely unusual. Examples of the success of this technique include the papers by Blake, Taib & Doherty (1986, 1987) where the gross behaviour of bubble motion both from experiments and from numerical calculations is plotted on the γ–δ parameter space and shows good agreement with the partitioning provided by the null impulse curve.

Further advances in the calculation of the null impulse curve were made by Best (1991), who takes account of the vertical motion of the bubble centroid. A system of coupled differential equations results, the solution of which gives a similar null impulse curve, but is shifted slightly for lower γ-values. In later work, Best & Blake (1994) formulated a scheme which yields a 'zone of attraction' about a body of revolution.

In this work the Kelvin impulse is calculated numerically throughout the lifetime of the bubble and is used to evaluate the gross behaviour of the bubble throughout the expansion and collapse phases. New techniques are introduced which allow the calculation of the Kelvin impulse associated with the liquid jet which forms in the final moments of collapse. This enables us to determine what proportion of the instantaneous 'wrench' is connected with the jetting phenomena and hence further our understanding of the non-spherical behaviour of the bubble.

2.8 Summary

In this chapter we have outlined the basic mathematical model which we employ throughout this work to examine bubble motion. Whilst we have omitted many complex physical phenomena, we have shown through physical reasoning that many of these play a limited rôle for much of the lifetime of the bubble. Though not all omissions were discussed, we shall show through comparison with experiments that the resulting model is a good one.

Chapter 3

BOUNDARY INTEGRAL METHOD: INFINITE FLUID AND RIGID BOUNDARY TECHNIQUES

In this chapter, we introduce the boundary integral method (BIM) as a tool for the numerical calculation of the motion of bubbles near boundaries. We begin by presenting an overview of previous boundary integral (BI) studies and related numerical techniques, primarily in the field of bubble dynamics, but encompassing several branches of fluid dynamics where necessary, in order to introduce techniques or present peripheral discussion. We note here the extensive use of BI techniques in solid mechanics which were important in inspiring early works in the field of bubble dynamics, notably the key work of Taib (1985); though discussion of this vigourously researched field is well beyond the scope of the current work.

Following this discussion, we outline the derivation of the required integral equation representation of the solution to Laplace's equation (2.1.3) upon which our techniques are founded. We then proceed to detail the numerical scheme required for the solution of this resulting equation. Following liquid jet impact, a necessary reformulation of the integral equation[1] is required; this is presented in Section 3.4.1 and followed by a complementary discussion of changes to the numerical scheme in Section 3.4.2. Following coverage of the basic numerical techniques we outline further methods which permit the calculation of physical quantities associated with the bubble and surrounding body of fluid. A number of results are then presented and discussed. Primary validation for our work is given in the form of the numerical calculation of energies associated with the bubble motion. In the

[1]Originally due to Best (1991).

section following this, our calculations are shown to compare well against experiments, thus justifying the assumptions which we made earlier. At the close of the chapter we discuss the success of our endeavours.

3.1 An Overview of Computational Studies

Over the past few decades, several computational techniques have been employed to calculate the motion of bubbles, cavities and drops for a wide range of physical problems. Many of these may be effectively reduced to inviscid potential problems which are valid for much of the lifetime of the respective bodies: thus requiring solution of Laplace's equation in the fluid domain. In the current work, we choose to use a direct boundary integral method based on Green's identity, which allows us to formulate the problem entirely on the boundaries of the fluid domain, effectively reducing the dimensions of the problem by one. However it is pertinent to add to our discussions in the introductory chapter of this thesis and further discuss complementary techniques.

Of key interest are spherical bubble models which have been employed since the inception of work in this field by Rayleigh (1917) and on whose work these models build. Although we are now fully aware of the non-spherical behaviour of bubbles in many physical situations, the assumption of a spherical bubble allows researchers to readily introduce the consideration of many physical phenomena into a simple equation of motion. Historically these included effects due to: the presence of nearby boundaries (for example, Herring 1941), surface tension and viscosity, or weakly compressible effects (Keller & Kolodner 1956 through Prosperetti & Lezzi 1986 and beyond). More recently, aspects such as the introduction of heat and mass transfer effects by Storey & Szeri (2000, 2001) are considered. Such models are mentioned as many of the effects may be included (albeit in some cases with a high degree of difficulty) within BI schemes (e.g. heat and mass transfer – see Szeri, Storey, Pearson & Blake 2002).

In ascertaining the motion of bubbles near boundaries, the consideration of non-spherical effects is paramount in obtaining an understanding of the physical problem. One class of techniques of note are the level-set methods which were briefly discussed in Section 1.3. Using one variant of the level-set method, Sussman & Smereka (1997)

examined a number of free boundary problems, wherein the interface is taken as the zero level-set of a continuous function and the motion of the fluid and gas is described by the solution of the incompressible Navier-Stokes equations. Computationally, the key feature of this technique is that all changes in geometry are accounted for automatically and no reformulation of the problem or changes to the code are required. This advantage is, however, outweighed by the need to solve the governing equations throughout the fluid domain. Despite the limitations placed on the grid resolution by Sussman & Smereka, results presented did compare well with previous studies.

More relevant to the current study is the indirect BIM used by Lundgren & Mansour (1988) to study the oscillation of drops with weak viscous effects. In this formulation, the potential is determined in terms of a dipole distribution over the interface. This leads to a Fredholm integral equation of the second-kind which must be solved iteratively and hence indirectly, with typically ten iterations per time step required. This and earlier work by Baker, Meiron & Orszag (1984) was compared with a direct BIM by Pelekasis, Tsamopoulos & Manolis (1992), who concluded the direct method was not only more computationally efficient, but also more stable. However it was found by Oğuz & Prosperetti (1990) that the problem of drop impact on a liquid surface, where surface tension effects dominate, required an indirect formulation in order to avoid stability problems. The inclusion of surface tension effects in an inviscid formulation produced problematic high-frequency, short capillary waves to occur. We note the use of a novel smoothing technique by Lundgren & Mansour (1988) which proves to be useful for the current work and is discussed later.

Despite the success of other methods and the increased availability of computer power, the direct BIM is chosen because of the excellent results it has produced for previous researchers in the field of bubble dynamics. It is felt the increase in computational expense negates any small increase in accuracy an indirect formulation and iterative method of solution would provide, especially as similar increases in accuracy may be obtained by a small, but non-prohibitive change in the time step used.

As previously noted in Chapter 1, the first application of the BIM to the field of bubble dynamics may be attributed to Lenoir (1976) who considers the collapse of an

initially spherical bubble near to both rigid and free boundaries. A more successful consideration of the collapse of a spherical void may be found in the conference paper by Guerri, Lucca & Prosperetti (1981), though the brevity of the paper somewhat limits the cases considered. Hence it is difficult to determine the accuracy of the numerical scheme employed. As we have stressed so far, in both these papers, the bubble is assumed to collapse from an initially spherical maximum volume, and as such, no consideration is given to the expansion phase of the bubble. Despite the proven, stable nature of the expansion phase (e.g. Prosperetti & Seminara 1978) it is essential to calculate the expansion phase of the bubble where any source of asymmetry is present in the flow field, since any perturbation from a spherical state during expansion may have great influence during the unstable collapse phase. This reasoning holds true even for bubbles formed several maximum radii from the boundary where surface geometry may appear spherical, yet is often not, with further non-spherical attributes becoming apparent if consideration is given to surface velocities or quantities in the surrounding fluid.

The earliest application of the BIM which considers both the growth and collapse of a bubble may be attributed to Taib (1985). In this work, the bubble is assumed to grow from a small, initially spherical shape (though care is taken to adjust the potential for the presence of nearby boundaries) up to maximum volume, following which, collapse ensues and the motion is followed (in most cases) through to the time of liquid jet impact. We regard this work as a key source of information for many basic aspects of axisymmetric BI calculations for bubbles, wherein great detail is given regarding the assembly of the required integrals and subsequent removal of singularities during collocation. Despite the primitive piecewise-linear representation of the surface geometry and potential used in this work and subsequent papers (Blake, Taib & Doherty 1986, 1987), these works provided benchmark calculations for the motion of vapour bubbles near to rigid and free boundaries for a number of years. The only shortcomings due to the scheme employed by Taib are the omission in these studies of calculations very close to an infinite free surface, when very narrow liquid jets are observed to form; and in several cases near to the null impulse state where unusual geometries arise and the calculations break down. In general, these cases are all ones in which regions of high curvature form. Several of

the cases considered by Taib (1985) provide an extreme test, capable of stretching even the revised schemes presented in this work. In particular, in the case of the buoyant bubble above a rigid boundary in Figure 4.9 of Taib (1985), which halts prior to jet formation, where we would expect an ultra-high speed very narrow liquid jet to form from the bottom of the bubble.

The implementation of the direct BIM was later improved by Kucera (see Best 1991, Best & Kucera 1992). In this scheme, the surface geometry and potential thereon are described by a series of cubic spline elements fitted through the collocation points on the interface. Such a scheme thus permits more accurate calculations in the problem cases mentioned above. Moreover, Best (1991) extended the BI formulation to examine the toroidal phase of an underwater explosion bubble which develops following liquid jet impact. This is achieved via the addition of a cut in the fluid domain to retain the singly connected topology post impact. In this early work, Best evolved the cut in time as a material surface. Whilst this permitted an added method of visualising the flow around the bubble, it was found to be computationally expensive, with the addition of more nodes being required in order to accurately capture the geometry of the cut. Due to the deformation of the cut, which often became wrapped around the bubble, it was difficult to obtain good results in close proximity to a rigid boundary.

This was later improved by Best (1994) who introduced a 'dynamic cut relocation algorithm', in which the cut is taken to be a simple disc, any deformation of which may be ignored as it may then be arbitrarily remapped at each time step to this simple geometry. By careful labelling of surface nodes, the cut may be kept entirely within the column of fluid which threads the bubble; this being necessary in order that the cut does not cross the surface of the bubble. This revised scheme enables calculations to be made in close proximity to boundaries as we later show. Furthermore, due to the simpler implementation of this scheme, results obtained have improved accuracy;[2] and without a need to track the cut, large computational savings are made.

The numerical scheme used in the current work is based on the techniques developed by Kucera and used with great success by Best (1991) and Best & Kucera (1992). Also

[2]Since the first-order approximations of the fluid velocity at the cut employed by Best (1991) are no longer required.

employed is the dynamic cut relocation algorithm due to Best (1994) in order to permit calculations in close proximity to boundaries. In this study, further refinements are made, thus improving computational accuracy. One key technique in doing this is the implementation of a smoothing method due to Lundgren & Mansour (1988) which is found to be sufficient to remove surface instabilities, yet has a lesser effect on the energies of the system than the often used technique of Longuet-Higgins & Cokelet (1976). A number of novel techniques are also developed to calculate physical quantities associated with the bubble, liquid jet and surrounding fluid. In later chapters, further advances are made to permit the inclusion of further boundaries in the fluid domain.

3.2 Boundary Integral Formulation

In our formulation of the problem in Chapter 2, it was shown that the behaviour of the fluid is governed by a velocity potential ϕ, which satisfies Laplace's equation (2.1.3) throughout the fluid domain. We begin the integral equation formulation by introducing an arbitrary function w and integrating over the domain Ω to yield

$$\int_{\Omega} \nabla^2 \phi \, w \, \mathrm{d}V = 0, \tag{3.2.1}$$

where $w \equiv w(r, z, t)$ and $\mathrm{d}V$ is a volume element of Ω. We now integrate by parts twice, which gives the mixed surface-volume equation

$$\int_{\partial\Omega} \left(\frac{\partial \phi}{\partial n} w - \phi \frac{\partial w}{\partial n} \right) \mathrm{d}S + \int_{\Omega} \phi \, \nabla^2 w \, \mathrm{d}V = 0, \tag{3.2.2}$$

where $\mathrm{d}S$ is an appropriate surface element of the boundary. We now replace our arbitrary function w with the Green's function $G(\boldsymbol{p}, \boldsymbol{q})$ which satisfies the equation

$$\nabla^2 G(\boldsymbol{p}, \boldsymbol{q}) = -\delta(\boldsymbol{p} - \boldsymbol{q}), \tag{3.2.3}$$

where $\delta(\boldsymbol{x})$ is the Dirac delta function, and $\boldsymbol{p}$ and $\boldsymbol{q}$ are points in the fluid domain. This yields the fundamental solution

$$G(\boldsymbol{p}, \boldsymbol{q}) = \frac{1}{4\pi |\boldsymbol{p} - \boldsymbol{q}|}. \tag{3.2.4}$$

In the case of bubble motion near a rigid boundary, we may circumvent the need to integrate over this infinite boundary via the use of a modified Green's function, which provides an exact solution. The appropriate Green's function is

$$G(\boldsymbol{p},\boldsymbol{q}) = \frac{1}{4\pi|\boldsymbol{p}-\boldsymbol{q}|} + \frac{1}{4\pi|\boldsymbol{p}-\boldsymbol{q}'|}, \tag{3.2.5}$$

where $\boldsymbol{q}'$ is the image of the point $\boldsymbol{q}$ in the rigid boundary.

In introducing the Green's function for either an infinite fluid or rigid boundary, we obtain an equation which is valid for some point $\boldsymbol{p}$ in the interior of the fluid, but not on the boundary (i.e. $\boldsymbol{p} \in \Omega \setminus \partial\Omega$). In order to make the equation valid there, we move the point, $\boldsymbol{p}$ to the boundary and consider a hemisphere of radius ϵ about the point (see Brebbia 1980). We may then replace the surface integral by

$$\int_{\partial\Omega} \longmapsto \int_{\partial\Omega\setminus\Sigma_\epsilon} + \int_{\Sigma_\epsilon}, \tag{3.2.6}$$

where Σ_ϵ signifies the curved surface of the hemisphere. The surface integrals may then be evaluated and the limit $\epsilon \to 0$ taken. In doing this a contribution from the term $\phi\,\partial G/\partial n$ arises. A similar method may be used for a point $\boldsymbol{p}$ occurring outside the fluid domain Ω. Hence the solution to Laplace's equation may be written

$$c(\boldsymbol{p})\phi(\boldsymbol{p}) = \int_{\partial\Omega} \left(\frac{\partial\phi(\boldsymbol{q})}{\partial n} G(\boldsymbol{p},\boldsymbol{q}) - \phi(\boldsymbol{q}) \frac{\partial G(\boldsymbol{p},\boldsymbol{q})}{\partial n} \right) \mathrm{d}S, \tag{3.2.7}$$

where the location dependent coefficient $c(\boldsymbol{p})$ is given by

$$c(\boldsymbol{p}) = \begin{cases} 1, & \boldsymbol{p} \in \Omega \setminus \partial\Omega, \\ \frac{1}{2}, & \boldsymbol{p} \in \partial\Omega. \end{cases} \tag{3.2.8}$$

We note here this is valid only so long as the boundary remains smooth. In the event this no longer holds true (where, for example, $\partial\Omega$ has a corner or edge) then equation (3.2.7) remains valid, but the value of $c(\boldsymbol{p})$ would differ from $1/2$ and may be calculated using the methods above. For examples of non-smooth geometries, see Seybert, Soenarko, Rizzo & Shippy (1985), who consider bodies such as cubes and cylinders.

3.3 Method of Solution

The method of solution may be summarised as follows. At some time t, both the shape of the bubble and the potential over its surface are known, so equation (3.2.7) is a Fredholm integral equation of the first-kind for the unknown normal velocity $\partial\phi/\partial n$ (hereafter denoted as ψ for convenience). Its solution yields the normal velocity directly and the r and z-components of velocity may be calculated with little effort, see page 57. Knowledge of the surface velocity allows us to advance both the surface geometry and potential using an Eulerian step so it is known at some time $t + \delta t$ shortly afterwards. Repetitions of this scheme allows us to advance the flow in time.

The surface geometry is advanced using the kinematic boundary condition, which for a given point $\boldsymbol{p}_i \in S$ is

$$\frac{\mathrm{D}\boldsymbol{p}_i}{\mathrm{D}t} = \boldsymbol{u}_i, \tag{3.3.1}$$

where $\boldsymbol{u}_i$ is the fluid velocity at the point $\boldsymbol{p}_i$. Knowledge of the fluid velocity allows us to integrate this expression yielding a new surface geometry. In a similar fashion, the rate of change of the velocity potential on the bubble surface is governed by the equation

$$\frac{\mathrm{D}\phi_i}{\mathrm{D}t} = \frac{\partial\phi_i}{\partial t} + |\nabla\phi_i|^2, \tag{3.3.2}$$

into which we substitute the boundary condition for the pressure which incorporates Bernoulli's equation[3] to yield the dimensionless equation

$$\frac{\mathrm{D}\phi_i}{\mathrm{D}t} = \frac{1}{2}|\boldsymbol{u}_i|^2 + 1 - \alpha\left(\frac{V_0}{V}\right)^{\kappa} - \delta^2(z_i - \gamma), \tag{3.3.3}$$

where a subscript i denotes that quantity evaluated at the point $\boldsymbol{p}_i$. For a point on the surface of the bubble, we know both $\boldsymbol{u}_i$ from the solution of (3.2.7) and may readily calculate the bubble volume, V. Hence equations (3.3.1) and (3.3.3) may be integrated numerically to yield a new surface geometry and potential thereon.

This numerical integration is performed using a second or fourth-order Runge-Kutta method, implemented in the following manner. For convenience, we define the vector

$$\boldsymbol{x}_i(t) = (r_i(t), z_i(t), \phi_i(t)), \tag{3.3.4}$$

[3]This may also include terms due to both surface tension and normal viscous stress, though these are omitted in the current computational studies.

containing the bubble shape and potential at the point $\boldsymbol{p}_i$. Solution of equation (3.2.7) allows us to define the quantity

$$\mathrm{d}\boldsymbol{x}_{i1} = \delta t \left.\frac{\mathrm{d}\boldsymbol{x}}{\mathrm{d}t}\right|_{(\boldsymbol{x}_i,t)}, \tag{3.3.5}$$

which represents the change in $\boldsymbol{x}_i$ at the first stage. From this stage, we define an intermediate bubble geometry and surface potential by

$$\boldsymbol{x}_{i1}(t+\delta t) = \boldsymbol{x}_i(t) + \mathrm{d}\boldsymbol{x}_{i1}. \tag{3.3.6}$$

Solving again for this intermediate geometry allows us to define

$$\mathrm{d}\boldsymbol{x}_{i2} = \delta t \left.\frac{\mathrm{d}\boldsymbol{x}}{\mathrm{d}t}\right|_{(\boldsymbol{x}_{i1},t+\delta t)}, \tag{3.3.7}$$

the changes in $\boldsymbol{x}_i$ at stage two. Hence the bubble geometry and potential at time $t+\delta t$ are given by

$$\boldsymbol{x}_i(t+\delta t) = \boldsymbol{x}_i(t) + \tfrac{1}{2}(\mathrm{d}\boldsymbol{x}_{i1} + \mathrm{d}\boldsymbol{x}_{i2}). \tag{3.3.8}$$

The fourth-order (four stage) method is implemented in a similar manner to that of the second-order method given above. A schematic of the program flow for the fourth-order method is given in Figure 3.1.

It is noted the use of a fourth-order method was discounted by Best (1991) as it was found to offer no noticeable increase in accuracy over the second-order method. However, it is shown later that energy is best conserved via the use of a fourth-order scheme, although there is no qualitative change in the results obtained. This negligible change in results was attributed by Best to the errors associated with the solution of equation (3.2.7) being of the same magnitude as those of the higher-order Runge-Kutta methods.

In order to solve equation (3.2.7) in an axisymmetric geometry ($\partial/\partial\theta = 0$), we employ a collocation method, choosing a set of n nodes: $\mathcal{N}_1, \mathcal{N}_2, \ldots, \mathcal{N}_n$, on the surface of the bubble. We denote the cylindrical coordinates of the i^{th} node by (r_i, z_i). As previously mentioned, we choose to represent the surface of the bubble using a set of cubic splines, which are fitted through the node points to produce $n-1$ surface elements, initially of equal arclength. The variation of the potential on the surface is also fitted as a cubic

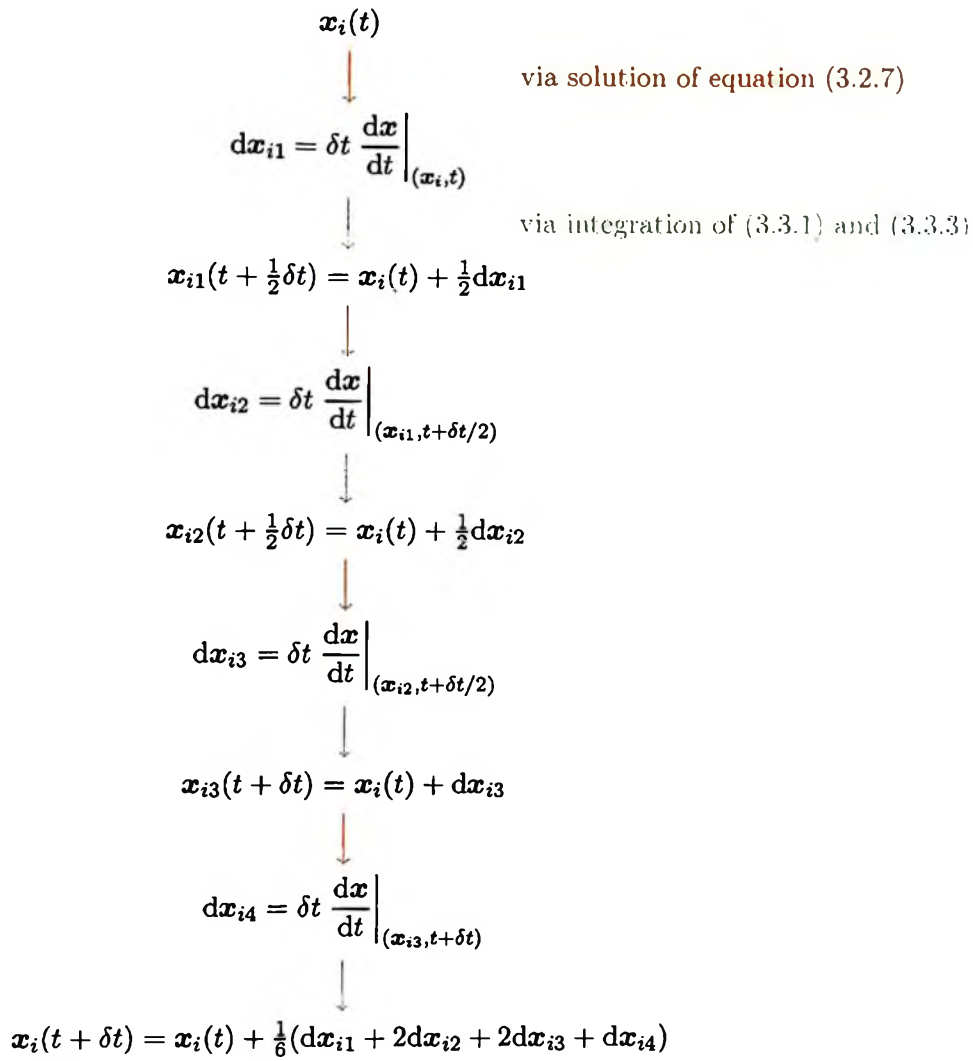

Figure 3.1: Implementation of fourth-order Runge-Kutta time-stepping scheme.

spline, whilst the unknown normal velocity, ψ is assumed to vary linearly between two nodes with respect to the arclength.

We define ξ_i as the arclength from node $\mathcal{N}_1$ to node $\mathcal{N}_i$ and also define the segment lengths as

$$\delta\xi_i = \xi_i - \xi_{i-1}, \qquad i = 2, 3, \ldots, n. \tag{3.3.9}$$

The spline functions for the surface geometry are thus written as

$$\mathcal{R}_i(\xi) = r_{1i} + r_{2i}(\xi - \xi_i) + r_{3i}(\xi - \xi_i)^2 + r_{4i}(\xi - \xi_i)^3, \tag{3.3.10a}$$

$$\mathcal{Z}_i(\xi) = z_{1i} + z_{2i}(\xi - \xi_i) + z_{3i}(\xi - \xi_i)^2 + z_{4i}(\xi - \xi_i)^3, \tag{3.3.10b}$$

for an arclength parameter in the range

$$\xi_i \leqslant \xi \leqslant \xi_{i+1} \qquad i = 1, 2, \ldots n-1. \tag{3.3.11}$$

In fact, in implementation, the coefficients are represented by, for example $R_{ji} = j!\, r_{ji}$ $(j = 1, \ldots, 4)$ so derivatives at a node are given directly by these coefficients. This is a legacy of the spline fitting routine due to de Boor (1978), whose formulation yields the coefficients in this fashion.[4]

At any given instant, the arclength is not known and must be calculated. This is done using an iterative method formulated by Kucera (see Best 1991). We begin by calculating an initial approximation to the arclength, using simply the rectilinear distance between successive points, hence

$$\delta\xi_i^{(0)} = \left|\boldsymbol{p}_i - \boldsymbol{p}_{i-1}\right|. \tag{3.3.12}$$

This is then used to fit an approximate set of spline functions $(\mathcal{R}_i^{(0)}(\xi), \mathcal{Z}_i^{(0)}(\xi))$ through the surface nodes. An improved arclength approximation is calculated via

$$\delta\xi_i^{(j+1)} = \int_{\xi_{i-1}^{(j)}}^{\xi_i^{(j)}} \sqrt{\left(\frac{\partial \mathcal{R}_{i-1}^{(j)}}{\partial \xi}\right)^2 + \left(\frac{\partial \mathcal{Z}_{i-1}^{(j)}}{\partial \xi}\right)^2}\, \mathrm{d}\xi, \tag{3.3.13}$$

where a bracketed superscript signifies the order of approximation of the arclength or spline function. Again, a corresponding set of spline functions are fitted and the process

[4] We note the code provided by de Boor is capable of dealing with various end conditions. (Prescribed first and second derivatives and not-a-knot conditions.) These are rewritten as single purpose routines (as required) to provide further optimisation.

iterated until a converged set of segment lengths is reached. (This is preferred to a convergent total arclength being achieved, which occurs prior to the convergence of segment lengths.) It was found by Kucera that an accurate representation could be found within only two or three iterations, however due to the availability of increased computing power, convergence testing is preferred as it ensures a very high degree of accuracy. It should be noted that more iterations are required when the bubble geometry includes regions of high curvature,[5] and in some extreme cases this method fails where the fixed iteration method would allow the computation to proceed, however in such a case, the fidelity of the solution may no longer be assured. Integration of equation (3.3.13) is performed numerically using a Gaussian quadrature scheme.

We are now in a position to fit the cubic spline representation of the potential over the surface of the bubble using our newly found arclength. As with the geometry splines, this is written

$$\Phi_i(\xi) = \phi_{1i} + \phi_{2i}\,(\xi - \xi_i) + \phi_{3i}\,(\xi - \xi_i)^2 + \phi_{4i}\,(\xi - \xi_i)^3\,. \tag{3.3.14}$$

It should be noted at this point that the spline functions are clamped at the first and last nodes in order to retain the axisymmetric geometry throughout the computation. These end conditions are prescribed as

$$\frac{\mathrm{d}r}{\mathrm{d}\xi} = 1, \qquad \frac{\mathrm{d}z}{\mathrm{d}\xi} = 0, \qquad \frac{\mathrm{d}\phi}{\mathrm{d}\xi} = 0, \qquad \text{at} \qquad \xi = \xi_1 = 0, \tag{3.3.15a}$$

and

$$\frac{\mathrm{d}r}{\mathrm{d}\xi} = -1, \qquad \frac{\mathrm{d}z}{\mathrm{d}\xi} = 0, \qquad \frac{\mathrm{d}\phi}{\mathrm{d}\xi} = 0, \qquad \text{at} \qquad \xi = \xi_n. \tag{3.3.15b}$$

Finally, the normal velocity, ψ is written as

$$\Psi_i(\xi) = \frac{\xi_{i+1} - \xi}{\delta\xi_{i+1}}\psi_i + \frac{\xi - \xi_i}{\delta\xi_{i+1}}\psi_{i+1}. \tag{3.3.16}$$

We are now in a position to consider collocation of equation (3.2.7). Making use of our functional forms for $\mathcal{R}, \mathcal{Z}, \Phi$ and Ψ, we obtain the system of linear equations

$$\tfrac{1}{2}\phi_i + \sum_{j=2}^{n} \mathcal{A}_{ij} = \sum_{j=2}^{n} \left(\mathcal{B}_{ij}\psi_{j-1} + \mathcal{C}_{ij}\psi_j\right), \qquad i = 1, 2, \ldots, n, \tag{3.3.17}$$

[5] This is typically seven or eight iterations, even when a tolerance of 10^{-10} is imposed on the segment lengths.

where we have written

$$\mathcal{A}_{ij} = \int_{\xi_{j-1}}^{\xi_j} \Phi_{j-1}(\xi)\mathcal{R}_{j-1}(\xi) \int_0^{2\pi} \frac{\partial G_i}{\partial n}(\xi,\theta)\,\mathrm{d}\theta\,\mathrm{d}\xi, \tag{3.3.18a}$$

$$\mathcal{B}_{ij} = \int_{\xi_{j-1}}^{\xi_j} \frac{\xi_j - \xi}{\delta\xi_j}\mathcal{R}_{j-1}(\xi) \int_0^{2\pi} G_i(\xi,\theta)\,\mathrm{d}\theta\,\mathrm{d}\xi, \tag{3.3.18b}$$

$$\mathcal{C}_{ij} = \int_{\xi_{j-1}}^{\xi_j} \frac{\xi - \xi_{j-1}}{\delta\xi_j}\mathcal{R}_{j-1}(\xi) \int_0^{2\pi} G_i(\xi,\theta)\,\mathrm{d}\theta\,\mathrm{d}\xi, \tag{3.3.18c}$$

and the Green's function evaluated at the i^{th} node, $\boldsymbol{p}_i$ is

$$G_i(\xi,\theta) = \frac{1}{4\pi\,|\boldsymbol{p}_i - \boldsymbol{q}(\xi,\theta)|}. \tag{3.3.19}$$

Here $\boldsymbol{q}(\xi,\theta)$ is the position of some point on S, the surface of the bubble. The integration of equations (3.3.18) is performed using a combination of two techniques. Firstly the azimuthal integration (with respect to θ) is performed analytically, yielding expressions in terms of elliptic integrals of the first and second-kinds, fourth-order polynomial approximations for which may be found in Abramowitz & Stegun (1965).[6] Secondly, the integrals with respect to arclength, ξ are performed using a Gauss-Legendre quadrature scheme.[7]

The equations given by (3.3.17) may then be assembled into the matrix equation

$$\mathbf{M\Phi} = \mathbf{N\Psi}, \tag{3.3.20}$$

which may be solved for the unknown $\mathbf{\Psi} \equiv (\psi_1, \psi_2, \ldots, \psi_n)^{\mathrm{T}}$ using standard elimination techniques. One method of increasing the accuracy of the system via the consideration of the Dirichlet and Neumann problems is given by Taib (1985), though this is valid only for single bubble problems and is not implemented in the work of later chapters.

Upon solution of (3.3.20) we obtain the values ψ_i for $i = 1, 2, \ldots, n$. Radial and

[6] Revised approximations calculated in the final months of research are presented in Appendix A and remove the requirement for smoothing where surface curvature is not too high. We note most of the results in this thesis were calculated prior to this discovery, and that smoothing is still required where regions of high curvature form, such as in bubble motion in close proximity to boundaries, or near the null impulse state where strange geometries develop.

[7] Further details concerning the manipulation of the integrals and subsequent removal of singularities may be found in Taib (1985).

vertical velocities may then be evaluated by solving for $\partial\phi/\partial r$ and $\partial\phi/\partial z$ in the system

$$\boldsymbol{u}\cdot\hat{\boldsymbol{n}} = \psi, \qquad \boldsymbol{u}\cdot\hat{\boldsymbol{t}} = \frac{\partial\phi}{\partial\xi}, \tag{3.3.21}$$

where $\boldsymbol{u}$ is the fluid velocity, and $\hat{\boldsymbol{n}}$ and $\hat{\boldsymbol{t}}$ are unit normal and tangential vectors respectively. This yields the expressions

$$u(\xi) = \frac{\partial\Phi}{\partial\xi}\frac{\partial\mathcal{R}}{\partial\xi} - \Psi\frac{\partial\mathcal{Z}}{\partial\xi}, \qquad v(\xi) = \frac{\partial\Phi}{\partial\xi}\frac{\partial\mathcal{Z}}{\partial\xi} + \Psi\frac{\partial\mathcal{R}}{\partial\xi}. \tag{3.3.22}$$

These may then be used to update the position and potential at the nodes in equations (3.3.1) and (3.3.3). Finally, it should be noted that a variable time-stepping scheme is employed so the computational effort is somewhat optimised by the choice of δt, using the expression

$$\delta t = \frac{\mathrm{d}\phi}{\max_i\left(1 + \frac{1}{2}|\boldsymbol{u}_i|^2 - \delta^2(z_i - z_0)\right)}, \tag{3.3.23}$$

so the maximum change in potential is bounded above by $\mathrm{d}\phi$.

3.4 The Toroidal Bubble

In this section, we consider the evolution of the bubble into the toroidal phase of motion. In doing this, the flow domain Ω changes topology from a singly connected to a doubly connected geometry via the liquid jet impact. It is accepted that the fluid mechanics of jet impact are indeed complex, with effects due to liquid compressibility, viscosity and surface tension expected to play a rôle. However in order to gain some appreciation of the bubble motion, it is necessary we neglect these factors and seek a solution to Laplace's equation in the doubly connected flow domain.

3.4.1 Reformulation of the Integral Equation

In order to do this, we outline the work of Best (1991) who considers the form of the boundary integral equation immediately prior to and after liquid jet impact. We shall denote the surface over which jet impact takes place as T and denote the remainder of the bubble surface as S. Further, we shall denote the upper and lower surfaces of T by T_+ and T_- respectively, such that $T \equiv T_+ \cup T_-$. An outward unit normal is defined over the two surfaces and is represented by $\boldsymbol{n}_\pm$, where the subscript $\pm$ denotes the quantities

evaluated on $T_\pm$, respectively. We also introduce here the superscripts b and a which are used to signify a quantity immediately before and after jet impact. A schematic of the geometry can be found in Figure 3.2. We choose some point $t \in T$ and write

$$\Delta\phi^{\mathrm{b}}(t) = \phi^{\mathrm{b}}_{+}(t) - \phi^{\mathrm{b}}_{-}(t), \tag{3.4.1}$$

which in general is non-zero. Physically the change from a singly connected to doubly connected topology gives rise to a circulation, which we denote by $\Delta\phi$. This is deemed necessary in order the Kelvin impulse is conserved. This circulation is obtained by integrating

$$\Gamma = \oint_C \boldsymbol{u} \cdot \boldsymbol{n}\, \mathrm{d}s = \Big[\phi\Big]_C, \tag{3.4.2}$$

where the notation $[\cdot]$ is used to signify a jump in potential. Immediately following impact, we know that

$$\phi^{\mathrm{a}}_{\pm}(t) - \phi^{\mathrm{b}}_{\pm}(t) = -\Pi_\pm/\rho, \tag{3.4.3}$$

on $T_\pm$ respectively, where $\Pi_\pm$ are the pressure impulses defined as $\Pi_\pm = \int p(t_\pm)\, \mathrm{d}t$, an integral over the impact duration. Since $T_\pm$ experience a common pressure during impact, so the pressure impulse is constant, i.e. $\Pi_+ = \Pi_-$, and hence

$$\phi^{\mathrm{a}}_{+}(t) - \phi^{\mathrm{a}}_{-}(t) = \phi^{\mathrm{b}}_{+}(t) - \phi^{\mathrm{b}}_{-}(t). \tag{3.4.4}$$

This tells us the jump in potential persists following impact and experiences no change in value. This may be written as

$$\Delta\phi^{\mathrm{a}}(t) = \Delta\phi^{\mathrm{b}}(t) = \Delta\phi(t). \tag{3.4.5}$$

So the circulation Γ is dependent on the point t, at which we begin and end our closed curve. For $\Delta\phi(t)$ non-uniform, the flow field will be rotational. Only if $\Delta\phi(t)$ is uniform will we have irrotational flow with a constant circulation $\Delta\phi$ on any circuit.

During impact, the pressure inside the bubble is constant and so over the remainder of the bubble's surface, S the pressure impulse at any given point is

$$\Pi_S = \int p\, \mathrm{d}t = p_{\mathrm{b}}\delta t, \tag{3.4.6}$$

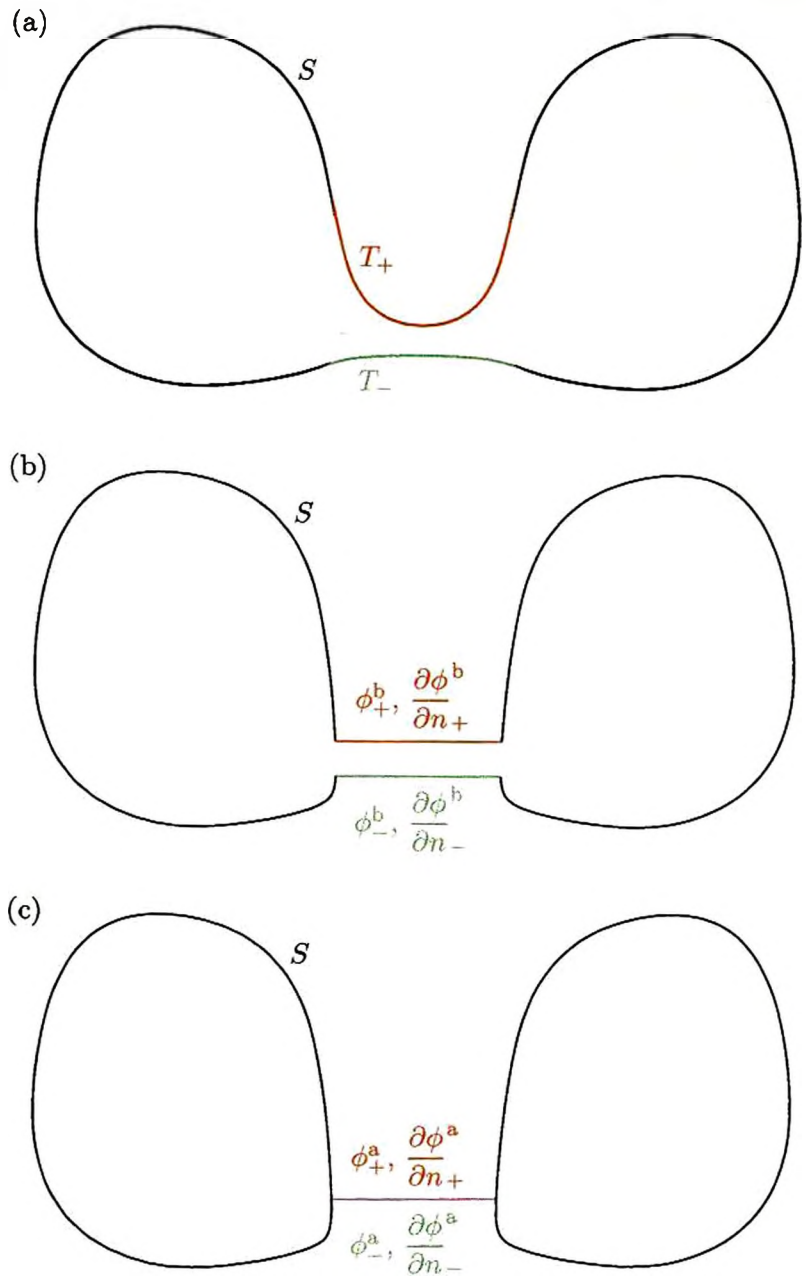

Figure 3.2: Schematic showing the transition to a toroidal bubble geometry: (a) the location of the regions $T_\pm$ on the surface of the bubble; (b) an idealised bubble prior to jet impact with the appropriate potentials and normal velocities on either surface; and (c) an idealised bubble following jet impact, again with the appropriate potentials and normal velocities on the cut.

where δt is the duration of the impact. If we now consider the duration of the impact $\delta t \to 0$ whilst p remains finite, then the pressure impulse, $\Pi_S = 0$. And hence we reason that during impact, there is no change in the potential on S.

The fluid velocity on T immediately following jet impact must also be considered, with the normal velocity being continuous. Whilst an expression for this velocity may not be obtained simply, we may formulate an equation, the solution of which yields the required normal velocity. We pause briefly to consider the tangential velocity on T. Since $T_\pm$ experiences a common pressure impulse, then

$$\nabla\Pi_+(t) \cdot \tau(t) = \nabla\Pi_-(t) \cdot \tau(t), \tag{3.4.7}$$

where we have introduced the tangential vector $\tau(t)$. This may be manipulated to yield

$$\left(\boldsymbol{u}_+^{\mathrm{a}}(t) - \boldsymbol{u}_+^{\mathrm{b}}(t)\right) \cdot \tau(t) = \left(\boldsymbol{u}_-^{\mathrm{a}}(t) - \boldsymbol{u}_-^{\mathrm{b}}(t)\right) \cdot \tau(t). \tag{3.4.8}$$

Hence the tangential velocity at $\boldsymbol{t} \in T$ changes by the same amount on both T_+ and T_- due to impact. Any inequality prior to jet impact will persist, resulting in the formation of a vortex sheet. Such a sheet would provide the rotation in the flow field necessary to yield the non-uniformity in $\Delta\phi$ mentioned above.

By equation (3.4.6) and the argument following it, we were able to reason that, over S, the non-impacting bubble surface, there is no change in potential. We now exploit this fact to formulate an equation whose solution yields the normal velocity on S immediately following jet impact. We begin by recalling the BI equation (3.2.7) for some point $\boldsymbol{p}$ on the surface of the bubble, which is

$$2\pi\phi^{\mathrm{b}}(\boldsymbol{p}) = \int\limits_{S \cup T_+ \cup T_-} \left(\frac{\partial \phi^{\mathrm{b}}(\boldsymbol{q})}{\partial n} G(\boldsymbol{p},\boldsymbol{q}) - \phi^{\mathrm{b}}(\boldsymbol{q}) \frac{\partial G(\boldsymbol{p},\boldsymbol{q})}{\partial n} \right) \mathrm{d}S. \tag{3.4.9}$$

Separating the integrals and introducing the appropriate potentials, derivatives and velocities on each surface, we have

$$\begin{aligned} 2\pi\phi^{\mathrm{b}} = \int\limits_S \left(\frac{\partial \phi^{\mathrm{b}}}{\partial n} G - \phi^{\mathrm{b}} \frac{\partial G}{\partial n} \right) \mathrm{d}S \\ + \int\limits_{T_+} \left(\frac{\partial \phi^{\mathrm{b}}}{\partial n_+} G - \phi_+^{\mathrm{b}} \frac{\partial G}{\partial n_+} \right) \mathrm{d}S + \int\limits_{T_-} \left(\frac{\partial \phi^{\mathrm{b}}}{\partial n_-} G - \phi_-^{\mathrm{b}} \frac{\partial G}{\partial n_-} \right) \mathrm{d}S. \end{aligned} \tag{3.4.10}$$

where we have omitted dependencies on $\boldsymbol{p}$ and $\boldsymbol{q}$ for brevity. We consider the spatial geometry of the two surfaces of T to be the same, and hence the Green's function, G remains the same whether on T_+ or T_-. Similarly, due to the opposing normals, $\partial G/\partial n_+ = -\partial G/\partial n_-$, and hence we have

$$2\pi\phi^{\mathrm{b}} = \int_S \left(\frac{\partial\phi^{\mathrm{b}}}{\partial n}G - \phi^{\mathrm{b}}\frac{\partial G}{\partial n}\right)\mathrm{d}S + \int_T \left(\frac{\partial\phi^{\mathrm{b}}}{\partial n_+} + \frac{\partial\phi^{\mathrm{b}}}{\partial n_-}\right)G\,\mathrm{d}S - \int_T \Delta\phi^{\mathrm{b}}\frac{\partial G}{\partial n_+}\mathrm{d}S. \quad (3.4.11)$$

Similarly, we may consider the integral equation post-impact. Following a similar line of reasoning to above, we obtain the equation

$$2\pi\phi^{\mathrm{a}} = \int_S \left(\frac{\partial\phi^{\mathrm{a}}}{\partial n}G - \phi^{\mathrm{a}}\frac{\partial G}{\partial n}\right)\mathrm{d}S + \int_T \left(\frac{\partial\phi^{\mathrm{a}}}{\partial n_+} + \frac{\partial\phi^{\mathrm{a}}}{\partial n_-}\right)G\,\mathrm{d}S - \int_T \Delta\phi^{\mathrm{a}}\frac{\partial G}{\partial n_+}\mathrm{d}S. \quad (3.4.12)$$

After liquid jet impact, the normal velocity over T is continuous and so the second integral in equation (3.4.12) is zero, hence

$$2\pi\phi^{\mathrm{a}} = \int_S \left(\frac{\partial\phi^{\mathrm{a}}}{\partial n}G - \phi^{\mathrm{a}}\frac{\partial G}{\partial n}\right)\mathrm{d}S - \int_T \Delta\phi^{\mathrm{a}}\frac{\partial G}{\partial n_+}\mathrm{d}S. \quad (3.4.13)$$

We now take account of equation (3.4.5) and the arguments around (3.4.6), which state the circulation and potential on S remain constant over the time of impact. Thus we combine equations (3.4.11) and (3.4.13) to yield

$$\int_S \frac{\partial\phi^{\mathrm{a}}}{\partial n}G\,\mathrm{d}S = \int_S \frac{\partial\phi^{\mathrm{a}}}{\partial n}G\,\mathrm{d}S + \int_T \left(\frac{\partial\phi^{\mathrm{b}}}{\partial n_+} + \frac{\partial\phi^{\mathrm{b}}}{\partial n_-}\right)G\,\mathrm{d}S. \quad (3.4.14)$$

This allows us to determine the normal velocity post impact in terms of quantities which are known or may be calculated prior to impact. In fact we may work entirely in known quantities if we eliminate the terms containing prior normal velocities, to yield

$$2\pi\phi^{\mathrm{b}} = \int_S \left(\frac{\partial\phi^{\mathrm{a}}}{\partial n}G - \phi^{\mathrm{b}}\frac{\partial G}{\partial n}\right)\mathrm{d}S - \int_T \Delta\phi^{\mathrm{b}}\frac{\partial G}{\partial n_+}\mathrm{d}S. \quad (3.4.15)$$

And hence we may write down a BI equation for the toroidal phase of the bubble motion as

$$c(\boldsymbol{p})\phi(\boldsymbol{p}) = \int_S \left(\frac{\partial\phi(\boldsymbol{q})}{\partial n}G(\boldsymbol{p},\boldsymbol{q}) - \phi(\boldsymbol{q})\frac{\partial G(\boldsymbol{p},\boldsymbol{q})}{\partial n}\right)\mathrm{d}S - \Delta\phi\int_T \frac{\partial G(\boldsymbol{p},t)}{\partial n_+}\mathrm{d}S, \quad (3.4.16)$$

with $c(\boldsymbol{p})$ as defined by (3.2.8), provided $\boldsymbol{p} \notin T$. Note the additional term in (3.4.16) over (3.2.7) requires integration over the impact surface, T. Finally for a point $\boldsymbol{p} \in T \setminus S$

(i.e. on the cut, but not on the surface of the bubble), we have

$$4\pi\phi(\boldsymbol{p}) = \int_S \left(\frac{\partial\phi(\boldsymbol{q})}{\partial n} G(\boldsymbol{p},\boldsymbol{q}) - \phi(\boldsymbol{q}) \frac{\partial G(\boldsymbol{p},\boldsymbol{q})}{\partial n} \right) \mathrm{d}S$$
$$- \Delta\phi \int_T \frac{\partial G(\boldsymbol{p},\boldsymbol{t})}{\partial n_{\boldsymbol{t}}} \mathrm{d}S + 2\pi\Delta\phi(\boldsymbol{t}). \quad (3.4.17)$$

3.4.2 Changes to the Method of Solution

Here we describe the changes to the numerical scheme in Section 3.3 in order to allow for the transition to a doubly connected fluid domain. In an idealised model, the impact occurs at a single point, across which a jump in the potential of $\Delta\phi$ occurs. Since the impact occurs at a point, $\Delta\phi$ is uniform and hence no vortex sheet is formed. In order to describe the flow field using a boundary integral method, we require a singly connected fluid topology and hence introduce a cut, T in Ω to render it thus. Initially the cut is a point, but through advancement of the flow, its geometry changes. In the early work of Best (1991), this is allowed to advance with the flow and in many cases becomes highly convoluted.[8] More recent work by Best (1994) shows the cut to be entirely arbitrary and it is hence remapped to a simple disc resulting in huge computational savings. In either scheme, the discontinuity in the potential is constant and equals $\Delta\phi$. We note that in the point contact limit, $\psi^{\mathrm{a}} = \psi^{\mathrm{b}}$ except at points in $S \cup T$ where the normal is undefined. One final comment should be made on the energy of the system. Physically, we would expect a loss of kinetic energy due to impact, manifesting itself as heat or acoustic radiation. However, for our idealised model of a point impact, energy is conserved. We now proceed to elaborate on the changes we are required to make to our numerical scheme in order to allow for integration over the cut, T and associated difficulties.

Up until the moment of impact, our prior scheme outlined in Section 3.3 is sound and yields the geometry, potential and normal velocity on the boundaries, $\partial\Omega$ of our flow domain. More specifically (at this stage) the surface of the bubble. Computationally, impact takes place when nodes $\mathcal{N}_1$ and $\mathcal{N}_n$ (which lie on the axis of symmetry) occur within some predetermined distance of each other; this is either fixed or relative to the

[8] The reader is referred to Figure 6.3.6 of Best (1991), in which the cut almost envelops the toroidal bubble.

vertical length-scale of the bubble. This yields the circulation of the successive flow as

$$\Delta\phi = \phi_n - \phi_1. \tag{3.4.18}$$

We recall over S (nodes $\mathcal{N}_2, \mathcal{N}_3, \ldots, \mathcal{N}_{n-1}$) the potential is unchanged, allowing evaluation of the fluid velocity as before. Similarly, the potential may be obtained at time $t + \delta t$, with t being the time of impact.

Although we initially know the position of the cut, after this initial step we have no idea of where this meets the surface of the bubble. This is circumvented by Best, who reasonably assumes that the regions of high curvature formed lead to very high surface velocities, whose physical manifestation is to immediately smooth the bubble surface through the action of surface tension. To perform this numerically, we remove nodes $\mathcal{N}_1$ and $\mathcal{N}_n$ from their position on the axis of symmetry and fit a smooth curve through the remaining nodes.[9] These nodes are then introduced back into the surface of the bubble mid-way between nodes $\mathcal{N}_{n-1}$ and $\mathcal{N}_2$. This position is given some credibility due to the spatially regular redistribution of nodes throughout preceding time steps. Hence the cut is taken as a disc of radius $r_1 \equiv r_n$, cutting the axis of symmetry at $z_1 \equiv z_n$, where the subscripts denote node number.

Having detailed the transitional scheme, we are now in a position to discuss the implementation of the BIM to solve equation (3.4.16). This technique is almost identical to that discussed in Section 3.3, except for the appearance of the final term in this equation, which requires us to integrate over the cut. We note here that the coincident nodes $\mathcal{N}_1$ and $\mathcal{N}_n$ lie in $S \cup T$ and so the normal there is undefined; hence neither is $\psi \equiv \partial\phi/\partial n$. For this reason, we choose not to collocate equation (3.4.16) there, but do so only for the $n-2$ nodes $\mathcal{N}_2, \mathcal{N}_3, \ldots, \mathcal{N}_{n-1}$. We do, however, require the position of these nodes as it defines the spatial location at which ϕ is discontinuous. In order that we may track this point, it is essential the normal velocity there is known. This is evaluated by considering the interval between $\mathcal{N}_{n-1}$ and $\mathcal{N}_2$ as a single segment, along which the normal velocity is necessarily taken to vary linearly with respect to arclength, as with

[9] In practice, it is often necessary to remove further nodes about the axis of symmetry in order to fit a sufficiently smooth surface geometry. In such cases, the following arguments remain valid following a trivial relabelling of nodes.

the other surface elements. To this end, we define its value as

$$\psi_1 \equiv \psi_n = \frac{\delta\xi_n\psi_2 + \delta\xi_2\psi_{n-1}}{\delta\xi_2 + \delta\xi_n}. \tag{3.4.19}$$

Collocation at the remaining nodes $\mathcal{N}_2, \mathcal{N}_3, \ldots, \mathcal{N}_{n-1}$ yields the $n-2$ linear equations

$$2\pi\psi_i + \Delta\phi\mathcal{D}_i + \sum_{j=2}^{n}\mathcal{A}_{ij} = \sum_{j=3}^{n-1}(\mathcal{B}_{ij}\psi_{j-1} + \mathcal{C}_{ij}\psi_j) + \mathcal{E}_i\psi_2 + \mathcal{F}_i\psi_{n-1},$$

$$i = 2, 3, \ldots, n-1, \tag{3.4.20}$$

where the $\mathcal{A}_{ij}$, $\mathcal{B}_{ij}$ and $\mathcal{C}_{ij}$ are as defined in (3.2.8). $\mathcal{D}_i$, $\mathcal{E}_i$ and $\mathcal{F}_i$ are defined as

$$\mathcal{D}_i = \int_{r_{1/n}}^{0} \xi \int_{0}^{2\pi} \frac{\partial G_i}{\partial n}(\xi,\theta)\,\mathrm{d}\theta\,\mathrm{d}\xi, \tag{3.4.21a}$$

$$\mathcal{E}_i = \mathcal{C}_{i2} + \delta\xi_n\frac{\mathcal{B}_{i2} + \mathcal{C}_{in}}{\delta\xi_2 + \delta\xi_n}, \tag{3.4.21b}$$

$$\mathcal{F}_i = \mathcal{B}_{in} + \delta\xi_2\frac{\mathcal{B}_{i2} + \mathcal{C}_{in}}{\delta\xi_2 + \delta\xi_n}, \tag{3.4.21c}$$

where $\mathcal{D}_i$ is the contribution to the potential which arises over the cut, T and $\mathcal{E}_i$ and $\mathcal{F}_i$ occur due to the form of the normal velocity at nodes $\mathcal{N}_1$ and $\mathcal{N}_n$ as per equation (3.4.19). These equations may then be solved using standard techniques to yield $\psi_2, \psi_3, \ldots, \psi_{n-1}$ which are used to update the geometry and potential as performed earlier.

Since we no longer have nodes on the axis of symmetry at our disposal, it is somewhat more complex to ensure the splines which represent the bubble geometry are smooth. In order to do this, we must necessarily specify values for $\partial r/\partial\xi$ and $\partial z/\partial\xi$ at node $\mathcal{N}_{1/n}$[10] at each stage prior to fitting the splines as detailed earlier. In order to find a good approximation to these derivatives, an intermediate stage is introduced into the calculations during which a secondary spline is fitted through nodes $\mathcal{N}_{n-m}, \mathcal{N}_{n-m+1}, \ldots, \mathcal{N}_{1/n}, \mathcal{N}_2, \ldots, \mathcal{N}_{m+1}$. On the free ends of this spline, the not-a-knot condition[11] is used. This requires a choice of $m \geqslant 1$, although a choice of $m = 4$ is more typical. Having fitted the secondary spline, the derivatives at node $\mathcal{N}_{1/n}$ are evaluated and used to clamp the splines. The splines which represent the potential are clamped

[10]This notation is used to denote the coincident position of node $\mathcal{N}_1$ and node $\mathcal{N}_n$ on the surface of the bubble. However we note the potential at these nodes differs by $\Delta\phi$.

[11]For further details, see de Boor (1978).

in a similar fashion, although care must be taken to ensure the jump in potential $\Delta\phi$ is accounted for.

As we mention above, care must be taken when dealing with the continuous portion of the bubble surface over which the jump in potential occurs. The other key area where this happens is in the damping routines. In this situation it has been found prudent not to damp at node $\mathcal{N}_{1/n}$ but instead to damp at the remaining $n-2$ nodes, then reposition $\mathcal{N}_{1/n}$ halfway (with respect to arclength) between nodes $\mathcal{N}_{n-1}$ and $\mathcal{N}_2$. Hence in order to yield the five-points required for our smoothing formula, it is necessary to utilise two nodes on the opposing side of the cut. Whilst this may be done quite readily for the r and z-values, special care must be taken to add or subtract $\Delta\phi$ where appropriate when dealing with the potential.

3.4.3 Dynamic Cut Relocation

The final and perhaps most necessary change to our method of solution is the dynamic cut relocation algorithm due to Best (1994). In effect this removes the need to follow the cut as a material surface as was previously done (see Best 1991) by arbitrarily remapping the cut to a simple disc following each time step. In doing this, however, it becomes necessary to keep the point at which the cut meets the surface of the bubble within the column of liquid which threads the bubble. We take $\boldsymbol{t}$ to denote the point at which the cut meets the surface of the bubble prior to relocation and let $\boldsymbol{t}'$ denote the new position of the cut. We may then redefine the potential throughout the flow domain via the equation

$$\phi'(\boldsymbol{p}) = \phi(\boldsymbol{t}') + \int_{\boldsymbol{t}'}^{\boldsymbol{p}} \boldsymbol{u} \cdot \mathrm{d}\boldsymbol{s}, \tag{3.4.22}$$

where a $'$ denotes a new quantity and $\mathrm{d}\boldsymbol{s}$ is a line element taken over any curve in the fluid connecting $\boldsymbol{t}'$ with $\boldsymbol{p}$ which does not cross the newly relocated cut, T'. If the point $\boldsymbol{p}$ lies outside the region bounded by S, T and T', then the potential at $\boldsymbol{p}$ remains the same, that is

$$\phi'(\boldsymbol{p}) = \phi(\boldsymbol{t}') + (\phi(\boldsymbol{p}) - \phi(\boldsymbol{t}')) = \phi(\boldsymbol{p}). \tag{3.4.23}$$

However, if $\boldsymbol{p}$ lies inside this bounded region, the redefined potential is given by

$$\phi'(\boldsymbol{p}) = \phi(\boldsymbol{t}') + (\phi(\boldsymbol{p}) - \phi(\boldsymbol{t}') + \Delta\phi) = \phi(\boldsymbol{p}) + \Delta\phi, \tag{3.4.24}$$

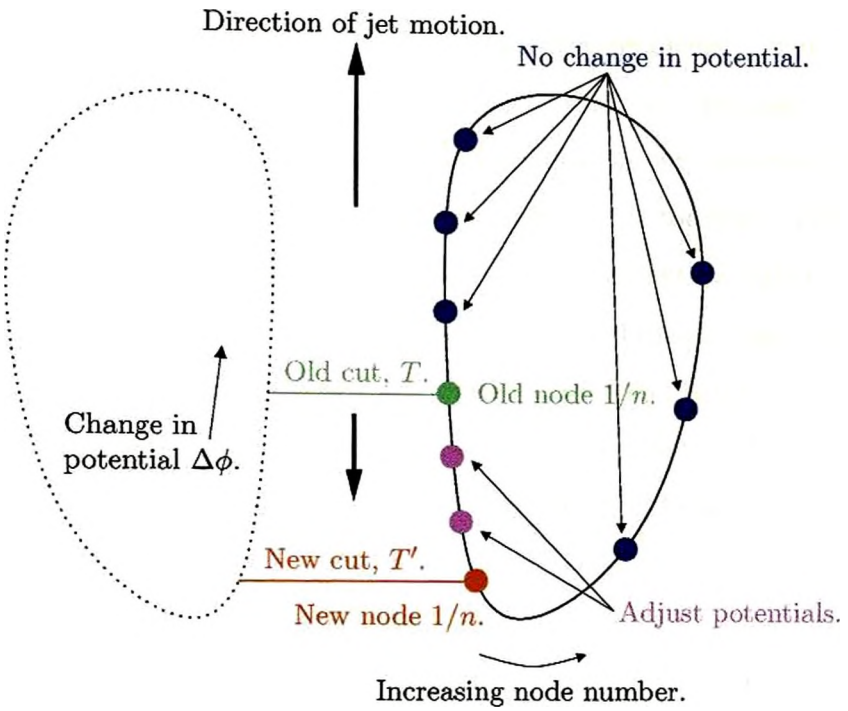

Figure 3.3: Schematic showing the remapping of the cut, a necessary part of the dynamic cut relocation algorithm due to Best (1994). Here we consider an upwardly directed jet and hence clockwise (with respect to the right hand side of this figure) circulation. As the flow evolves, the cut approaches the top of the bubble. It is hence remapped to near the bottom of the bubble allowing calculations to continue.

and so the value of the potential there has changed by $\Delta\phi$. This is summarised in the schematic diagram in Figure 3.3, which shows in a simple fashion which nodes must be adjusted. Although it should be noted in practical use, the old cut is often deformed by the flow from the simple disc shape shown.

3.5 Smoothing Techniques

In common with previous work in this field, during evolution of the flow, a high-frequency saw-tooth instability is found to occur. This is purely a facet of the numerical scheme and has to some extent been eliminated in our most recent work. Investigations suggest the cause is twofold. Firstly, many studies utilise polynomial approximations for the elliptic integrals. Whilst this is a valid technique, these studies often purport to employ the approximations calculated by Hastings (1955): this is due to their ready availability in Abramowitz & Stegun (1965). In recent work, Roumeliotis (2000) considers many

numerical aspects in formulating a BI scheme for Stokes-flow problems. These include the calculation of improved polynomial approximations, which are discussed in more detail in Appendix A. Recent implementation of these ideas in our numerical scheme eliminates the need for smoothing where surface curvature is not too high. This leads us directly to the other observed cause of these problematic instabilities, regions of high curvature. The exact reason for these problems remains unclear. Possible suggestions and avenues of solution are considered in Section 6.4. Since many of the results in this thesis were calculated prior to the inclusion of the improved approximations and the problem is not yet fully resolved, we proceed to consider the smoothing techniques employed in our numerical scheme.

In order to eliminate these instabilities, two differing methods of explicit smoothing[12] are employed. The first is the classic method due to Longuet-Higgins & Cokelet (1976), originally used to remove instabilities of this type in calculations on surface-wave problems. This method is outlined below, then extended for use on an irregular node distribution for later use on an infinite free surface. An alternative method is used by Lundgren & Mansour (1988) and is based on a diffusion-like fourth-order PDE and so in effect damps higher-order modes whilst leaving lower modes virtually unchanged. Due to the occurrence of a smoothing parameter, this method offers a variable degree of damping, so for bubbles over a certain distance from the boundary where the instabilities grow more slowly, a lesser degree of smoothing may be applied, and hence less 'energy' is lost in our numerical scheme. For this reason, this is our preferred method of smoothing the surface of the bubble. We note that hereafter, these two methods are denoted LHC and LM respectively.

[12] We note that redistribution of nodes at each time step may be viewed as an implicit form of smoothing.

3.5.1 LHC Smoothing

Regular Node Distribution

This method assumes a function $f(x)$ which is defined on a regular grid, and in which alternate points lie on a smooth curve, may be approximated by the polynomial

$$g(x;j) = \underbrace{(a_0 + a_1 x + a_2 x^2 + \cdots + a_n x^n)}_{\text{Smooth mean curve.}} + \underbrace{(-1)^j (b_0 + b_1 x + \cdots + b_{n-1} x^{n-1})}_{\text{Remainder.}}, \quad (3.5.1)$$

where it should be noted the remainder oscillates with period two in j, the node number. It is then assumed the coefficients $a_0, a_1, \ldots, a_n, b_0, \ldots, b_{n-1}$ may be chosen such that $f(x) \equiv g(x;j)$ on the $2n+1$ consecutive points about node $\mathcal{N}_j$: $x_{j-n}, x_{j-n+1}, \ldots, x_{j+n}$. The smoothed function may then be taken to be

$$\bar{g}(x) = (a_0 + a_1 x + a_2 x^2 + \cdots + a_n x^n). \quad (3.5.2)$$

Here we utilise the five-point formula given via the choice of $n = 2$ in the above. This yields the expression

$$\bar{f}_j = \tfrac{1}{16}(-f_{j-2} + 4f_{j-1} + 10f_j + 4f_{j+1} - f_{j+2}), \quad (3.5.3)$$

where $\bar{f}_j$ is the smoothed function at node $\mathcal{N}_j$, calculated from the five nodal values f_{j-2}, f_{j-1}, $\ldots$, f_{j+2}.

Irregular Node Distribution

In order to apply the smoothing formula of Longuet-Higgins & Cokelet above, requires the regular redistribution of nodes prior to the application of equation (3.5.3). This, however, is impractical when applied to an infinite free surface, as this leads to a rapid spreading of the liquid spike formed thereon. It is possible, however, to reformulate the above smoothing method, relaxing the constraint that the mesh be regularly spaced. Introducing the same approximating function as above (3.5.1), setting $n = 2$ and solving for the coefficients yields an expression of the form

$$\bar{f}_j = c_{-2j} f_{j-2} + c_{-1j} f_{j-1} + c_{0j} f_j + c_{1j} f_{j+1} + c_{2j} f_{j+2}, \quad (3.5.4)$$

where

$$c_{-2j} = \frac{1}{2}\frac{(\xi_j - \xi_{j-1})(\xi_j - \xi_{j+1})}{(\xi_{j-2} - \xi_j)(\xi_{j-2} - \xi_{j+2})}, \tag{3.5.5a}$$

$$c_{-1j} = \frac{1}{2}\frac{\xi_{j+1} - \xi_j}{\xi_{j+1} - \xi_{j-1}}, \tag{3.5.5b}$$

$$c_{0j} = \frac{1}{2}\left[1 + \frac{(\xi_j - \xi_{j-1})(\xi_j - \xi_{j+1})}{(\xi_j - \xi_{j-2})(\xi_j - \xi_{j+2})}\right], \tag{3.5.5c}$$

$$c_{1j} = \frac{1}{2}\frac{\xi_{j-1} - \xi_j}{\xi_{j-1} - \xi_{j+1}}, \tag{3.5.5d}$$

$$c_{2j} = \frac{1}{2}\frac{(\xi_j - \xi_{j-1})(\xi_j - \xi_{j+1})}{(\xi_{j+2} - \xi_{j-2})(\xi_{j+2} - \xi_j)}. \tag{3.5.5e}$$

We note that if we take $\delta = \xi_i - \xi_{i-1}$ for $i = j-1,\ j,\ \ldots,\ j+2$, then we recover the smoothing function (3.5.3) from equations (3.5.4) and (3.5.5).

3.5.2 LM Smoothing on an Irregular Node Distribution

As mentioned earlier, the method of smoothing employed by Lundgren & Mansour (1988) is our favoured technique for the smoothing of bubbles as it provides a means of adjusting the severity of the damping, and hence the numerical energy loss experienced during calculations. Along with the frequency at which we apply the smoothing, this provides a second means of fine-tuning the damping.

The method is based on the fourth-order partial differential equation

$$\frac{\partial f}{\partial t} = -\lambda \frac{\partial^4 f}{\partial \xi^4}, \tag{3.5.6}$$

where f is the function to be smoothed, ξ is arclength and λ is a 'diffusive' constant. We first make a Taylor-series expansion for the function f at the nodes $\mathcal{N}_{j-2}$, $\mathcal{N}_{j-1}$, ..., $\mathcal{N}_{j+2}$. These may then be used to calculate a five-point finite-difference expression for $\partial^4 f/\partial \xi^4$ at node j. Using a simple forward difference expression for $\partial f/\partial t$ allows us to write the expression for the smoothed function, $\bar{f}$ as

$$\bar{f}_j = f_j - \lambda\,\delta t\,(\bar{c}_{-2j} f_{j-2} + \bar{c}_{-1j} f_{j-1} + \bar{c}_{0j} f_j + \bar{c}_{1j} f_{j+1} + \bar{c}_{2j} f_{j+2}), \tag{3.5.7}$$

where the variable coefficients are given by

$$\tilde{c}_{-2j} = \frac{24}{(\xi_{j-2} - \xi_{j-1})(\xi_{j-2} - \xi_j)(\xi_{j-2} - \xi_{j+1})(\xi_{j-2} - \xi_{j+2})}, \tag{3.5.8a}$$

$$\tilde{c}_{-1j} = \frac{24}{(\xi_{j-1} - \xi_{j-2})(\xi_{j-1} - \xi_j)(\xi_{j-1} - \xi_{j+1})(\xi_{j-1} - \xi_{j+2})}, \tag{3.5.8b}$$

$$\tilde{c}_{0j} = \frac{24}{(\xi_j - \xi_{j-2})(\xi_j - \xi_{j-1})(\xi_j - \xi_{j+1})(\xi_j - \xi_{j+2})}, \tag{3.5.8c}$$

$$\tilde{c}_{1j} = \frac{24}{(\xi_{j+1} - \xi_{j-2})(\xi_{j+1} - \xi_{j-1})(\xi_{j+1} - \xi_j)(\xi_{j+1} - \xi_{j+2})}, \tag{3.5.8d}$$

$$\tilde{c}_{2j} = \frac{24}{(\xi_{j+2} - \xi_{j-2})(\xi_{j+2} - \xi_{j-1})(\xi_{j+2} - \xi_j)(\xi_{j+2} - \xi_{j+1})}. \tag{3.5.8e}$$

In practice, the use of a physical time step is combined with the diffusive constant λ. Hence we choose a value for D such that on a regular grid this method reduces to

$$\bar{f}_j = f_j - D\,(f_{j-2} - 4f_{j-1} + 6f_j - 4f_{j+1} + f_{j+2})\,. \tag{3.5.9}$$

In our irregular formulation, we must scale this D so we obtain the corresponding damping. This leads to a choice of

$$\widehat{D} = 24\,D\,\overline{\delta\xi}^4, \tag{3.5.10}$$

where $\overline{\delta\xi}$ is the average arclength; averaged over the surface of the bubble. After scaling thus, we damp our surface using the expression

$$\bar{f}_j = f_j - \widehat{D}\,(\tilde{c}_{-2j} f_{j-2} + \tilde{c}_{-1j} f_{j-1} + \tilde{c}_{0j} f_j + \tilde{c}_{1j} f_{j+1} + \tilde{c}_{2j} f_{j+2})\,, \tag{3.5.11}$$

with the $\tilde{c}_{ij}$'s as above in (3.5.8). We note on a regularly spaced grid, the choice of $D = 1/16$ recovers the smoothing formula (3.5.3) due to Longuet-Higgins & Cokelet (1976). In practice we are able to adequately smooth the bubbles with a choice of $D < 1/16$ and for bubbles at a distance from the boundary, a choice of $D = 0.01$ is fine.

3.6 The Calculation of Physical Quantities

In order we may better understand the behaviour of a bubble as it evolves in time, it is useful to calculate a number of physical quantities associated with the motion. Some such as the internal pressure and volume of the bubble are required in order to update the potential on the surface so calculations may proceed. Others such as the centroid

and Kelvin impulse allow us to better understand the physical behaviour of the bubble. Thirdly, by calculating the energy associated with the system under consideration we are able to evaluate the performance of the model and code in a straightforward manner. Following discussion of quantities relating to the bubble as a whole, techniques for the calculation of the kinetic energy and Kelvin impulse of the liquid jet are introduced. Due to the requirement of calculating the potential close to, but not on, the surface of the bubble, we introduce some novel techniques. In the following section, methods for the calculation of pressure and velocity fields throughout the fluid domain are given.

3.6.1 Volume, Pressure and Temperature

The calculation of the volume is a straightforward exercise and simply requires integration to be performed over a number of volume elements, given in cylindrical polar coordinates by $\mathrm{d}V = r\,\mathrm{d}r\,\mathrm{d}\theta\,\mathrm{d}z$. The integrations with respect to r and θ may be performed analytically and the variable of integration changed to ξ, to yield

$$V = \pi \sum_{i=1}^{n-1} \int_{\xi_i}^{\xi_{i+1}} \mathcal{R}_i{}^2(\xi) \frac{\mathrm{d}\mathcal{Z}_i(\xi)}{\mathrm{d}\xi}\,\mathrm{d}\xi, \tag{3.6.1}$$

where $\mathcal{R}_i(\xi)$ and $\mathcal{Z}_i(\xi)$ are as defined earlier. This is written more simply as

$$V = \pi \int_{\xi_1}^{\xi_n} \mathcal{R}^2(\xi) \frac{\mathrm{d}\mathcal{Z}(\xi)}{\mathrm{d}\xi}\,\mathrm{d}\xi. \tag{3.6.2}$$

Finally the integration with respect to ξ is carried out numerically using Gaussian quadrature. We note that equation (3.6.2) may be used to calculate the volume of both pre-toroidal and toroidal bubbles.

Once we have the volume of the bubble, this yields directly the pressure in the bubble via equation (2.3.1) which in dimensionless form is

$$p = \alpha \left(\frac{V_0}{V} \right)^{\kappa}. \tag{3.6.3}$$

In the case of a vapour bubble the pressure is constant.

Similarly, the dimensionless temperature of the bubble is calculated as

$$T = \left(\frac{V_0}{V} \right)^{\kappa - 1}, \tag{3.6.4}$$

where we recall that V_0 is the initial volume and κ is the ratio of specific heats.

3.6.2 Centroid

Due to the axisymmetric nature of the current work, the centroid will lie on the axis of symmetry, with the z-coordinate being given by

$$z_c = \frac{1}{V}\int_V z \, \mathrm{d}V, \tag{3.6.5}$$

which, after integrating as above, gives

$$z_c = \frac{\pi}{V}\int_{\xi_1}^{\xi_n} \mathcal{R}^2(\xi)\mathcal{Z}(\xi)\frac{\mathrm{d}\mathcal{Z}(\xi)}{\mathrm{d}\xi}\,\mathrm{d}\xi. \tag{3.6.6}$$

Again, integrations over the arclength, ξ are performed numerically using a Gaussian quadrature scheme. We note that equation (3.6.6) is suitable for both pre-toroidal and toroidal bubbles.

3.6.3 Kelvin Impulse

Even with spherical bubble approximations, the Kelvin impulse has been shown to be a very good indicator of the nature of collapse. Here it is calculated numerically to examine the gross behaviour of the fluid associated with our flows throughout the lifetime of the bubble.

Pre-Toroidal Bubble

Again, due to the axisymmetric nature of our system, only the z-component is of interest, which is given by

$$I_z^* = -\rho \, \boldsymbol{e}_z \cdot \int_S \phi \boldsymbol{n} \, \mathrm{d}S, \tag{3.6.7}$$

where the star denotes the dimensional form of the impulse. We note the minus sign is due to the fact that the surface normal, $\boldsymbol{n}$ is directed outward with respect to the fluid; and so into the bubble. We also note that a surface element is given by $\mathrm{d}S = r\,\mathrm{d}\theta\,\mathrm{d}\xi$. Hence for a pre-toroidal bubble, we have

$$I_z = 2\pi\int_{\xi_1}^{\xi_n} \Phi(\xi)\mathcal{R}(\xi)\frac{\mathrm{d}\mathcal{R}(\xi)}{\mathrm{d}\xi}\,\mathrm{d}\xi, \tag{3.6.8}$$

where we recall that $\Phi(\xi)$ is the piecewise cubic representation of the potential.

Toroidal Bubble

In order to calculate the Kelvin impulse of a toroidal bubble, it is necessary to modify the above, so that integration is also performed across the cut. Hence

$$I_z^* = -\rho\, \boldsymbol{e}_z \cdot \int_{S \cup T} \phi \boldsymbol{n}\, \mathrm{d}S. \tag{3.6.9}$$

Performing azimuthal integrations analytically and changing the variable of integration to ξ yields

$$I_z = 2\pi \int_{\xi_1}^{\xi_n} \Phi(\xi)\mathcal{R}(\xi)\frac{\mathrm{d}\mathcal{R}(\xi)}{\mathrm{d}\xi}\,\mathrm{d}\xi - \pi\Delta\phi\, r_{1/n}^2, \tag{3.6.10}$$

where we recall $r_{1/n}$ is the r-coordinate of the point at which the cut meets the surface of the bubble. We note it is possible to perform the integration across the cut analytically due to the constant jump in potential thereon.

3.6.4 Kinetic Energy

The principle of conservation of energy has great implications in the physical world around us. In this work, it provides a means by which we are able to check the fidelity of our calculations. By making approximations in our model and in the numerical scheme we employ, we expect there to be some degree of error; and we reason that the success of our work may be judged by the magnitude of this error. Furthermore, the calculation of energies associated with the motion of the bubble and surrounding fluid helps to provide further insight into the physical problems we consider.

An expression for the kinetic energy due to the motion of the bubble is given by

$$E_{\mathrm{k}}^* = \frac{\rho}{2}\int_S \phi\frac{\partial\phi}{\partial n}\,\mathrm{d}S, \tag{3.6.11}$$

which yields the numerical integration to be performed as

$$E_{\mathrm{k}} = \pi \int_{\xi_1}^{\xi_n} \mathcal{R}(\xi)\Phi(\xi)\Psi(\xi)\,\mathrm{d}\xi, \tag{3.6.12}$$

where we recall that $\Psi(\xi)$ is the functional form of the normal velocity, which varies linearly with respect to arclength.

Although this integral may appear similar in nature to that which we are required to perform in order to calculate the Kelvin impulse, the addition of the normal velocity introduces severe difficulties in extending this calculation to the toroidal phase of bubble motion. In the previous section we were able to utilise the constant nature of the potential across the cut to calculate the Kelvin impulse of the toroidal bubble. However, it is obvious[13] the normal velocity on the cut is not constant. Therefore in order to calculate this integral on the cut would require the calculation of the normal velocity thereon. Whilst techniques have been envisaged for this purpose, these would only be approximate. Due to this, values of the kinetic energy for the toroidal bubble would not be suitable for validation of the code. Furthermore, since energy is conserved in our model, a better estimate may be obtained by subtracting calculated values for the potential energy of compression and/or gravitational potential energy (where pertinent) from a reference energy: this may be taken, for example, to be the total energy at initiation; or to take into account any energy losses from the pre-toroidal phase of motion, at the time of liquid jet impact.

3.6.5 Potential Energy

Here potential energy refers to the work done in changing the bubble's volume from its initial size, V_0 to some volume, $V(t)$; and not the gravitational potential energy of the system, which is considered below.[14] The potential energy of the bubble is given by

$$E_{\mathrm{p}}^{*} = -\int_{V_0}^{V} (p - p_{\infty})\, \mathrm{d}V, \tag{3.6.13}$$

where p is the time varying pressure given by the sum of the vapour pressure, p_{v} and the gas pressure given by equation (2.3.1), which we recall here for convenience is

$$p = p_{\mathrm{v}} + p_0 \left(\frac{V_0}{V}\right)^{\kappa}. \tag{3.6.14}$$

[13] Consider the distortion of the cut in the work by Best (1991).

[14] We note this may be referred to as internal energy by some authors.

Here we also recall our pressure scale $\Delta p = p_\infty - p_v$, which we use to non-dimensionalise equation (3.6.14). Substituting this into (3.6.13) yields

$$E_p = -\int_{V_0}^{V} \left[\alpha\left(\frac{V_0}{V}\right)^\kappa - 1\right] \mathrm{d}V. \tag{3.6.15}$$

Special notice must be paid to the lower limit of integration, V_0, which henceforth implies that E_p is the change in potential energy from the initial state. In this case, the integration of equation (3.6.15) may be performed simply, and analytically, to yield the expression

$$E_p = V - V_0 - \frac{\alpha V_0^\kappa}{1-\kappa}\left(V^{1-\kappa} - V_0^{1-\kappa}\right), \tag{3.6.16}$$

where α is the compression ratio and κ is the ratio of specific heats. Recall that $\alpha = 0$ when considering vapour bubbles.

With the inclusion of buoyancy effects and where pressure is no longer scaled by that at the inception depth, the expression for the potential energy becomes

$$E_p = (1-\delta^2\gamma)(V - V_{eq}) - \frac{\alpha V_0^\kappa}{1-\kappa}\left(V^{1-\kappa} - V_{eq}^{1-\kappa}\right), \tag{3.6.17}$$

where V_{eq} is the volume of the equivalent spherical bubble at the pseudo-equilibrium radius given by equation (2.5.10) and at the inception depth.

3.6.6 Gravitational Potential Energy

Finally, we consider contributions made to the total energy of the system by the potential energy stored in the fluid through which a bubble under the action of buoyancy may rise. An expression for the gravitational potential energy (GPE) may be readily found in the literature[15] as

$$E_g^* = -\frac{\rho g}{4}\int_S z\boldsymbol{p}\cdot\boldsymbol{n}\,\mathrm{d}S, \tag{3.6.18}$$

where $\boldsymbol{p}$ and $\boldsymbol{n}$ denote position and normal vectors for a point on the surface of the bubble, ρ is the density of the fluid and g is the acceleration due to gravity. Non-dimensionalising and performing the azimuthal integration analytically yields an expression for the GPE

[15]For example, Oğuz & Prosperetti (1993).

as

$$E_{\mathrm{g}} = -\frac{\pi\delta^2}{2}\int_{\xi_1}^{\xi_n} \mathcal{R}(\xi)(\mathcal{Z}(\xi)-\gamma)\left(\mathcal{R}(\xi)\frac{\mathrm{d}\mathcal{Z}(\xi)}{\mathrm{d}\xi} - (\mathcal{Z}(\xi)-\gamma)\frac{\mathrm{d}\mathcal{R}(\xi)}{\mathrm{d}\xi}\right)\mathrm{d}\xi. \tag{3.6.19}$$

As with all potential energy, a zero level may be chosen arbitrarily, which is taken to be the initial state. As the flow evolves and the bubble rises, we expect a decrease in the GPE, which is converted to other forms of energy.

3.6.7 Kelvin Impulse of the Liquid Jet

In Section 2.7, we introduced the concept of the Kelvin impulse as a local measure of fluid momentum, noting that physically it may be thought of as an instantaneous wrench which may be applied to the fluid in order to generate that motion from rest. In Section 3.6.3, we outlined the required numerical integrations required to calculate the Kelvin impulse for both pre-toroidal and toroidal bubbles. In the current section, we will outline the techniques required in order to calculate the Kelvin impulse for the volume of fluid which constitutes the liquid jet. Hence we obtain an idea of the instantaneous wrench which would be required to set the liquid jet in motion.

For the purposes of our calculations, we consider the liquid jet to be the volume of fluid which may be bounded by some part of the surface of the bubble, $S_J \subset S$ and a circular lid, L placed on top of, or beneath, the bubble. See the schematic in Figure 3.4, where this volume of fluid is coloured magenta. We introduce at this stage the integral required to calculate the Kelvin impulse of the jet, which is

$$I_z^* = -\rho\, \boldsymbol{e}_z \cdot \int_{S_J \cup L} \phi\, \boldsymbol{n}\, \mathrm{d}S, \tag{3.6.20}$$

which has the requirement that we integrate over $S_J \subset S$, which may be performed as for the Kelvin impulse of the bubble (with a little care where integration over a partial segment of the bubble surface is necessary), and across the circular lid, L. This is somewhat more difficult, since this requires the calculation of ϕ at points $l \in L$ not on the surface of the bubble, but within the body of fluid surrounding the bubble.

In order to present an uncluttered outline of the techniques we employ to calculate ϕ across the whole of L, details for the calculation of ϕ at a point not too close to S

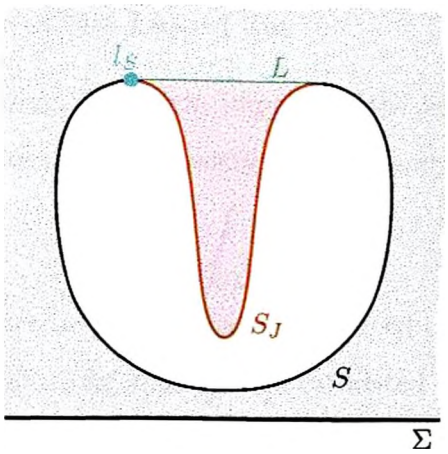

Figure 3.4: Schematic showing the volume of fluid which we call the jet (magenta). This is bounded by S_J a subset of the surface of the bubble and a flat circular lid L placed atop the bubble. The point $l_S \in S_J \cap L$.

are detailed in Section 3.7. However, some of the points on L do lie close to S. Indeed, during the earliest moments of jet formation, all points $l \in L$ lie close to S. Instead, we concentrate on calculating the Kelvin impulse of the jet at some time later once a more obvious jet may be observed, typically 30 iterations after the first occurrence of a concave portion of S.[16] At this and subsequent times, much of L lies sufficiently far from S that the potential may be calculated accurately. We also know the potential at the point $l_S \in S_J \cap L$. Crucially, we also know the derivative of ϕ along L, which is $\partial\phi/\partial r$; this is simply the r-component of surface velocity at l_S. Using our values for ϕ on the central portion of L and the value of ϕ and its derivative at l_S, we may fit a series of cubic spline elements through the known data.[17] Values for ϕ may then be calculated at points on L, close to S, where required. Hence the integral along L may be calculated using Gaussian quadrature. Time steps at which erroneous values of ϕ propagate into the final solution are readily identified by visual inspection of the final data and may then be discarded. This problem occurs only during early times and does not affect data beyond a certain instant.

[16] Though of course this is dependent on the size of the time steps taken.
[17] The splines are kept smooth on the axis of symmetry by imposing the derivative $\partial\phi/\partial r = 0$ there.

3.6.8 Kinetic Energy of the Liquid Jet

The techniques for calculating the Kelvin impulse of the liquid jet detailed above are readily extended to calculate the kinetic energy therein, and is given by

$$E_{\mathrm{k}}^{*} = \frac{\rho}{2} \int_{S_J \cup L} \phi \frac{\partial \phi}{\partial n} \, \mathrm{d}S. \tag{3.6.21}$$

We note the difficulty is increased somewhat by the need to also calculate the normal velocity, ψ on L. Again, values for ϕ and ψ are calculated on the central portion of L and at the point l_S which also lies on the surface of the bubble. Despite the fact that we do not know the derivative of ψ at l_S, splines may still be fitted to the data using not-a-knot end conditions at the outer end of L, whilst retaining the prescribed derivative, $\partial\phi/\partial r = 0$, on the axis of symmetry. Even with the use of the not-a-knot condition, we are confident that the splines adequately capture the behaviour of ψ along L, since any errors are readily noticeable in the final value for the Kinetic energy of the jet and may be removed after inspection.

Figure 3.5 shows an example of the variation in potential and normal velocity across L at the 30^{th} time step following the initial jet formation in a cavitation bubble. We note that data is calculated explicitly using the BIM at twelve points: the first on the axis of symmetry, the last at l_S, the remaining ten at the ten abscissas nearest the axis of symmetry which are required for numerical integration using sixteen point Gaussian quadrature. Splines are fitted to this calculated data and the further six values required for quadrature at the end nearest l_S interpolated. We note the non-constant nature of these quantities which shows these techniques to be necessary.

3.7 Pressure and Velocity Fields

One aspect in which our numerical calculations offer physical insight beyond that afforded our experimental colleagues is in the calculation of quantities throughout the flow field. Whilst it is possible to record information at the boundaries, such as the pressures thereon (see Tomita & Shima 1986), it is not easily possible to record this data within the body of the fluid. Especially since regions of interest are often in close proximity to the bubble, where recording devices would invariably have a great influence on the motion of the

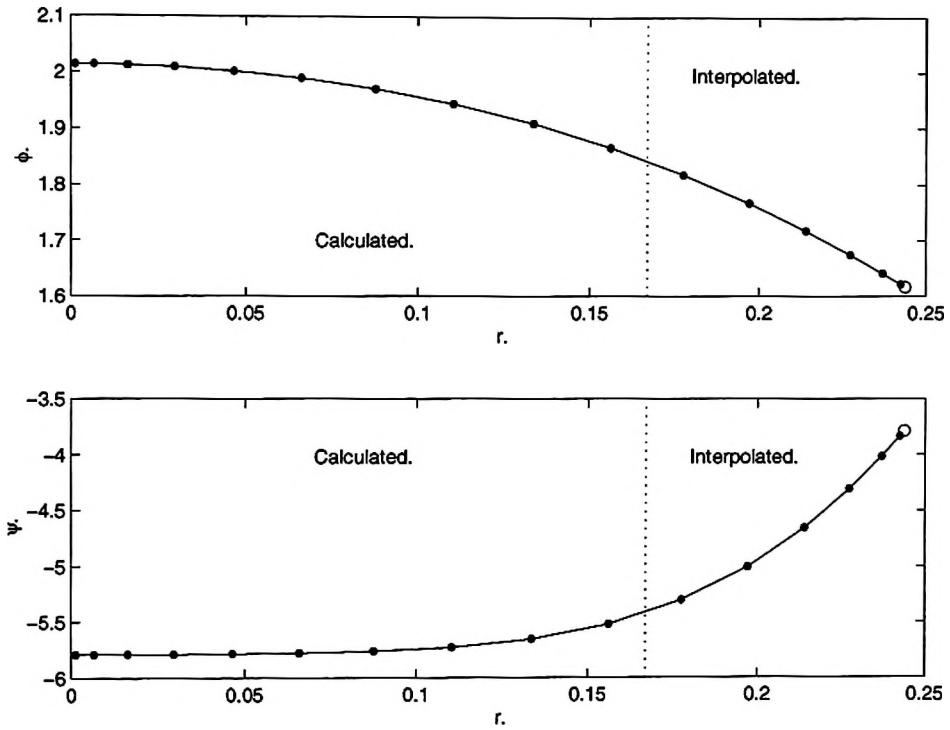

Figure 3.5: Potential and velocity across the lid, L at the 30^{th} time step following initial jet formation for bubble motion characterised by $\alpha = 500$, $\gamma = 1.1$, $\delta = 0.0$ and $\kappa = 1.4$. Dots denote points at which data is required for the integration by Gaussian quadrature, with calculated values to the left of the vertical dotted line, and interpolated values to the right. Data on the bubble is denoted by an open circle.

bubble. Furthermore, where information is recorded at the boundary, the range of cases may be limited due to damage caused to, for example, pressure transducers by the violent collapse of the bubble.

In this section we detail techniques for the calculation of pressure and velocity fields surrounding the bubble. Whilst such techniques have been previously employed by, for example, Taib (1985) and Best (1991), the accuracy and/or resolution of their calculation will unquestionably have been affected: in the former case, by the accuracy of the governing BI scheme; and to a lesser extent in the latter by the computational resources available. Techniques developed for the current work also prevent spurious data being calculated inside, and near to, the surface of the bubble.

3.7.1 Instantaneous Velocities Within the Fluid

We begin by detailing the method of calculating the fluid velocity at a point within the body of the fluid, i.e. at some point $\boldsymbol{p} \in \Omega \setminus \partial\Omega$. We recall that in our scheme, the motion of the fluid is governed by the velocity potential ϕ and as such the r and z-components of fluid velocity, (u, v) are given by

$$(u, v) = \left(\frac{\partial \phi}{\partial r}, \frac{\partial \phi}{\partial z} \right). \tag{3.7.1}$$

Here we choose to calculate these using a five-point formula for the derivatives. To such end, the derivative of ϕ with respect to some variable ζ, at the point ζ_i are given by

$$\left. \frac{\partial \phi}{\partial \zeta} \right|_{\zeta_i} = a_i \phi_{i-2} + b_i \phi_{i-1} + c_i \phi_i + d_i \phi_{i+1} + e_i \phi_{i+2}, \tag{3.7.2}$$

with

$$a_i = \frac{(\zeta_i - \zeta_{i+2})(\zeta_i - \zeta_{i+1})(\zeta_i - \zeta_{i-1})}{(\zeta_{i-2} - \zeta_{i+2})(\zeta_{i-2} - \zeta_{i+1})(\zeta_{i-2} - \zeta_i)(\zeta_{i-2} - \zeta_{i-1})}, \tag{3.7.3a}$$

$$b_i = \frac{(\zeta_i - \zeta_{i+2})(\zeta_i - \zeta_{i+1})(\zeta_i - \zeta_{i-2})}{(\zeta_{i-1} - \zeta_{i+2})(\zeta_{i-1} - \zeta_{i+1})(\zeta_{i-1} - \zeta_i)(\zeta_{i-1} - \zeta_{i-2})}, \tag{3.7.3b}$$

$$c_i = \frac{1}{(\zeta_i - \zeta_{i+2})} + \frac{1}{(\zeta_i - \zeta_{i+1})} + \frac{1}{(\zeta_i - \zeta_{i-1})} + \frac{1}{(\zeta_i - \zeta_{i-2})}, \tag{3.7.3c}$$

$$d_i = \frac{(\zeta_i - \zeta_{i+2})(\zeta_i - \zeta_{i-1})(\zeta_i - \zeta_{i-2})}{(\zeta_{i+1} - \zeta_{i+2})(\zeta_{i+1} - \zeta_i)(\zeta_{i+1} - \zeta_{i-1})(\zeta_{i+1} - \zeta_{i-2})}, \tag{3.7.3d}$$

$$e_i = \frac{(\zeta_i - \zeta_{i+1})(\zeta_i - \zeta_{i-1})(\zeta_i - \zeta_{i-2})}{(\zeta_{i+2} - \zeta_{i+1})(\zeta_{i+2} - \zeta_i)(\zeta_{i+2} - \zeta_{i-1})(\zeta_{i+2} - \zeta_{i-2})}, \tag{3.7.3e}$$

where ζ may be taken as r, z, or later, t, as appropriate. As these velocities are also required in the calculation of the pressure field, we choose the spatial steps as an average of the temporal steps between the preceding two and following two time steps, so the errors in the calculation of these derivatives are of the same order. Hence for the r and z-derivatives, equations (3.7.3) reduce to the much simpler form

$$a_i = \frac{1}{12\mathrm{d}\zeta}, \qquad b_i = -\frac{2}{3\mathrm{d}\zeta}, \qquad c_i = 0, \qquad d_i = \frac{2}{3\mathrm{d}\zeta}, \qquad e_i = -\frac{1}{12\mathrm{d}\zeta}, \tag{3.7.4}$$

where $\mathrm{d}\zeta$ represents the regular change in ζ between points.

In order that velocity data is not calculated inside the bubble, where the velocity potential is not defined; or too close to the boundaries of the fluid domain, where singularities in the Green's function cause any potential calculated to be erroneous; we use the following method. For a given fluid boundary, cubic splines are fitted to the surface geometry. At each node, the normal thereon is calculated and is used to calculate a new node at a distance ϵ from the original, which lies inside the body of the fluid. To this new set of nodes, we again fit cubic splines, essentially creating a new boundary at a distance ϵ from the original fluid boundary. For each of the five points required to calculate a derivative, we then check that none of these occur within the newly defined surface through the calculation of a winding number.[18] If any of the five points fail

[18]The winding number, $n(\gamma, w)$ is defined as the complex contour integral

$$n(\gamma, w) = \frac{1}{2\pi i}\int_{\gamma} \frac{\mathrm{d}\bar{z}}{\bar{z} - w}, \tag{3.FN18.1}$$

about the fixed point w. In order to calculate a winding number for our bubble, we construct the contour $\gamma(\xi) = \mathcal{R}(\xi) + i\mathcal{Z}(\xi)$. Further, we let $w = r + iz$ denote a fixed point with coordinates (r, z). We now transform this integral into one with respect to arclength, ξ, hence

$$n(S, w) = \frac{1}{2\pi i}\int_{S} \frac{\gamma'(\xi)\,\mathrm{d}\xi}{\gamma(\xi) - w}, \tag{3.FN18.2}$$

where a $'$ represents a derivative with respect to ξ. It may be confirmed numerically that the imaginary part of this integral is zero. For a toroidal bubble, where the integral from ξ_0 to ξ_n is closed, the winding number is given by

$$n(S, w) = \frac{1}{2\pi}\int_{\xi_0}^{\xi_n} \frac{\mathcal{Z}'(\xi)[\mathcal{R}(\xi) - r] - \mathcal{R}'(\xi)[\mathcal{Z}(\xi) - z]}{[\mathcal{R}(\xi) - r]^2 + [\mathcal{Z}(\xi) - z]^2}\,\mathrm{d}\xi. \tag{3.FN18.3}$$

For a bubble in the pre-toroidal phase of motion, we are required to close the curve $\gamma(\xi)$. This yields the required integral as

$$n(S, w) = \frac{1}{2\pi}\int_{\xi_0}^{\xi_n} \left[\frac{\mathcal{Z}'[\mathcal{R} - r] - \mathcal{R}'[\mathcal{Z} - z]}{[\mathcal{R} - r]^2 + [\mathcal{Z} - z]^2} + \frac{\mathcal{Z}'[\mathcal{R} + r] - \mathcal{R}'[\mathcal{Z} - z]}{[\mathcal{R} + r]^2 + [\mathcal{Z} - z]^2}\right] \mathrm{d}\xi. \tag{3.FN18.4}$$

this test, then the calculation at the central point is omitted from pressure and velocity calculations. This essentially allows us to define, as a parameter of our scheme, a distance from any fluid interface in which we expect the potential calculated therein to be erroneous. Typically a value of $\epsilon = 0.01$ is fine, though where this point is near to a region of high curvature, it may be necessary to increase this value. This may be due to the inappropriateness of using a linear representation for the normal velocity between two nodes. Once the points have been deemed to be a sufficient distance from any fluid boundary, the potential at each of the points required is calculated by taking a value of $c(\boldsymbol{p}) = 1$ in equation (3.2.7) which gives

$$\phi(\boldsymbol{p}) = \int_{\partial\Omega} \left(\frac{\partial\phi(\boldsymbol{q})}{\partial n} G(\boldsymbol{p},\boldsymbol{q}) - \phi(\boldsymbol{q}) \frac{\partial G(\boldsymbol{p},\boldsymbol{q})}{\partial n} \right) \mathrm{d}S, \tag{3.7.5}$$

where all values on the right hand side of this equation are known *a priori*. At this stage, we also recall the analogous equation for the toroidal bubble, which is

$$\phi(\boldsymbol{p}) = \int_{S} \left(\frac{\partial\phi(\boldsymbol{q})}{\partial n} G(\boldsymbol{p},\boldsymbol{q}) - \phi(\boldsymbol{q}) \frac{\partial G(\boldsymbol{p},\boldsymbol{q})}{\partial n} \right) \mathrm{d}S - \Delta\phi \int_{T} \frac{\partial G(\boldsymbol{p},\boldsymbol{t})}{\partial n} \mathrm{d}S. \tag{3.7.6}$$

Given the potentials at the required five points, the appropriate derivative is calculated from equation (3.7.2).

3.7.2 Instantaneous Pressures Within the Fluid

In order to calculate the pressure throughout the body of the fluid, we appeal to the dimensionless Bernoulli pressure equation

$$p = 1 - \frac{\partial\phi}{\partial t} - \frac{1}{2}|\nabla\phi|^2 - \delta^2(z - \gamma), \tag{3.7.7}$$

which requires the fluid velocity at the point in question (as calculated above) and also the time derivative of the potential. This is calculated using the five-point scheme as detailed above. Due to the variable time stepping scheme we employ, the variable step form of the coefficients given by equations (3.7.3) is used. At each time step, the point $\boldsymbol{p}$ is checked so that it does not lie close to any boundaries using the method detailed in Section 3.7.1.

Once raw data for the pressure within the fluid and on the boundaries of the fluid domain are calculated, these are imported into MATLAB which is used to amalgamate

the data onto a hybrid grid created from the r and z-values at which we have pressure data. This is then interpolated to produce a dense grid of pressure values which are contoured using standard MATLAB routines. We note that several of the steps required in the final processing are computationally expensive using standard routines, so several of these are rewritten to suit our purposes, providing good optimisation.

3.8 Numerical Calculations

In this section we present results concerning the motion of vapour and gas bubbles both in an infinite fluid and in close proximity to a rigid boundary. We begin by considering the motion of a vapour bubble in an infinite fluid, using this as a test case so that energies for the motion of the bubble may be examined in order to determine the accuracy of our numerical scheme. Following this we briefly consider the motion of a vapour bubble close to a rigid boundary, before looking at the motion of bubbles with a gaseous content, again near to a rigid boundary. For this latter problem we thoroughly examine the physical quantities associated with the motion in order to gain further physical insight. Following this we present a short discussion concerning bubble motion near the null-impulse state which requires the inclusion of buoyancy effects. In the following section, we compare specific cases against experiments as a further means of validating our calculations.

3.8.1 Vapour Bubble in an Infinite Fluid – The Rayleigh Bubble

We begin by considering the motion of a vapour bubble in an infinite fluid, the motion of which was first considered analytically by Besant (1859) and Lord Rayleigh (1917). In the current work, this problem is used to examine the accuracy of our numerical scheme through the calculation of energies associated with the motion of the bubble.

The bubble is grown from an initial radius of $r_0 = 0.1$, starting at time $t_0 = 0.0015495456$ with a corresponding initial potential $\phi_0 = -2.5806976$. In this section, motion is allowed to continue until the bubble volume reaches a value of 10^{-5}, at which time calculations are ceased. Figure 3.6 shows the kinetic and potential energies and variation in total energy for the motion of the bubble using a fourth-order Runge-Kutta time-stepping scheme, with LM smoothing applied every eight time steps with $D = 0.01$,

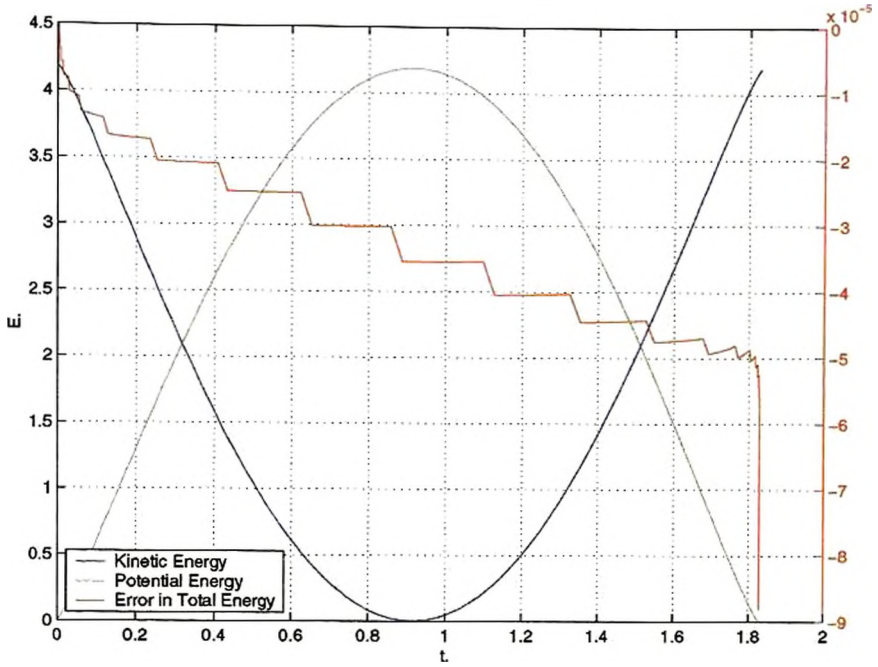

Figure 3.6: The kinetic and potential energies and variation in total energy (right-hand scale) associated with the motion of the Rayleigh bubble. Calculated using fourth-order Runge-Kutta time stepping with LM smoothing, $D = 0.01$ every 8 time steps and $\mathrm{d}\phi = 0.03$.

and an imposed maximum change in potential of $\mathrm{d}\phi = 0.03$. We will shortly discuss our choice of this scheme and parameters. The key aspect of this figure is the red curve denoting the variation in total energy, wherein we note the total energy loss is of the order 10^{-4} which is approximately 0.002% of the total energy of the system. From this we can also determine the major energy losses are due to numerical errors when the bubble is small in size and due to the smoothing applied, which causes the step-like trend through the middle of this curve.

In Figure 3.6 we present curves for the variation in total energy for the calculated motion of the Rayleigh vapour bubble for both second and fourth-order Runge-Kutta schemes and for both LM and LHC damping. The particular choices for the maximum change in potential were those which afforded least energy loss for that particular scheme. We note the much reduced energy loss through the use of a fourth-order time-stepping scheme using the LHC smoothing techniques over the second-order equivalent, which was employed by Best (1991). This is primarily due to the much larger time steps we are able

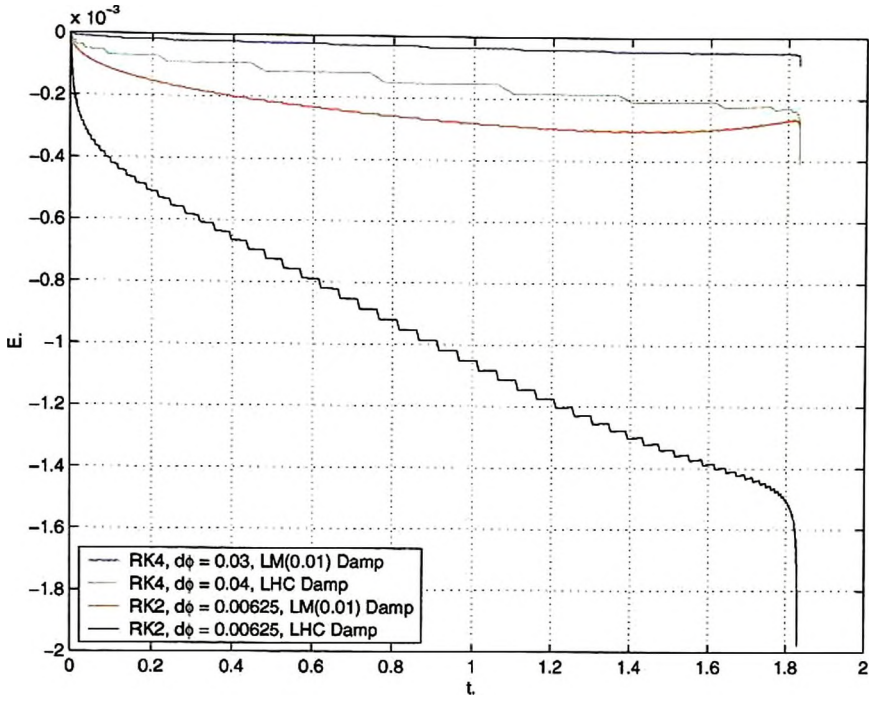

Figure 3.7: Comparison of variation in total energy for second and fourth-order Runge-Kutta schemes and different damping techniques for the motion of the Rayleigh bubble.

to take due to the improved accuracy, thus the smoothing is applied far less frequently. The reduced energy loss through the use of LM smoothing in the second-order schemes is also impressive. Since similar time steps are taken, so the number of applications of the respective smoothing techniques will be similar, hence the improvements are entirely due to the reduced amount of energy which the LM smoothing technique removes from the system.

We compare the energy losses due to differing values of the maximum change in potential for both second and fourth-order time-stepping schemes which employ the LM smoothing technique in Figures 3.8 and 3.9 respectively. We notice that for the second-order scheme, accuracy is improved through reduction in $d\phi$, down to very small values. We also note that for most choices of $d\phi$, energy is removed from the system during expansion then returned during collapse. However, for the fourth-order scheme there is an optimum choice of $d\phi$ for which we obtain maximal accuracy. We note that we discount choices of $d\phi$ where the variation in total energy increases during the final moments of collapse. Trends for LHC smoothing are very similar to those shown for LM

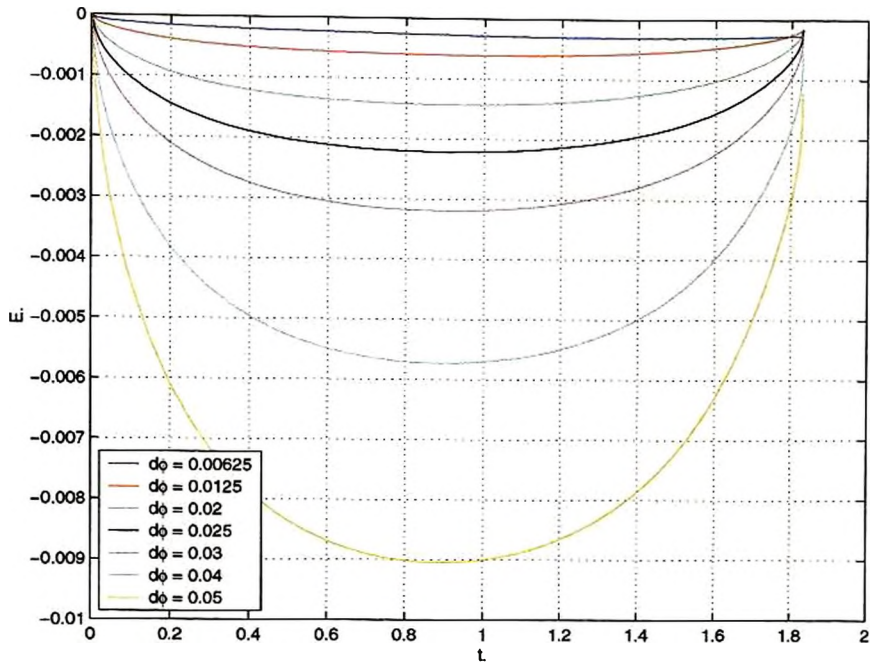

Figure 3.8: Comparison of variation in total energy for different maximum changes in potential for second-order Runge-Kutta schemes using LM smoothing techniques for the motion of the Rayleigh bubble.

smoothing, though the magnitude of the errors is greater.

Finally we consider the kinetic, potential and gravitational potential energy and variation in total energy for the motion of a buoyant explosion bubble in Figure 3.10. We notice the reduction in GPE as the bubble rises, with this energy being converted to other forms of energy. The trend in the variation in total energy is characteristic of any bubble in which a liquid jet forms, with the majority of energy lost in the system following formation of the liquid jet. This is to be expected since the smoothing techniques we employ are used to remove free surface spikes. Hence much of the energy loss may be attributed to smoothing near the tip of the liquid jet.

For the remainder of the results calculated in this chapter, we employ the numerical scheme and parameters which were used in calculating the energies of the Rayleigh bubble in Figure 3.6. Namely a fourth-order time-stepping scheme with LM damping every eight time steps, with $D = 0.01$ and an imposed maximum change in potential of $\mathrm{d}\phi = 0.03$.

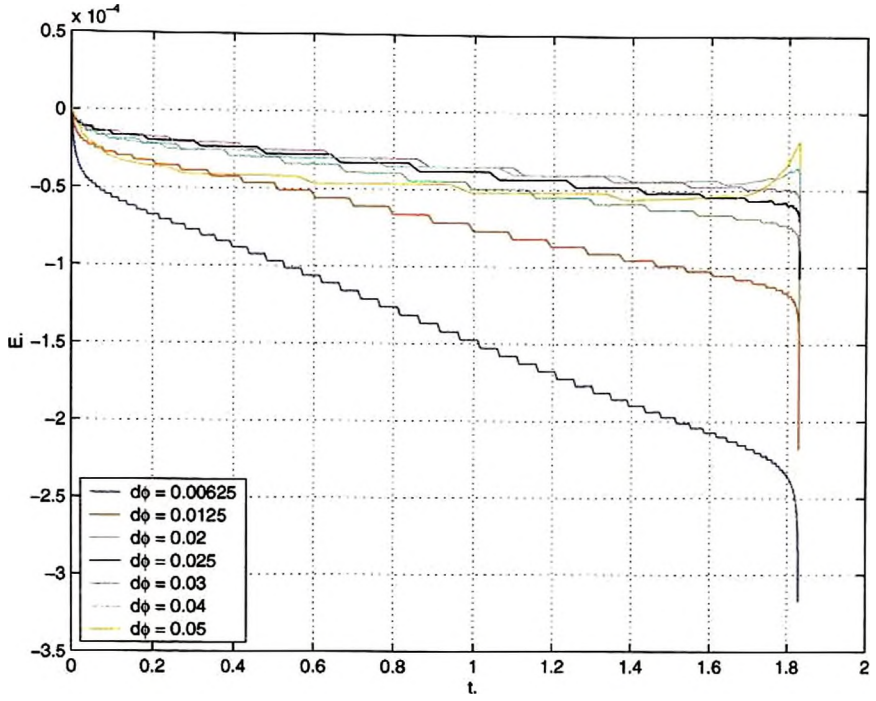

Figure 3.9: Comparison of variation in total energy for different maximum changes in potential for fourth-order Runge-Kutta schemes using LM smoothing techniques for the motion of the Rayleigh bubble.

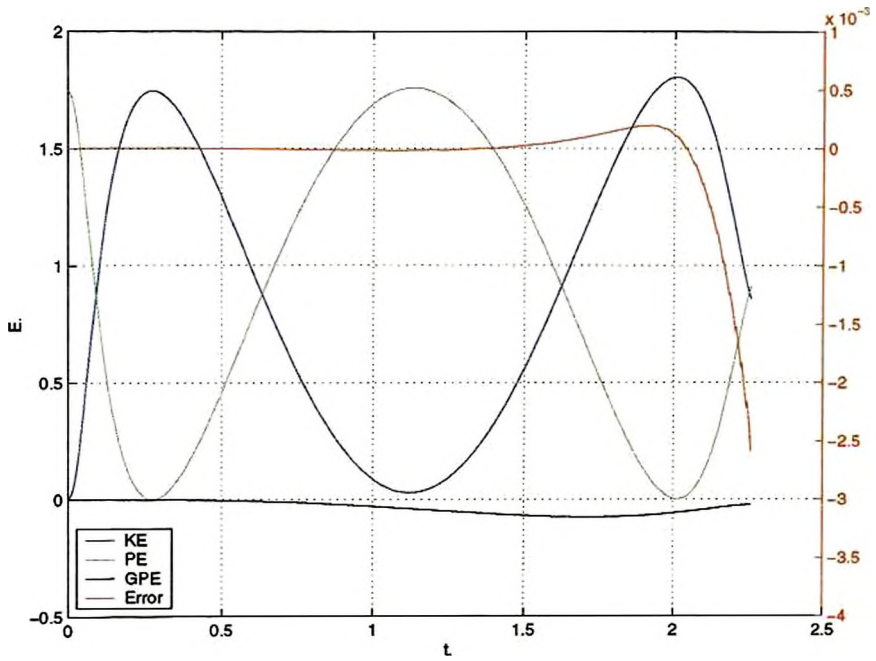

Figure 3.10: Kinetic, potential and gravitational potential energies and variation in total energy (right-hand scale) for the motion of a buoyant explosion bubble in an infinite fluid characterised by $\alpha = 10$, $\delta = 0.35$, $\kappa = 1.25$.

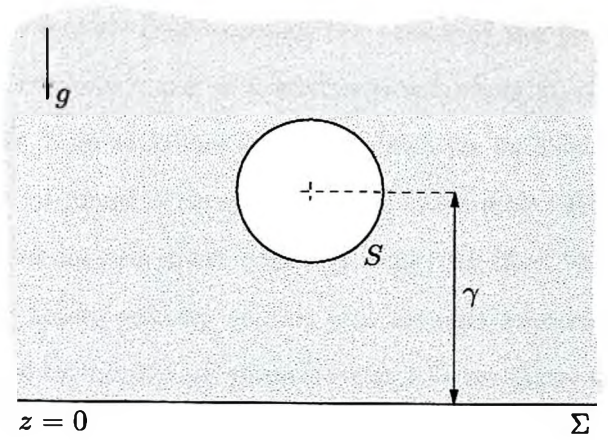

Figure 3.11: Schematic showing a bubble near a rigid boundary. The bubble is generated at a dimensionless distance γ from the boundary.

3.8.2 Vapour Bubble Near a Rigid Boundary

We begin the discussion of our results concerning bubble motion near boundaries by briefly considering the motion of a vapour bubble near a rigid boundary. In fact we will give only one example of this type, since we will shortly examine the motion of a bubble with a mixed vapour and gas content near to a rigid boundary. The inclusion of a gaseous content in the bubble allows a much more detailed examination of the physical quantities associated with motion to be undertaken. Prior to discussion of our results, we reproduce the schematic representation of a bubble near a rigid boundary from Chapter 2, though we note we have now labelled this in dimensionless form so as to remind the reader of the notation γ, the dimensionless standoff from the rigid boundary. This may be seen in Figure 3.11.

Figure 3.12 shows the motion of a vapour bubble generated at a standoff distance, $\gamma = 1$ from a rigid boundary. In Figure 3.12a we present half-rendered bubble shapes for both the pre-toroidal and toroidal phases of motion. Frames 1 and 2 show the bubble at the start of our calculations and at maximum volume respectively. We note the flattening of the underside of the bubble at maximum volume due to the close proximity of the boundary. Frames 3 through 6 show the collapse phase up until the time of liquid jet impact. Due to the Bjerknes force of attraction, both the migration of the centroid and the direction of the liquid jet are towards the boundary. Following jet impact, the

resulting circulation channels fluid through the centre of the bubble. This fluid then impacts against the boundary and is forced outward along it. Due to the continued collapse of the bubble, fluid continues to rush in from the far-field. Where the opposing flows meet, a 'splash' of liquid is thrown up inside the bubble. Further consideration is given to the splash phenomenon in the paper by Tong, Schiffers, Shaw, Blake & Emmony (1999). Figure 3.12b shows velocity vectors and pressure contours within the body of the fluid and show the region of high pressure which forms above the bubble and drives the flow. Following jet impact, a region of higher pressure forms on the rigid boundary, which then continues to spread outwards as the flow evolves. This and the circulation around the bubble may be observed in Figure 3.12c.

Finally in this section, we pause to comment on the effects of surface tension which have been omitted in this study. During the pre-toroidal phase of motion, local curvature is typically $O(10^1)$ for much of the lifetime of the bubble, rising to $O(10^2)$ over portions of the bubble surface as the liquid jet forms. Since in Section 2.6 we noted that surface tension effects will play a rôle only when local curvature becomes $O(10^3)$, it is unlikely surface tension will have a significant effect. However, we note the likelyhood that both the implicit and explicit forms of smoothing in our numerical scheme may have kept calculated values of the local curvature artifically small, especially at the tip of the jet, and so we may not totally discount surface tension effects there. During the toroidal phase of motion however, calculated values for the local curvature occasionally rose to $O(10^3)$, though these were quickly smoothed. Hence we recommend that surface tension effects are included during the toroidal phase of motion once requirement for smoothing is removed from our numerical scheme, though at the moment smoothing artificially plays this rôle.

3.8.3 Gas Bubble Near a Rigid Boundary

Here we present a much fuller discussion of the motion of a cavitation bubble near to a rigid boundary. Although in many cases a good agreement with experiments may be achieved by simply considering the motion of a vapour bubble, key features of the motion around minimum volume, where phenomena are associated with the compression of gas

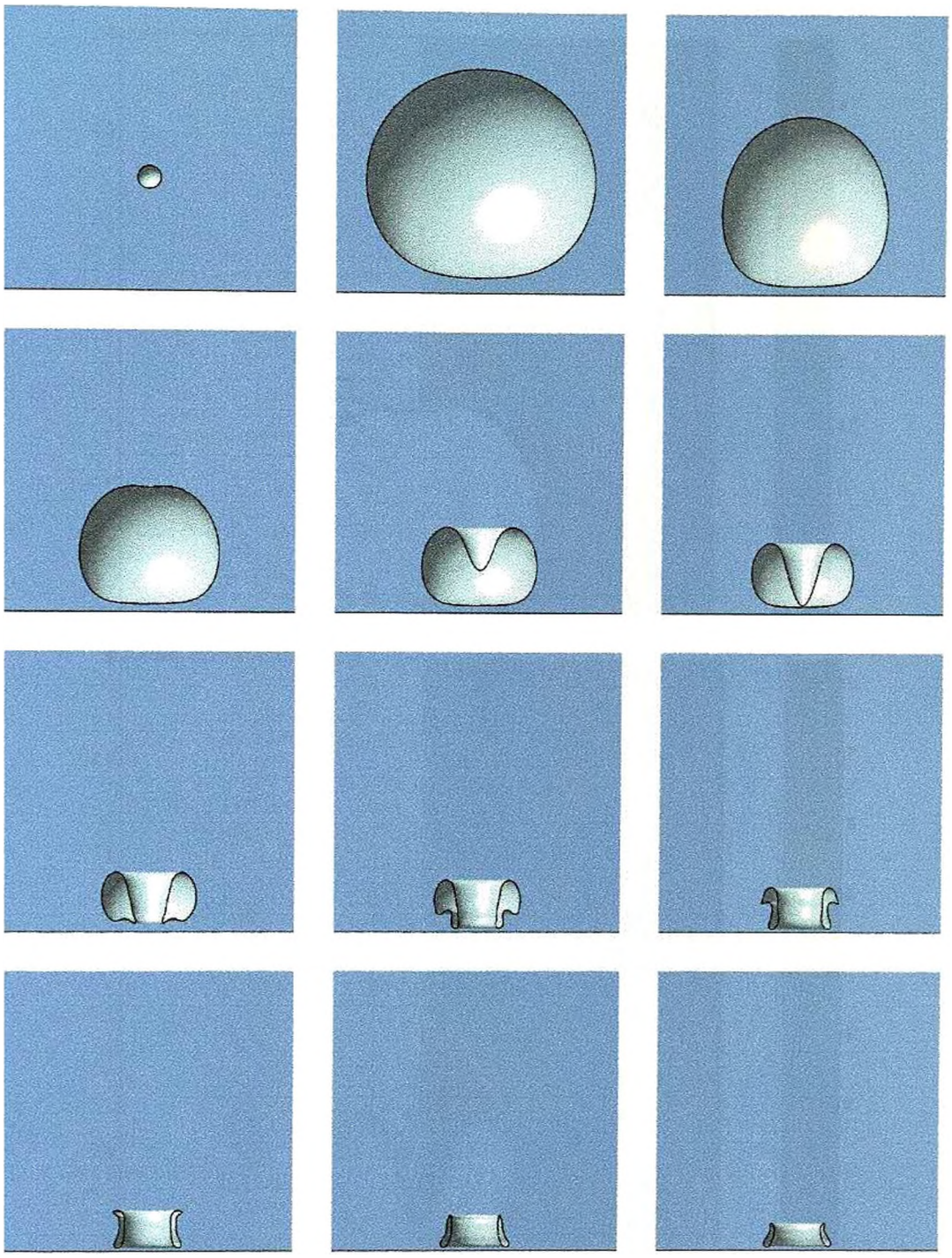

(a) Half-rendered bubble shapes. Horizontal and vertical axes are $r \leqslant 1.25$, $0 \leqslant z \leqslant 2.5$. The rigid boundary is visible at the bottom of each frame. Times are 0.0015, 1.0536, 1.7747, 1.9565, 2.0488, 2.0850, 2.0995, 2.1071, 2.1212, 2.1387, 2.1478 and 2.1518 respectively.

Figure 3.12: Motion of a vapour bubble near a rigid boundary with $\gamma = 1.0$.

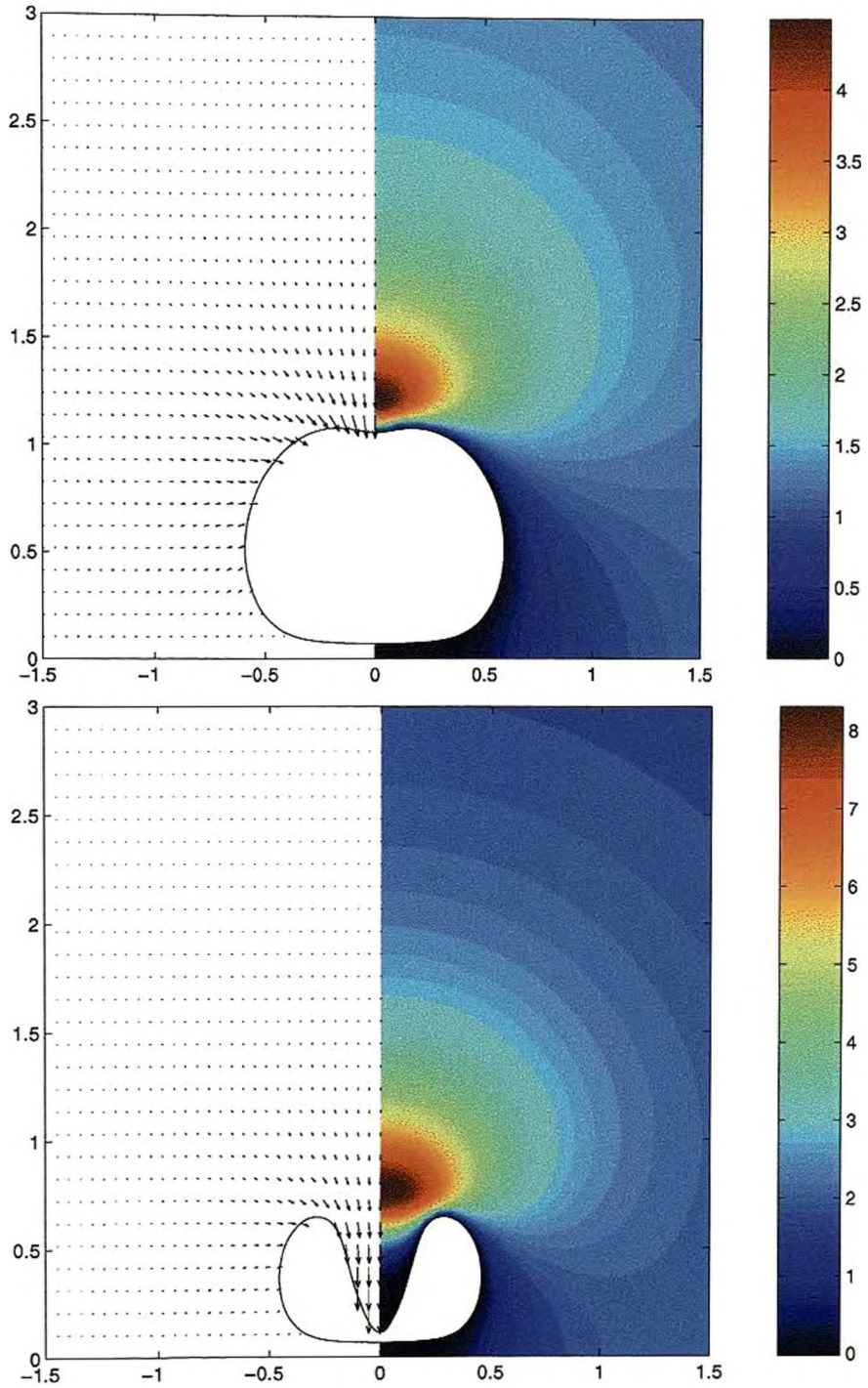

(b) Velocity vectors and pressure contours during the pre-toroidal phase of motion. Times are 1.9628 and 2.0802 respectively.

Figure 3.12 continued: Motion of a vapour bubble near a rigid boundary with $\gamma = 1$.

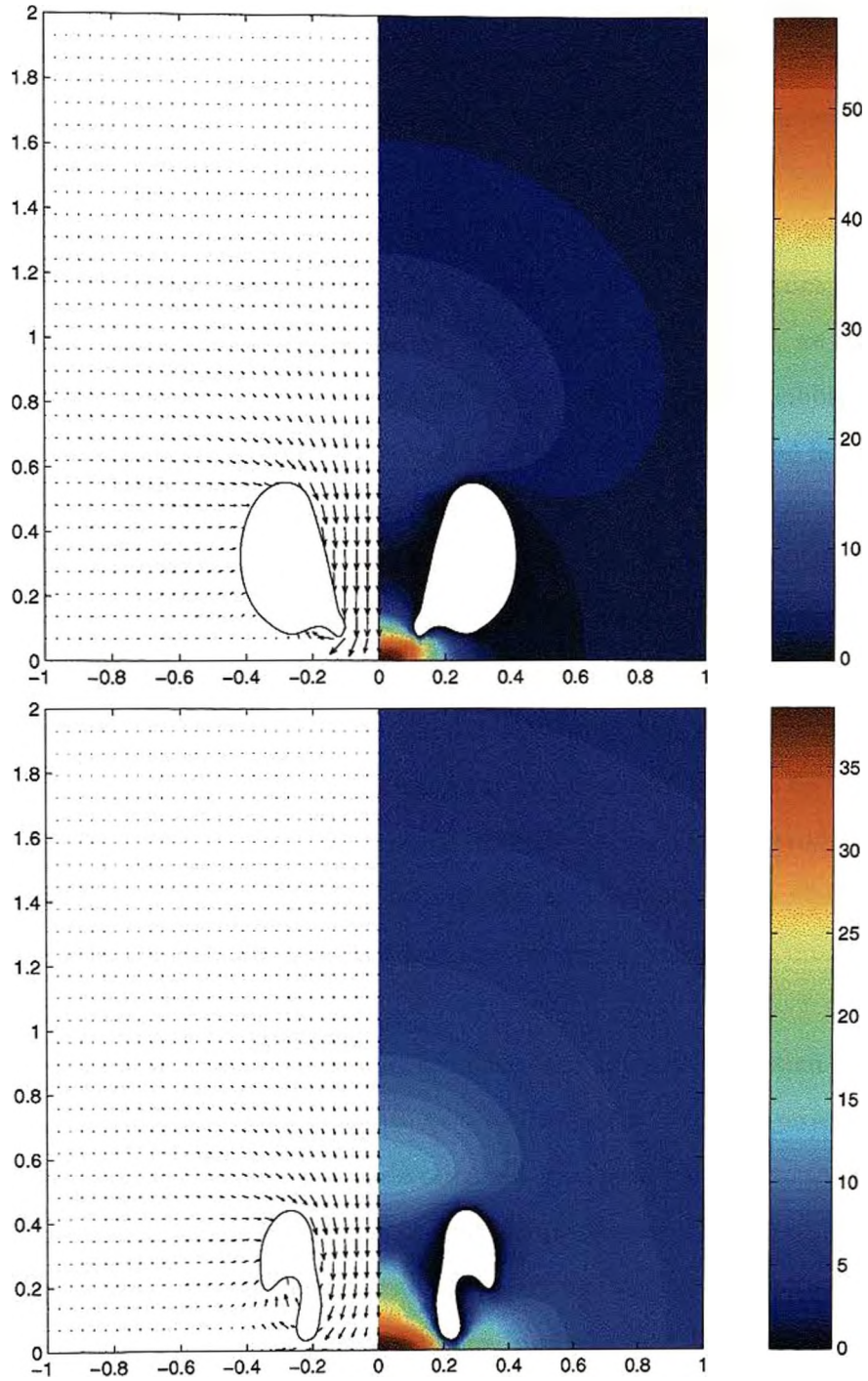

(c) Velocity vectors and pressure contours during the toroidal phase of motion. Times are 2.0958 and 2.1112 respectively.

Figure 3.12 continued: Motion of a vapour bubble near a rigid boundary with $\gamma = 1$.

within the bubble, may be lost. In particular, the speed of the liquid jet during final collapse may be greatly affected. This is of consequence where bubbles of highly disparate maximum bubble radii, and hence period of oscillation, are considered. Although in this chapter we only consider single bubble systems, we will later show the importance of the consideration of these effects for systems of two or more bubbles.

We begin by looking at the motion of cavitation bubbles generated over a range of standoff distances from a rigid boundary and for the two compression ratios $\alpha = 100$ and 1000. In order to give an idea of the bubble geometries which develop, we consider the shape of the bubble at the time of liquid jet impact. Half-rendered bubble shapes for $\alpha = 100$, and standoff distances over the range $\gamma = 0.7 - 6.0$ are presented in Figure 3.13. For standoff distance of $\gamma = 1.0$ and below, the bubble is characterised by a wide liquid jet and flattened underside, which becomes more pronounced as the bubble is initiated closer to the boundary. As the point of initialisation is moved further from the boundary, the expansion phase quickly becomes almost spherical in nature[19] as the influence of the boundary lessens. Furthermore, due to the decrease in the Bjerknes force of attraction, the bubble attains a smaller volume at the time of jet impact up to a certain standoff distance. Beyond this distance, the bubble actually begins to re-expand prior to jet impact. One other feature which may be regarded as a function of standoff distance is breadth of the liquid jet, which becomes first proportionally wider, then much thinner as γ is increased.

Corresponding shapes for bubbles generated with a compression ration of $\alpha = 1000$ are presented in Figure 3.14 over the range $\gamma = 0.75 - 6.0$. In close proximity to the boundary (i.e. $\gamma \leqslant 1.5$), the bubble shapes observed are almost identical to those observed for $\alpha = 100$ in Figure 3.13. This indicates that the predominant influence on motion in this range is the boundary and not the internal pressure of the bubble. For larger standoff distances, the volumes at jet impact are typically smaller and the jets which form are wider than those observed for $\alpha = 100$ at a given standoff distance.

As noted above, up to a critical distance from the boundary, the volume of the bubble at the time of liquid jet impact decreases as the standoff increases. Beyond this

[19] Although evidence is not given here, it may be inferred from the more rounded undersides observed on the bubble shapes at the time of jet impact.

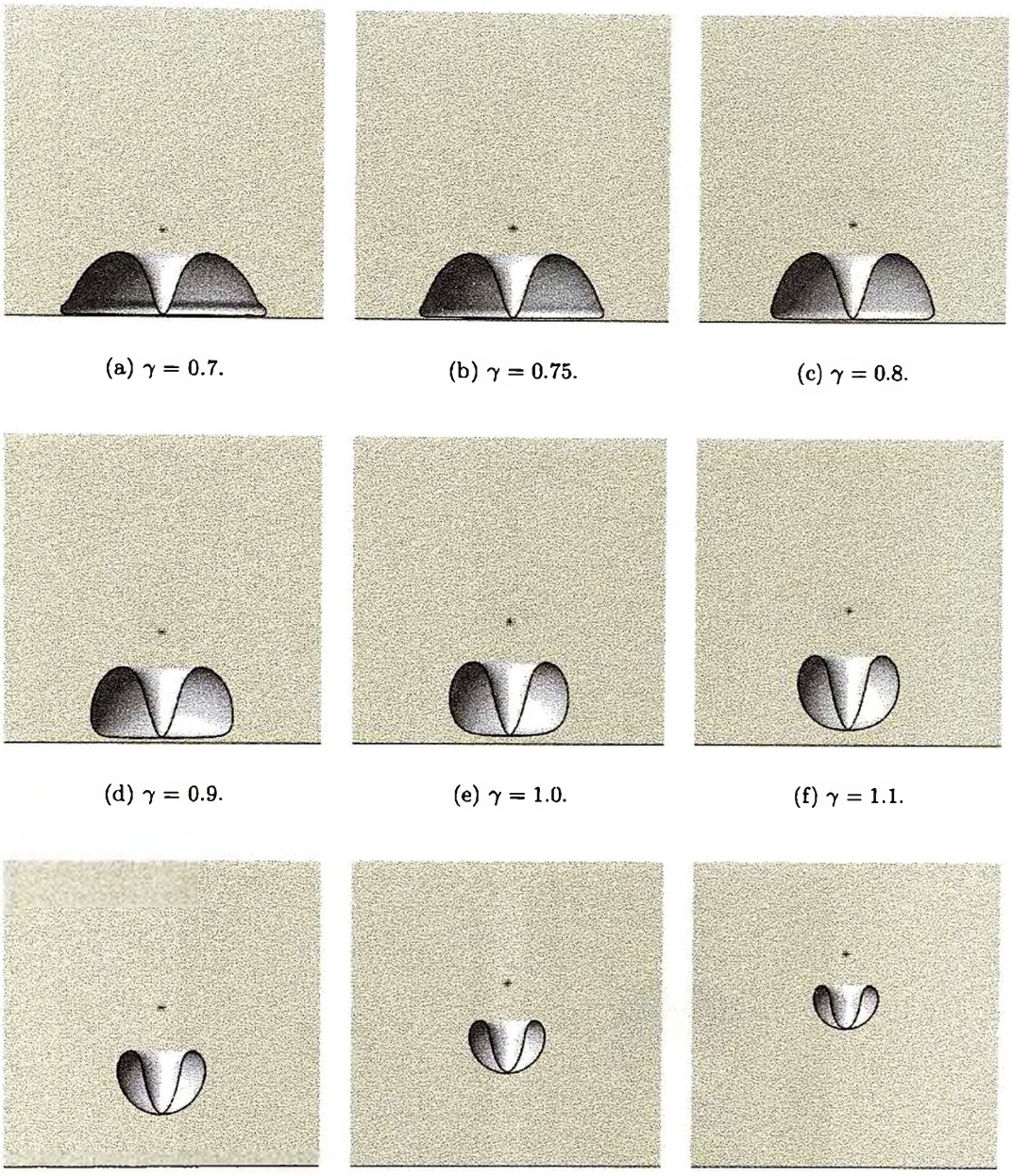

(a) $\gamma = 0.7$. (b) $\gamma = 0.75$. (c) $\gamma = 0.8$.

(d) $\gamma = 0.9$. (e) $\gamma = 1.0$. (f) $\gamma = 1.1$.

(g) $\gamma = 1.3$. (h) $\gamma = 1.5$. (i) $\gamma = 1.75$.

Figure 3.13: Half-rendered bubble shapes showing the geometry of a cavitation bubble, $\alpha = 100$ above a rigid boundary for a range of standoff distances at the time of jet impact. Horizontal and vertical axes are: (a) through (i) $r \leqslant 1.25$, $0 \leqslant z \leqslant 2.5$; (j) through (q) $r \leqslant 1.25$, $|z - \gamma| \leqslant 1.25$. The black star denotes the point of initialisation. The boundary is visible at the bottom of frames (a) through (i).

(j) $\gamma = 2.0$. (k) $\gamma = 2.5$. (l) $\gamma = 3.0$.

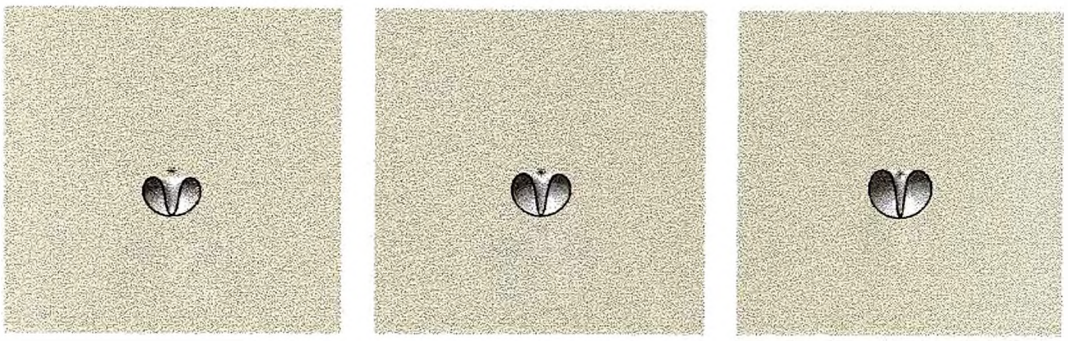

(m) $\gamma = 3.5$. (n) $\gamma = 4.0$. (o) $\gamma = 4.5$.

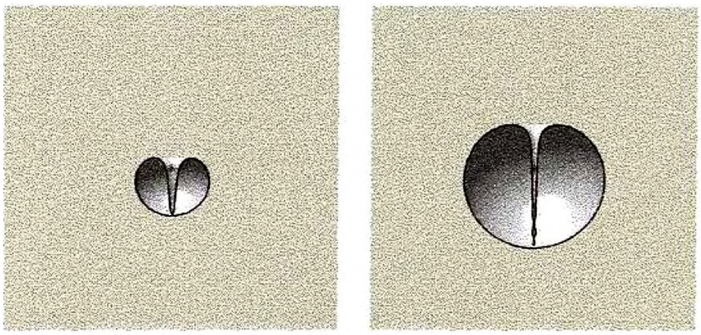

(p) $\gamma = 5.0$. (q) $\gamma = 6.0$.

Figure 3.13 continued: Half-rendered bubble shapes showing the geometry of a cavitation bubble, $\alpha = 100$ above a rigid boundary for a range of standoff distances at the time of jet impact. Horizontal and vertical axes are: (a) through (i) $r \leqslant 1.25$, $0 \leqslant z \leqslant 2.5$; (j) through (q) $r \leqslant 1.25$, $|z - \gamma| \leqslant 1.25$. The black star denotes the point of initialisation. The boundary is visible at the bottom of frames (a) through (i).

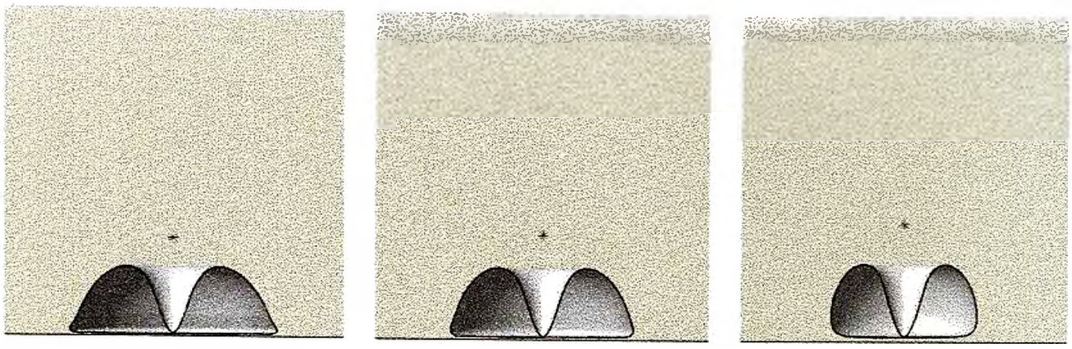

(a) $\gamma = 0.75$. (b) $\gamma = 0.8$. (c) $\gamma = 0.9$.

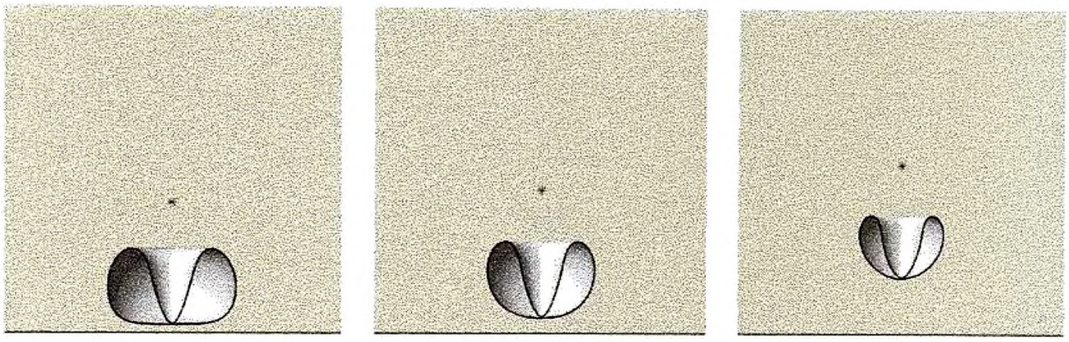

(d) $\gamma = 1.0$. (e) $\gamma = 1.1$. (f) $\gamma = 1.3$.

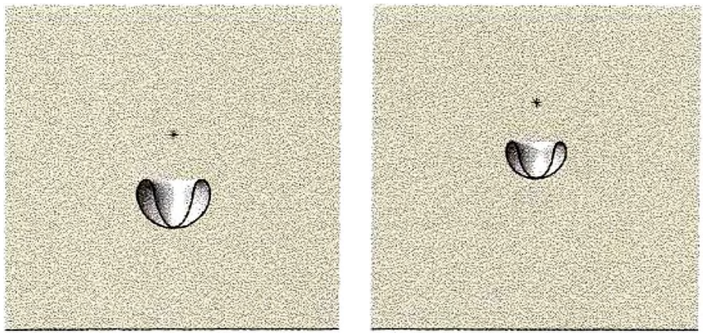

(g) $\gamma = 1.5$. (h) $\gamma = 1.75$.

Figure 3.14: Half-rendered bubble shapes showing the geometry of a cavitation bubble, $\alpha = 1000$ above a rigid boundary for a range of standoff distances at the time of jet impact. Horizontal and vertical axes are (a) through (h) $r \leqslant 1.25$, $0 \leqslant z \leqslant 2.5$; (i) through (p) $r \leqslant 0.75$, $|z - \gamma| \leqslant 0.75$. The black star denotes the point of initialisation. The boundary is visible at the bottom of frames (a) through (h).

(i) $\gamma = 2.0$. (j) $\gamma = 2.5$. (k) $\gamma = 3.0$.

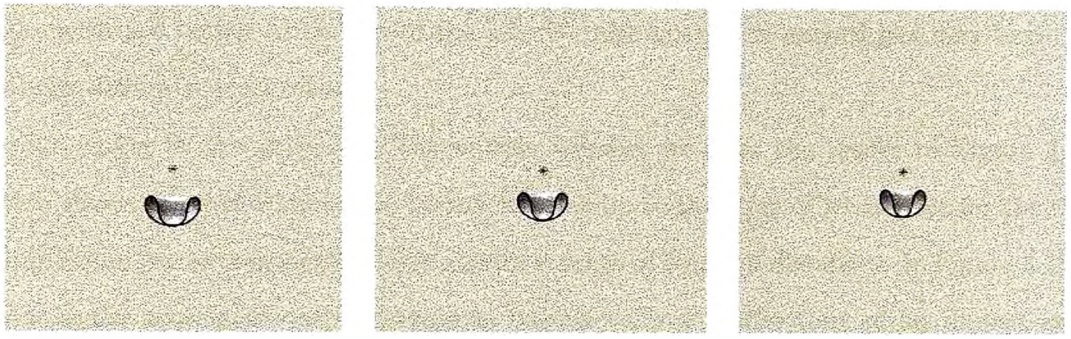

(l) $\gamma = 3.5$. (m) $\gamma = 4.0$. (n) $\gamma = 4.5$.

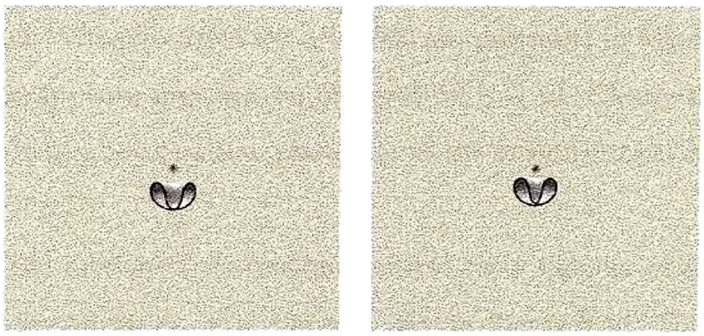

(o) $\gamma = 5.0$. (p) $\gamma = 6.0$.

Figure 3.14 continued: Half-rendered bubble shapes showing the geometry of a cavitation bubble, $\alpha = 1000$ above a rigid boundary for a range of standoff distances at the time of jet impact. Horizontal and vertical axes are (a) through (h) $r \leqslant 1.25$, $0 \leqslant z \leqslant 2.5$; (i) through (p) $r \leqslant 0.75$, $|z - \gamma| \leqslant 0.75$. The black star denotes the point of initialisation. The boundary is visible at the bottom of frames (a) through (h).

distance, the bubble reaches minimum volume and begins to re-expand. For a further range of γ values, the liquid jet will impact on the opposing face of the bubble during re-expansion. Then beyond this second critical standoff, jet impact will not occur. Due to the current requirement for smoothing in our numerical scheme, it would be useless to attempt to calculate these critical distances as they may be greatly affected by the frequency and strength of the smoothing employed. Furthermore, calculations may be further affected by computational difficulties which are caused by very narrow liquid jets. See, for example, Figure 3.13q where oscillatory behaviour may be observed near the tip of the jet. Such oscillatory behaviour may also be observed in experiments and is due to surface tension. Here the problem is due to errors which propagate from the high-curvature region at the tip of the jet. We also note such narrow jets may begin to coalesce during re-expansion.

Returning to the subject of the bubble volume, we refer the reader to Figure 3.15 which shows the evolution of the bubble volume up to the time of jet impact for the two compression ratios considered above and for a range of standoff distances. In Figure 3.15a, we note the aforementioned decrease in bubble volume at the time of jet impact as γ increases. We note the slight upturn at the end of the curve for $\gamma = 2.5$, thus showing that the bubble is starting to re-expand. At $\gamma = 7.5$, the bubble re-expands significantly prior to jet impact. Volume curves for $\alpha = 1000$ are presented in Figure 3.15b, wherein a small re-expansion phase may just be observed for $\gamma = 10$. Clearly beyond this value bubbles undergo longer re-expansion phases up to the second critical standoff discussed above.

We consider the motion of the bubble centroid for a number of standoff distances at the two compression ratios, $\alpha = 100$ and 1000 in Figure 3.16. For bubbles formed close to the boundary, the expansion phase is characterised by upward motion of the centroid as the bubble expands, displacing fluid as it does so. As the point of initiation is moved further from the boundary, the bubble expands more uniformly about its point of inception; though there is still some movement away from the boundary for $\gamma = 2.5$. During collapse, the Bjerknes force of attraction draws the bubble towards the boundary. The downward centroid movement increases rapidly as the jet forms and bubble volume

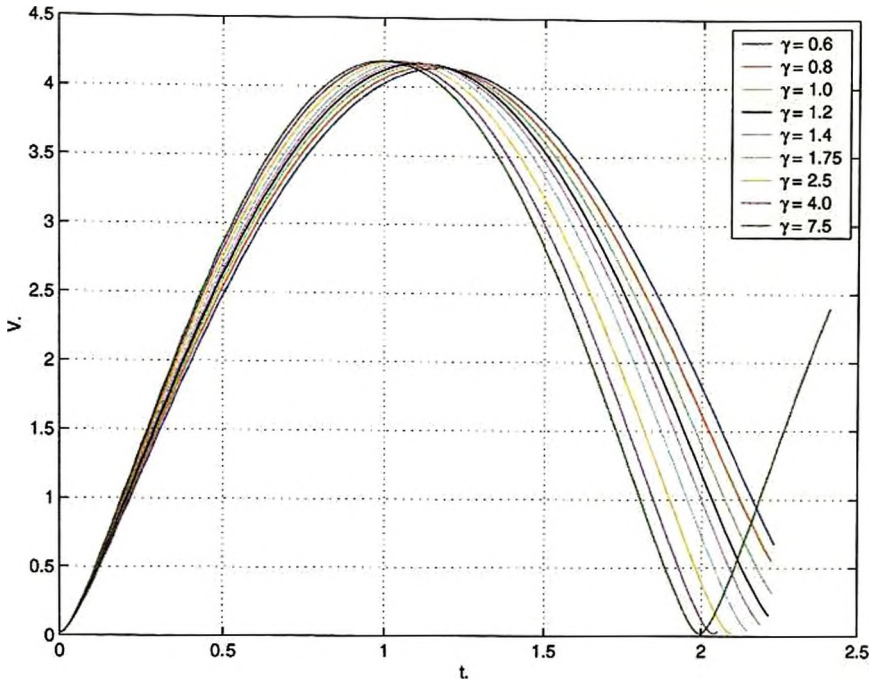

(a) $\alpha = 100$.

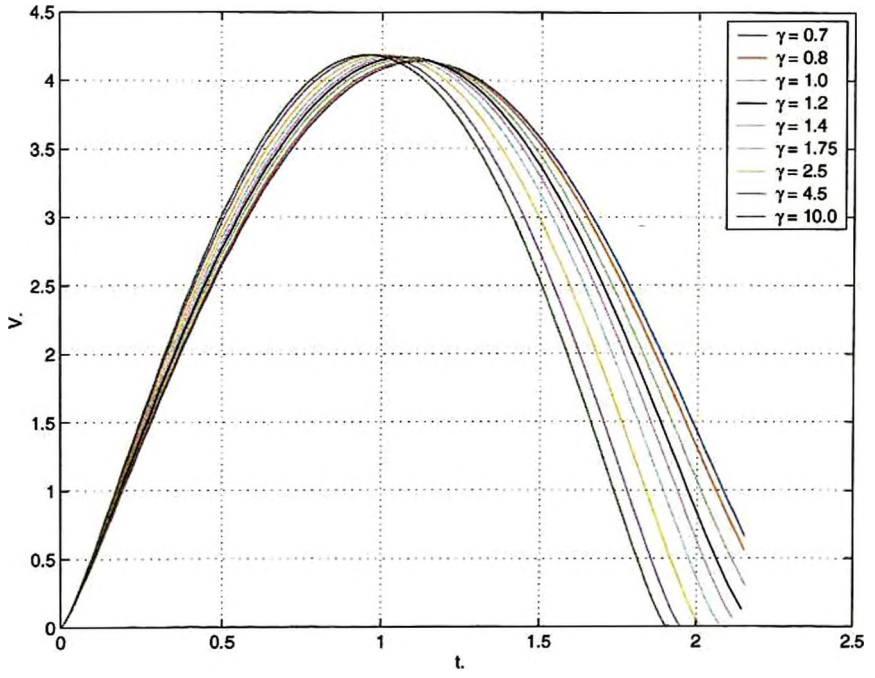

(b) $\alpha = 1000$.

Figure 3.15: Evolution of the volume of a cavitation bubble generated above a rigid boundary for two compression ratios, $\alpha = 100$ and 1000 for a range of standoff distances up until the time of jet impact.

is lost progressively from the top down at a rapid rate. For bubbles formed at standoff distances greater than or equal to 4.0, there is little centroid movement until the jet forms, after which there is a very rapid downward movement. In Figure 3.16a we note centroid motion for $\gamma = 7.5$, which remains almost stationary until just prior to minimum volume, when it experiences rapid downward movement due to the initial formation of the jet. As previously noted, the bubble starts to re-expand before this jet may impact on the opposing face of the bubble, though the gentle downward trend in this curve is consistent with the jet finally impacting. We note such behaviour is observed in buoyant spherical bubble models.

Figure 3.17 shows our calculations for the Kelvin impulse for a range of standoff distances for the two compression ratios considered. We note the strong influence of the boundary on the bubbles formed closest to it is characterised by the larger magnitudes of the Kelvin impulse; the negative values indicate a downward influence. Also of importance are the more rapid increases in the impulse during the early expansion phase and final collapse when the liquid jet forms. Physically, we recall the Kelvin impulse may be thought of as an instantaneous wrench which would generate the motion from rest and so the trends noted here are indicative of rapidly changing fluid momentum near the bubble during early expansion and final collapse.

The numerical calculation of the energies of the system was used earlier as a means by which to validate our numerical code and to provide an idea of optimal parameters for our calculations. However it also provides useful information about the motion of the bubble. Figure 3.18 shows the kinetic and potential energies associated with the motion of bubbles formed over a range of γ values for $\alpha = 100$. In Figure 3.18a we show the energies calculated up until the time of liquid jet impact. We note the rapid change from potential energy to kinetic energy during the earliest moments of the lifetime of the bubble as the high pressures within the bubble rapidly accelerate the fluid–gas interface, and the reverse process as the high surface velocities which develop during collapse re-compress the gas within the bubble. Figure 3.18b shows the first minimum in kinetic energy which corresponds to maximum bubble volume.[20] We note for bubbles formed at

[20] Since energy is conserved, minimum kinetic energy corresponds to maximum potential energy. Hence the pressure within the bubble will be at a minimum, which occurs at maximum volume.

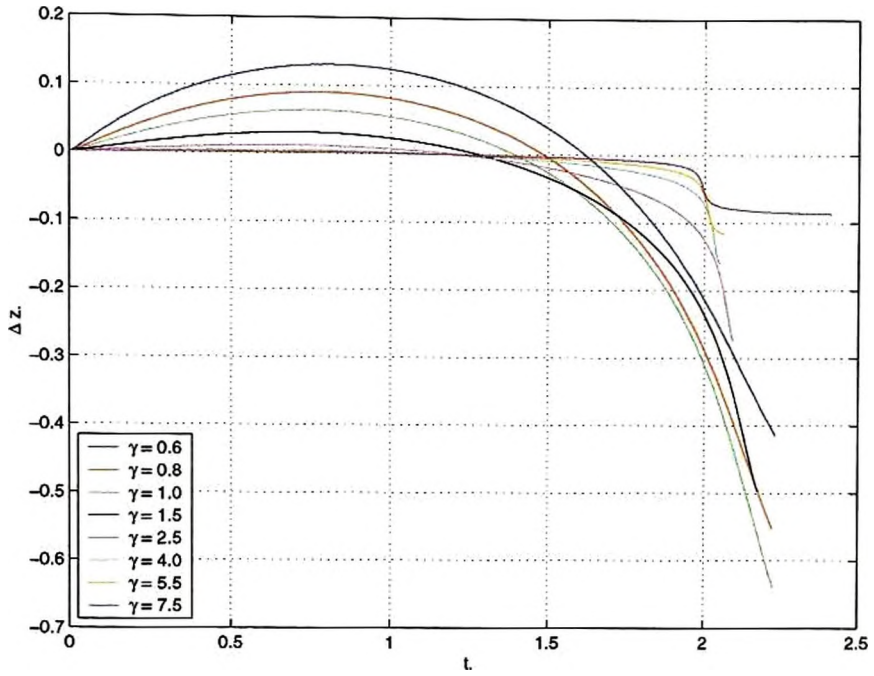

(a) $\alpha = 100$.

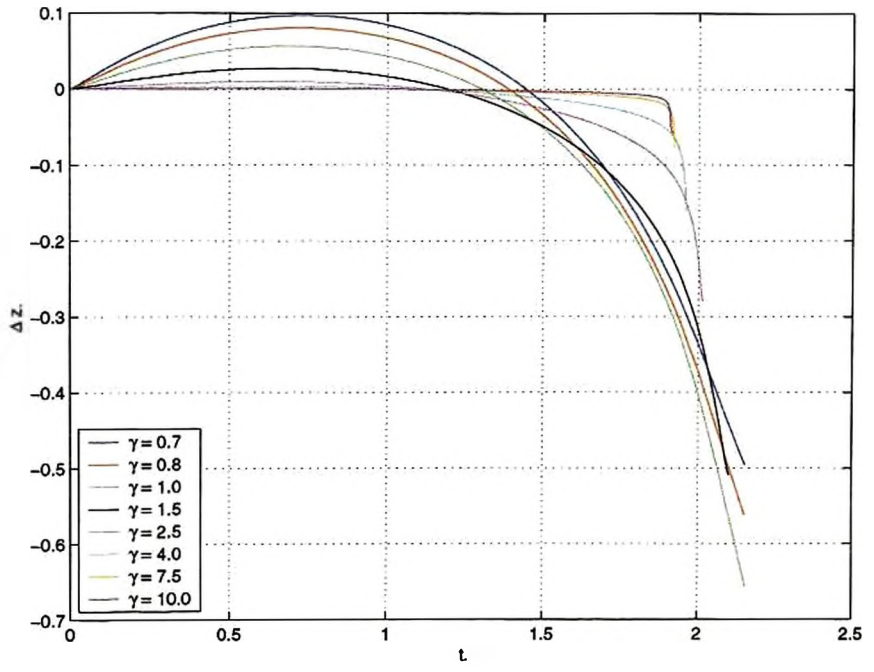

(b) $\alpha = 1000$.

Figure 3.16: Changes in centroid position for the motion of a cavitation bubble generated above a rigid boundary for two compression ratios, $\alpha = 100$ and 1000 for a range of standoff distances up until the time of jet impact.

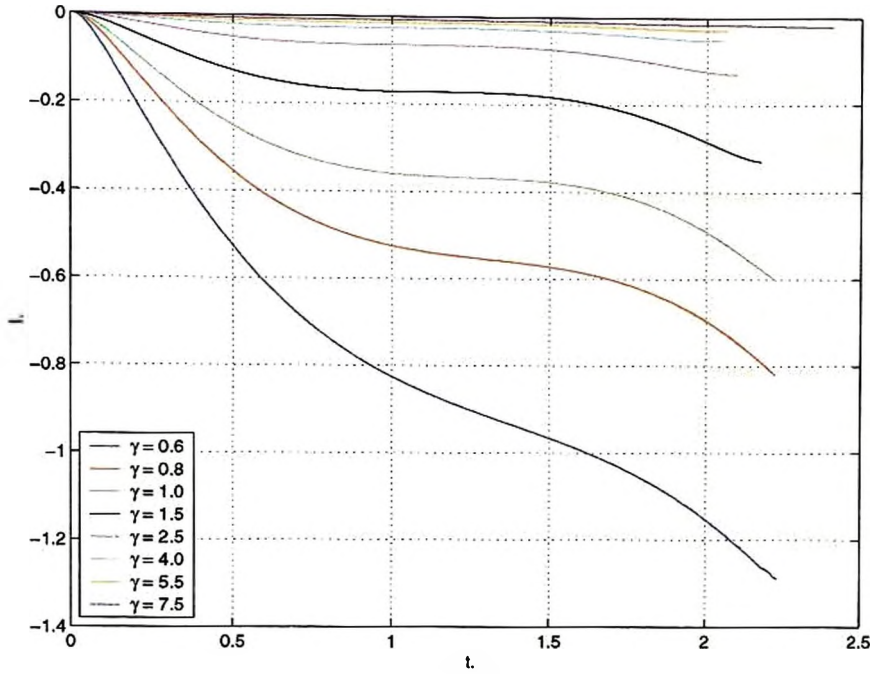

(a) $\alpha = 100$.

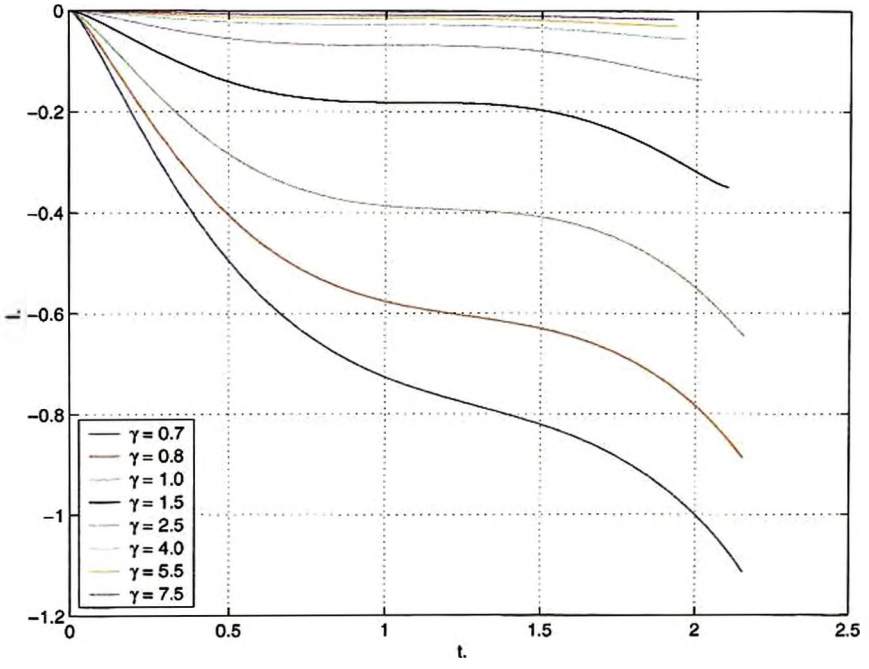

(b) $\alpha = 1000$.

Figure 3.17: The Kelvin impulse associated with the motion of a cavitation bubble generated above a rigid boundary for two compression ratios, $\alpha = 100$ and 1000 for a range of standoff distances up until the time of jet impact.

some distance from the boundary this minimum is virtually zero, hence the entire surface of the bubble has zero velocity which will only occur if the bubble behaves spherically. For bubbles formed close to the boundary, this minimum is non-zero which is indicative of some part of the surface of the bubble being in motion, so even through the stable expansion phase, the bubble has developed non-spherical attributes. The non-smooth nature of these curves is due to relatively large time steps which may be taken when the surface of the bubble is slowly moving. The second minimum in kinetic energy is shown in Figure 3.18c, and corresponds to minimum bubble volume. Here we note the minimum values of the kinetic energy are all non-zero indicating highly non-spherical behaviour, which should be expected following collapse. Finally we note the increases in kinetic energy for $\gamma = 2.75$ and 3.0, following their respective minima. This indicates jet impact occurs during re-expansion.

The corresponding energy calculations for $\alpha = 1000$ are presented in Figure 3.19. Many of the above arguments may be applied to these results directly, so further discussion is limited to Figure 3.19c, where we note the increases in kinetic energy following the second minimum for $\gamma = 5.0$, 6.0 and 7.0, which indicates that jet impact occurs following minimum volume. We note the larger total energy (over that for $\alpha = 100$) is indicative of the increased amount of energy required to drive the initially smaller bubble to the same maximum radius of unity.

We now proceed to discuss our calculations concerning the Kelvin impulse and kinetic energy of the liquid jet. Having just concluded our discussions of the energy of the bubble as a whole, it is pertinent to discuss the kinetic energy of the jet first. Figure 3.20 shows the percentage of the total energy which is manifested as kinetic energy within the liquid jet. We recall the energy is calculated from a time shortly following jet formation[21] up until the time of jet impact. For both $\alpha = 100$ and 1000, we note the largest percentage of kinetic energy within the jet is of the order of 30% at the time of jet impact and occurs at a standoff distance of $\gamma = 1.2$. For bubbles generated closer to the boundary, this percentage decreases steadily as γ decreases. For bubbles generated further from the boundary, we have a steady decrease in this percentage. One interesting feature

[21] Typically 30–40 iterations after the appearance of a concave section at the upper pole of the bubble.

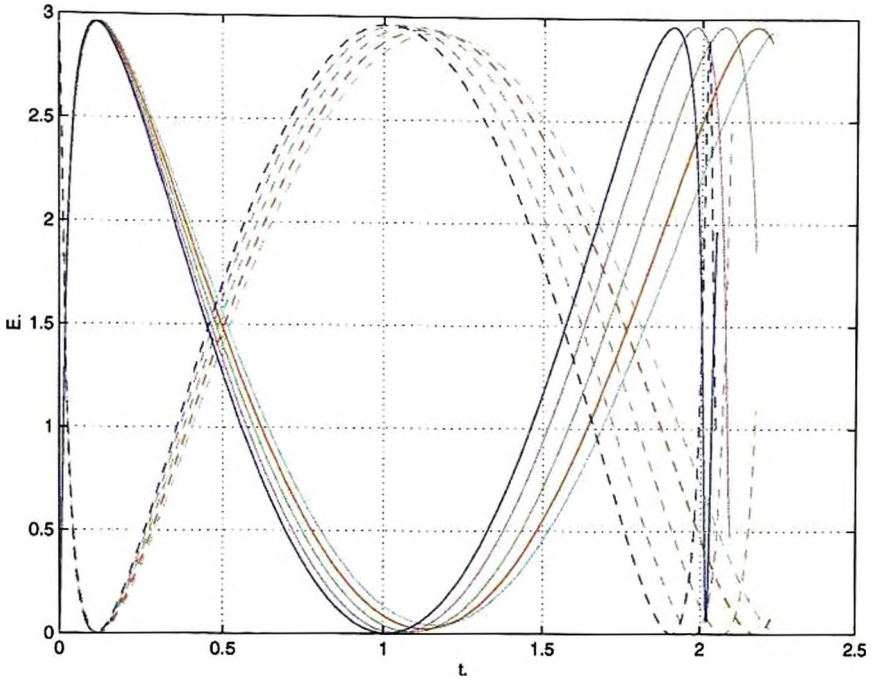

(a) $\gamma = 0.7$, 1.0, 1.5, 2.5 and 5.0. See legend in (b).

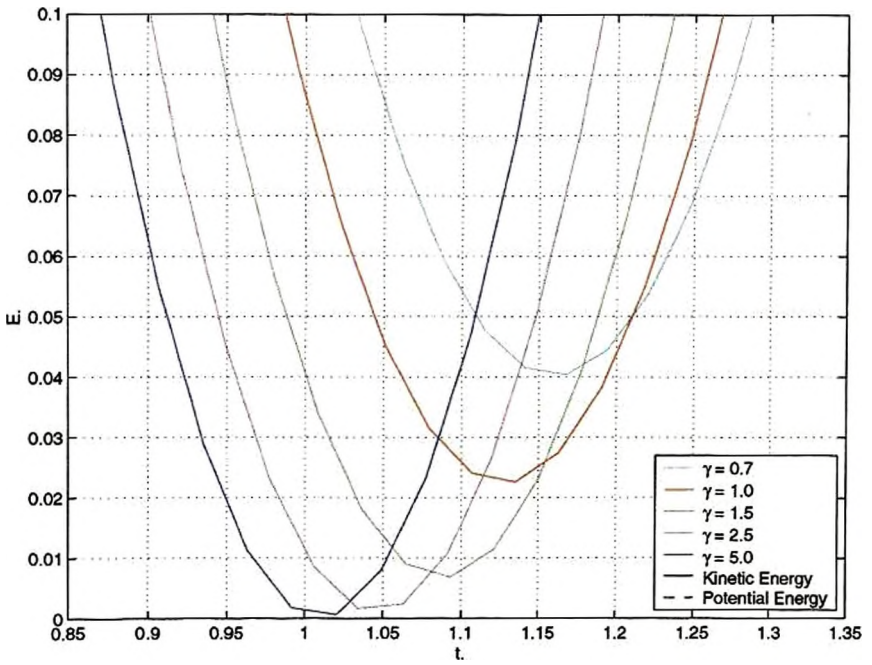

(b) First minimum in kinetic energy, corresponding to maximum bubble volume. $\gamma = 0.7$, 1.0, 1.5, 2.5 and 5.0.

Figure 3.18: The kinetic and potential energies associated with the motion of a cavitation bubble, $\alpha = 100$ generated above a rigid boundary for a range of standoff distances up until the time of jet impact. (Total energy = 2.9615).

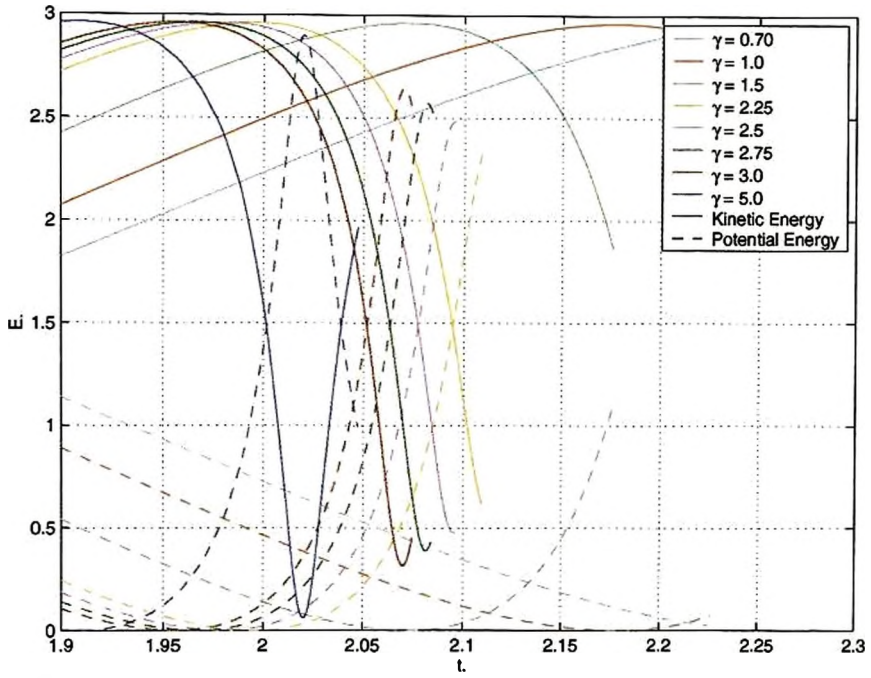

(c) Second minimum in kinetic energy, corresponding to minimum bubble volume. $\gamma = 0.7$, 1.0, 1.5, 2.25, 2.5, 2.75, 3.0 and 5.0.

Figure 3.18 continued: The kinetic and potential energies associated with the motion of a cavitation bubble, $\alpha = 100$ generated above a rigid boundary for a range of standoff distances up until the time of jet impact. (Total energy = 2.9615.)

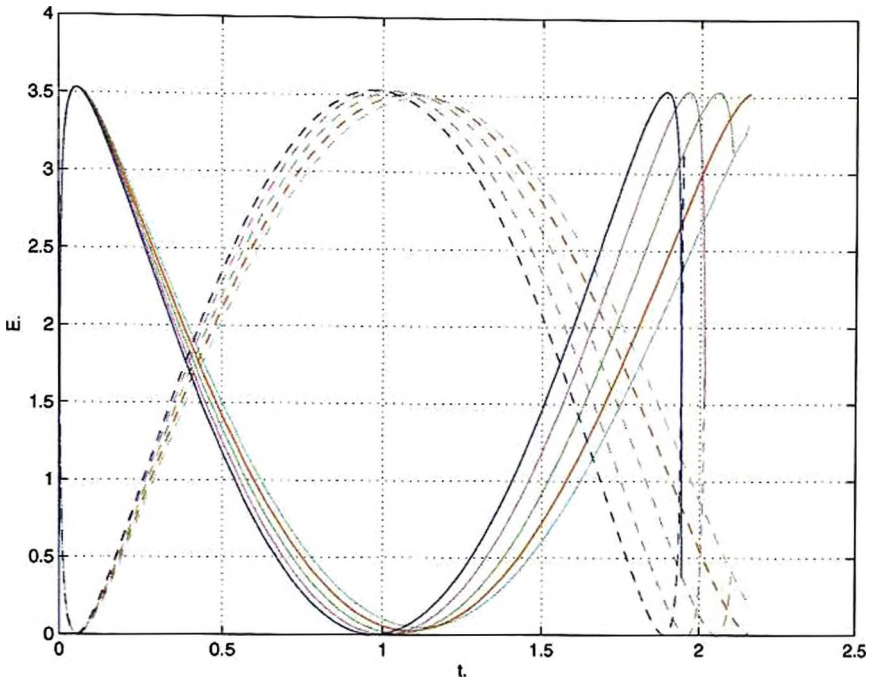

(a) $\gamma = 0.7$, 1.0, 1.5, 2.5 and 5.0. See legend in (b).

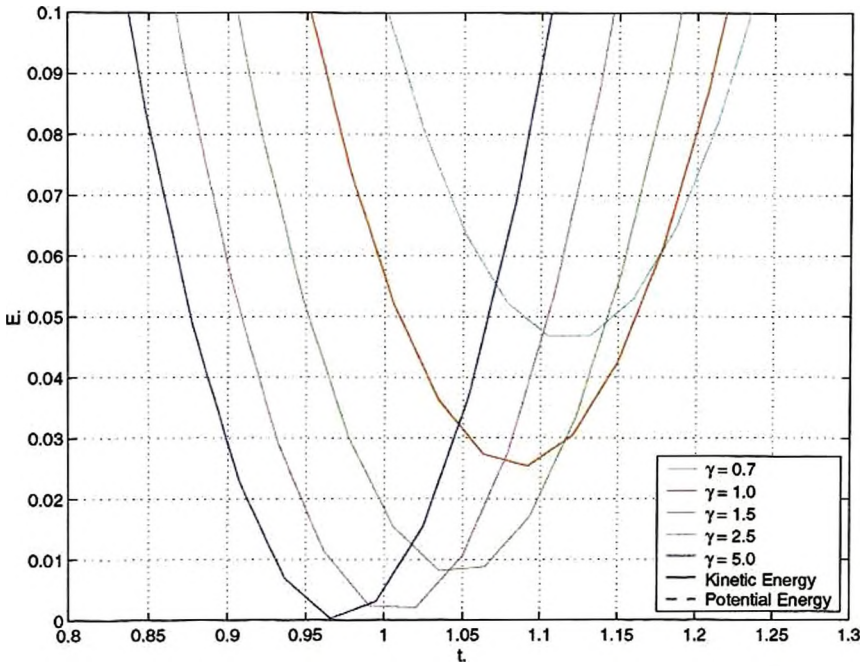

(b) First minimum in kinetic energy, corresponding to maximum bubble volume. $\gamma = 0.7$, 1.0, 1.5, 2.5 and 5.0.

Figure 3.19: The kinetic and potential energies associated with the motion of a cavitation bubble, $\alpha = 1000$ generated above a rigid boundary for a range of standoff distances up until the time of jet impact. (Total energy = 3.5315.)

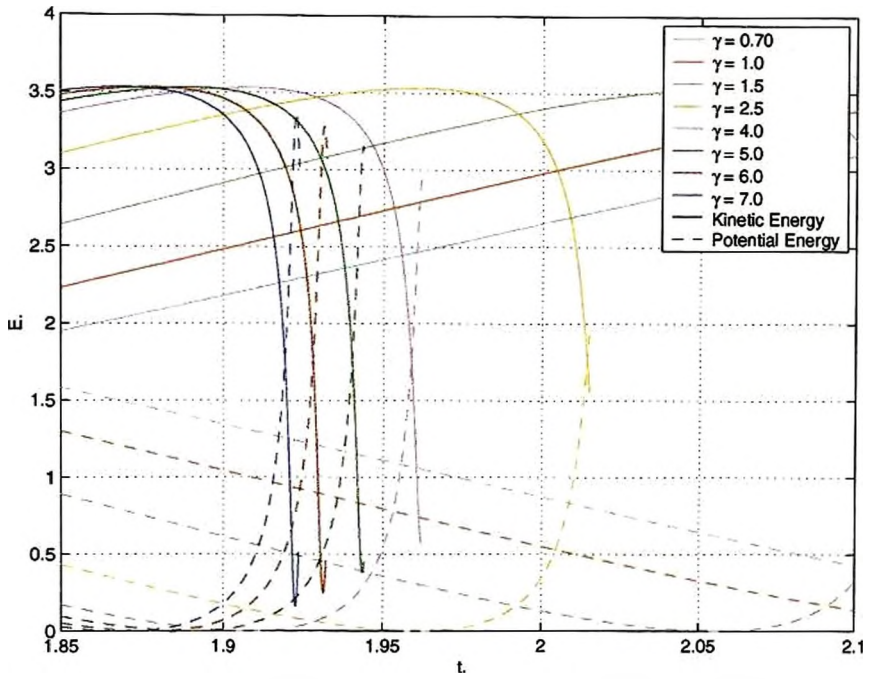

(c) Second minimum in kinetic energy, corresponding to minimum bubble volume. $\gamma = 0.7$, 1.0, 1.5, 2.25, 2.5, 2.75, 3.0 and 5.0.

Figure 3.19 continued: The kinetic and potential energies associated with the motion of a cavitation bubble, $\alpha = 1000$ generated above a rigid boundary for a range of standoff distances up until the time of jet impact. (Total energy = 3.5315.)

of these calculations may be seen by looking at the curve for $\gamma = 4.5$ or $\gamma = 5.0$ in Figure 3.20a. Here the kinetic energy in the jet reaches a fixed percentage of the total energy, then becomes almost constant. This may be attributed to the deceleration of the liquid within the jet due to compression of gas within the bubble as its volume decreases, then subsequent acceleration of the remaining surface of the bubble which does not bound the liquid jet due to high internal pressures.

Figure 3.21 shows the kinetic energy in the liquid jet at the time of jet impact for several compression ratios and over a range of standoff distances. We see that for compression ratios from $\alpha = 100 - 1000$, the maximum amount of energy within the jet occurs at a standoff distance of $\gamma \approx 1.2$. For larger compression ratios, there is a greater amount of energy within the jet, yet the percentage of the total is approximately equal at just over 30%. For γ-values smaller than this we also see that the percentage of total energy contained within the liquid jet is roughly equal over the range of compression ratios considered. This is due to the strong influence of the boundary over the motion, as noted earlier. This may also be seen if we consider the circulations formed following jet impact in Figure 3.22, where we note the circulations are roughly equal over the range of $\alpha = 100 - 1000$ up to $\gamma \approx 1.75$.

Finally we consider the Kelvin impulse within the liquid jet. This is shown in Figure 3.23 as a percentage of the instantaneous Kelvin impulse of the bubble. We see that up to $\gamma \approx 1.5$, these percentages are roughly equal for $\alpha = 100$ and 1000. As γ increases beyond this value, we see that over 50% of the Kelvin impulse, a measure of the local fluid momentum is contained within the liquid jet. For bubbles at a large distance from the boundary, this starts to decrease as the influence of the boundary decreases.

3.8.4 The Null Impulse State

In this section, we briefly consider the motion of a buoyant bubble formed above a rigid boundary, such as might be generated in reduced pressure cavitation experiments or by an underwater explosion. Here the motion of the bubble is influenced by the two opposing pressure gradients due to buoyancy and the Bjerknes force of attraction towards the rigid boundary. In close proximity to the boundary, the motion will be influenced

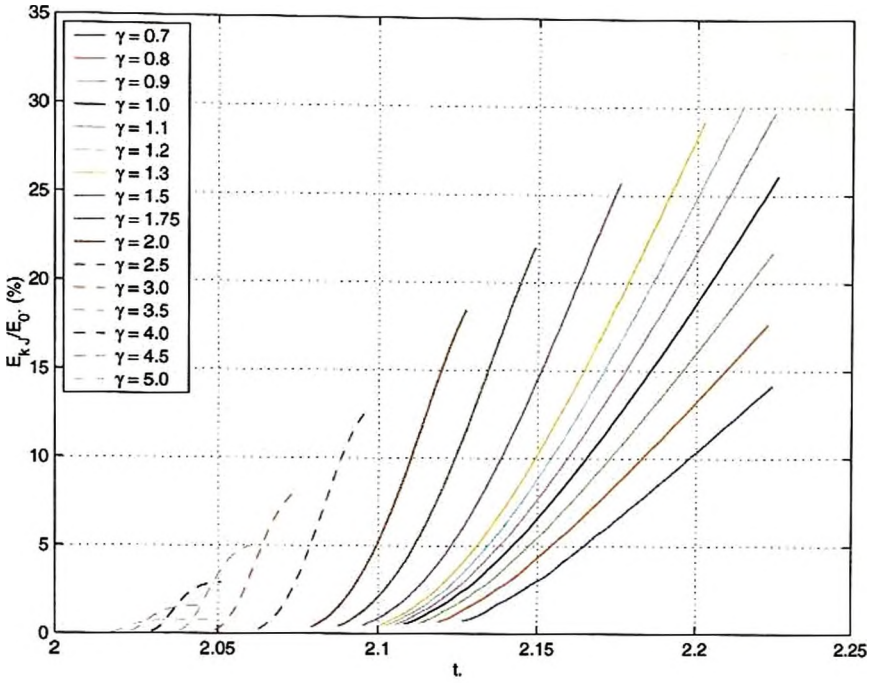

(a) $\alpha = 100$.

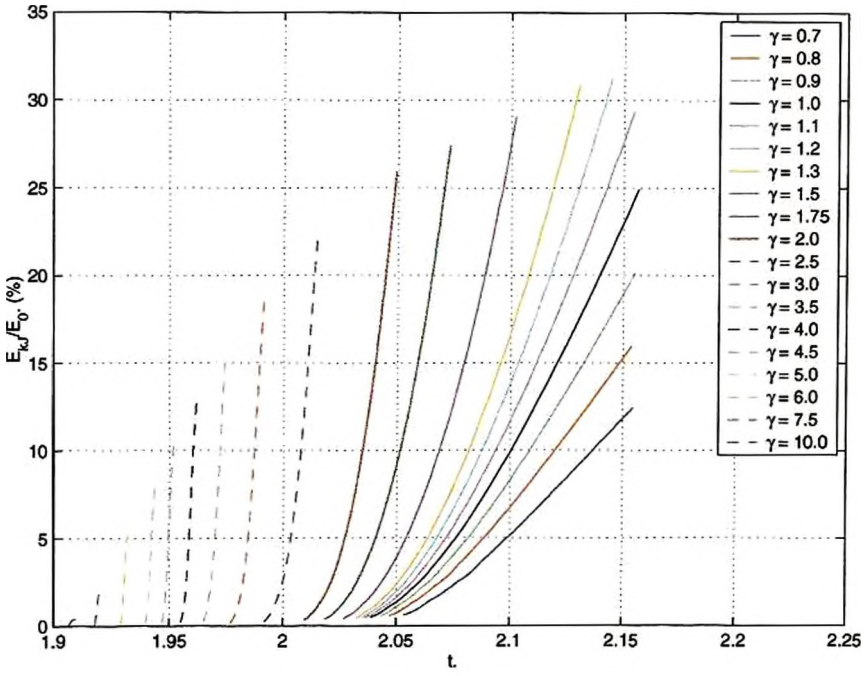

(b) $\alpha = 1000$.

Figure 3.20: Percentage of total energy manifested as kinetic energy within the liquid jet for two compression ratios, $\alpha = 100$ and 1000 for a range of standoff distances from a time shortly following jet formation up until the time of jet impact.

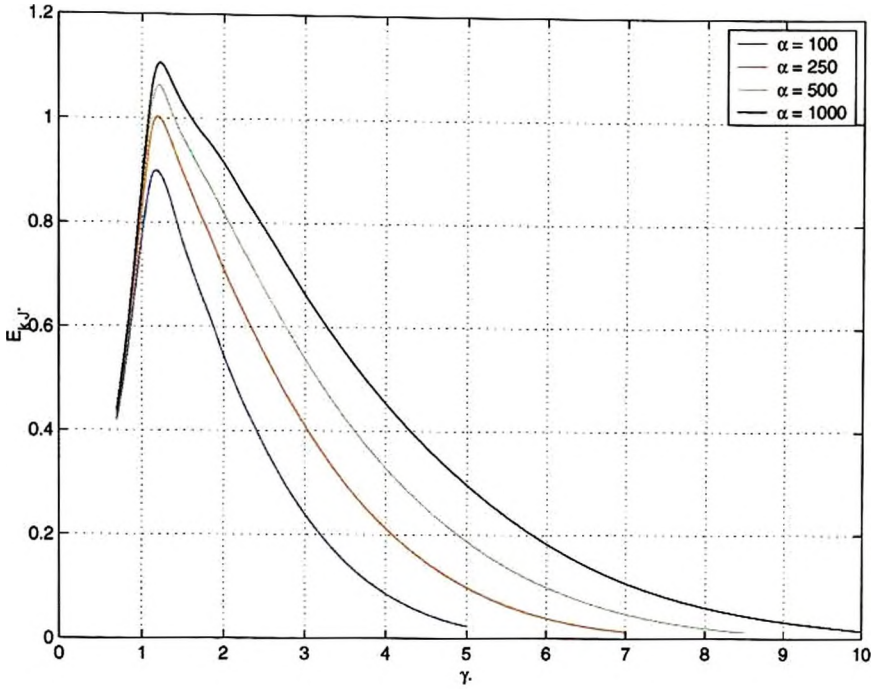

(a) Dimensionless energy units.

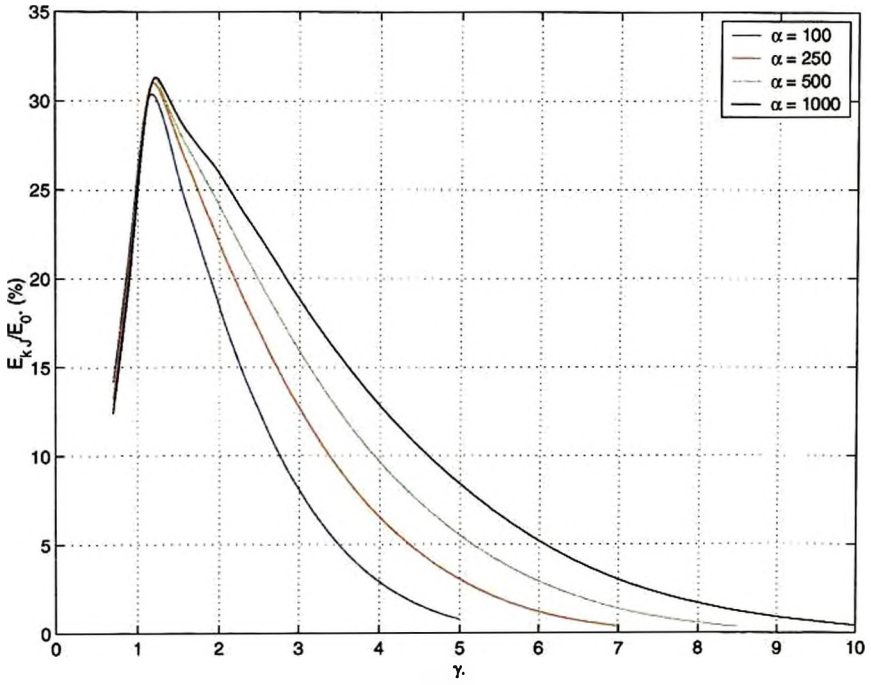

(b) As a percentage of total energy.

Figure 3.21: Kinetic energy within the liquid jet at the time of jet impact over a range of standoff distances and for several compression ratios.

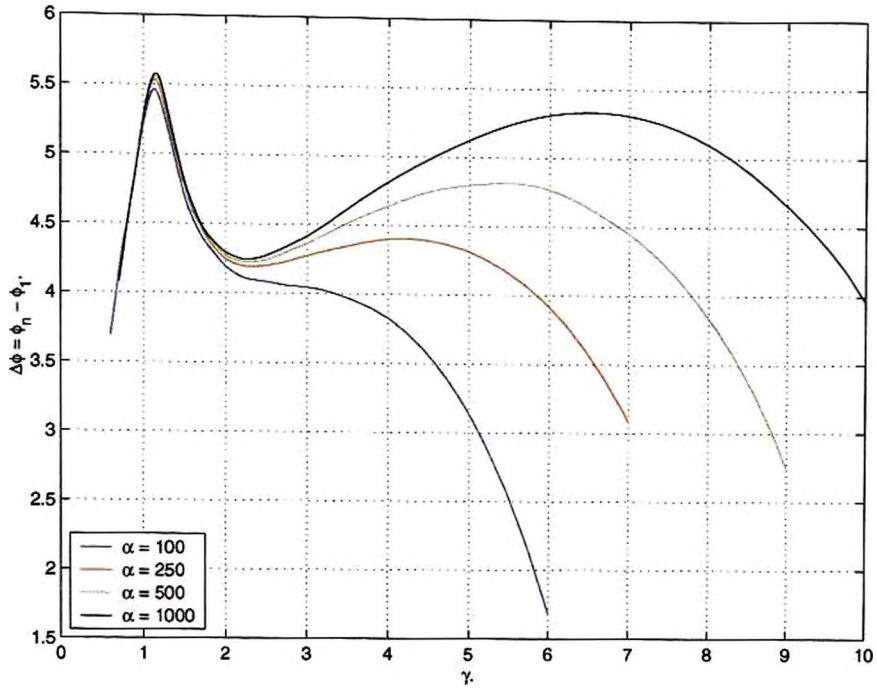

Figure 3.22: Circulations formed at jet impact over a range of standoff distances and for several compression ratios.

primarily by the attractive force of the boundary, so bubble migration and jet formation will be directed towards the boundary. At large standoff distances the influence of the boundary is negligible and so the motion will be governed by the pressure gradient due to buoyancy, with bubble migration and jet formation directed away from the boundary. It is therefore evident that there will exist some intermediate standoff distance (dependent on the strength of buoyancy forces) at which the forces due to the opposing pressure gradients balance. Due to the close relationship between force and the Kelvin impulse, this is often termed the null impulse state (see Blake 1988, Best 1991).

Several estimates for the null impulse state using spherical bubble approximations have previously been calculated. Blake (1988) employs the leading-order source term for a vapour bubble with a fixed centroid undergoing radial motion in order to determine an analytic form for the null impulse curve. This yields an expression for the Kelvin impulse (scaled by $R_m^3(\rho\Delta p)^{1/2}$) at the time of collapse of a Rayleigh vapour cavity of the form

$$I_z(t_c) = \frac{2\sqrt{6}\pi}{9}\left[2\delta^2 \mathrm{B}\left(\frac{11}{6},\frac{1}{2}\right) - \frac{1}{\gamma^2}\mathrm{B}\left(\frac{7}{6},\frac{3}{2}\right)\right], \tag{3.8.1}$$

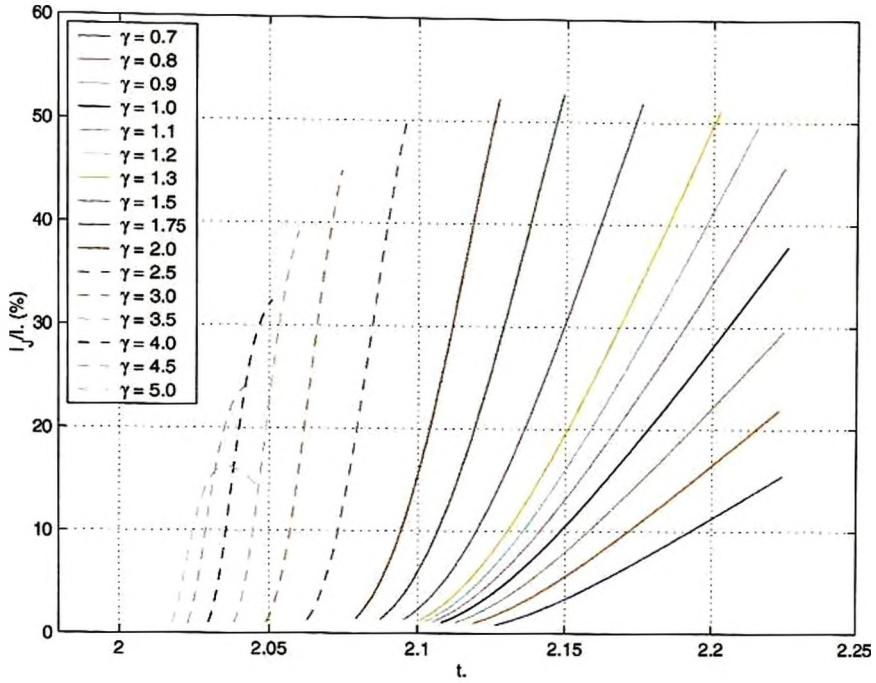

(a) $\alpha = 100$.

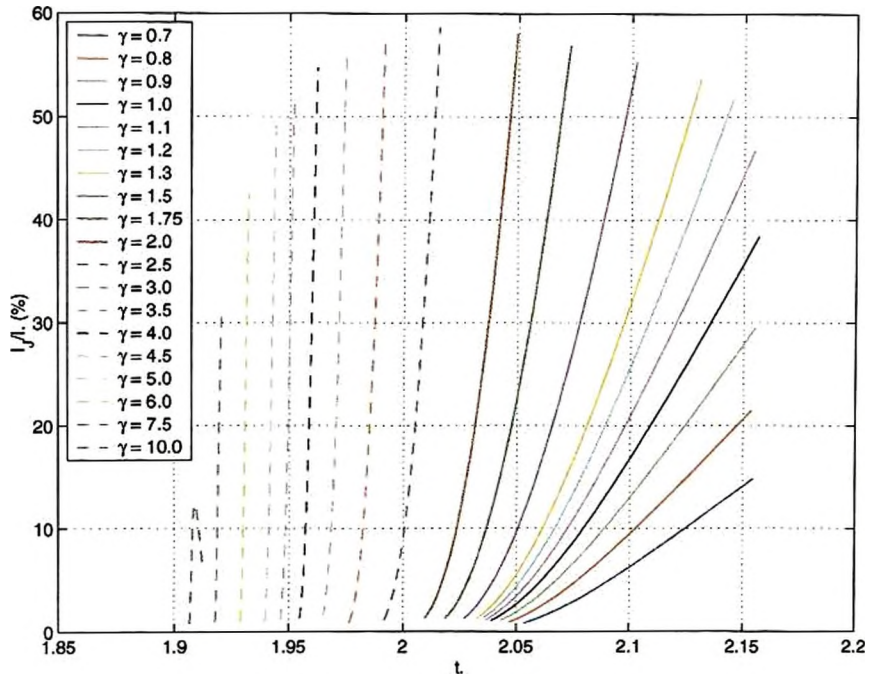

(b) $\alpha = 1000$.

Figure 3.23: Percentage of the instantaneous total Kelvin impulse of the bubble within the liquid jet for two compression ratios, $\alpha = 100$ and 1000 for a range of standoff distances from a time shortly following jet formation up until the time of jet impact.

which is zero when

$$\gamma\delta = \left[\frac{\mathrm{B}\,(7/6, 3/2)}{2\mathrm{B}\,(11/6, 1/2)}\right]^{\frac{1}{2}} \approx 0.442, \tag{3.8.2}$$

where $\mathrm{B}(x, y)$ is a Beta function. A revised calculation of the null impulse curve for a vapour bubble was undertaken by Best (1991). In this work, a dipole correction to the leading-order source term is added and the bubble centroid allowed to move, resulting in a set of coupled ODE's for the radial and vertical motion of the bubble which must be solved numerically. Recently Brujan (see Brujan, Pearson & Blake 2002) added the effects of an adiabatic gas in order to examine the influence this has on motion, and to determine the null impulse state at the end of the first collapse. These revised null impulse curves (which may be seen in Figure 3.24) are shown to provide a good agreement with boundary integral calculations which attain a null impulse state at the time of jet impact or bubble splitting, which is unusual given the multitude of strange geometries which develop and the varying bubble volumes at the time calculations are ceased. At this point, it is helpful to comment on the evolution of the Kelvin impulse for our non-spherical bubbles. During the early lifetime of the bubble, the Bjerknes force of attraction towards the rigid boundary plays the key rôle in governing motion, signified by a negative value of the Kelvin impulse. As the bubble reaches maximum volume and begins to collapse, buoyancy forces have a comparatively stronger influence on the motion, and so the Kelvin impulse begins to increase, later becoming positive. As the bubble continues to evolve, so the effects of the boundary again become important and the Kelvin impulse decreases, so that at the time of jet impact or bubble splitting, it is zero. Due to the decreasing Kelvin impulse at this time, were calculations allowed to continue for the toroidal phase of motion, or following bubble splitting, for the two bubble system, a negative Kelvin impulse state would again be attained. Therefore, in order to obtain a suitable analogue to the null impulse curves obtained from spherical bubble theory using our boundary integral code, we would be required to continue calculations through to minimum volume (for a gas bubble) or final collapse (vapour bubble). Due to the highly complex geometries attained, this would prove to be a difficult and time consuming task.[22]

[22]Take for example, a bubble which attains an hourglass shape and is pinched to form a two bubble system. In order to evolve this two bubble system to a minimum volume will most likely require both these bubbles to attain a toroidal geometry. Whilst this is possible using our current techniques, this is a time consuming task.

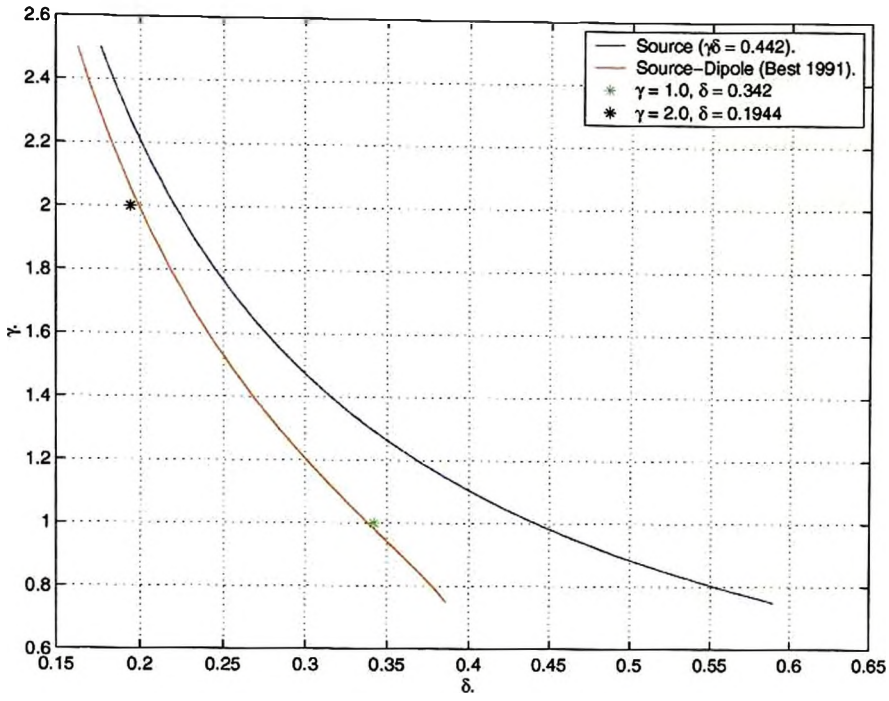

Figure 3.24: Null impulse curves calculated from source and source–dipole approximations. Stars denote the two cases considered in Figures 3.25 and 3.26.

A more detailed discussion of the null impulse state and comparisons with the results of recent boundary integral calculations may be found in the paper by Brujan, Pearson & Blake (2002), wherein the centroid motion is carefully examined in order to determine the null impulse state. Herein two cases are considered with parameters very close to those chosen in the aforementioned paper. These show the motion of buoyant bubbles which attain a numerically calculated null impulse state at the time of bubble splitting or jet impact. This is not necessarily true of the cases considered in the aforementioned paper.

In Figure 3.25, we consider the motion of a buoyant bubble characterised by the parameters $\gamma = 1.0$, $\delta = 0.342$, $\alpha = 100$, $\kappa = 1.4$ with an initial radial velocity $\dot{R} = 10.0$. During expansion, the bubble grows almost spherically, with only a slight flattening of the underside of the bubble due to the presence of the boundary. (See Frame 1 which shows the bubble at maximum volume.) It is during collapse when interesting behaviour is observed. In the absence of buoyancy, we would expect the bubble to collapse from above due to the Bjerknes forces of attraction. However, due to the upwardly directed pressure

gradient caused by buoyancy, the bubble also has a desire to collapse from beneath. The balance between these forces results in the formation of a ring of high pressure which surrounds the bubble (see Frame 3); this causes the bubble to collapse from the side. A further region of high pressure situated below the first, but on the rigid boundary also causes the lower hemisphere of the bubble to collapse. As the flow evolves further, a single high-pressure ring about the middle of the bubble develops and grows in magnitude, driving the fluid at high velocities until the bubble is pinched about its middle. Physically we would expect the bubble to split here, though calculations pertaining to these effects are not presented herein. Moreover, following bubble splitting, surface tension effects coupled with the central region of high pressure would drive narrow, high-speed liquid jets in both halves of the bubble, ultimately forming two toroidal bubbles. These liquid jets will be directed vertically outwards from the pinched region, with that in the lower half being driven towards the rigid boundary at high speed. Clearly there is scope for erosion damage as this impacts against the boundary.

Figure 3.26 shows the motion of a buoyant cavitation bubble characterised by the parameters $\gamma = 2.0$, $\delta = 0.1944$, $\alpha = 100$, $\kappa = 1.4$ and $\dot{R} = 10.0$. We note the spherical expansion phase with no visible deformation of the bubble due to the increased standoff distance at which the bubble is generated. During the collapse phase, a region of high pressure develops in close proximity to the lower pole of the bubble (Frame 1 of Figure 3.26b), whilst the remainder of the pressure field about the bubble remains uniform. This increases in magnitude and begins to drive a narrow liquid jet from the lower pole of the bubble. At this time a second high-pressure region forms above the upper pole of the bubble (Frame 2). Ultimately, this upper region of high pressure surpasses the magnitude of the lower, driving a much higher speed liquid jet from the upper pole (Frame 4).

For further discussion and calculations concerning bubble motion near the null impulse state, the reader is referred to the paper by Brujan, Pearson & Blake (2002) and the references contained therein.

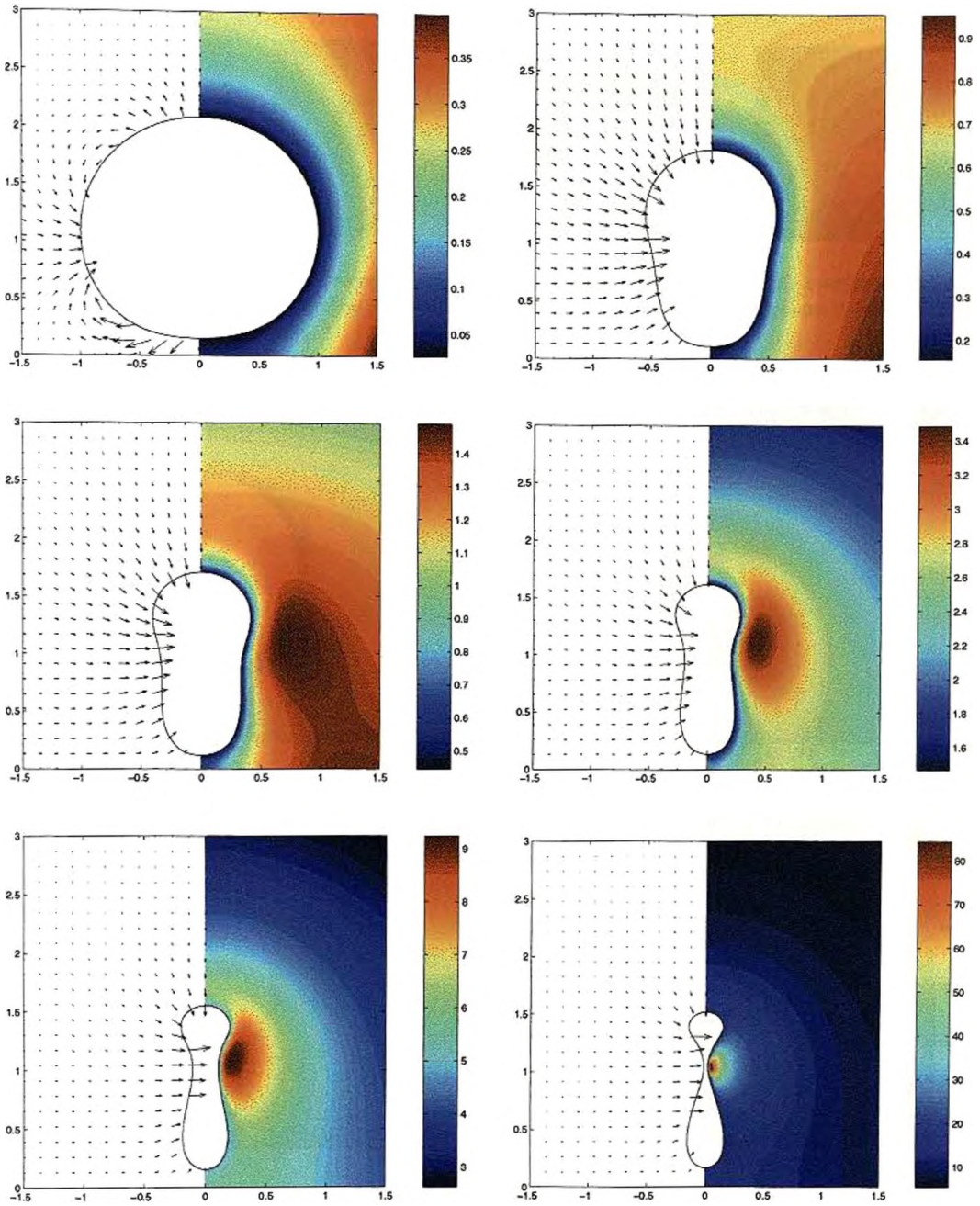

Figure 3.25: Velocity vectors and pressure contours showing the motion of a buoyant cavitation bubble above a rigid boundary characterised by the parameters $\gamma = 1.0$, $\delta = 0.342$, $\alpha = 100$, $\kappa = 1.4$ and $\dot{R}_0 = 10.0$ up until the time of bubble splitting. Frame 1 shows the bubble at maximum volume. Times are 1.0939, 1.9741, 2.0821, 2.1417, 2.1697 and 2.1833 respectively.

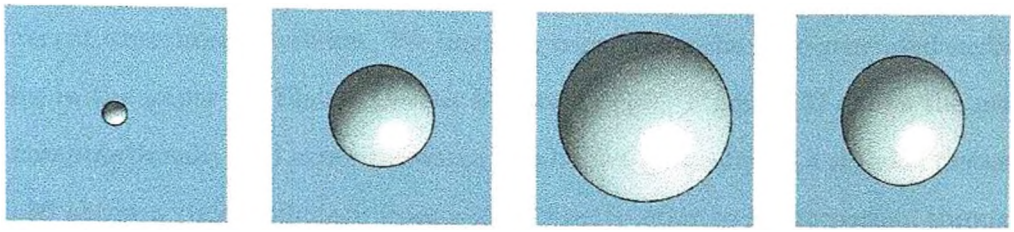

(a) Rendered bubble shapes. Frames 1 and 3 show the bubble initially and at maximum volume respectively. Horizontal and vertical axes are: $r \leqslant 1.25$, $0.75 \leqslant z \leqslant 3.25$. Times are 0.0000, 0.1582, 1.0184 and 1.7647 respectively.

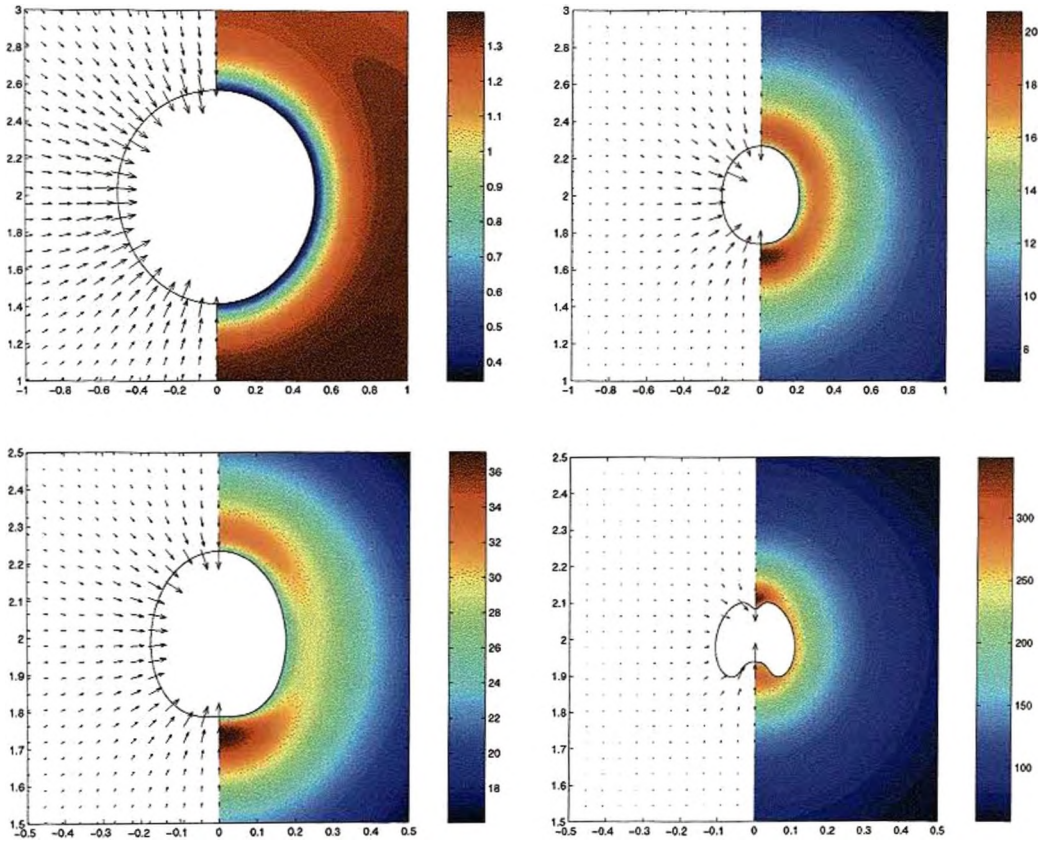

(b) Velocity vectors and pressure contours. Horizontal and vertical axes are: Frames 1 and 2: $r \leqslant 1$, $1 \leqslant z \leqslant 3$; Frames 3 and 4: $r \leqslant 0.5$, $1.5 \leqslant z \leqslant 2.5$. Times are 1.9142, 2.0309, 2.0362 and 2.0461 respectively.

Figure 3.26: Motion of a buoyant cavitation bubble above a rigid boundary characterised by the parameters $\gamma = 2.0$, $\delta = 0.1944$, $\alpha = 100$, $\kappa = 1.4$ and $\dot{R}_0 = 10.0$.

3.9 Comparison with Experiments

In the penultimate section of this chapter, we discuss the success of our work in relation to some recent experimental studies. We begin by considering the laser-generated cavitation bubbles in the paper by Blake, Tomita & Tong (1998). Figure 3.27 shows the motion, both computationally and experimentally, of a bubble generated at a standoff distance of $\gamma = 0.86$ above a rigid boundary from a time shortly prior to jet formation, through jet impact (Frame 4) and into the toroidal phase of motion. The black lines midway down the frames of the experimental images are pressure transducers which were used to record pressure data within the flow field, which will invariably have an effect on the motion of the bubble. We note although the interior of the bubble is not visible due the lighting techniques used, there is an excellent agreement between the external profiles observed. Further, we note the splash which is thrown up inside the bubble due to the opposing flows from fluid in the liquid jet and from fluid which rushes in from the far-field; the geometry is then further convoluted due the circulation set up following jet impact.

Figure 3.28 shows experimental high-speed photographs (reproduced with permission from Figure 6 of Blake, Tomita & Tong 1998) sandwiched between numerical calculations for the collapse phase of a cavitation bubble generated at a standoff distance, $\gamma = 1.41$. In this case, the motion is characterised by a visually spherical expansion phase. As the bubble begins to collapse, it becomes elongated due to the Bjerknes force of attraction of the boundary (see Frame 1). Again, due to the lighting used, it is difficult to observe the initial formation of the liquid jet, though this may be inferred from the flattening at the upper pole of the bubble (Frame 3 – experiments). Following jet impact the bubble geometry becomes convoluted, though in this case the geometry is not so mushroom-like as in the previous example (Frame 8). We show in the following chapter such geometries may give rise to bubble splitting where the splash meets the wall of the jet, hence forming a pair of toroidal bubbles.

A more recent experimental study which employs a number of novel visualisation techniques is that of Lindau (2001). Of particular interest are a number of experimental photograph series which are viewed at an elevated angle of 45° above the boundary. This permits the examination of radial instabilities which may form during the unstable

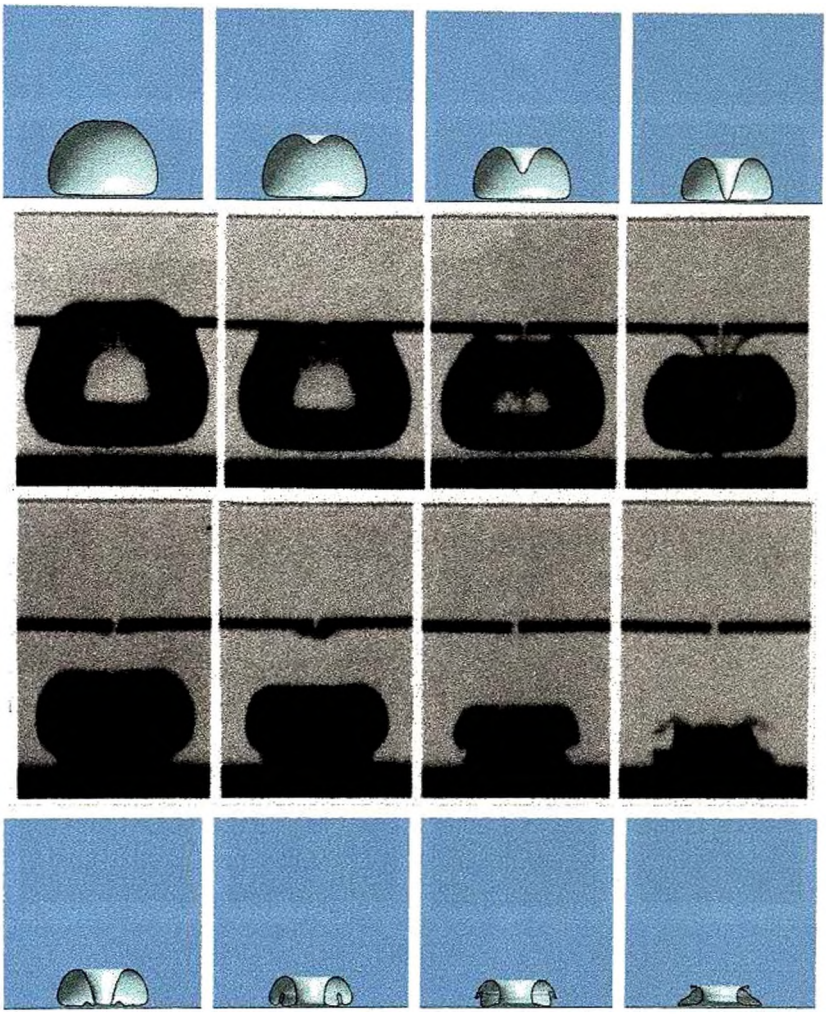

Figure 3.27: Comparison of calculations and experiments for the motion of a cavitation bubble above a rigid boundary at a standoff distance, $\gamma = 0.86$. Experimental high-speed photographs reproduced with permission from Blake, Tomita & Tong (1998).

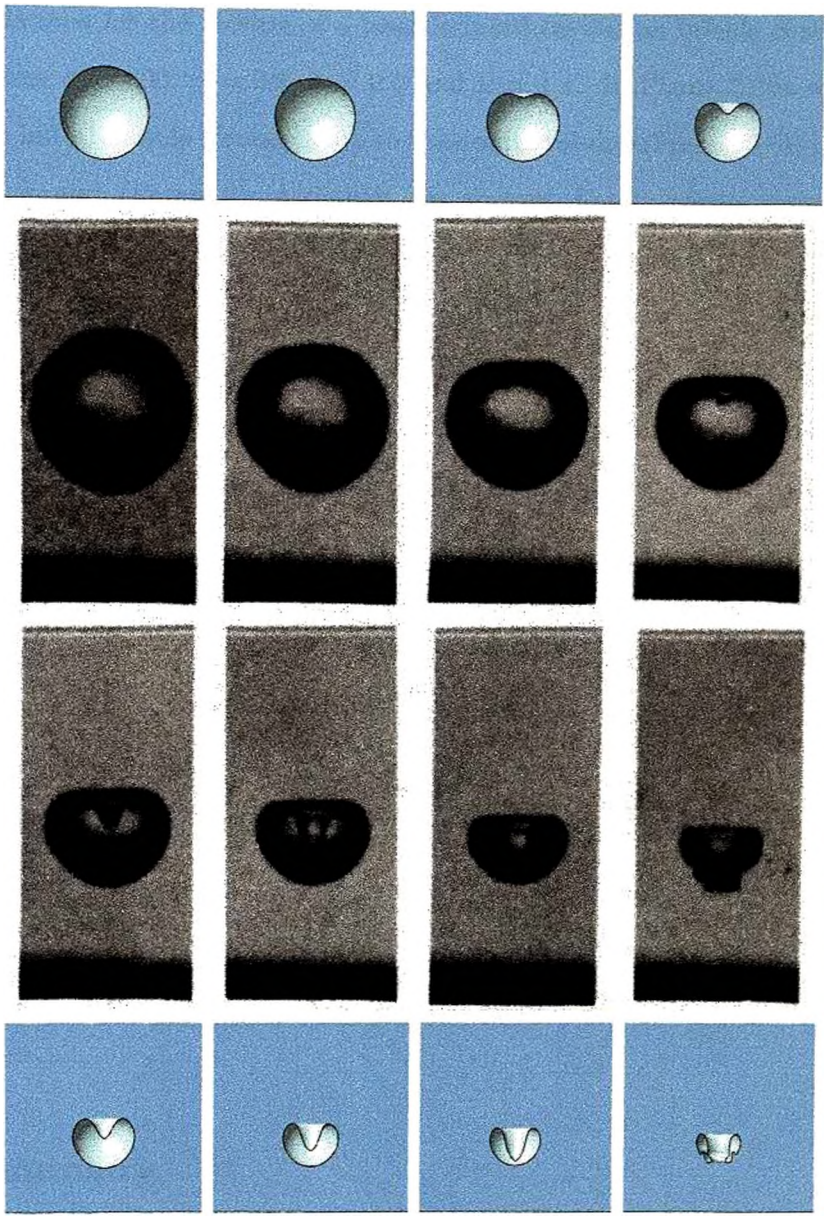

Figure 3.28: Comparison of calculations and experiments for the motion of a cavitation bubble above a rigid boundary at a standoff distance, $\gamma = 1.41$. Experimental high-speed photographs reproduced with permission from Blake, Tomita & Tong (1998).

collapse phase. Further these photograph series are captured using an ultra-high speed camera capable of up to 100 million frames per second allowing detailed study of the toroidal phase of motion which occurs on comparatively short time-scales. Figure 3.29 shows calculations for the motion of a laser-induced cavitation bubble characterised by the parameters $\alpha = 600$, $\gamma = 0.8$, $\delta = 0.0$ and $\kappa = 1.4$. In Figure 3.29a we follow the motion from initial bubble formation up to maximum volume (Frames 1–3) then through to liquid jet impact (Frame 9). Although less obvious than in results viewed in profile, we note during the expansion phase, the underside of the bubble is flattened against the rigid boundary. Following jet impact, a toroidal bubble geometry is formed (Frame 1 of Figure 3.29b) and a liquid splash thrown up inside the bubble. The motion of this splash may be followed as it is driven towards the outer edge of the bubble and is visible as the lighter coloured ring at the base of the bubble in Frames 2–8 of Figure 3.29b. Calculations cease when this splash meets the outer edge of the bubble. High-speed experimental photographs for this case are reproduced in Figure 3.30, wherein jet impact is visible around Frame 4–5. We note the liquid splash is clearly visible as a darkened ring at the base of the bubble in the third row of images in this figure. It is somewhat unclear as to how the splash develops as it reaches the outer edge of the bubble, though it is likely surface tension effects act to prevent this becoming so large as to meet the outer surface of the bubble as in our calculations. In the final three rows of experimental images, the bubble reaches minimum volume as a narrow toroidal ring, following which it begins to re-expand. We note surface instabilities around the bubble are clearly visible at this stage.

3.10 Summary

In this chapter, we have detailed a boundary integral scheme for the calculation of both the pre-toroidal and toroidal phases of motion of a single bubble either in an infinite fluid or, through the use of an appropriate image system, near to a rigid boundary. Using non-standard smoothing techniques and a fourth-order time integration scheme, numerical energy losses have been reduced, resulting in more accurate calculations. We have also obtained further physical insight into the problems we consider through the

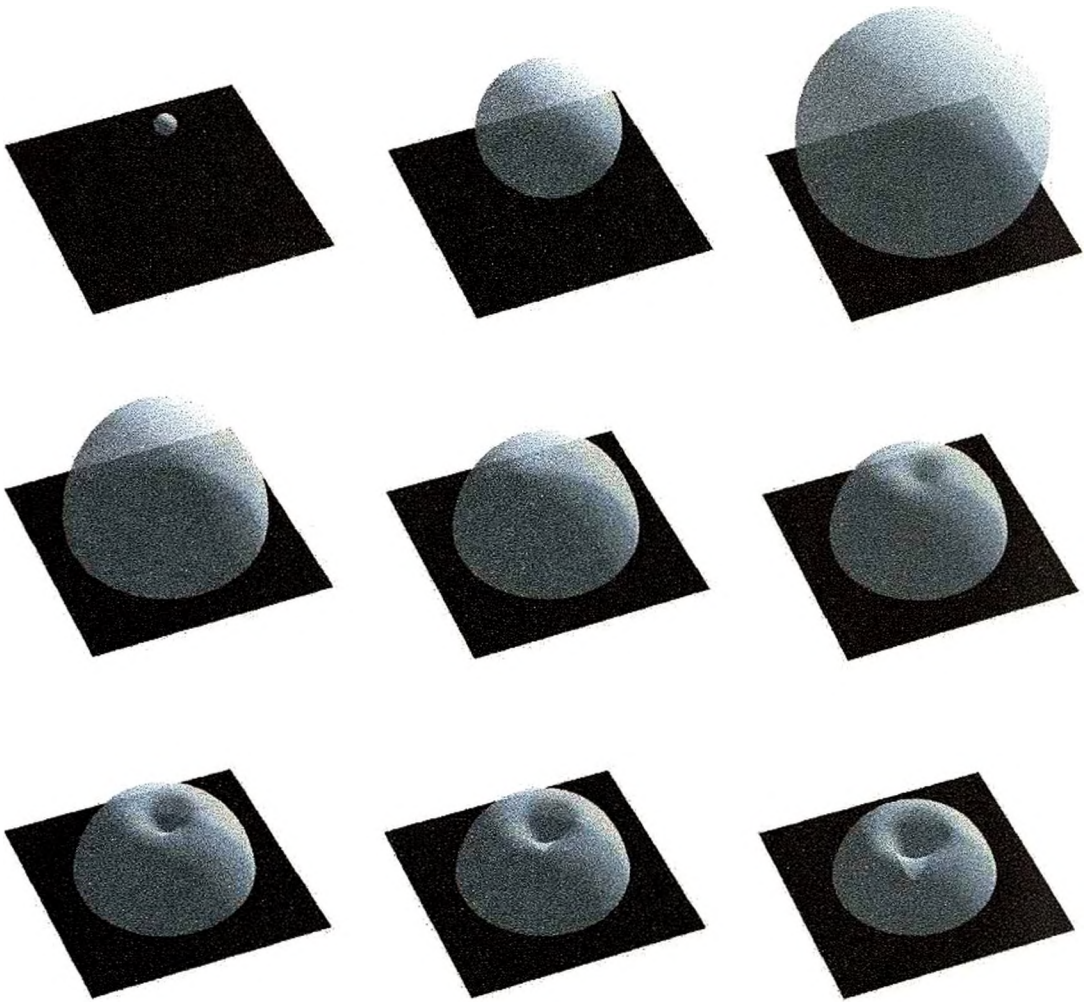

(a) Motion prior to liquid jet impact. Times are 0.0000, 0.1505, 1.1082, 1.8952, 2.0369, 2.0724, 2.0975, 2.1213 and 2.1654 respectively.

Figure 3.29: Rendered transparent bubble shapes showing the motion of a cavitation bubble near a rigid boundary for the parameters $\alpha = 600$, $\gamma = 0.8$, $\delta = 0.0$ and $\kappa = 1.4$. The square portion of the rigid boundary shown is $2R_{\mathrm{m}} \times 2R_{\mathrm{m}}$ and angle of elevation is 45°.

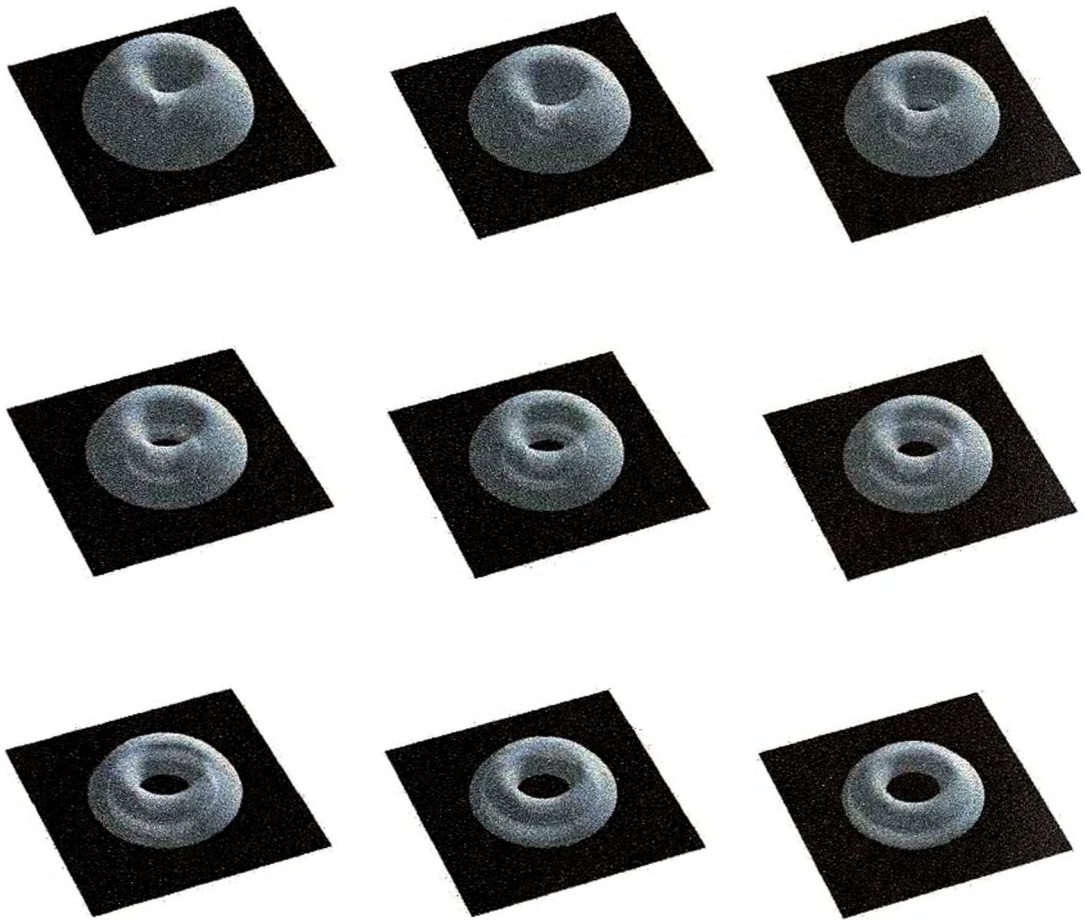

(b) Motion following liquid jet impact. Times are 2.1654, 2.1938, 2.2016, 2.2100, 2.2195, 2.2298, 2.2408, 2.2518 and 2.2615 respectively.

Figure 3.29 continued: Rendered transparent bubble shapes showing the motion of a cavitation bubble near a rigid boundary for the parameters $\alpha = 600$, $\gamma = 0.8$, $\delta = 0.0$ and $\kappa = 1.4$. The square portion of the rigid boundary shown is $2R_{\mathrm{m}} \times 2R_{\mathrm{m}}$ and angle of elevation is 45°.

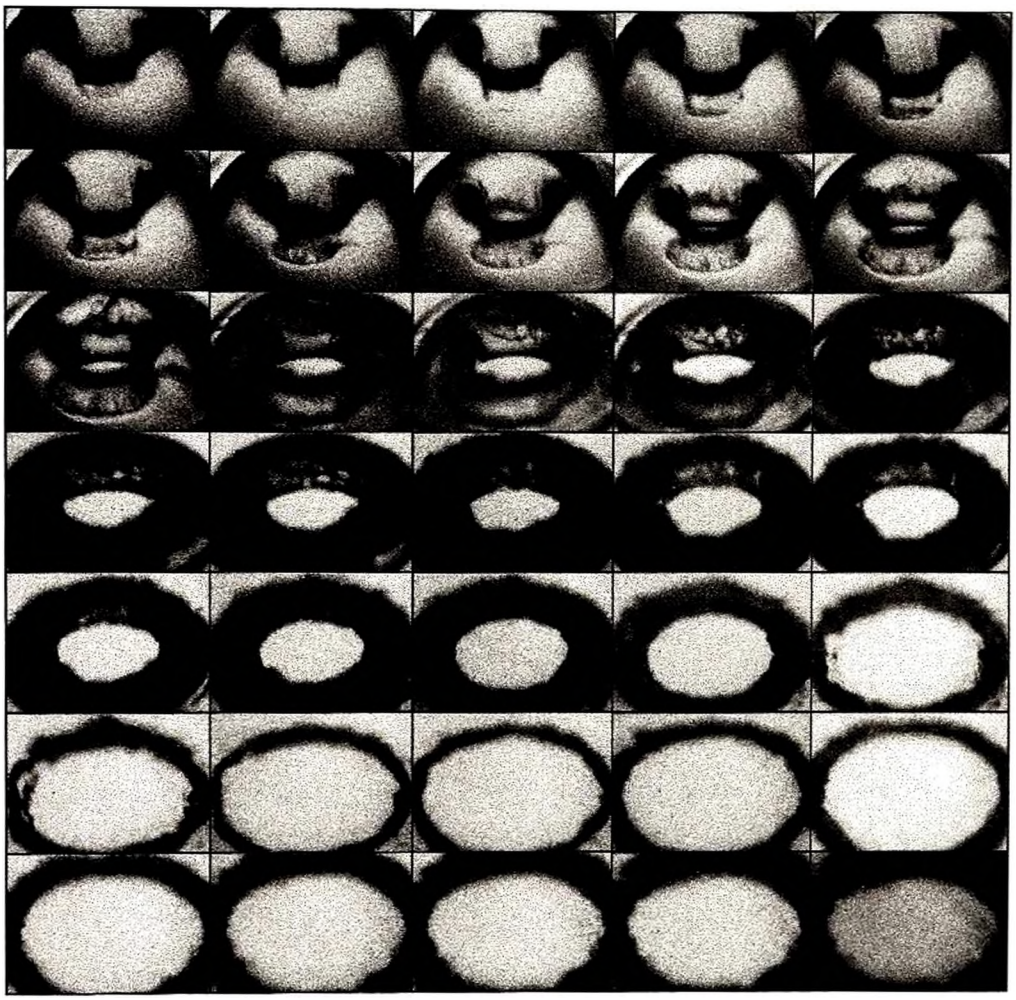

Figure 3.30: The final stages of collapse and rebound of a laser-generated cavitation bubble near a rigid boundary characterised by $\alpha = 600$, $\gamma = 0.8$, $\delta = 0.0$ and $\kappa = 1.4$. Motion is viewed from an angle of 45° above the rigid boundary. Reproduced with permission from Lindau (2001).

calculation of physical quantities associated with the bubble and surrounding fluid. Several of these, most notably the Kelvin impulse and kinetic energy associated with the liquid jet, have not previously been examined and provide new information about the highly non-spherical aspects of the motion in close proximity to the rigid boundary. Furthermore, the techniques employed to calculate velocity and pressure contours have been improved over previous works thus providing more detailed information about the fluid flow around the bubble. We also note visualisation techniques have necessarily been improved in order to allow comparison with recent experimental results which are viewed at an elevated angle, in stark contrast to earlier experiments wherein motion is generally recorded in profile.

In the following chapter, we further extend out numerical scheme in order to permit calculations where an infinite free surface or additional bubbles are introduced into the flow field. Furthermore, this also allows consideration of bubble motion in a shallow layer of fluid through the use of an appropriate image system.

Chapter 4

MULTIPLE BUBBLES, AN INFINITE FREE SURFACE AND A SHALLOW FLUID LAYER

In this chapter, we outline further developments to the techniques discussed in Chapter 3 in order to permit the consideration of flows induced by the motion of a bubble near to an infinite free surface and/or by multiple bubbles. In order to accomplish this, we require a numerical scheme capable of dealing with multiple boundaries on the flow domain.[1] Prior to our discussion of the changes to the numerical scheme, it is important we detail some of the computational and experimental work pertaining to bubble motion near an infinite free surface. Following this discussion of previous work and of the necessary reformulation of our scheme, results are presented. Herein we consider the motion of both a single vapour bubble and of two vapour bubbles formed in a vertical column beneath an infinite free surface. Finally, we consider the motion of both vapour and gas bubbles formed in a shallow fluid layer through the inclusion of a rigid boundary in the flow field. At the close of the chapter, we summarise key features and discuss further avenues of research.

4.1 An Overview of Theory and Experiments

The problem posed by the motion of a bubble near a free surface is a poor relation to that of bubble motion near a rigid boundary with respect to both experimental and theoretical investigations, with comparatively little work performed in either area. Rightly, much of

[1] We recall the rigid boundary considered in Chapter 3 was introduced into the flow field by means of an image system, and so we were required to consider only the surface of the bubble during solution of the boundary integral equation.

the work which does exist concerns underwater explosion bubbles and their interactions with the surface of the ocean. One such recent work is that of Rogers & Szymczak (1997), in which calculations and experiments concerning violent surface motion are presented. Figure 4 of this paper shows the effects both experimentally and computationally of a shallow depth ($\gamma = -0.67$) detonation. The entrainment of the bubble within the raised ocean surface and bubble jetting from above are both also readily observed in small-scale cavitation experiments. The key feature of the large-scale work is the formation of plumes of spray caused by the explosion and the rapid initial expansion and subsequent rebound of the bubble. Whilst a boundary integral scheme may not capture this feature, similar results presented later show much of the qualitative behaviour observed. For this reason, we now restrict our attention to much smaller-scale experiments concerning cavitation bubbles and associated theoretical and computational studies.

As noted above, the number of experimental works concerning the motion of cavitation bubbles near an infinite free surface is far less than for the rigid-boundary case. The key studies in this area are those of Blake & Gibson (1981), Chahine (1982), Robinson, Blake, Kodama, Shima & Tomita (2001) and Tomita & Kodama (2001). Blake & Gibson (1981) used a spark-discharge method of cavity generation in a reduced pressure environment to examine the motion of both the bubble and free surface in order to provide comparison with an approximate integral equation approach to modelling the motion. Despite the limited series of results presented, these experiments (in particular Figure 10, which was reproduced earlier in Figure 1.2 on page 9) have been used in a number of theoretical and computational studies for comparative purposes. Of key importance on the theoretical side is the paper by Longuet-Higgins (1983) who models the tip of the free surface 'spike' as a Dirichlet hyperboloid, thus permitting the calculation of the velocities thereon, which are in excellent agreement with the experiments of Blake & Gibson. A critical angle for the motion of the free surface is also determined, beyond which the rapid development of the spike is assured; we consider this matter later.

The later work by Robinson, Blake, Kodama, Shima & Tomita (2001) and Tomita & Kodama (2001) utilises laser-discharge techniques to generate both a single bubble and two bubbles in a vertical column beneath the free surface. In the former paper, two

bubbles of a similar maximum volume are considered, and a boundary integral scheme employed to calculate the motion of a pair of vapour bubbles, with a high degree of success. In the latter paper, two bubbles of significantly different maximum volume (and hence period of oscillation) are considered experimentally. We later show due to the differing timescales of motion between the two bubbles, it is no longer sufficient to model these as vapour bubbles as the motion of the smaller bubble may be slowed during final collapse due to adiabatic compression of gas therein, thus changing the relative motion of the bubbles. We note the omission of calculations relating to this matter in the current work, which are reserved for a future collaborative study.

Prior to further discussion of computational studies, we pause to note the papers by Blake & Cerone (1982) and Blake (1988) which employ the Kelvin impulse to detail the gross motion of a bubble near an infinite free surface amongst the numerous boundary types considered. Here the Bjerknes force generated by the boundary on the bubble is shown to have opposing sign to that in the rigid boundary case, indicating bubble migration and jet formation will be away from the boundary. Such behaviour is readily observed in both experiments and calculations, further indicating calculation of the Kelvin impulse is an important technique in obtaining information about the physical behaviour of a bubble.

Computational studies concerning the motion of a bubble near an infinite free surface are more abundant, though again not so plentiful as with the rigid-boundary problem. Early studies in this area dating back to the Second World War are concerned with the motion of underwater explosion bubbles: for example the work by Herring (1941) and subsequent numerical study by Taylor (1942). These necessarily model the bubble as spherical and so the effects of buoyancy and nearby boundaries are to displace the bubble rather than deform its shape. One early consideration of the non-spherical motion of the bubble was performed by Lenoir (1976), who employed a boundary integral technique to model the motion of the bubble. The success of this study is questionable, since results presented show a narrow liquid jet directed towards the free surface as well as the expected broader (though in these calculations, slower) jet directed away from the free surface. This is most likely due to the omission of the expansion phase when fundamentally

different pressure gradients are formed in the fluid due to asymmetries. As noted above, Blake & Gibson (1981) employed an approximate integral equation technique to model the motion of the bubble and free surface. During expansion and early collapse, the calculated motion was shown to be in good agreement with experiments. However, upon formation of the liquid jet within the bubble, this model fails and calculations are ceased. Later work by Kucera & Blake (1990) has shown such approximate methods to compare well with boundary integral studies for bubbles not too close to a boundary, with a reasonable agreement possible down to standoff distances of about 2.0, up until the time of jet formation. More recent calculations using these techniques may be found in Cox (2001).

The boundary integral study of Blake, Taib & Doherty (1987) goes some way to improving this matter. As with the companion paper (Blake, Taib & Doherty 1986), calculations continue even after formation of the liquid jet. However, due to the simple piecewise-linear forms used for the surface geometry and potential thereon, these calculations often do not follow the motion up until the time of jet impact. These failures may be attributed to the difficulty in dealing with both the very narrow liquid jets which form within bubbles in close proximity to the boundary, and with the very 'square' jets which form at greater standoff distances. Furthermore, due to the linear distribution of nodes with respect to arclength on the free surface, the motion of the free surface spike is not captured with sufficient accuracy, leading to much shorter, wider spikes than may be observed in experiments.

A more recent and demanding study may be found in the paper by Boulton-Stone & Blake (1993), which considers the bursting of gas bubbles at a free surface. This work employs a highly accurate boundary integral scheme which also necessarily includes surface tension and viscous effects through the introduction of a boundary layer.

We now return to consider the computational aspects of the paper by Robinson, Blake, Kodama, Shima & Tomita (2001), the experimental aspects of which were outlined above. In this work, a boundary integral method is used to calculate the motion of both one and a vertical stack of two bubbles beneath the free surface. In this work, cubic splines are used to represent the surface of the bubble and the infinite free surface, with

a non-linear distribution of nodes being employed on the free surface in order to more accurately capture the motion of the free surface spike, which experiments show to be narrow and pronounced where bubbles are generated close to the boundary. Furthermore, the calculations show excellent agreement with experiments in both the one and two-bubble cases. As such we use this work as a basis for modifying our boundary integral scheme to deal with bubble motion near an infinite free surface.

We now proceed to detail the changes to our numerical scheme in order to allow calculations for multi-bubble systems, with or without an infinite free surface. We note this scheme is also suitable for calculations in a shallow layer of fluid through the addition of a rigid boundary using the image system technique discussed in Chapter 3.

4.2 Revised Boundary Integral Scheme

The numerical scheme employed to calculate the motion of a bubble near an infinite free surface or of multi-bubble systems is much like that used to calculate bubble motion near a rigid boundary, as detailed in Chapter 3, but with several key differences which we discuss here. Primarily we note we may no longer use an image system to account for the presence of the free surface as was done with the rigid boundary earlier.[2] As previously commented upon, the remedy is to introduce a second boundary into the flow field, over which we must also integrate. The infinite extent of this boundary poses a second problem, in that we are required to integrate over a surface of infinite area, an issue which is readily resolved by assuming a dipolar far-field. Similarly, an additional boundary is added for each bubble under consideration. Due to this, the complexity of the code is increased by the need to track more than one interface, though the problem here is one of accountancy and is not mathematical.

We begin by recalling the boundary integral equation (3.2.7), which is

$$c(\boldsymbol{p})\phi(\boldsymbol{p}) = \int_{\partial\Omega} \left(\frac{\partial\phi(\boldsymbol{q})}{\partial n} G(\boldsymbol{p},\boldsymbol{q}) - \phi(\boldsymbol{q}) \frac{\partial G(\boldsymbol{p},\boldsymbol{q})}{\partial n} \right) \mathrm{d}S, \tag{4.2.1}$$

with $c(\boldsymbol{p})$ as given by (3.2.8). We now note $\partial\Omega$, the boundaries of the fluid domain, consist of not only the surface of a single bubble, but also the infinite free surface, which

[2] Though this would prove to be a valid technique for the consideration of a bubble formed at a large distance from the free surface, whereon surface motion and displacement will be negligible.

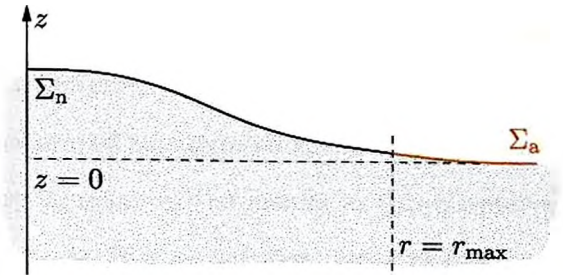

Figure 4.1: Schematic showing the numeric (Σ_n) and analytic (Σ_a) portions of the free surface for numerical purposes.

we denote by Σ; plus any additional bubbles considered. We deal with the infinite extent of Σ by using an analytic form for the variables in the far-field, so in order to differentiate between the numeric and analytic potions of the free surface, we use the subscripts n and a respectively. So that $\Sigma \equiv \Sigma_n \cup \Sigma_a$. See Figure 4.1. Further we denote the surfaces of N bubbles by $S_1, S_2, \ldots, S_N$ and hereafter represent these by S so that $S \equiv S_1 \cup S_2 \cup \ldots \cup S_N$. Hence $\partial\Omega \equiv S \cup \Sigma \equiv S_1 \cup S_2 \cup \ldots \cup S_N \cup \Sigma_n \cup \Sigma_a$.

As in Chapter 3, we utilise a fourth-order Runge-Kutta scheme for the time integrations, with the kinematic boundary condition as in (3.3.1) valid on all boundaries, which is

$$\frac{\mathrm{D}\boldsymbol{p}_i}{\mathrm{D}t} = \boldsymbol{u}_i, \tag{4.2.2}$$

where we recall $\boldsymbol{u}_i$ is the fluid velocity at the point $\boldsymbol{p}_i$, and $\mathrm{D}/\mathrm{D}t$ is the material derivative. The dynamic boundary condition at the surface of a bubble is of the form given by (3.3.3), with that on the infinite free surface taking a similar but simpler form due to the differences in hydrostatic pressure and the lack of any forcing pressure. These are, respectively

$$\frac{\mathrm{D}\phi_i}{\mathrm{D}t} = \frac{1}{2}|\boldsymbol{u}_i|^2 + 1 - \alpha\left(\frac{V_0}{V}\right)^{\kappa} - \delta^2 z_i, \qquad \text{on} \qquad S, \tag{4.2.3a}$$

$$\frac{\mathrm{D}\phi_i}{\mathrm{D}t} = \frac{1}{2}|\boldsymbol{u}_i|^2 - \delta^2 z_i, \qquad \text{on} \qquad \Sigma. \tag{4.2.3b}$$

As mentioned earlier, the nodes on the free surface are distributed non-linearly with respect to arclength in order we may more accurately capture the narrow pronounced free surface spike which develops for bubbles generated at small standoff distances. The primary motivation for this is that any application of smoothing algorithms to the free

surface leads to rapid spreading and a reduction in the height of this spike. In our most recent work, the requirement for smoothing on the free surface has been removed through the use of the improved approximations for elliptic integrals given in Appendix A; though as with Chapter 3, many of the results in this chapter were calculated prior to this modification in our code. It is nonetheless useful to retain this distribution of nodes however, since it ensures we capture the most narrow of spikes accurately. Here we choose to follow the work of Robinson, Blake, Kodama, Shima & Tomita (2001), where the nodes are distributed along Σ_n at

$$\xi_i = \frac{\xi_{n_{\Sigma_n}}}{2}\left(\frac{i}{n_{\Sigma_n}}\right)^a\left[1+\frac{1}{(n_{\Sigma_n}+1-i)^2}\right], \qquad i=1,2,\ldots,n_{\Sigma_n}, \tag{4.2.4}$$

where n_{Σ_n} is the number of nodes on the numeric portion of the free surface and a is a distribution parameter. A value of $a = 1.3$ is suggested by Robinson *et al.*, however we have used $a = 1.1$ resulting in a higher node density about the axis of symmetry in order to lessen the effects of smoothing.

Collocation of equation (4.2.1) yields the system of linear equations

$$\tfrac{1}{2}\phi_{s\,i} + \sum_{\tilde{s}=1}^{N+1}\sum_{j=2}^{n_{\tilde{s}}}\mathcal{A}_{s\tilde{s}\,ij} + \mathcal{P}_{s\hat{s}\,i} = \sum_{\tilde{s}=1}^{N+1}\sum_{j=2}^{n_{\tilde{s}}}(\mathcal{B}_{s\tilde{s}\,ij}\psi_{\tilde{s}\,j-1} + \mathcal{C}_{s\tilde{s}\,ij}\psi_{\tilde{s}\,j}) + \mathcal{Q}_{s\hat{s}\,i}\psi_{\hat{s}\,n_{\hat{s}}},$$
$$s = 1,2,\ldots,N+1, \qquad i = 1,2,\ldots,n_s, \tag{4.2.5}$$

where this differs from equation (3.3.17) since we need to integrate and collocate over all material surfaces. Collocation over the additional surfaces yields n_s equations for each of $s = 1,2,\ldots,N+1$, whilst additional integrations over the $N+1$ surfaces are represented via the extra summation over $\tilde{s}$. In equation (4.2.5) the upper limit of the sum is given to be $N+1$, thus signifying N bubbles plus an infinite free surface are considered, though this need not be the case and the upper limit may readily be changed. We further note the upper limit of the second sum over j is dependent on the number of nodes, $n_{\tilde{s}}$ on

surface $\tilde{s}$. The revised forms of the $\mathcal{A}_{s\tilde{s}ij}$, $\mathcal{B}_{s\tilde{s}ij}$ and $\mathcal{C}_{s\tilde{s}ij}$ are

$$\mathcal{A}_{s\tilde{s}ij} = \int_{\xi_{\tilde{s}j-1}}^{\xi_{\tilde{s}j}} \Phi_{\tilde{s}j-1}(\xi_{\tilde{s}})\mathcal{R}_{\tilde{s}j-1}(\xi_{\tilde{s}}) \int_0^{2\pi} \frac{\partial G_{si}}{\partial n}(\xi_{\tilde{s}}, \theta_{\tilde{s}})\,\mathrm{d}\theta\,\mathrm{d}\xi, \tag{4.2.6a}$$

$$\mathcal{B}_{s\tilde{s}ij} = \int_{\xi_{\tilde{s}j-1}}^{\xi_{\tilde{s}j}} \frac{\xi_{\tilde{s}j} - \xi_{\tilde{s}}}{\delta\xi_{\tilde{s}j}}\mathcal{R}_{\tilde{s}j-1}(\xi_{\tilde{s}}) \int_0^{2\pi} G_{si}(\xi_{\tilde{s}}, \theta_{\tilde{s}})\,\mathrm{d}\theta\,\mathrm{d}\xi, \tag{4.2.6b}$$

$$\mathcal{C}_{s\tilde{s}ij} = \int_{\xi_{\tilde{s}j-1}}^{\xi_{\tilde{s}j}} \frac{\xi_{\tilde{s}} - \xi_{\tilde{s}j-1}}{\delta\xi_{\tilde{s}j}}\mathcal{R}_{\tilde{s}j-1}(\xi_{\tilde{s}}) \int_0^{2\pi} G_{si}(\xi_{\tilde{s}}, \theta_{\tilde{s}})\,\mathrm{d}\theta\,\mathrm{d}\xi, \tag{4.2.6c}$$

and the Green's function evaluated at the i^{th} node on the collocation surface, $\boldsymbol{p}_{si}$ is

$$G_{si}(\xi_{\tilde{s}}, \theta_{\tilde{s}}) = \frac{1}{4\pi\,|\boldsymbol{p}_{si} - \boldsymbol{q}(\xi_{\tilde{s}}, \theta_{\tilde{s}})|}. \tag{4.2.7}$$

We note these differ from the forms given in Chapter 3 through the addition of the subscripts s and $\tilde{s}$ which are used to denote the respective surfaces over which the collocations and integrations are performed. The additional terms $\mathcal{P}_{s\hat{s}i}$ and $\mathcal{Q}_{s\hat{s}i}$ occur due to the requirement to integrate over the analytic portion of the free surface, $s = \hat{s}$, if required. These are defined as

$$\mathcal{P}_{s\hat{s}i} = \int_{\xi_{\hat{s}n_{\hat{s}}}}^{\infty} \phi_{\hat{s}n_{\hat{s}}} \left(\frac{r_{\hat{s}n_{\hat{s}}}}{\mathcal{R}_{\hat{s}}(\xi_{\hat{s}})}\right)^3 \mathcal{R}_{\hat{s}}(\xi_{\hat{s}}) \int_0^{2\pi} \frac{\partial G_{si}}{\partial n}(\xi_{\hat{s}}, \theta_{\hat{s}})\,\mathrm{d}\theta\,\mathrm{d}\xi, \tag{4.2.8a}$$

$$\mathcal{Q}_{s\hat{s}i} = \int_{\xi_{\hat{s}n_{\hat{s}}}}^{\infty} \left(\frac{r_{\hat{s}n_{\hat{s}}}}{\mathcal{R}_{\hat{s}}(\xi_{\hat{s}})}\right)^3 \mathcal{R}_{\hat{s}}(\xi_{\hat{s}}) \int_0^{2\pi} G_{si}(\xi_{\hat{s}}, \theta_{\hat{s}})\,\mathrm{d}\theta\,\mathrm{d}\xi. \tag{4.2.8b}$$

A discussion of these forms follows in due course.

In effect, this may be thought of as forming the matrix equation

$$\mathbf{M}\boldsymbol{\Phi} = \mathbf{N}\boldsymbol{\Psi}, \tag{4.2.9}$$

where, for the motion of a single bubble near an infinite free surface, the matrices $\mathbf{M}$ and

N take the block form

Collocation on free surface nodes. Integration over free surface.	Collocation on free surface nodes. Integration over bubble surface.
Collocation on bubble nodes. Integration over free surface.	Collocation on bubble nodes. Integration over bubble surface.

(4.2.10)

This may readily be extended to the N bubbles and free surface case, giving matrices of the form

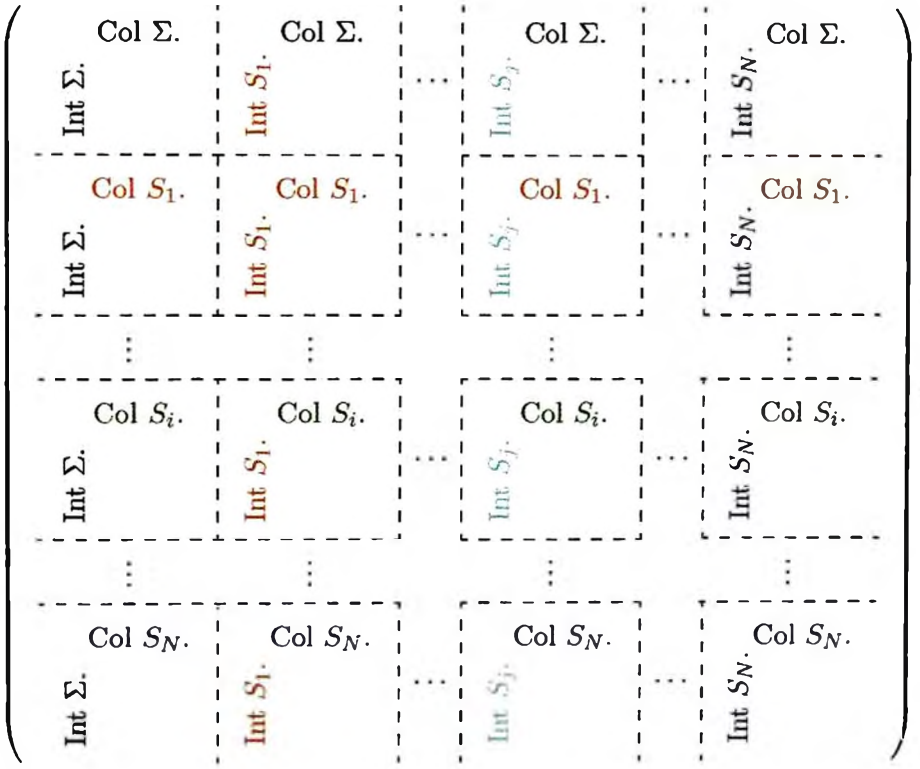

(4.2.11)

where we have coloured entries for like surfaces in order to emphasise the structure of this matrix. We note in practice the term $\mathbf{M\Phi}$ is assembled as a vector directly as all information is known *a priori*.

As noted earlier, the far-field free surface, Σ_a is dealt with by means of analytic techniques. It may be argued (see Pearson 2000) that the leading order of the behaviour is like that due to a dipole, with the velocity decaying at $O(|r|^{-3})$. Hence we take the

quantities z, ϕ and ψ to be of the form

$$f(r,t) = \left(\frac{r_{\max}}{r}\right)^3 f(r_{\max},t), \qquad |r| > r_{\max}. \tag{4.2.12}$$

Here $r_{\max}$ denotes the r value at the outermost end of Σ_n, the numerical part of the free surface. At this point it is convenient to introduce suitable clamped end conditions for the splines. The bubble is dealt with as before. (See equations (3.3.15).) The end of Σ_n which lies on the axis of symmetry may be dealt with by continuity conditions as with the bubble, which yields

$$\frac{\mathrm{d}r}{\mathrm{d}\xi} = 1, \qquad \frac{\mathrm{d}z}{\mathrm{d}\xi} = 0, \qquad \frac{\mathrm{d}\phi}{\mathrm{d}\xi} = 0, \qquad \text{at} \qquad \xi = \xi_1 = 0. \tag{4.2.13}$$

At the far end, we are required to calculate a value for $\mathrm{d}r/\mathrm{d}\xi$. This is done by differentiating

$$\xi = \int \sqrt{1 + \left(\frac{\mathrm{d}z}{\mathrm{d}r}\right)^2}\, \mathrm{d}r, \tag{4.2.14}$$

an expression for the arclength. Following rearrangement, we obtain

$$\frac{\mathrm{d}r}{\mathrm{d}\xi} = \left[1 + \left(\frac{3z}{r}\right)^2\right]^{-\frac{1}{2}}. \tag{4.2.15}$$

Hence by taking z and ϕ to be of the form (4.2.12), through simple application of the chain rule we obtain the clamped end conditions

$$\frac{\mathrm{d}r}{\mathrm{d}\xi} = \frac{1}{c}, \qquad \frac{\mathrm{d}z}{\mathrm{d}\xi} = -\frac{3z}{cr}, \qquad \frac{\mathrm{d}\phi}{\mathrm{d}\xi} = -\frac{3\phi}{cr}, \qquad \text{at} \qquad \xi = \xi_{n_{\Sigma_n}}, \tag{4.2.16}$$

where $c = (1 + (3z/r)^2)^{\frac{1}{2}}$.

We conclude this section by commenting on the smoothing techniques which are applied to the free surface and bubble(s). As previously noted, our recent work which employs the improved polynomial approximations for the elliptic integrals removes the requirement for smoothing on the infinite free surface. However, the results presented in this chapter were calculated prior to the inclusion of these improved approximations in our code, and so employ smoothing on the free surface in order to remove the high-frequency oscillations which develop. We note here if a regular node distribution is used, even the most infrequent application of smoothing quickly leads to a spreading of the raised free surface spike. For the narrow spikes generated by the motion of a

bubble in close proximity to the surface, the results produced are unacceptable. Hence the need for the irregular node distribution. Due to this, the use of our favoured LM smoothing is no longer permissible, since it utilises a finite difference approximation for the fourth-order derivative required. However, this proves to be only a minor problem, since the instabilities develop much more slowly upon the free surface and so application of the LHC smoothing method is required only every 50 time steps. On the bubble, surface instabilities again develop most readily at regions of high curvature. For bubbles generated very close to the free surface where very narrow liquid jets are observed within the bubble, these regions are found at both the tip and the mouth of the liquid jet. In bubbles generated at larger standoff distances where very square jets develop, the instabilities occur most readily at the 'corners' or the jet. As with bubble motion near a rigid boundary, the use of the improved polynomial approximations is insufficient to prevent the onset of instabilities, and so at present smoothing is still required on the bubble. Due to the regular distribution of nodes on the bubble, we again use the LM smoothing method.

Having detailed the required changes to the numerical scheme, we now proceed to discuss results concerning the motion of bubbles near to an infinite free surface and, via the addition of a rigid boundary, in a shallow layer of fluid.

4.3 Numerical Calculations

In this section, we present results calculated using out revised boundary integral scheme for the following cases:

1. A vapour bubble near an infinite free surface.
2. Two vapour bubbles formed in a vertical column beneath an infinite free surface.
3. A single vapour bubble in a shallow layer of fluid.
4. A gas bubble in a shallow fluid layer.

Where suitable examples exist, high-speed photograph series are reproduced and compared against our calculations.

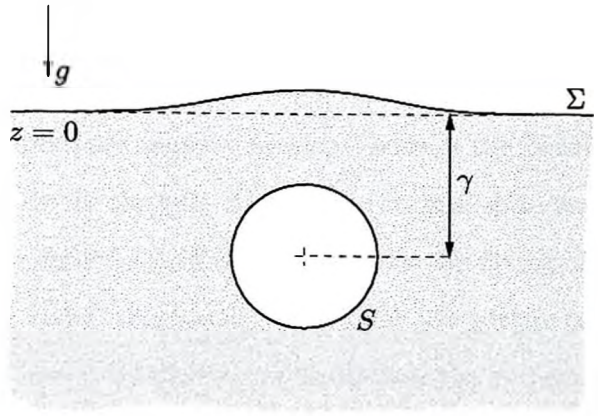

Figure 4.2: Schematic showing a bubble near an infinite free surface. The bubble is generated at a dimensionless distance γ from the boundary.

4.3.1 Vapour Bubble Near an Infinite Free Surface

We begin the discussion of our results by considering the motion of a single vapour bubble generated near an infinite free surface in the absence of buoyancy effects. Here the critical parameter is the standoff distance, γ, the dimensionless distance between bubble and boundary scaled with respect to the maximum radius the bubble would attain in an infinite fluid. See Figure 4.2. As in Chapter 3, the motion is driven by an initial velocity imposed on the bubble wall. As such, the bubble grows until all kinetic energy is imparted to the fluid at maximum volume. Following this, the bubble collapses unhindered by the compression of gas within the bubble.

Figure 4.3 shows the motion of a vapour bubble formed at a standoff distance of $\gamma = -0.45$ beneath an infinite free surface, up until the time of liquid jet impact. We note that physically there is a question as to whether a bubble formed in such close proximity to the surface would burst. Certainly for bubbles of more than a few millimetres in diameter, it is likely that the violence of the motion would overcome surface tension effects and bursting would occur. However, this case is presented here to exhibit the accuracy of our calculations even in such close proximity to the boundary. This minimum standoff distance is much less than we are able to attain with our rigid boundary code and is due to the actual displacement of the boundary as the bubble expands. Key features to note include the entrainment of the bubble in the raised free surface wherein the upper

pole of the bubble becomes pointed. This is due to the relative ease with which the bubble displaces the free surface compared with the infinite extent of fluid below. We later show that high-pressure regions develop between the bubble and free surface in such situations. This drives the very narrow free surface spike and liquid jet within the bubble. We note the rounded tip of the jet is due to the fitting of cubic splines through a set of evenly spaced nodes; this has an effect much like surface tension. In future work, we plan to use a non-linear distribution of nodes over the surface of the bubble in order to overcome these restrictions on curvature, thus permitting the consideration of physical surface tension effects.

In Figure 4.4 we present calculations pertaining to the often reproduced experiments of Blake & Gibson (1981) concerning the motion of a vapour bubble formed at a standoff distance of $\gamma = -0.56$ beneath an infinite free surface. A high-speed experimental photograph series showing the motion of the spark-discharge generated bubbles was reproduced from Figure 10 of the paper by Blake & Gibson in Figure 1.2.[3] These experiments show that for the centimetre sized bubbles produced, the bubble does not burst. Here Figure 4.4a shows rendered transparent bubble and surface shapes for the pre-toroidal phase of motion, wherein we note the entrainment of the bubble within the raised free surface and narrow liquid jet and free surface spike formed during collapse. In Figure 4.4b we consider the subsequent motion following liquid jet impact and the transition to a toroidal bubble geometry. We note the continued collapse of the bubble due to our omission of any gaseous content, the continued growth of the free surface spike and the unusual geometries which form due to the liquid splash thrown up inside the bubble and circulation within the flow field. In order to further understand the behaviour of this system, we present velocity vectors and pressure contours within the body of the fluid in Figure 4.4c. In the first frame, we note the region of high pressure which develops beneath the bubble as the bubble tries to displace the fluid beneath it, in addition the the thin veneer of liquid separating the bubble and free surface, wherein the pressure is reduced due to dis-

[3]This figure was also reproduced for comparative purposes in the papers by Longuet-Higgins (1983) and Robinson, Blake, Kodama, Shima & Tomita (2001), and may also be viewed in 'An Album of Fluid Motion' by Van Dyke (1982). We note that pressure contours calculated for this thesis were used to replace earlier calculations in the paper by Robinson *et al.* (2001) for publication. These experiments have also been compared against calculations in papers such as that by Blake, Taib & Doherty (1987).

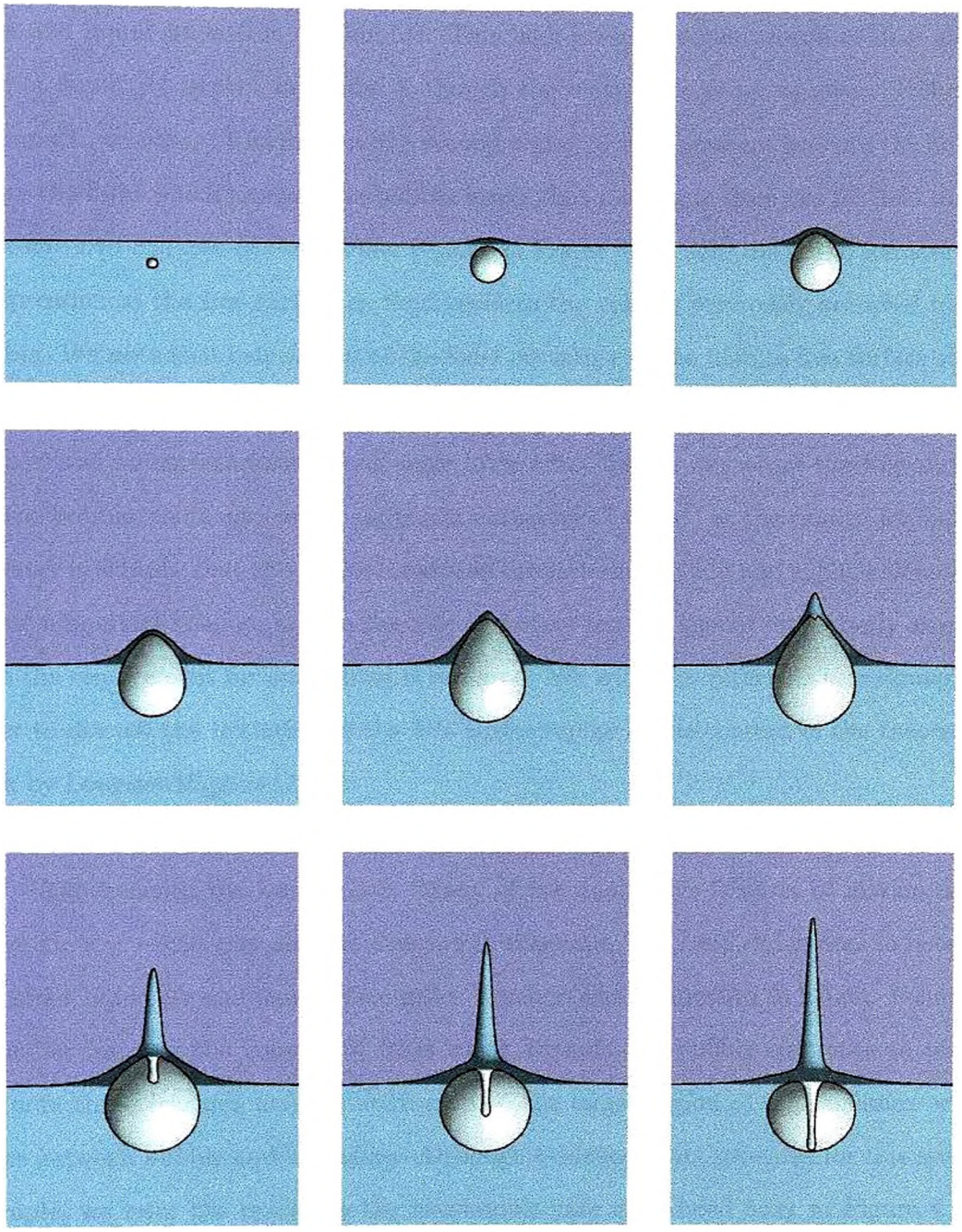

Figure 4.3: Half-rendered bubble and surface shapes showing the motion of a vapour bubble near an infinite free surface for $\gamma = -0.45$ up until the time of jet impact. Horizontal and vertical axes are $r \leqslant 3$, $-3 \leqslant z \leqslant 5$. Times are 0.0015, 0.0327, 0.0830, 0.1570, 0.2531, 0.3476, 0.5727, 0.7063 and 0.8353 respectively.

placement of the free surface. In Frames 2 and 3, we note the formation of a high-pressure region between the bubble and free surface, which drives the motion of the free surface spike and liquid jet within the bubble. This high-pressure region is still evident at the time of liquid jet impact in Frame 4, though the magnitude is not so great. Following jet impact, we note the formation of a second region of high pressure beneath the bubble where the fluid which threads the bubble meets that rushing in from the far-field due to the continued collapse of the bubble. Finally in Frame 6, we note the initial formation of a depression in the free surface as fluid replaces the volume previously occupied by the bubble. We note that calculation of the local curvature of the infinite free surface shows this to be of $O(10^2)$ at the tip of the free surface spike at the time of jet impact in the bubble, and so surface tension will have little effect on the motion of the free surface. On the bubble, there also exists regions of curvature of $O(10^2)$ at the time of jet impact. However is is likely that this figure is reduced through the implicit and explicit smoothing in our numerical scheme, and so the rôle of surface tension should be properly assessed once the requirement for smoothing is removed. We will later return to this example in order to discuss the initiation of the free surface spike in the context of the theoretical work by Longuet-Higgins (1983).

Figure 4.5 shows the motion of a vapour bubble generated at a standoff distance of $\gamma = -0.65$ beneath the free surface. Many of the qualitative features of motion noted above for $\gamma = -0.56$ may also be observed in this case. The main differences to note are the wider liquid jet and free surface spike, which is also diminished in height. Following liquid jet impact, the column of fluid which threads the bubble continues to widen. We note these features may be attributed to the larger region of high pressure which forms between bubble and boundary. Although evidence is not provided for this specific example, we refer the reader to the two-bubble case considered later in Figure 4.21b, where the upper bubble is generated at a standoff distance, $\gamma = -0.75$ beneath the free surface and a much larger region of high pressure over that for $\gamma = -0.56$ is observed.

In order to consider the effects of generating bubbles at larger standoff distances from the infinite free surface, Figure 4.6 shows bubble and surface geometries at the time of jet impact over the range of standoff distances $-0.45 \geqslant \gamma \geqslant -1.3$. We note the very narrow

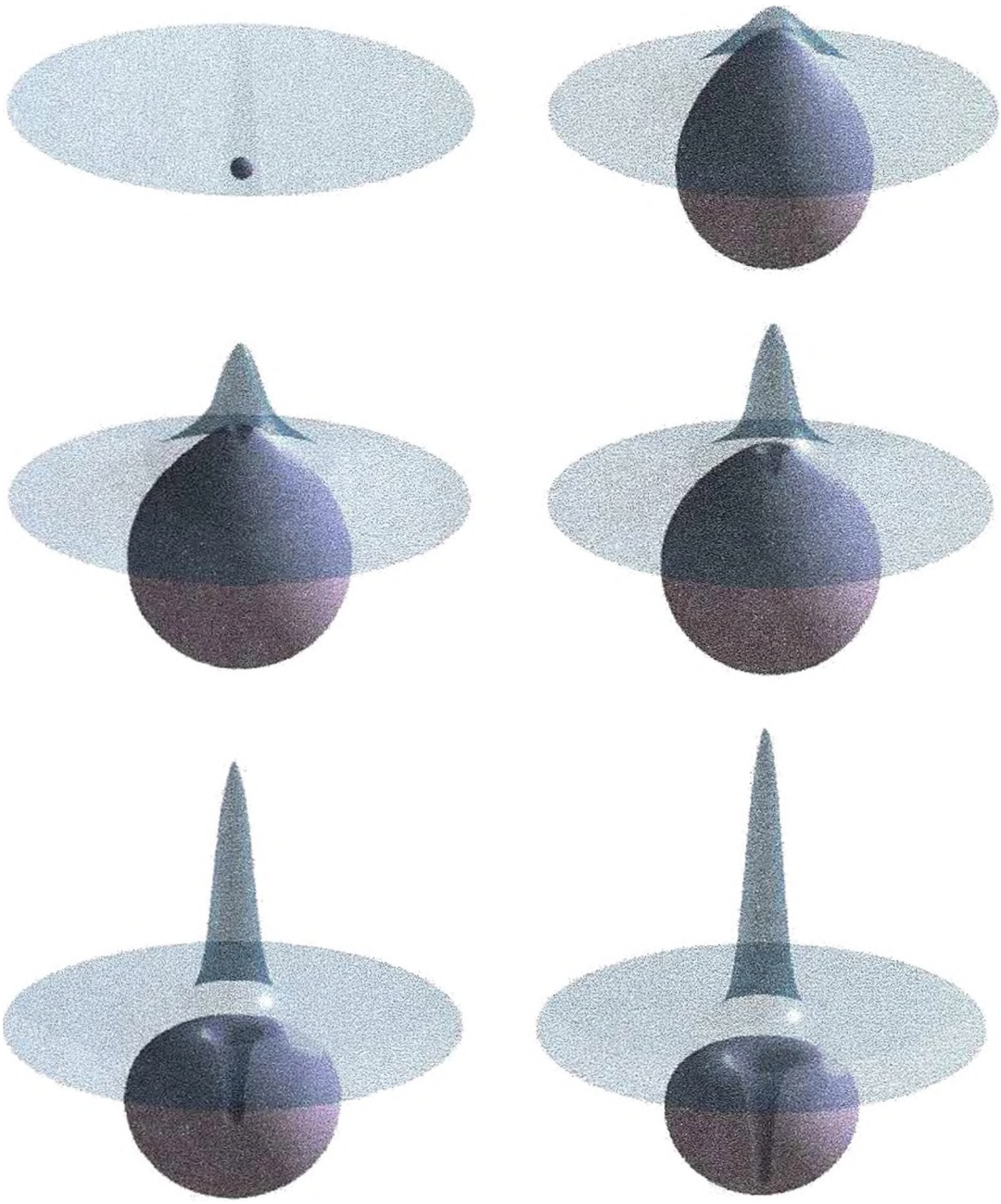

(a) Rendered transparent bubble and surface shapes showing the motion up until the time of jet impact. The circular portion of the free surface shown is $2R_m$ in radius. Times are 0.0015, 0.3515, 0.5309, 0.6151, 0.9125 and 1.0402 respectively.

Figure 4.4: Motion of a vapour bubble near an infinite free surface for $\gamma = -0.56$.

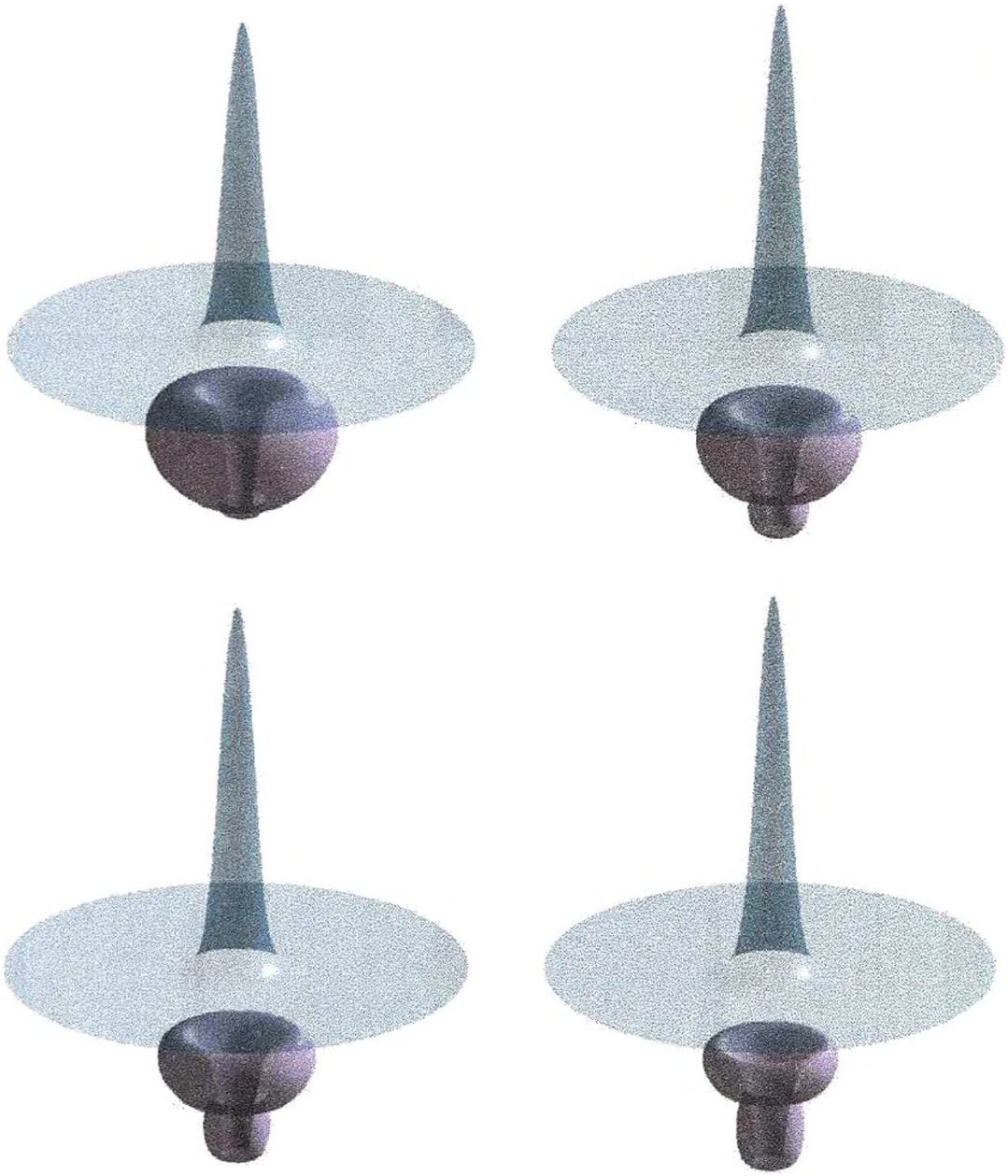

(b) Rendered transparent bubble and surface shapes showing the toroidal phase of motion up until the time of bubble splitting. The circular portion of the free surface shown is $2R_m$ in radius. Times are 1.1069, 1.1895, 1.2335 and 1.2798 respectively.

Figure 4.4 continued: Motion of a vapour bubble near an infinite free surface for $\gamma = -0.56$.

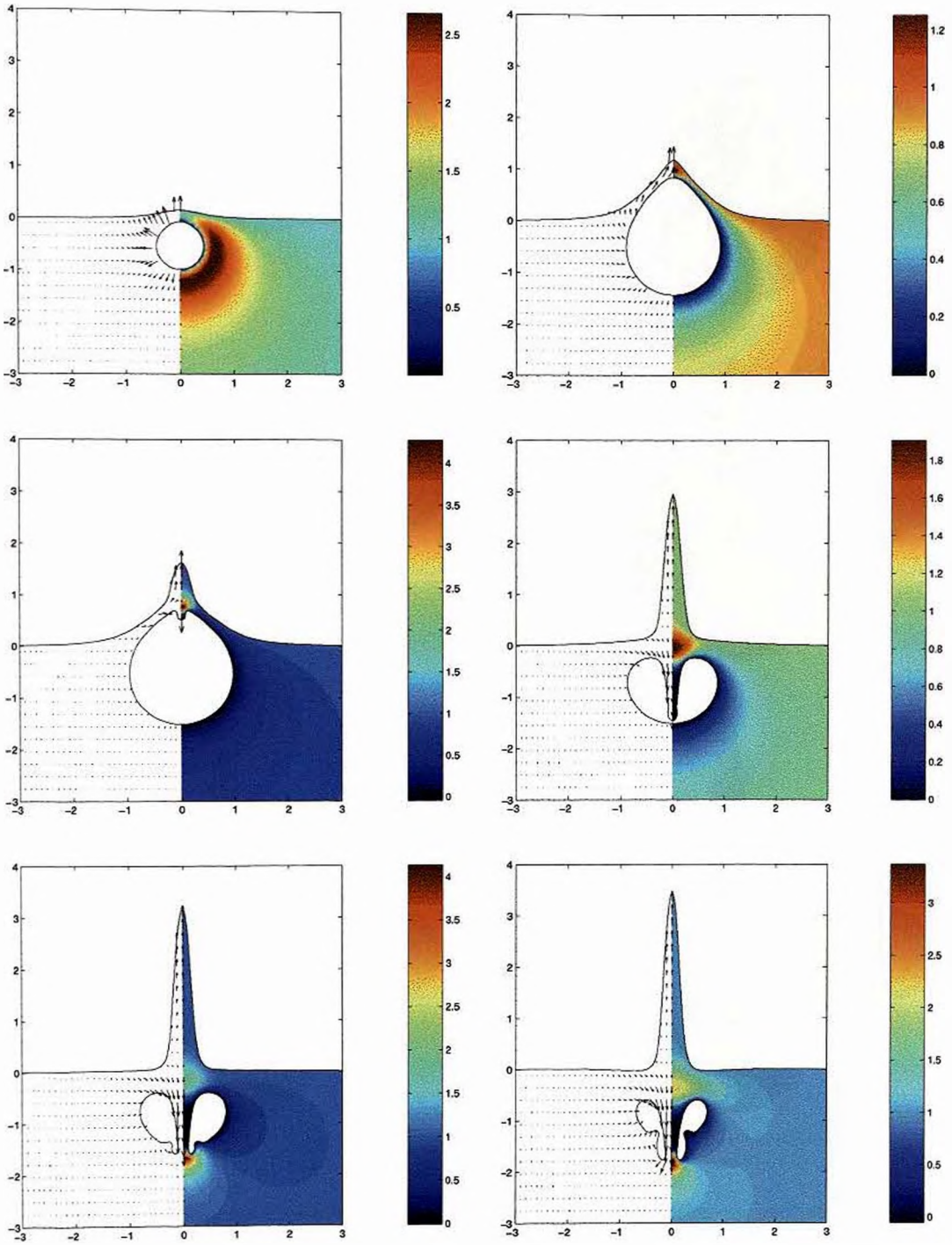

(c) Velocity vectors and pressure contours. Arrow sizes are scaled with respect to the maximum instantaneous velocity in each frame. The pressure scales are shown to the right of each figure. Times are 0.0506, 0.3940, 0.5523, 1.0306 1.1225 and 1.2247 respectively.

Figure 4.4 continued: Motion of a vapour bubble near an infinite free surface for $\gamma = -0.56$.

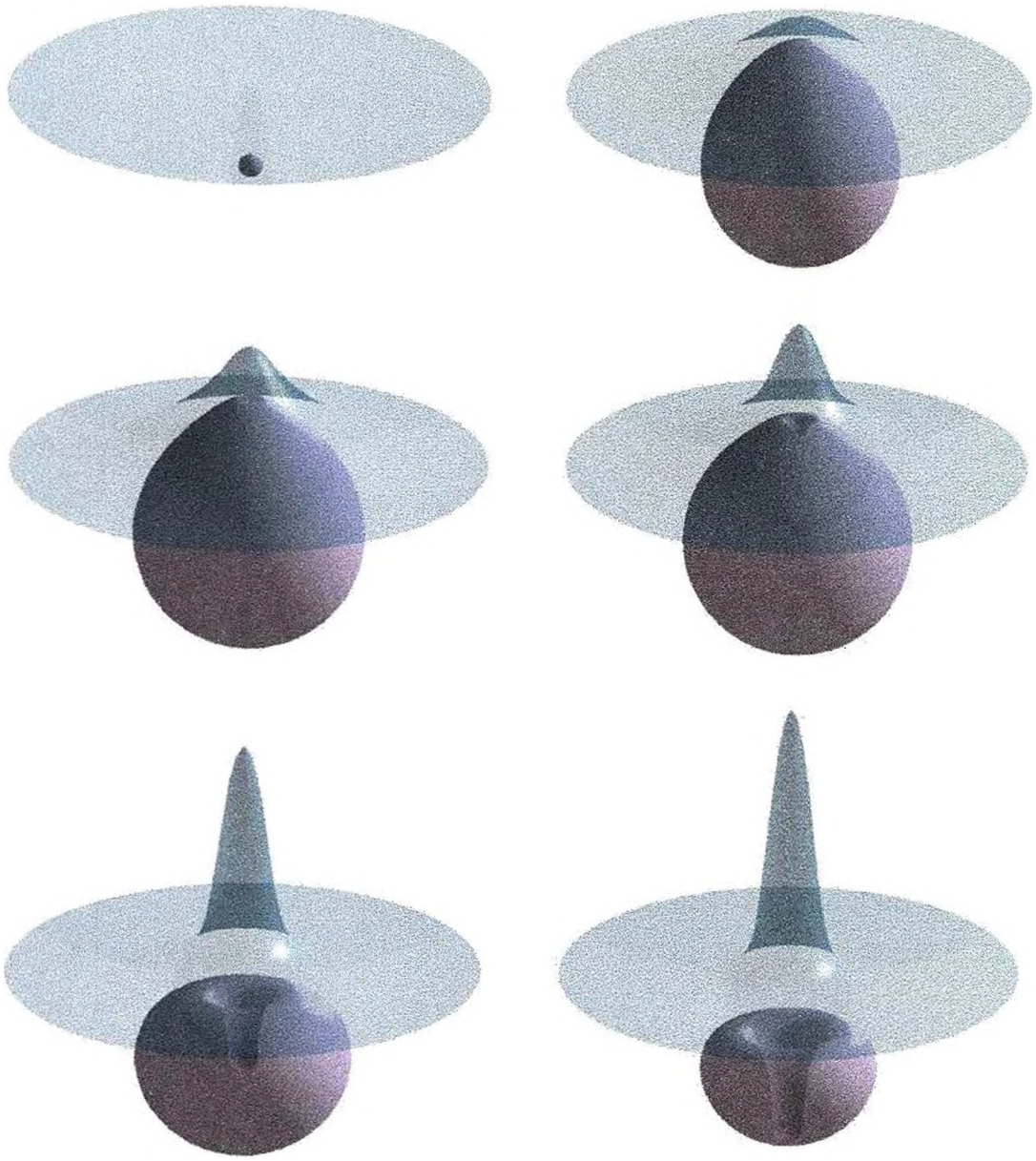

(a) Rendered transparent bubble and surface shapes showing the motion up until the time of jet impact. The circular portion of the free surface shown is $2R_m$ in radius. Times are 0.0015, 0.3296, 0.5205, 0.6464, 1.0219 and 1.2005 respectively.

Figure 4.5: Motion of a vapour bubble near an infinite free surface for $\gamma = -0.65$.

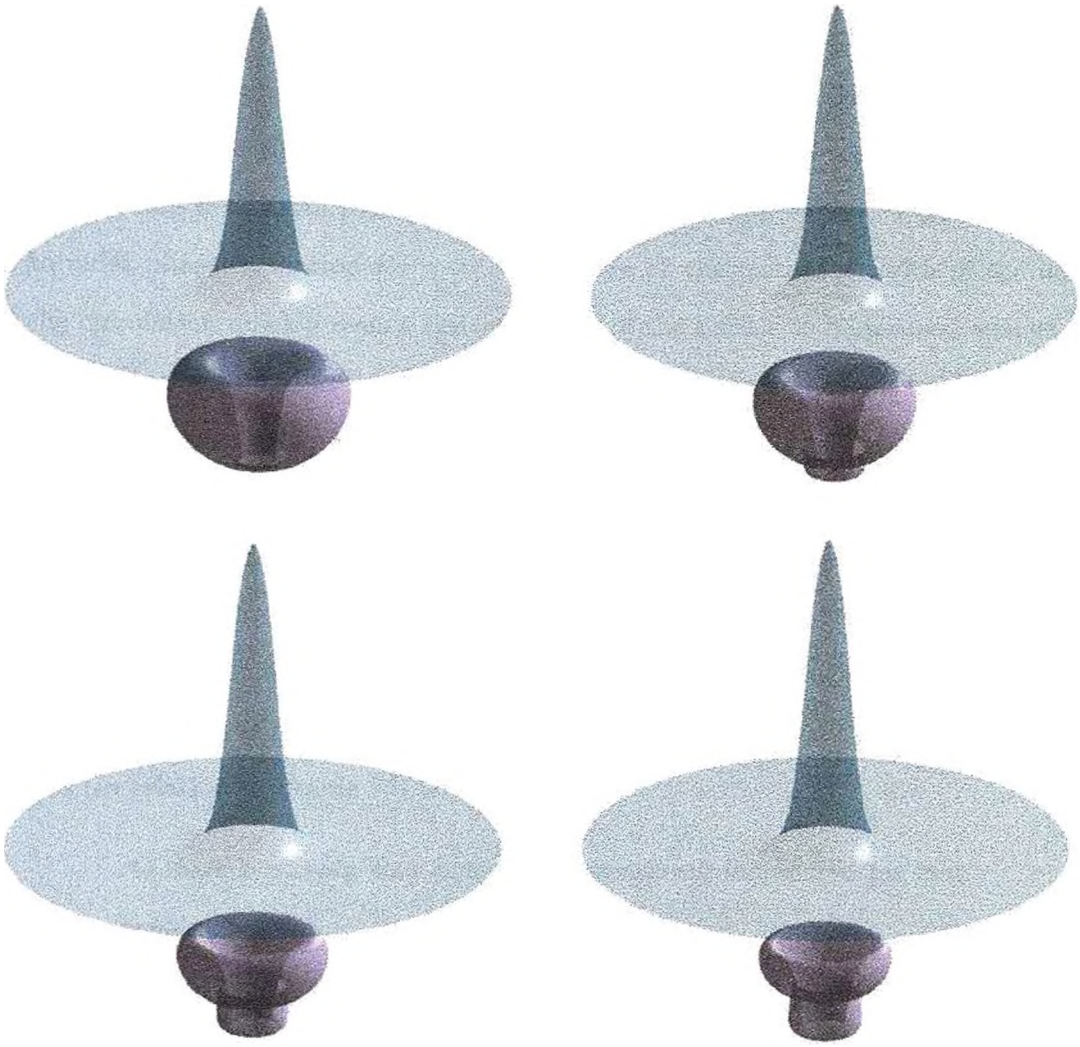

(b) Rendered transparent bubble and surface shapes showing the toroidal phase of motion up until the time of bubble splitting. The circular portion of the free surface shown is $2R_m$ in radius. Times are 1.2350, 1.2763, 1.3189 and 1.3459 respectively.

Figure 4.5 continued: Motion of a vapour bubble near an infinite free surface for $\gamma = -0.65$.

liquid jet and free surface spike for $\gamma = -0.45$ as commented upon earlier. As the point of initiation is moved further from the boundary, both the liquid jet and free surface spike increase in width; the free surface spike is also reduced in height. At $\gamma = -0.9$, we observe that jet impact occurs over a relatively wide area due to the very 'square' nature of the liquid jet. For $\gamma = -1.0$, jet impact does not occur on the axis of symmetry, instead occurring on a ring around the bubble. As γ is further decreased, this ring of impact occurs higher up the outer wall of the bubble. Physically we note this may lead to the shedding of a small toroidal ring from the top of the bubble. Figure 4.7 shows the toroidal phase of motion for $\gamma = -0.8$. Due to the increased width of the liquid jet, the circulation quickly causes the outer wall of the bubble to be pinched against the central column of fluid. Physically there is a question as to whether this bubble will split or motion continues with the surface sliding against each other. However since we have no physical model for the problem of bubble splitting, we are unable to determine the lengthscales on which this phenomenon will occur, and hence when to split the bubble. So the calculations are ceased. In regard to Figure 6 of Robinson, Blake, Kodama, Shima & Tomita (2001) which shows the motion of a laser-induced cavitation bubble, generated at a standoff distance of $\gamma = -0.94$ (reproduced here in Figure 4.8), it is noted by the authors (in relation to Frame 14) that:

> *"...there is a very thin liquid film connecting the two vortex ring bubbles."*

Although our model permits this phenomenon, we note that computational difficulties due to the close proximity of two material surfaces prevents the calculation of such motions.

Prior to discussion of some physical quantities associated with the motion of the bubble, we pause to consider the transition to the toroidal phase of motion in relation to the very broad jets observed in bubble motion near an infinite free surface. We recall from Chapter 3 that in order our model be irrotational, we require jet impact to occur at a point. Here this still proves to be the case, with nodes on the axis of symmetry meeting, or more accurately, falling within the required tolerance for transition prior to other nodes on the broadened face of the jet. However, following the transition to a

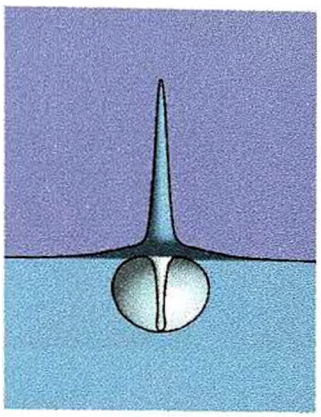

(a) $\gamma = -0.45$.

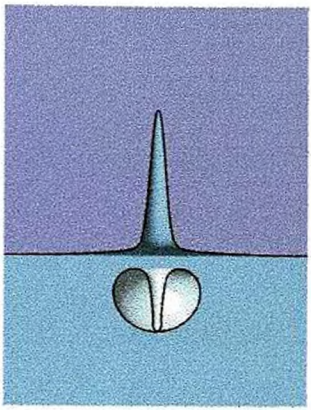

(b) $\gamma = -0.56$.

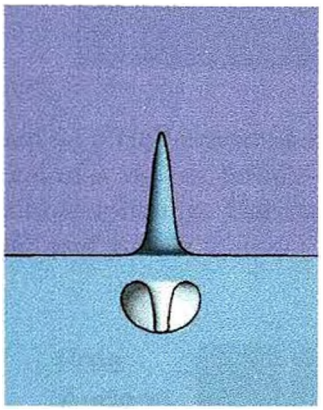

(c) $\gamma = -0.65$.

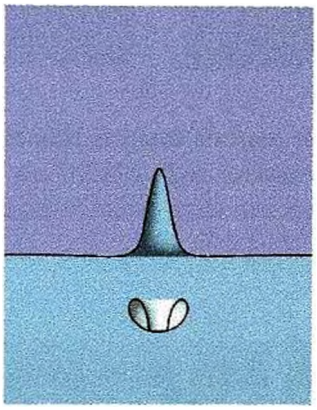

(d) $\gamma = -0.80$.

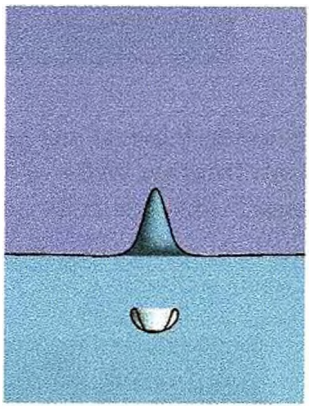

(e) $\gamma = -0.90$.

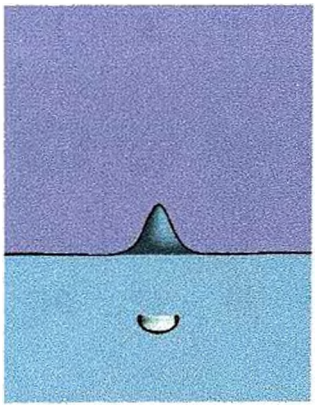

(f) $\gamma = -1.0$.

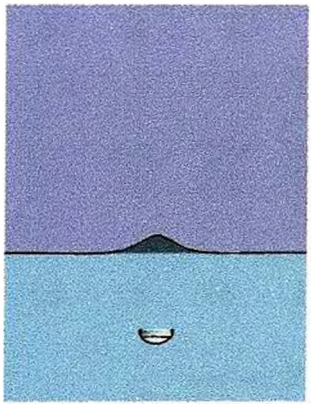

(g) $\gamma = -1.3$.

Figure 4.6: Half-rendered bubble and surface shapes showing the geometry of a vapour bubble near an infinite free surface for a range of standoff distances at the time of jet impact. Horizontal and vertical axes are $r \leqslant 3$, $-3 \leqslant z \leqslant 5$.

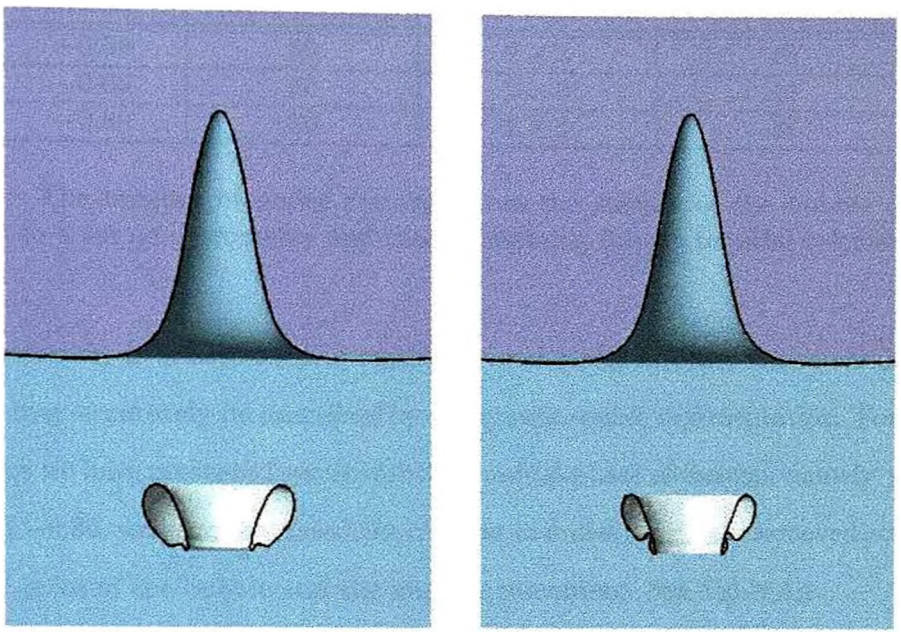

Figure 4.7: Half-rendered bubble and surface shapes showing the toroidal phase of the motion of a vapour bubble near an infinite free surface for $\gamma = -0.80$ up until the time of bubble splitting. Horizontal and vertical axes are $r \leqslant 1.5$, $-2 \leqslant z \leqslant 2.5$. Times are 1.4055 and 1.4230.

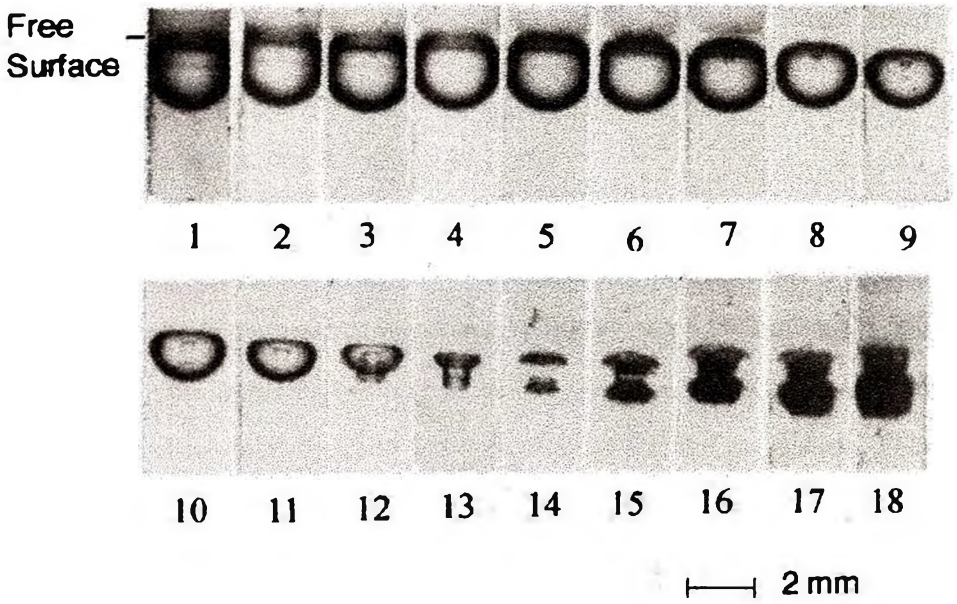

Figure 4.8: Experimental high-speed photographs showing the motion of a laser-induced cavitation bubble generated at a standoff distance of $\gamma = -0.94$. Frame interval is 10μs (100,000 frames per second) and exposure 2μs. Reproduced with permission from Robinson, Blake, Kodama, Shima and Tomita (2001).

Standoff, γ.	Nodes initially.	Nodes removed.	Nodes remaining.
-0.56	50	2×2	46
-0.65	50	2×3	44
-0.80	50	2×6	38

Table 4.1: The number of nodes removed from the surface of the bubble during the transition to a toroidal geometry and those remaining for the toroidal calculations.

toroidal geometry it is necessary to remove several nodes in order the remaining surface geometry may accurately be described by a piecewise-cubic representation. For the three cases where we have presented results for the toroidal phase of motion, namely $\gamma = -0.56$, -0.65 and -0.80, we have tabulated the number of nodes which are removed at the upper and lower poles of the bubble and the number remaining. See Table 4.1.

Figure 4.9 shows the volume of the bubbles considered in Figure 4.6. For the three standoff distances where the toroidal motion was considered earlier, these volume curves include the toroidal phase of motion. In all other cases, the curves show the evolution of the volume up until the time of liquid jet impact. We note for bubbles formed very close to the boundary, the shape of the bubble at maximum volume is egg-like and hence far from spherical, thus reducing the volume achieved. As bubbles are initiated at greater distances from the boundary, the expansion phase becomes more spherical and so the maximum volume tends to the infinite fluid limit.

In Figure 4.10 we show the Kelvin impulse associated with the motion of the vapour bubbles considered in Figure 4.6. As with the motion of bubbles near a rigid boundary, we note the greatest magnitudes of the Kelvin impulse occur for bubbles formed closest to the free surface. We further note that as in Chapter 3, the sign of the Kelvin impulse is negative, though here the boundary is above the bubble and not below. This signifies bubble migration and jet formation are directed away from the boundary, as we expect from, for example, the Kelvin impulse studies of Blake & Cerone (1982). One marked difference between the trends presented here for the free surface and those in Chapter 3 for bubble motion near a rigid boundary may be observed for small standoff distances. Here the maximum Kelvin impulse is attained not during final collapse, but as the bubble becomes entrained in the raised free surface. The magnitude of the Kelvin impulse then

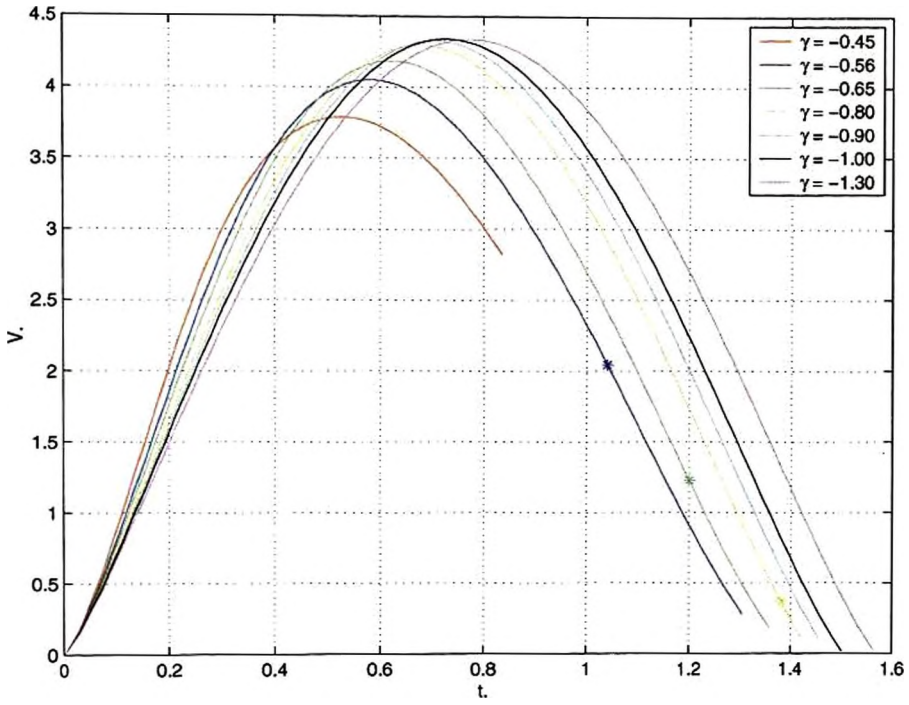

Figure 4.9: Evolution of the volume of a vapour bubble generated above a rigid boundary for a range of standoff distances. For the three standoff distances $\gamma = -0.56$, -0.65 and -0.80, the toroidal phase of motion is included and the time of jet impact denoted by a star. In all other cases, the curves show the volume up until the time of liquid jet impact.

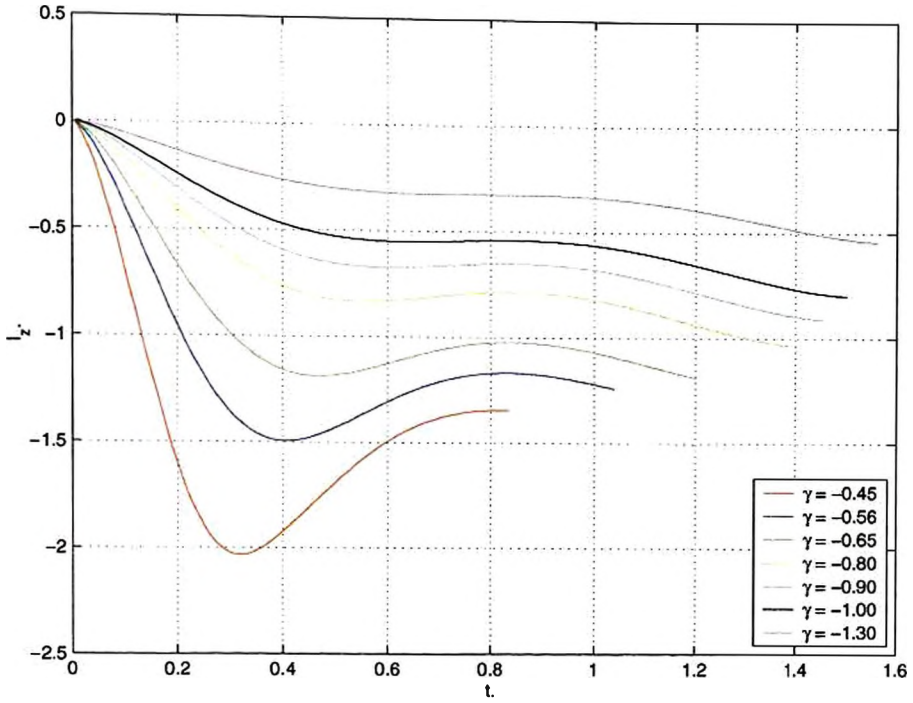

Figure 4.10: The Kelvin impulse associated with the motion of a vapour bubble generated below a free surface for a range of standoff distances up until the time of jet impact.

decreases as the free surface spike is initiated. We will further discuss the initiation and evolution of the free surface spike later.

Finally, Figure 4.11 shows the magnitude of circulations formed by liquid jet impact. We note the highest circulations are formed for bubbles generated closest to the boundary. Below $\gamma \approx -0.9$, jet impact no longer occurs on the axis of symmetry, but on a ring around the bubble, hence the circulation around the bubble is undefined in the normal sense, though were we to consider the shedding of a toroidal ring from the upper surface, a circulation may be set up around it.

Initiation and Evolution of the Free Surface Spike

Here we consider the initiation of the free surface spike in connection with the analytic studies of Longuet-Higgins (1983). In his paper, Longuet-Higgins models the tip of the raised free surface about the axis of symmetry as a Dirichlet hyperboloid. It was shown that if the angle between the generators falls below a critical angle of 109°, then a rapid acceleration of the free surface ensues and a pronounced free surface spike is generated.

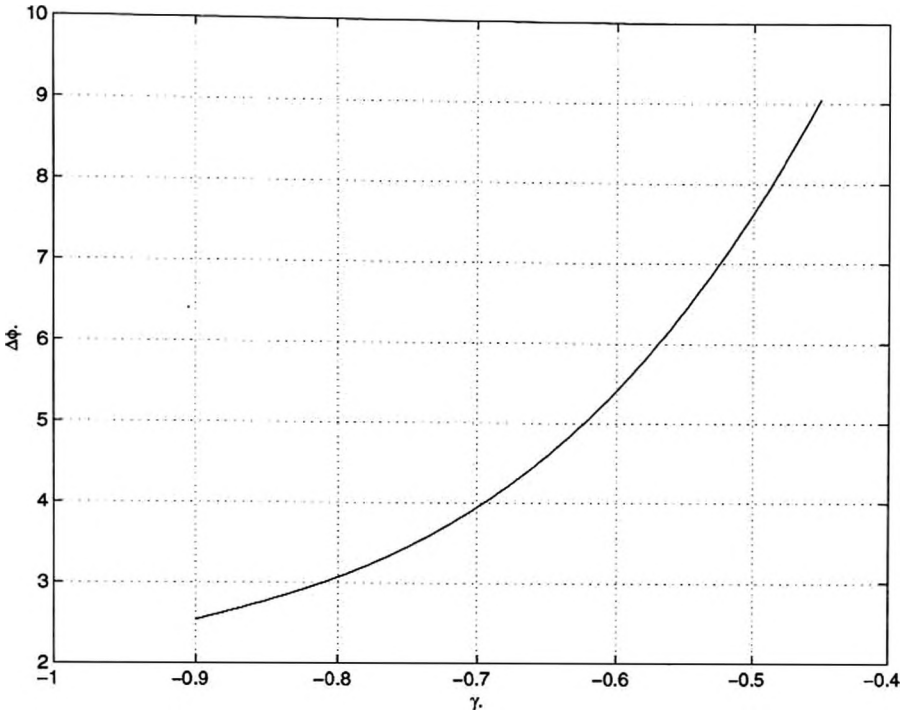

Figure 4.11: Circulations formed at jet impact over a range of standoff distances.

Following the initial formation of the spike, it is shown to grow in height at a constant rate, as observed in the experiments of Blake & Gibson (1981). In Figure 4.12, we present half-rendered bubble and surface shaped for the motion of a vapour bubble generated at a standoff distance of $\gamma = -0.56$ around the time of the initial spike formation. In this figure we have coloured the edge of the free surface white where the angle between the local tangents falls below the critical angle of 109°, as stipulated by Longuet-Higgins. In Frame 1, we see that no portion of the free surface does so. As the bubble continues to expand and the free surface is further displaced, a small portion of the surface attains sufficient slope (Frame 2). Frames 3 and 4 show this region expand to encompass the tip of the raised free surface. Finally in Frames 5 and 6, the free surface spike may clearly be seen to grow. In order to show the spike grows with constant velocity, we have plotted the evolution of the height of the free surface spike for the vapour bubbles considered above in Figure 4.13. Here we note the curves for $\gamma = -0.56$, -0.65 and -0.80 also show the continued growth of the spike through the toroidal phase of motion up until such time as we may expect the toroidal bubble to split; a star denotes the time of liquid

jet impact within the bubble. For other values of γ the toroidal phase of motion is not considered. In this figure, the dashed lines are straight lines fitted to data during the collapse phase of the bubble, so as to emphasise the the constant rates of growth. We note the open circles on the curve for $\gamma = -0.56$ show the timing of the frames presented in Figure 4.12, with the curve straightening significantly around Frames 3 – 4. Finally we note the rise and fall of the free surface for the case $\gamma = -1.3$, where the asymptotes to the tip of the free surface do not fall below the critical angle, despite the very noticeable displacement.

4.3.2 Two Vapour Bubbles near an Infinite Free Surface

In this section, we consider the motion of two vapour bubbles formed in a vertical column beneath an infinite free surface. The problem posed by the interaction of two cavitation bubbles with a rigid boundary was considered both experimentally and theoretically by Blake, Robinson, Shima & Tomita (1993). High-speed photography was used to record the motion of two laser-generated bubbles in close proximity to the boundary and compared against the motion of two vapour bubbles calculated using the boundary integral method. In a follow-up paper, Robinson, Blake, Kodama, Shima & Tomita (2001) considered the motion of both a single bubble and a pair of similar sized bubbles near an infinite free surface, wherein experimental images were again compared against boundary integral calculations. We note several figures in this paper detailing the pressure and velocity fields within the flow field were recalculated prior to publication using the improved numerical techniques described in this work. Further experiments concerning two bubbles of significantly different maximum volumes, and hence periods of oscillation were presented in the paper by Tomita & Kodama (2001).

Robinson, Blake, Kodama, Shima & Tomita (2001) calculated the motion of the bubbles assuming they contained only liquid vapour as in the earlier work concerning bubble motion near a rigid boundary. We later show this is sufficiently accurate where the timescales of motion of the two bubbles are similar, but as the relative timescales begin to differ such as may be observed when bubbles of differing maximum volumes are considered, this is no longer true. In the following discussion, we note the upper bubble

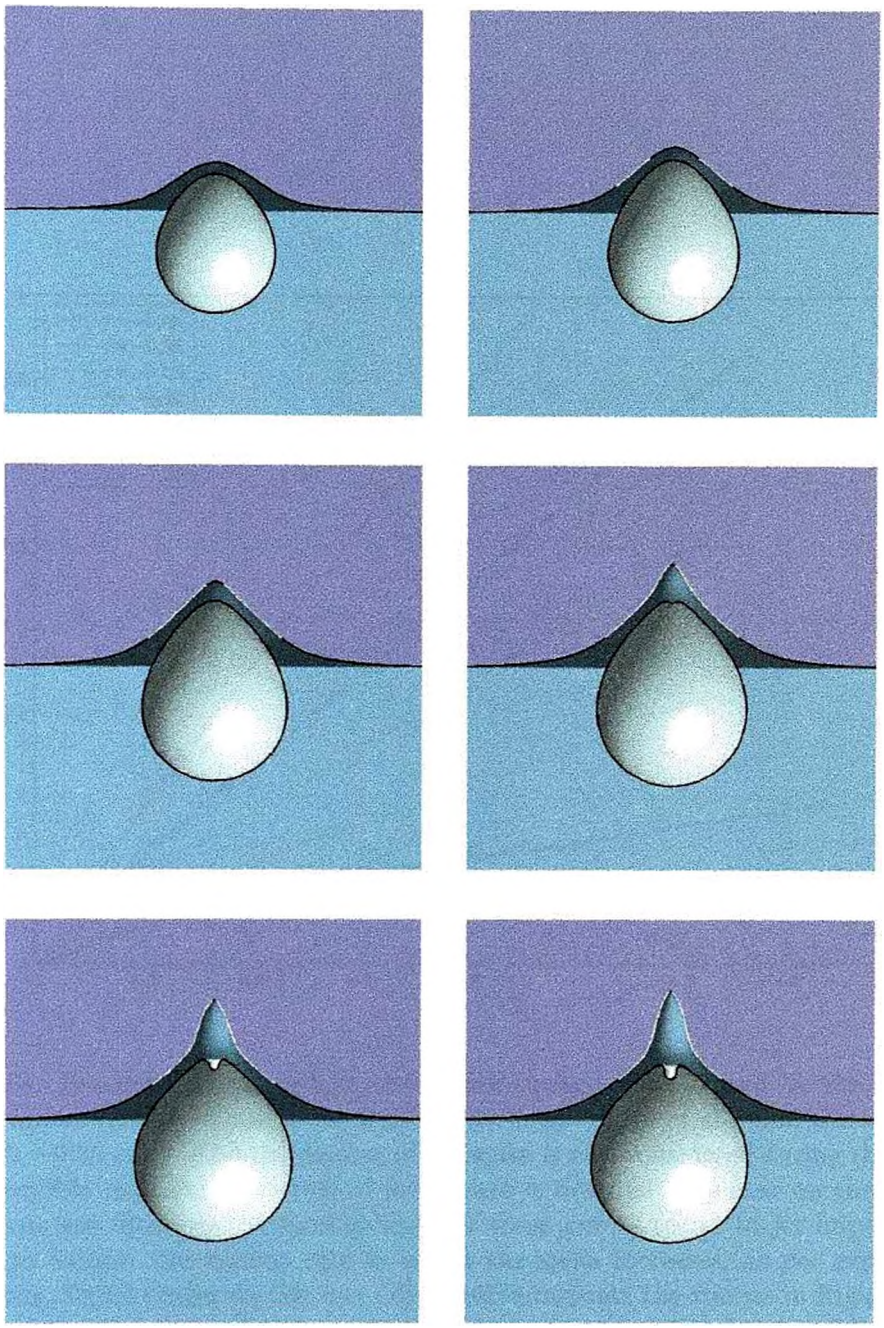

Figure 4.12: Half-rendered bubble and surface shapes showing the initiation of the free surface spike generated by vapour bubble motion near an infinite free surface for $\gamma = -0.56$. The white sections of the free surface denote the angle between the tangents there falls below the 109° stipulated by Longuet-Higgins (1983). Horizontal and vertical axes are $r \leqslant 2.5$, $-2.5 \leqslant z \leqslant 2.5$. Frames are 160 through 260, intervals are 20 frames. Times are 0.1879, 0.2651, 0.3515, 0.4353, 0.5109 and 0.5523 respectively.

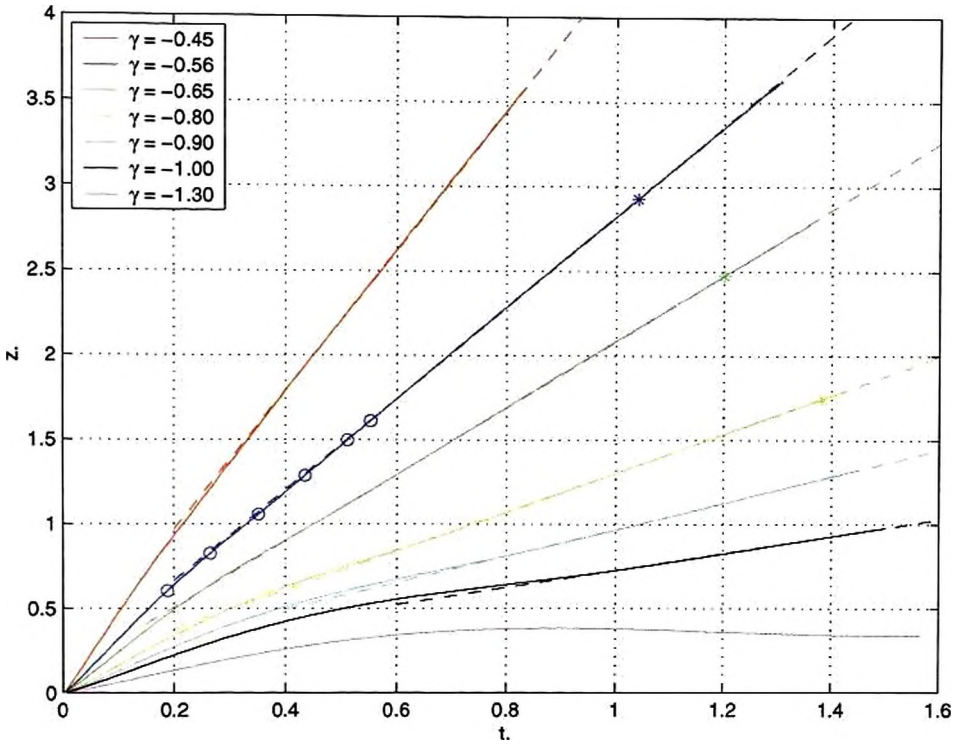

Figure 4.13: Evolution of the height of the free surface spike caused by the motion of a single vapour bubble beneath the free surface for a range of standoff distances. For $\gamma = -0.56$, -0.65 and -0.80 the motion of the spike is also considered during the toroidal phase of bubble motion. The time of jet impact is denoted by a star on these curves. Dashed lines are fitted to the final sections of these curves (prior to jet impact, where relevant) to exhibit the regular rate at which the spike increases, as per experimental observations. Open circles on the $\gamma = -0.56$ curve indicate the frames in Figure 4.12.

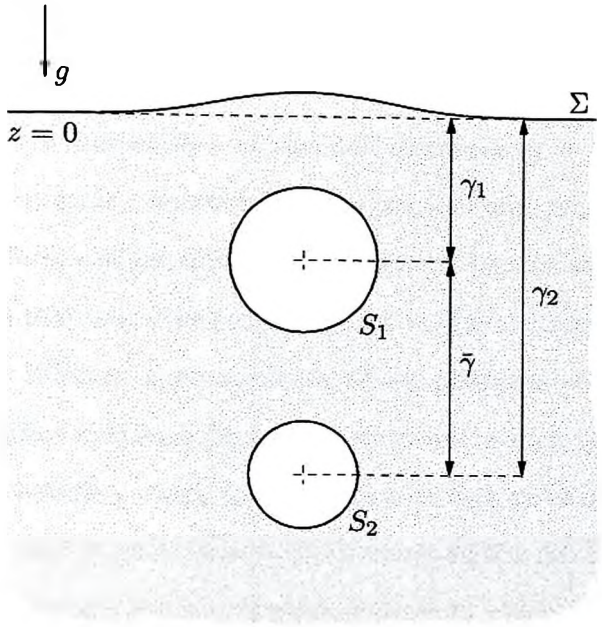

Figure 4.14: Schematic diagram showing two bubbles formed in a vertical column beneath an infinite free surface. The bubbles are generated at dimensionless standoff distances γ_1 and γ_2 from the free surface. The dimensionless distance between the two bubbles is denoted by $\bar{\gamma}$.

is denoted as Bubble 1 (having surface S_1) and the lower bubble as Bubble 2 (surface S_2). See Figure 4.14 for a schematic representation of the system. This convention differs from the works mentioned above, wherein the larger bubble is always numbered surface 1.

Finally we note the results presented herein are limited to the consideration of pre-toroidal vapour bubbles as in Robinson, Blake, Kodama, Shima & Tomita (2001) due to the complex response of the bubbles given a small change in the initial parameters. Our numerical code may, however, be applied to consider any, or all of: the adiabatic compression of gas within the bubble, buoyancy or the effects of the toroidal phase of motion upon the second bubble. As mentioned earlier, comparison with experiments may not be totally valid due to the omission of any gas content within the bubble, however this removes the need to determine the compression ratios, which is a difficult task with non-spherical bubbles. This is best done at the experimental stage when spherical bubbles may be produced concurrently with the adjusting of bubble sizes, by their creation in a sufficiently large volume of fluid. Regardless, an excellent qualitative agreement with

experiments where bubble sizes are similar is still obtained.

We begin by considering the motion of two initially identical bubbles ($R_1 = R_2 = 1.0$) formed beneath the free surface at standoff distances $\gamma_1 = -2.25$ and $\gamma_2 = -4.5$ ($\bar{\gamma} = 2.25$). In Figure 4.15a, we show velocity vectors and pressure contours at four stages covering the lifetime of the bubbles. The velocity vectors should not be compared between frames since they are scaled with respect to the maximum velocity within the fluid at that instant. Further, the magnitude of the pressures are given to the right of each figure. Shortly after initiation (Frame 1), we note the high fluid velocities imposed on the surface of the bubbles, which cause a region of high pressure around the bubbles as the moving bubble wall imparts motion on the surrounding fluid. Physically, at such a short time following initiation, such a region is one area in which shocks may be observed; though in our incompressible model, none may develop. As such it may also be the case that the predominant effects are those due to compressibility and so the model is no longer valid for these early times. In Frame 2, the bubbles are near maximum volume and have an almost spherical shape, though a slight flattening of the bubble wall closest to the partnering bubble may be observed. It is interesting to note the pressure contours at this stage, since they merge within a few maximum bubble radii and so in the far-field, fluid pressures belie the presence of two distinct bubbles. Indeed, given a sufficient depth below the free surface, the far-field pressure signature may almost be regarded as emanating from a point source. We observe the motion at some time later during the collapse phase in Frame 3. The lower bubble begins to collapse and migrate upwards due to the Bjerknes force of attraction of the upper bubble. (Neglecting for a moment the free surface, the upper bubble may be regarded as forming an image system for the motion of the lower bubble beneath a rigid boundary.) In the upper bubble, the initial stages of the formation of a liquid jet may be observed. This is caused by both the attraction of the bubble beneath it and repulsion of the free surface above. Thus a region of high pressure forms, which drives the motion. Finally in Frame 4, we present fluid pressures and velocities just prior to jet impact in the upper bubble. We note the increased magnitude of the high-pressure region above the stack which drives the motion in the upper bubble. Meanwhile a second region of high pressure has formed

beneath the bubble stack where we note the flattening and initial jet formation in the lower bubble. Of key importance is the shape of the liquid jet observed in the upper bubble which is not so square as we would expect for a bubble formed at such a large standoff from the free surface, indicating the significant influence of the bubble beneath it. Figure 4.15b shows the centroid motion of the two bubbles. During expansion there is a slight outward displacement in the centroids, indicative of the interaction between the bubbles. During collapse, we note the centroids migrate towards each other due to Bjerknes forces of attraction. The upper bubble is displaced more due to the repulsion of the free surface, the lesser effects of which also retard the motion of the lower bubble. Finally in Figure 4.15c, we show the Kelvin impulse calculated for the two bubbles. We note the magnitude of the impulse for the upper bubble is almost double that of the lower bubble due to the combined influence of the lower bubble and free surface, whereas in the lower bubble the forces counteract. Throughout the motion, we note there is little free surface displacement, due to the relatively large standoff distances.

As noted earlier in this chapter, several sets of pressure fields were calculated for inclusion in the paper by Robinson, Blake, Kodama, Shima & Tomita (2001). Due to the often succinct nature of academic papers, pressure contours were not provided for all the experimental cases considered, and so are included here alongside the experimental photographs which were kindly supplied by Prof. Tomita. Further, velocity vectors are also presented for all cases, providing the reader with additional information at each chosen instant.

Figure 4.16 shows the motion of two initially almost identical vapour bubbles near an infinite free surface, having dimensionless maximum radii of $R_1 = 1.0$ and $R_2 = 0.99$ respectively. Where this differs from the case considered above in Figure 4.15 is in the standoff distances at which the bubbles are generated, namely $\gamma_1 = -1.37$ and $\gamma_2 = -3.24$ ($\bar{\gamma} = 1.87$). So the bubbles are generated closer together, with the upper bubble almost one maximum bubble radius closer to the free surface. Hence we expect a much stronger bubble interaction and more importantly, between the free surface and bubbles. Figure 4.16a shows rendered transparent bubble and surface shapes for the motion. Key features to note are the increased displacement of the free surface and

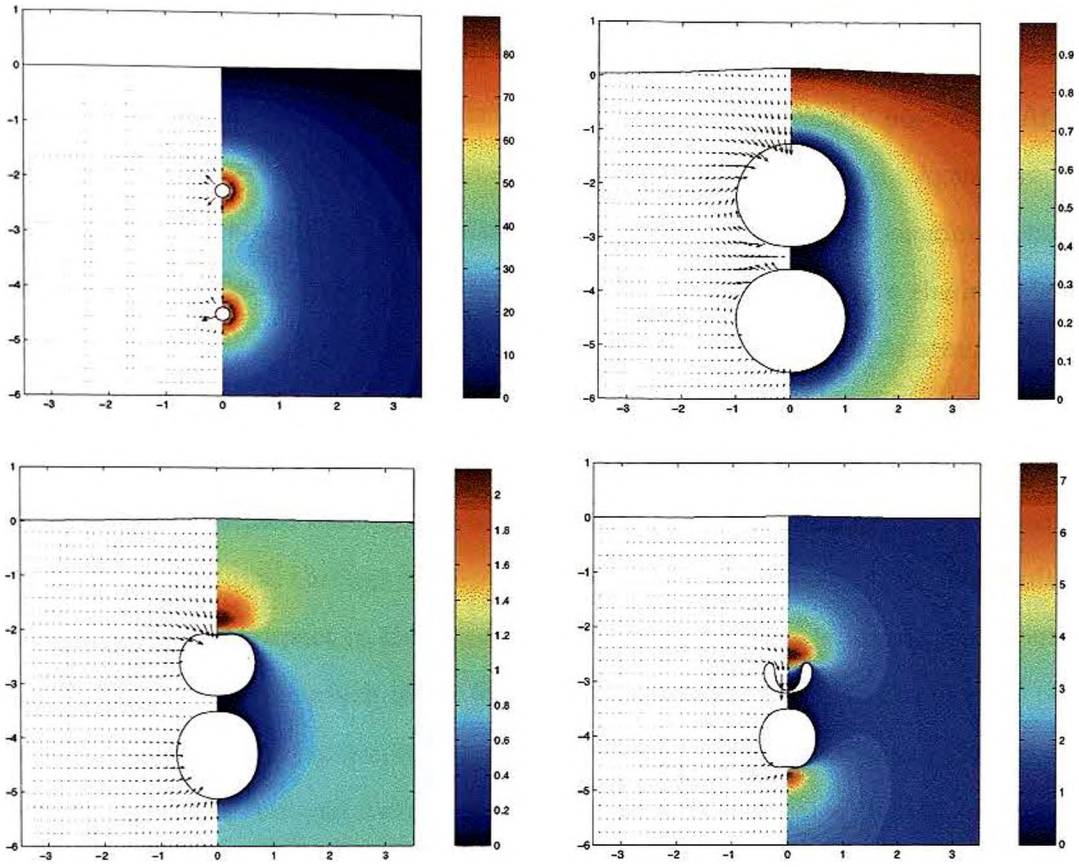

(a) Velocity vectors and pressure contours. Times are 0.0024, 0.9564, 1.6604 and 1.8554 respectively.

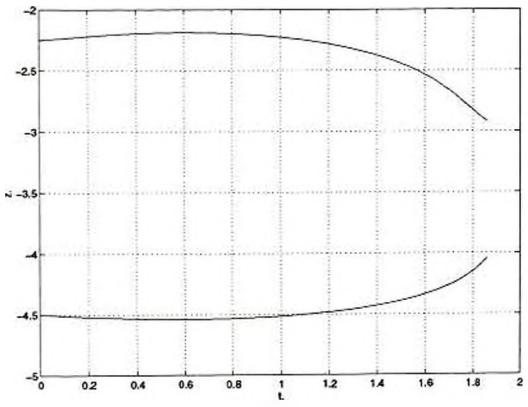

(b) Centroid motions.

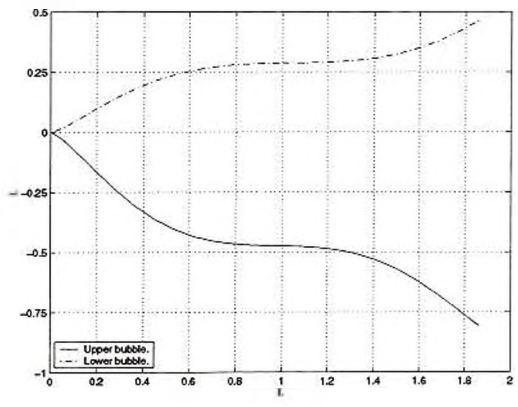

(c) Kelvin impulses.

Figure 4.15: Motion of two vapour bubbles near an infinite free surface for $\gamma_1 = -2.25$, $\gamma_2 = -4.5$ and $R_1 = R_2 = 1.0$.

formation of a very square jet in the upper bubble, typical of motion close to a free surface. In Figure 4.16b, we show the pressure and velocity fields around the bubbles at two instants during the motion. In the first frame, the bubbles are near maximum volume, and the flattened faces of the bubbles may be more clearly observed. At this time, the fluid between the two bubbles is forced radially outward. Again, we note the pressure fields around the two bubbles merge, and within a few maximum bubble radii, the pressure fields appear as though they might be generated by a single elongated bubble. In Frame 2, we show the pressure and velocity within the fluid around the two bubbles just prior to jet impact in the upper bubble. Here we note the region of high pressure above the upper bubble which drives the liquid jet. Further, a second region of high pressure has formed beneath the lower bubble, which will ultimately strengthen and drive a column of liquid through the lower bubble. We add, however, that the circulation formed following jet impact in the upper bubble may also affect jet formation about the upper pole. At this time, much of the free surface has flattened due to the collapse of the bubble, though a raised portion remains above the region of high pressure. Figures 4.16c and 4.16d show the centroid motion and Kelvin impulse calculated for the two bubbles respectively. Due to the stronger interactions between the two bubbles and boundary, we note the greater centroid displacements during expansion and the larger magnitudes of the Kelvin impulse over the previous case. High-speed photographs showing the experiments of Robinson, Blake, Kodama, Shima & Tomita (2001) for this case are reproduced in Figure 4.16e, showing a good agreement with our calculations.

In Figure 4.17 we show calculations pertaining to two vapour bubbles generated at standoff distances $\gamma_1 = -1.41$ and $\gamma_2 = -3.5$ ($\bar{\gamma} = 2.09$). In this case, however the size of the lower bubble has been reduced somewhat so the two bubbles would reach maximum radii of $R_1 = 1.0$ and $R_2 = 0.86$ in an infinite fluid. Rendered transparent bubble and surface shapes are presented in Figure 4.17a from the initial formation of the bubbles (Frame 1) through maximum volume (around Frame 2) up until jet impact in the lower bubble (Frame 6). Figure 4.17b shows velocity vectors and pressure contours within the fluid as the bubbles collapse. We note the parameters for this example are taken from Figure 12 of Robinson, Blake, Kodama, Shima & Tomita (2001), wherein pressure

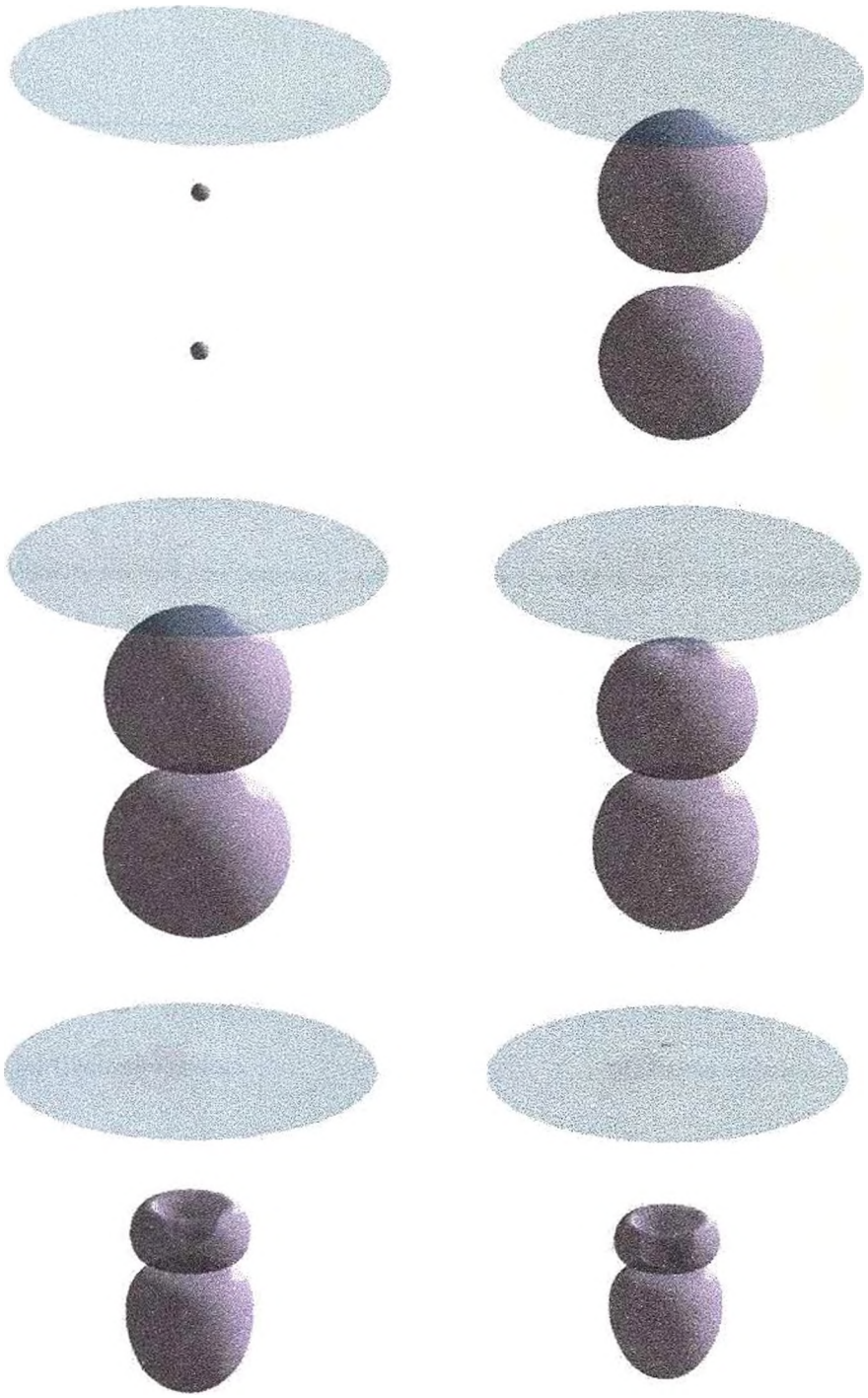

(a) Rendered transparent bubble and surface shapes. The circular portion of free surface shown is $2R_m$ in radius. Times are 0.0015, 0.4953, 1.0508, 1.3337, 1.6801 and 1.7576 respectively.

Figure 4.16: Motion of two vapour bubbles near an infinite free surface for $\gamma_1 = -1.37$, $\gamma_2 = -3.24$, $R_1 = 1.0$ and $R_2 = 0.99$. Parameters and experiments from Figure 11 of Robinson, Blake, Kodama, Shima & Tomita (2001).

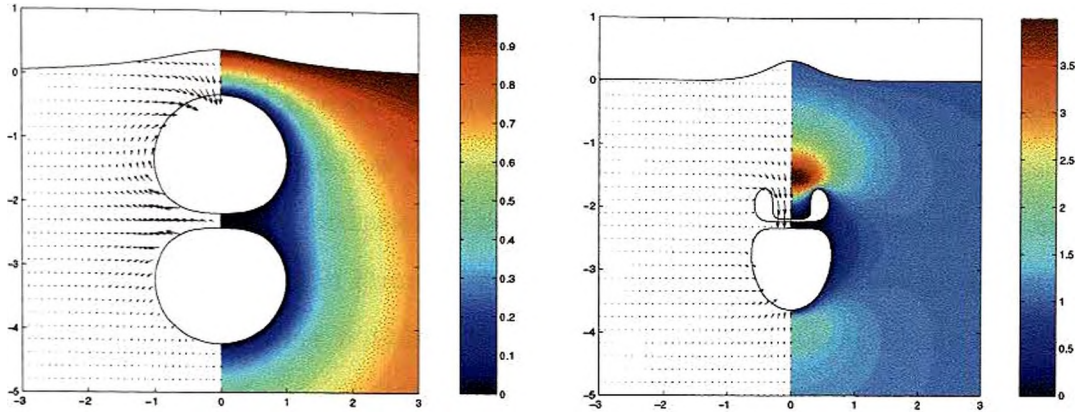

(b) Velocity vectors and pressure contours. Times are 0.8425 and 1.7367 respectively.

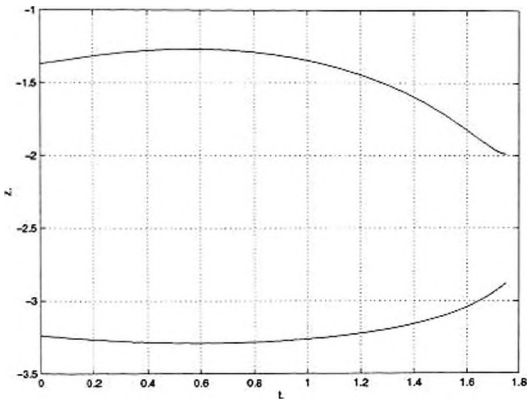

(c) Centroid motions.

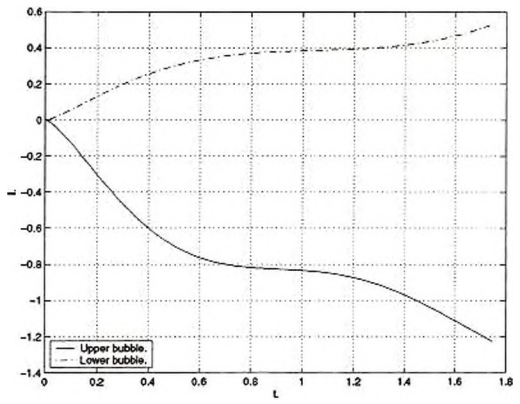

(d) Kelvin impulses.

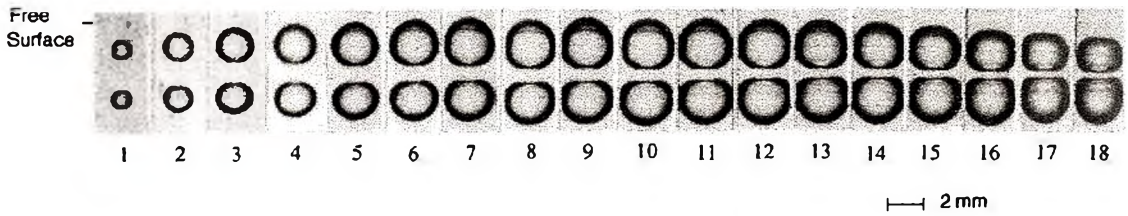

(e) Experimental high-speed photographs with frame interval $10\mu s$ (100,000 frames per second) and exposure $2\mu s$. Reproduced with permission.

Figure 4.16 continued: Motion of two vapour bubbles near an infinite free surface for $\gamma_1 = -1.37$, $\gamma_2 = -3.24$, $R_1 = 1.0$ and $R_2 = 0.99$. Parameters and experiments from Figure 11 of Robinson, Blake, Kodama, Shima & Tomita (2001).

contours were given for the motion. Here, however, we provide further information about the fluid flow through the addition of velocity vectors to the left-hand side of the figures. We note the familiar pressure distribution around the two bubbles near maximum volume in Frame 1. In Frame 2, a high pressure region may be seen to form between the upper bubble and free surface, with the initial formation of a liquid jet visible in the upper bubble. As the flow evolves, this high pressure region grows in magnitude, but we also witness the formation of a second high-pressure region beneath the bubble stack (Frame 3). Finally in Frame 4 we show the pressure and velocity fields just prior to jet impact in the lower bubble. Here we note the high pressure driving this jet has increased significantly in magnitude (over ten times the difference between atmospheric pressure and the vapour pressure of the liquid, our pressure scaling) to drive a much higher speed jet through this bubble, compared to that which continues to develop in the upper bubble. This is due in some part to the lifetime of the lower bubble being shorter than that of the upper bubble. As with previous cases, we present the centroid motion and calculated Kelvin impulse for the two bubbles in Figures 4.17c and 4.17d respectively, with the trends qualitatively as before. Experimental high-speed photographs for this case are reproduced from Robinson *et al.* (2001) in Figure 4.19a, though looking at Frame 18 of this figure, the liquid jet in the lower bubble is not visible. Indeed, from our calculations it is likely this shows the bubbles prior to the formation of the liquid jet in the lower bubble.

The final comparison with the experimental work of Robinson, Blake, Kodama, Shima & Tomita (2001) is considered in Figure 4.18. Here the effects of strong interaction between the upper bubble and free surface are shown to great effect. Again, lengths are scaled with respect to the equivalent maximum radius of the upper bubble (so $R_1 = 1.0$) generated at a standoff distance $\gamma_1 = -0.76$. Effects due to the lower bubble are decreased by generating a smaller ($R_2 = 0.82$) bubble at a greater standoff distance than in previous examples ($\gamma_2 = -3.26$, so $\bar{\gamma} = 2.5$). In Frame 1 of Figure 4.18a, motion is shown some time shortly after initiation. Herein the pressure around the lower bubble is constant on a vertical ring around the bubble, whilst for the upper bubble, the pressure distribution is similar to that observed for a single bubble close to a free surface (as in, for example,

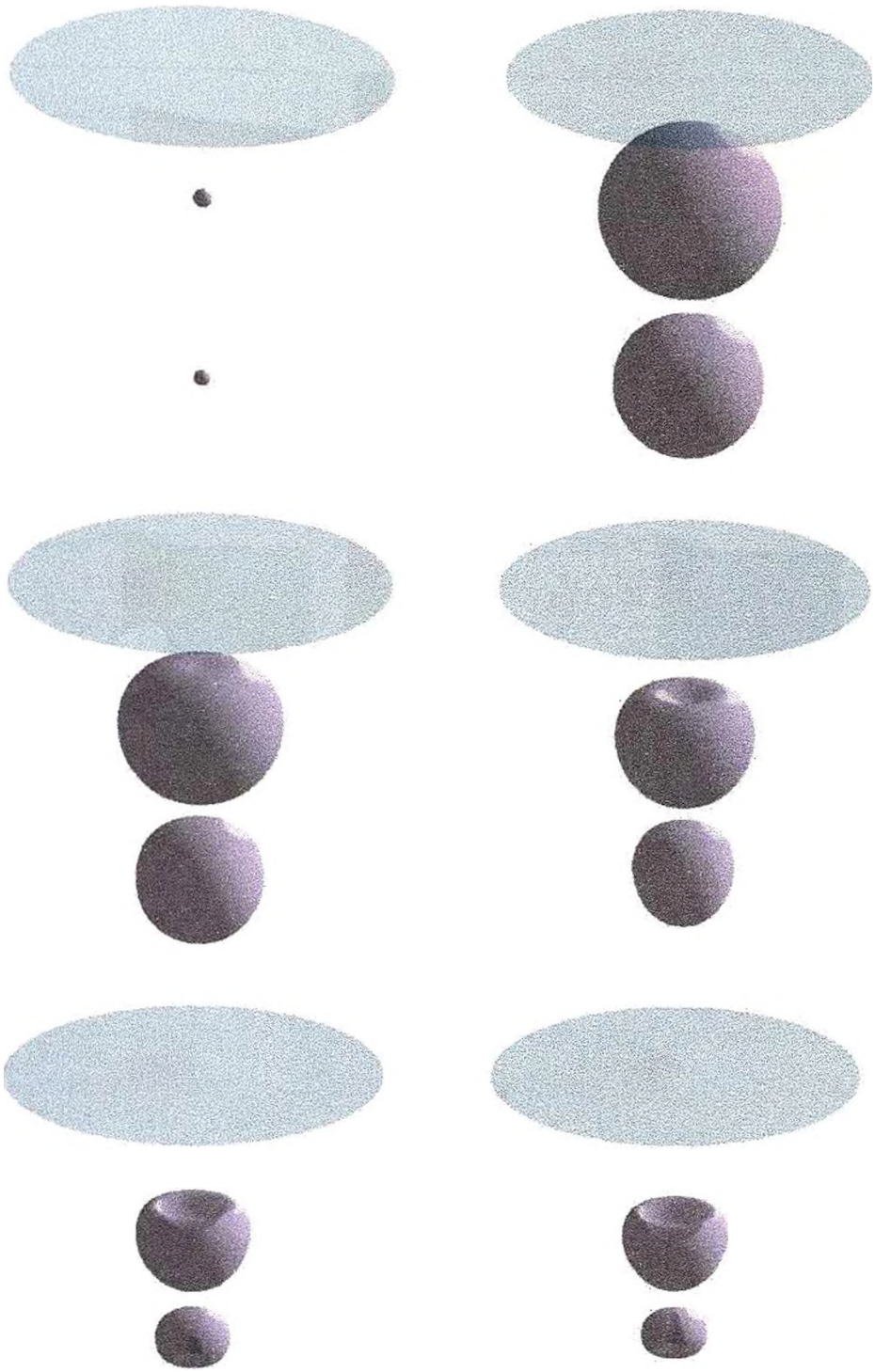

(a) Rendered transparent bubble and surface shapes. The circular portion of free surface shown is $2R_m$ in radius. Times are 0.0015, 1.0609, 1.3486, 1.4905, 1.6311 and 1.6581 respectively.

Figure 4.17: Motion of two vapour bubbles near an infinite free surface for $\gamma_1 = -1.41$, $\gamma_2 = -3.50$, $R_1 = 1.0$ and $R_2 = 0.86$. Parameters taken from Figure 12 of Robinson, Blake, Kodama, Shima & Tomita (2001).

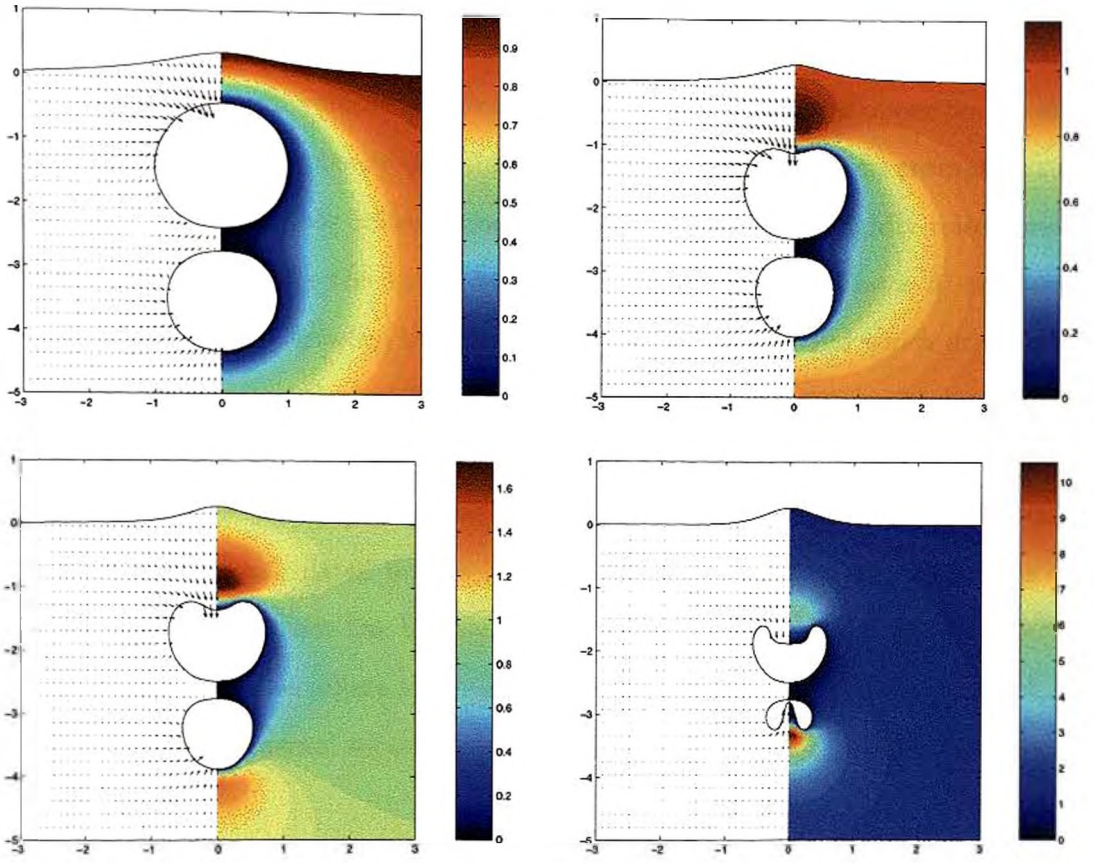

(b) Velocity vectors and pressure contours. Times are 0.9644, 1.4145, 1.5034 and 1.6553 respectivcly.

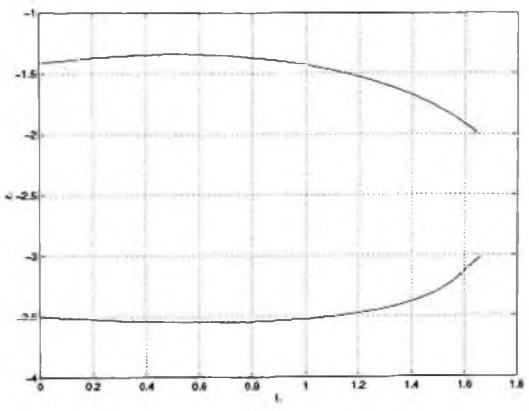

(c) Centroid motions.

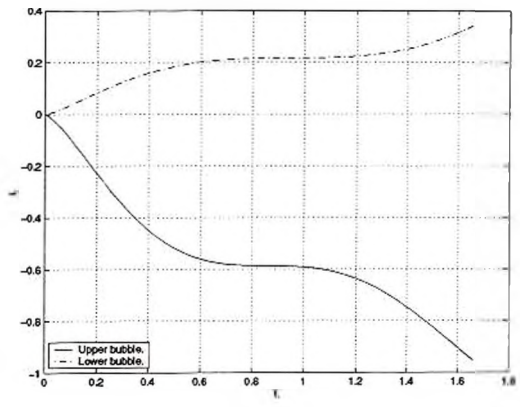

(d) Kelvin impulses.

Figure 4.17 continued: Motion of two vapour bubbles near an infinite free surface for $\gamma_1 = -1.41$, $\gamma_2 = -3.50$, $R_1 = 1.0$ and $R_2 = 0.86$. Parameters taken from Figure 12 of Robinson, Blake, Kodama, Shima & Tomita (2001).

Figure 4.4c) where higher pressures are formed beneath the bubble and lower pressures above when compared with those about the lower bubble. Thus the bubble expands upwards and becomes entrained in the raised free surface, leading to an egg-shaped bubble about maximum volume (see Frame 2). Despite the unusual upper bubble shape, the regular pressure field observed about maximum volume in previous cases still extends around much of the bubble column, though there is a region of slightly raised pressure between the bubbles. As the upper bubble begins to collapse (Frame 3) the familiar region of high pressure between bubble and free surface is observed which drives a high-speed liquid jet through the bubble. Due to the increased distance between the bubbles there is little effect on the lower bubble, though some elongation may be observed in Frame 4 at the time the liquid jet totally threads the upper bubble. The centroid motion and Kelvin impulse calculated for the lower bubble which may be seen in Figures 4.18b and 4.18c show a trend for the bubble to move slightly upward, though the effects are small compared to cases where the bubbles are much closer, as we would expect. The corresponding experimental motion, reproduced from Robinson *et al.* (2001), is depicted in Figure 4.19b.

As we have seen, the motion can be greatly affected by the initial displacement of the upper bubble from the free surface, the distance between bubbles and by the relative size of the two bubbles. We briefly investigate the third of these factors in Figure 4.20 where we consider two vapour bubbles generated at standoff distances of $\gamma_1 = -1.5$ and $\gamma_2 = -3.5$ beneath the infinite free surface. The following three cases are considered:

(a) Two bubbles with identical equivalent maximum bubble radii ($R_1 = R_2 = 1.0$).

(b) A smaller lower bubble ($R_1 = 1.0$, $R_2 = 0.8$).

(c) A smaller upper bubble ($R_1 = 0.8$, $R_2 = 1.0$).

In Figures 4.20a through 4.20c (each letter corresponding to the cases above) we present two frames of velocity vectors and pressure contours from our calculations, the first showing the bubbles around maximum volume and the second during the final moments of our calculations, just prior to liquid jet impact in one of the two bubbles. The motion for Case (a) is very similar to that considered in Figure 4.16 which is to be expected as

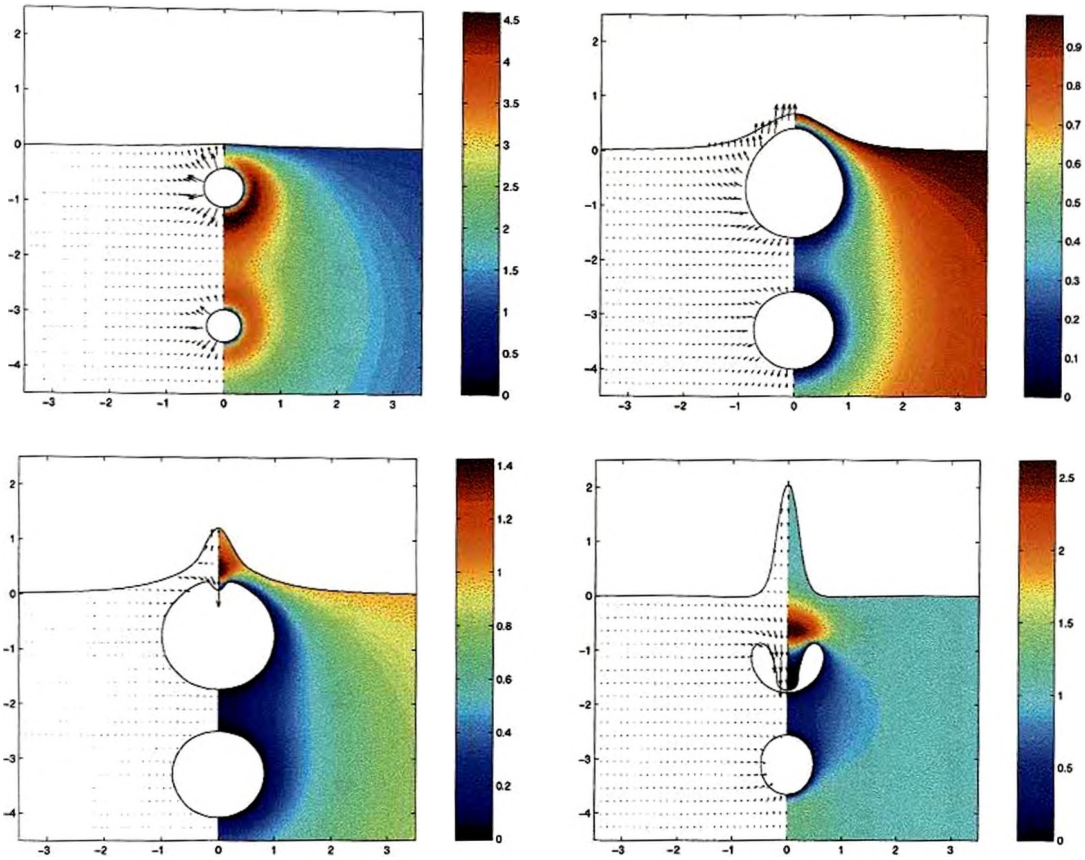

(a) Velocity vectors and pressure contours. Times are 0.0306, 0.3849, 0.7919 and 1.4125 respectively.

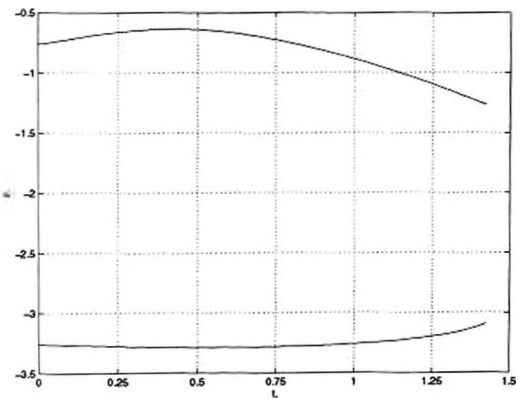

(b) Centroid motions.

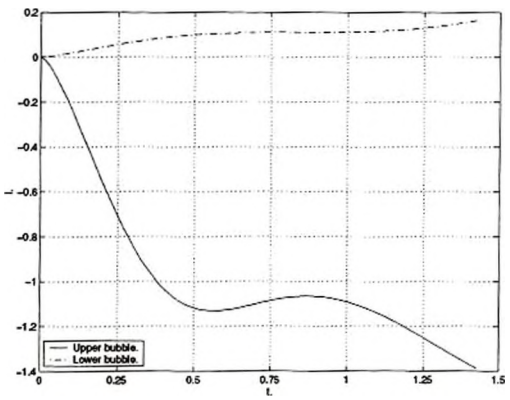

(c) Kelvin impulses.

Figure 4.18: Motion of two vapour bubbles near an infinite free surface with $\gamma_1 = -0.76$, $\gamma_2 = -3.26$, $R_1 = 1.0$ and $R_2 = 0.82$. Parameters taken from Figure 13 of Robinson, Blake, Kodama, Shima & Tomita (2001). Corresponding high-speed photographs may be seen in Figure 4.19b.

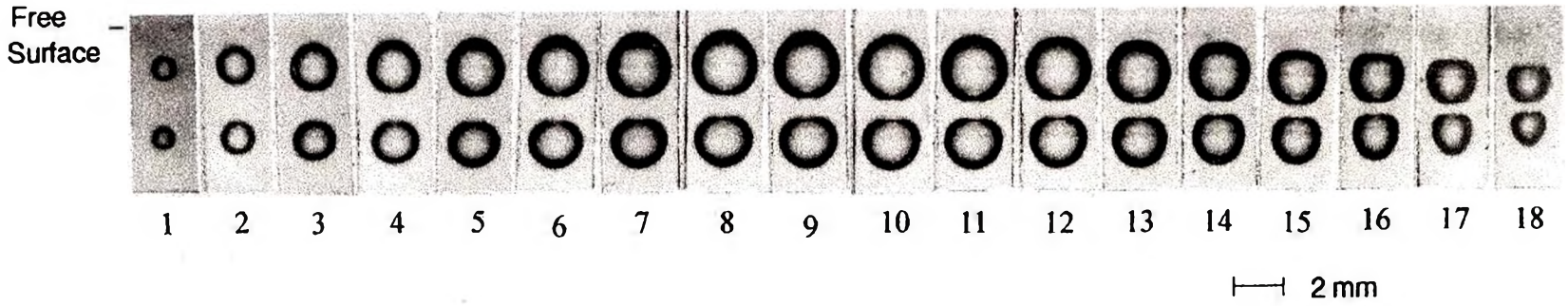

(a) $\gamma_1 = -1.41$, $\gamma_2 = -3.50$, $R_1 = 1.0$ (1.42mm) and $R_2 = 0.86$ (1.22mm).

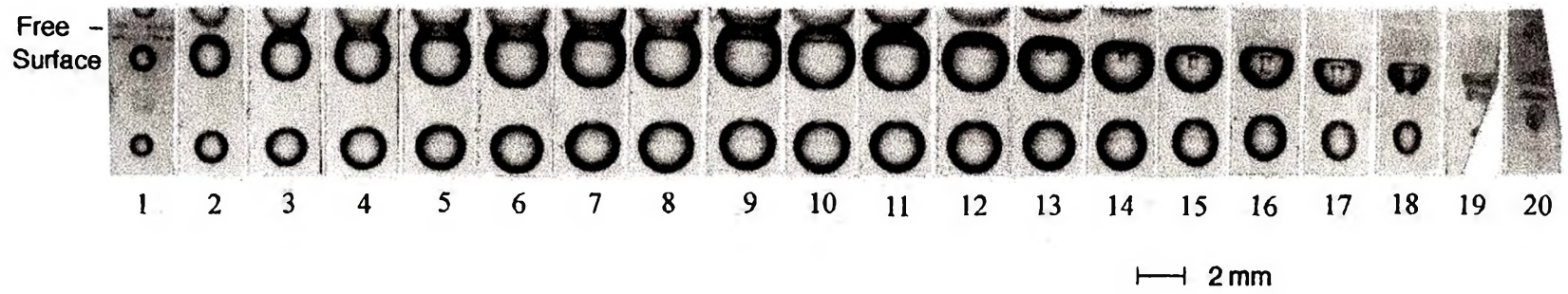

(b) $\gamma_1 = -0.76$, $\gamma_2 = -3.26$, $R_1 = 1.0$ (1.55mm) and $R_2 = 0.82$ (1.27mm).

Figure 4.19: High-speed photograph series of two bubbles generated beneath a free surface. Frame interval 10μs (100,000 frames per second), exposure 2μs. Reproduced with permission from Figures 12a and 13a respectively of Robinson, Blake, Kodama, Shima & Tomita (2001).

the parameters are very similar, with a wide square jet threading the upper bubble from above. In Case (b), where we consider a smaller lower bubble, the motion is like that observed in Figure 4.17 with the initial formation of a liquid jet in the upper bubble prior to a much higher speed jet driven by the region of high pressure below the bubble stack, which threads the smaller lower bubble from below. Here the jet in the upper bubble is not so developed due to the slightly greater distance between the upper bubble and boundary, so the force of repulsion from the surface is not so strong. Finally in Case (c), the problem of a smaller upper bubble is considered. Here the upper bubble collapses much more quickly than in the case of two initially equal bubbles due to the shorter lifetime of the bubble. The jet shape is also narrower and more rounded signifying the attraction of the lower bubble has a proportionally greater effect over a smaller bubble, since the square nature of the jets arises from free surface effects. Centroid motion for the three cases considered are plotted in Figure 4.20d. The key features which should be noted on this figure are the relative lifetimes of the three systems and the smaller centroid displacement of the larger bubbles when paired with a smaller bubble. Figure 4.20e shows the Kelvin impulse calculated for the two bubbles in the three cases considered. The largest impulses arise for two initially equal bubbles when forces of attraction between the bubbles will be greatest and the upper bubble is forced slightly closer to the free surface due to the expansion of a larger lower bubble. If the size of the lower bubble is decreased then the impulse due to attraction between the bubbles diminishes. Slightly lower repulsion effects from the free surface on the upper bubble are expected, since the lower bubble does not displace this quite so much towards the surface. Impulses are lessened further in the case of a smaller upper bubble. Attractive forces between the bubbles will be similar to the previous case, but surface repulsion effects are lowest, since the smaller upper bubble does not come so close to the surface.

For our final example in this section, we consider the case of two bubbles of highly disparate maximum volumes and hence periods of oscillation. Here, we choose to consider the motion of the two laser-generated bubbles from Figure 5a of Tomita & Kodama (2001), which are generated at standoff distances of $\gamma_1 = -0.75$ and $\gamma_2 = -2.93$ ($\tilde{\gamma} = 2.18$), with equivalent maximum radii of $R_1 = 1.0$ and $R_2 = 0.66$ respectively.

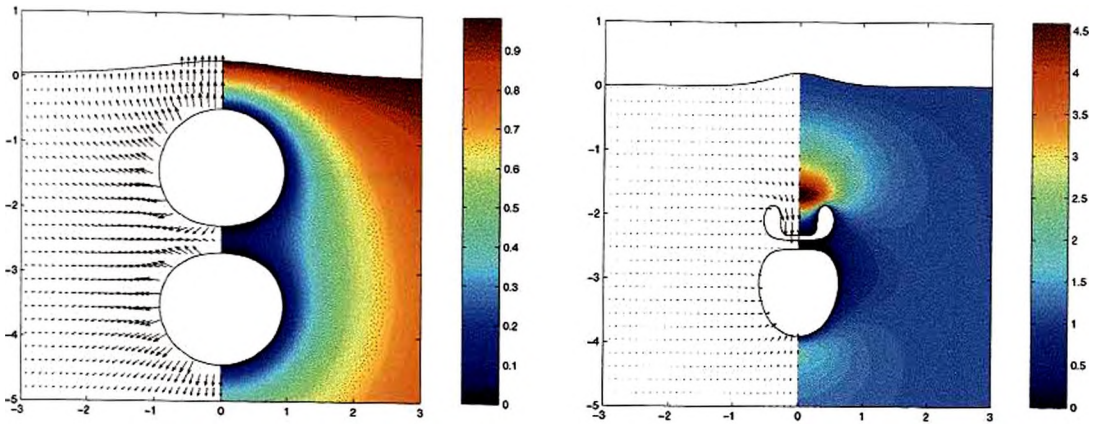

(a) Velocity vectors and pressure contours. $R_1 = 1.0$, $R_2 = 1.0$. Times are 0.5323 and 1.7588 respectively.

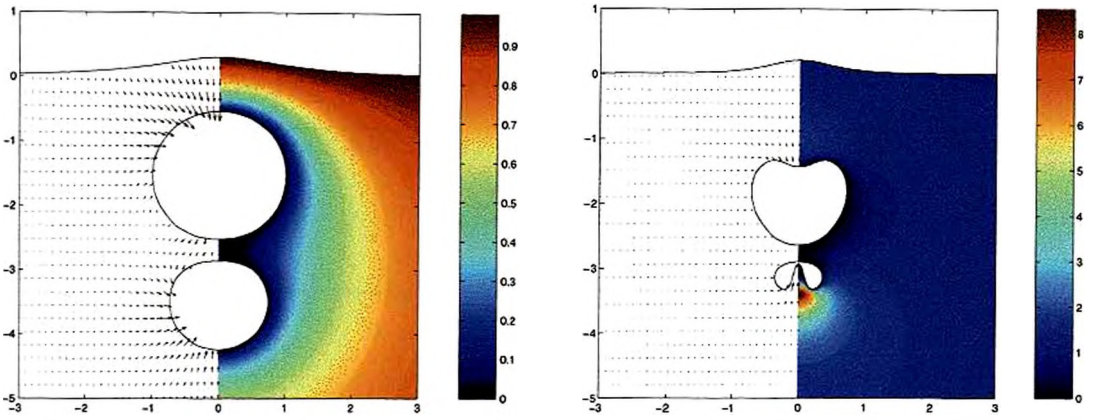

(b) Velocity vectors and pressure contours. $R_1 = 1.0$, $R_2 = 0.8$. Times are 0.9867 and 1.5316 respectively.

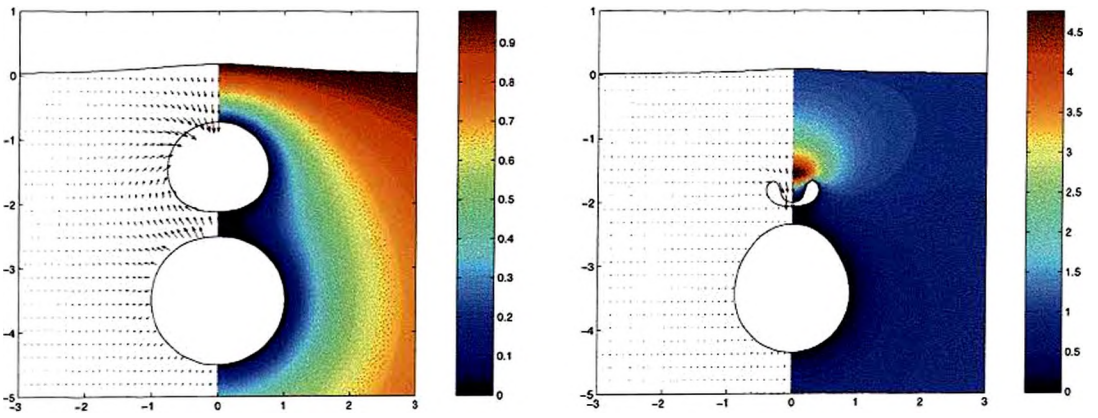

(c) Velocity vectors and pressure contours. $R_1 = 0.8$, $R_2 = 1.0$. Times are 0.8141 and 1.4008 respectively.

Figure 4.20: Comparison of the motion of two vapour bubbles near an infinite free surface for $\gamma_1 = -1.5$, $\gamma_2 = -3.5$ where the relative size of the bubbles is varied.

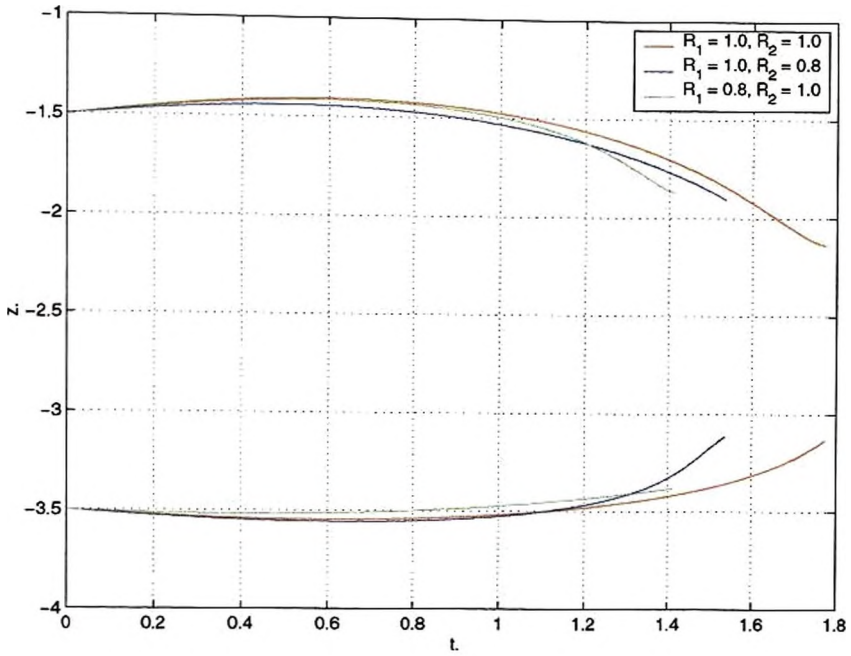

(d) Centroid motions.

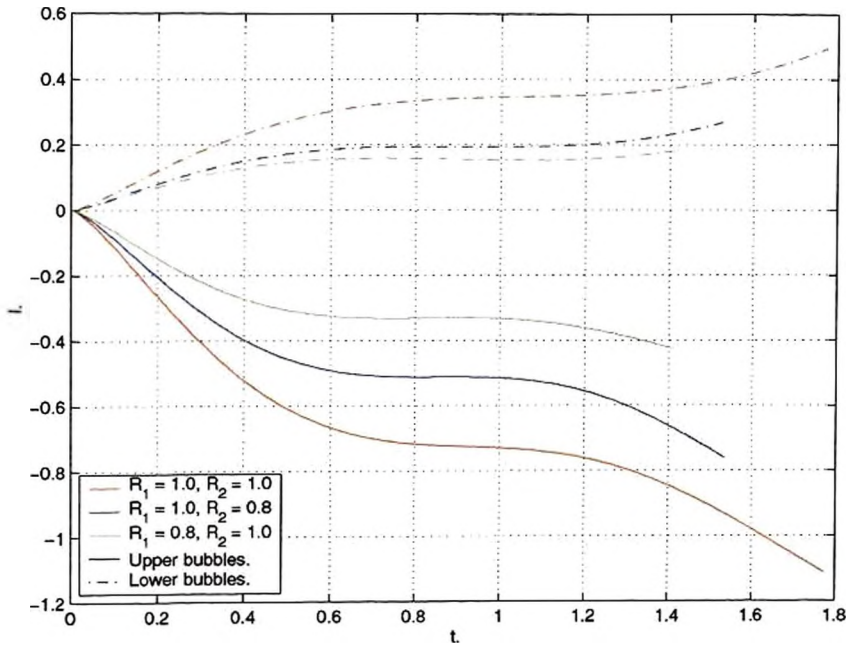

(e) Kelvin impulses.

Figure 4.20 continued: Comparison of the motion of two vapour bubbles near an infinite free surface with $\gamma_1 = -1.5$, $\gamma_2 = -3.5$ where the relative size of the bubbles is varied.

Figure 4.21 shows rendered transparent bubble and surface shapes for the motion of two vapour bubbles generated with these parameters. We again note the entrainment of the upper bubble in the raised free surface and liquid jet driven from above. However, as in Figure 4.17, we note the subsequent collapse of the lower bubble, wherein a high-speed jet threads the bubble. At the time of jet impact in the lower bubble, the much broader jet which may be observed in the upper bubble has only traversed about half the vertical height of the bubble. This is in stark contrast to experiments (see Figure 4.22), where this jet may clearly be seen to travel three-quarters of the way to the opposing face of the bubble. As noted at the start of this section, this may be attributed to the omission of any gaseous content in the bubbles, since during final collapse, effects due to adiabatic compression of the gas act to slow the speed of the liquid jet. We note the theoretical consideration of this and similar cases presented by Tomita & Kodama (2001) is earmarked for future study once suitable compression ratios are determined from the experimental data.

4.3.3 Vapour Bubble in a Shallow Fluid Layer

In this and the following section, we consider the motion of bubbles formed in a shallow layer of fluid. Although here we consider the motion of non-buoyant bubbles such as those created in cavitation experiments for ease of comparison with our rigid boundary results in Chapter 3 and those concerning bubble motion near an infinite free surface earlier in this chapter, the most likely applications for such a study are underwater explosions in finite depths of fluid. Such shallow depth explosions may occur due to the mining of inland waterways or harbours, or in attacks close to the coastline. In either case the presence of the seabed may have great bearing on the motion of the bubbles formed. For ease of comparison, we now proceed to discuss the motion of vapour bubbles formed in a shallow fluid layer bounded below by a rigid boundary and above by an infinite free surface. See Figure 4.23 for a schematic representation of the system. We note from this figure the dimensionless depth of the fluid is denoted by D and that we have defined two standoff distances: γ_{FS} from the free surface, and γ_{RB} from the rigid boundary; we will later use the most appropriate in order to facilitate discussion. Finally, we note the fluid

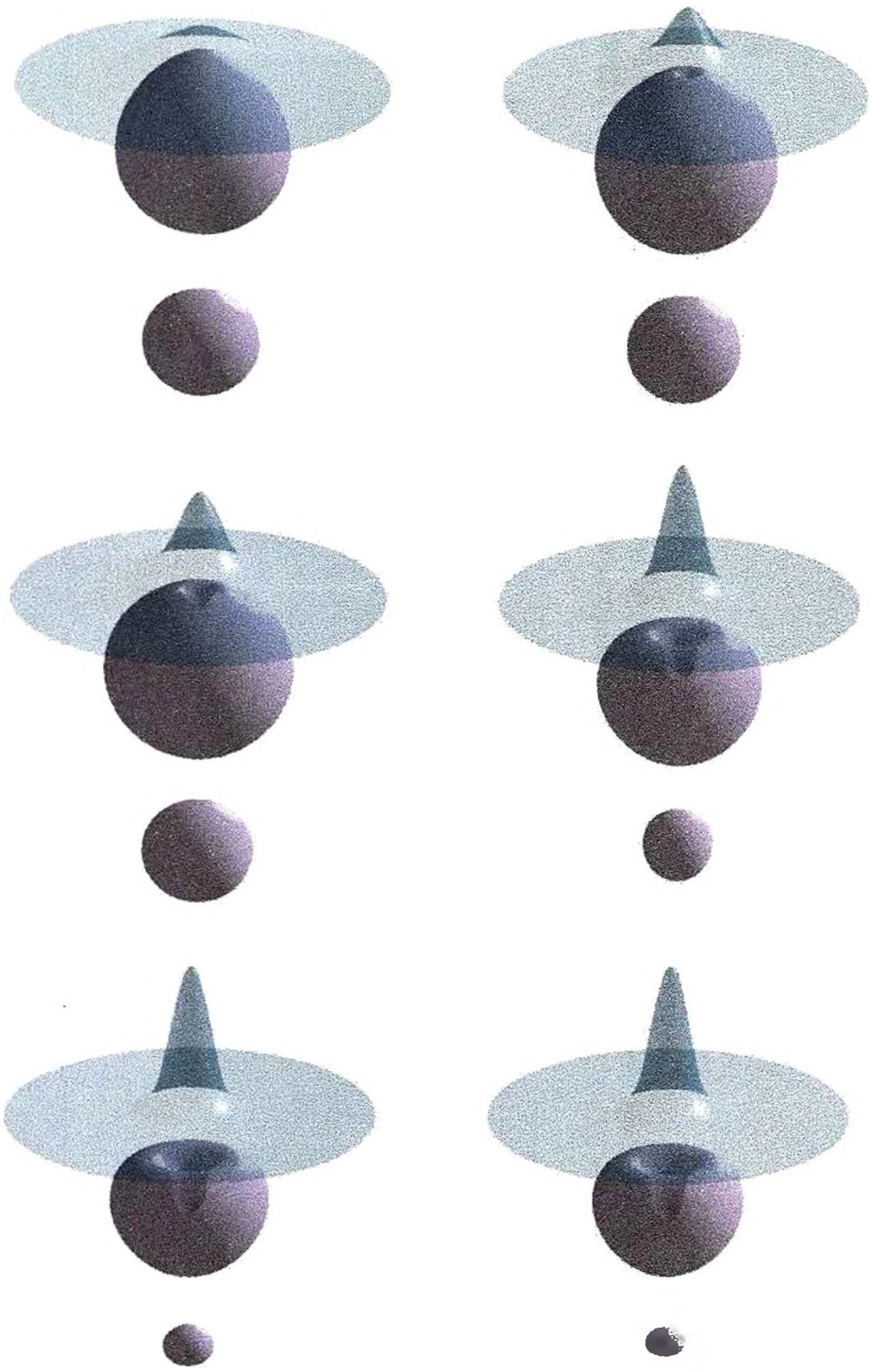

Figure 4.21: Rendered transparent bubble and surface shapes showing the motion of two vapour bubbles near an infinite free surface for $\gamma_1 = -0.75$, $\gamma_2 = -2.93$, $R_1 = 1.0$ and $R_2 = 0.66$. The circular portion of free surface shown is $2R_m$ in radius. Times are 0.4338, 0.7142, 0.8429, 1.1204, 1.2070 and 1.2289 respectively. Parameters taken from Figure 5a of Tomita & Kodama (2001).

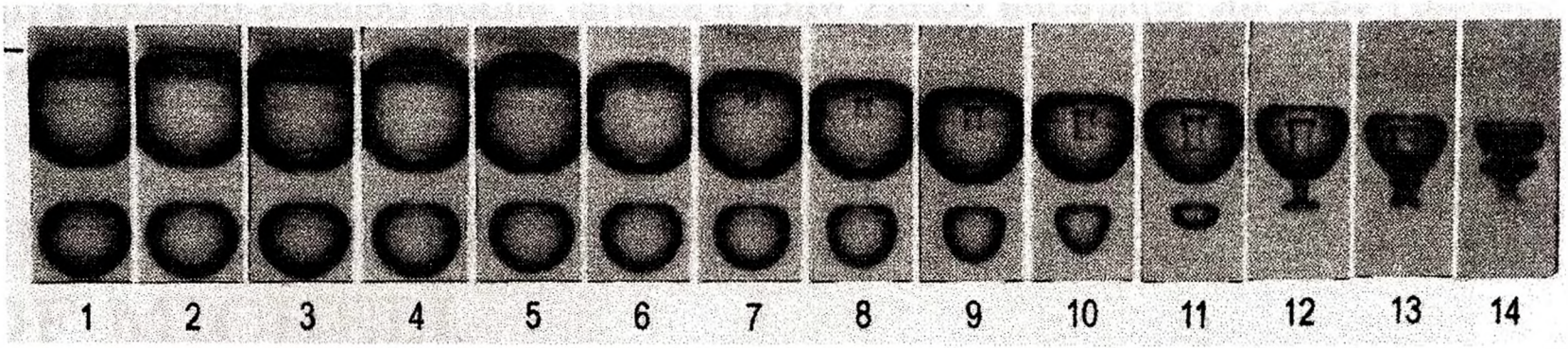

Figure 4.22: High-speed photograph series of two bubbles generated beneath a free surface for $\gamma_1 = -0.75$, $\gamma_2 = -2.93$, $R_1 = 1.0$ (1.37mm) and $R_2 = 0.66$ (0.90mm). Frame interval 10μs (100,000 frames per second), exposure 2μs. Reproduced with permission from Figure 5a of Tomita & Kodama (2001).

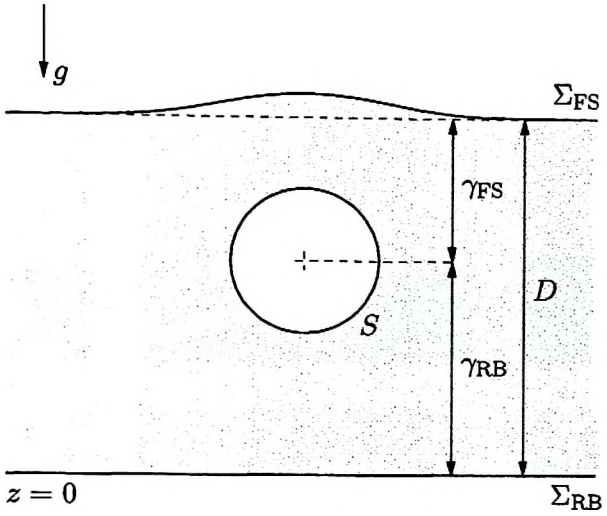

Figure 4.23: Schematic diagram showing a single bubble in a shallow layer of fluid of (dimensionless) depth D. The distance from the initial centroid of the bubble to the free surface is denoted by γ_{FS} and the distance from the bubble to the rigid boundary by γ_{RB}.

layers considered herein are very shallow in order to illicit strong interactions between the bubble and boundaries, though this need not be the case: comparing typical sizes for explosion bubbles and inland or coastal water depths, a fluid depth of tens of maximum bubble radii may be considered.

We begin by considering the motion of a vapour bubble formed mid-way between the rigid boundary and free surface in a fluid of depth $D = 1.4$. Previous calculations have shown the standoff distance to the rigid boundary of $\gamma_{RB} = 0.7$ is the minimum with which our numerical scheme is able to cope in a semi-infinite fluid, though we note the displacement of the free surface above allows smaller standoffs to be considered. Further the free surface standoff distance $\gamma_{FS} = -0.7$ is well within acceptable limits for our calculations near a free surface, though the flattened bubble underside may cause additional fluid to be displaced above the bubble during expansion. Half-rendered bubble and surface shapes for this case are presented in Figure 4.24a. We note during expansion both a flattening of the underside of the bubble as previously noted in our rigid boundary studies and the entrainment of the bubble within the raised free surface as seen earlier in this chapter. During collapse, jet formation is induced by the pointed bubble geometry at the upper pole of the bubble though development of the jet is hastened by the combined

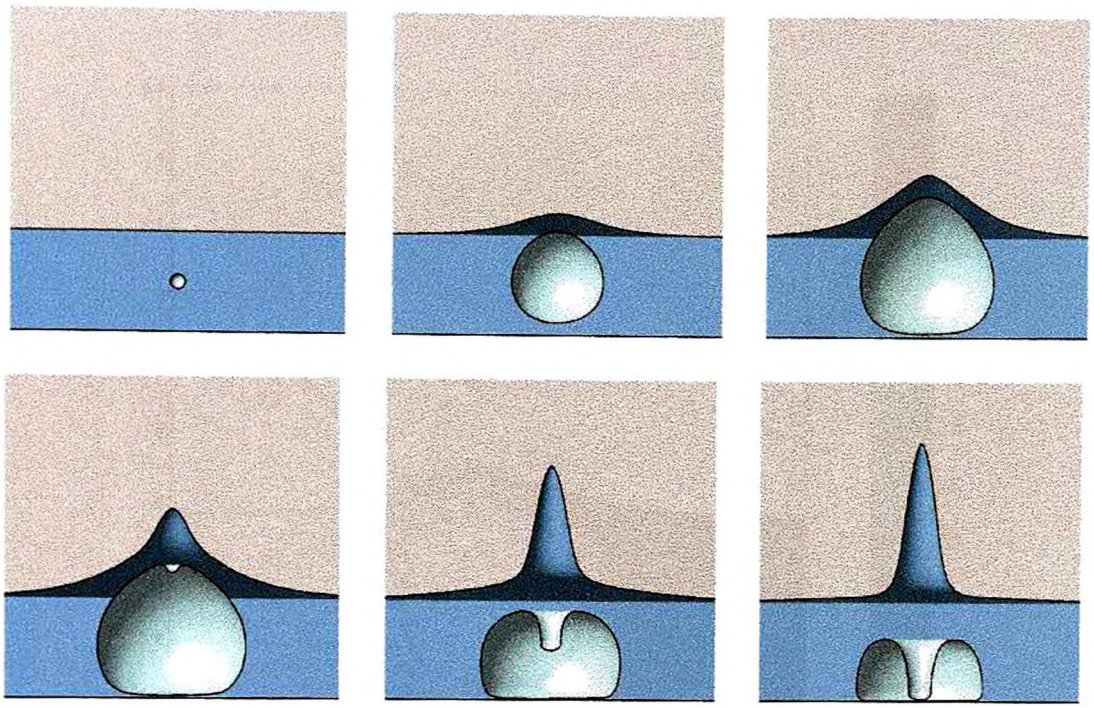

(a) Half-rendered bubble and surface shapes. Horizontal and vertical axes are $r \leqslant 2.25$, $0 \leqslant z \leqslant 4.5$. Times are 0.0015, 0.1402, 0.4533, 0.6690, 1.0457 and 1.2540 respectively.

Figure 4.24: Motion of a vapour bubble in a shallow layer of fluid for $D = 1.4$, $\gamma_{RB} = 0.7$ ($\gamma_{FS} = -0.7$) up until the time of jet impact.

influence of the Bjerknes forces of repulsion from the free surface and attraction towards the rigid boundary. Figure 4.24b shows pressure contours and velocity vectors at two instants during the motion. In Frame 1 we note the region of high pressure in a wide ring around the bubble. This is due to the continued expansion of the bubble forcing fluid radially outward and upward. We note there is no high pressure region below the bubble as the motion of the lower surface has been slowed during early expansion. In Frame 2, we note the familiar region of high pressure above the bubble which drives the motion.

In our second example, we consider the motion of a bubble initiated in a slightly deeper fluid $D = 2.0$, again mid-way between the two boundaries. See Figure 4.25. Here the flattening against the rigid boundary and entrainment within the raised free surface are much reduced. Further we note the development of a much wider liquid jet which is again induced by the interaction of the bubble with the free surface. In Figure 4.25b

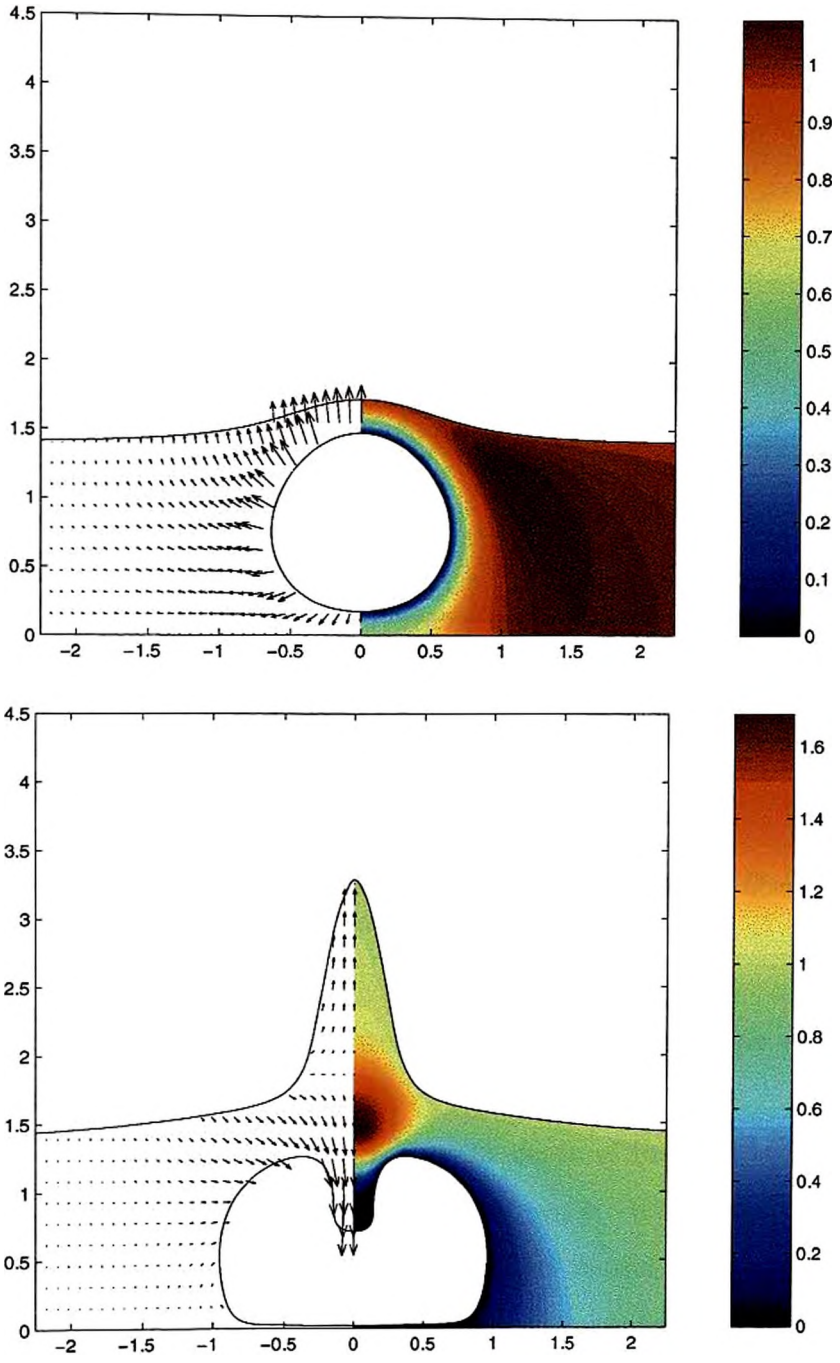

(b) Velocity vectors and pressure contours. Times are 0.1402 and 1.0376 respectively.

Figure 4.24 continued: Motion of a vapour bubble in a shallow layer of fluid for $D = 1.4$, $\gamma_{RB} = 0.7$ ($\gamma_{FS} = -0.7$) up until the time of jet impact.

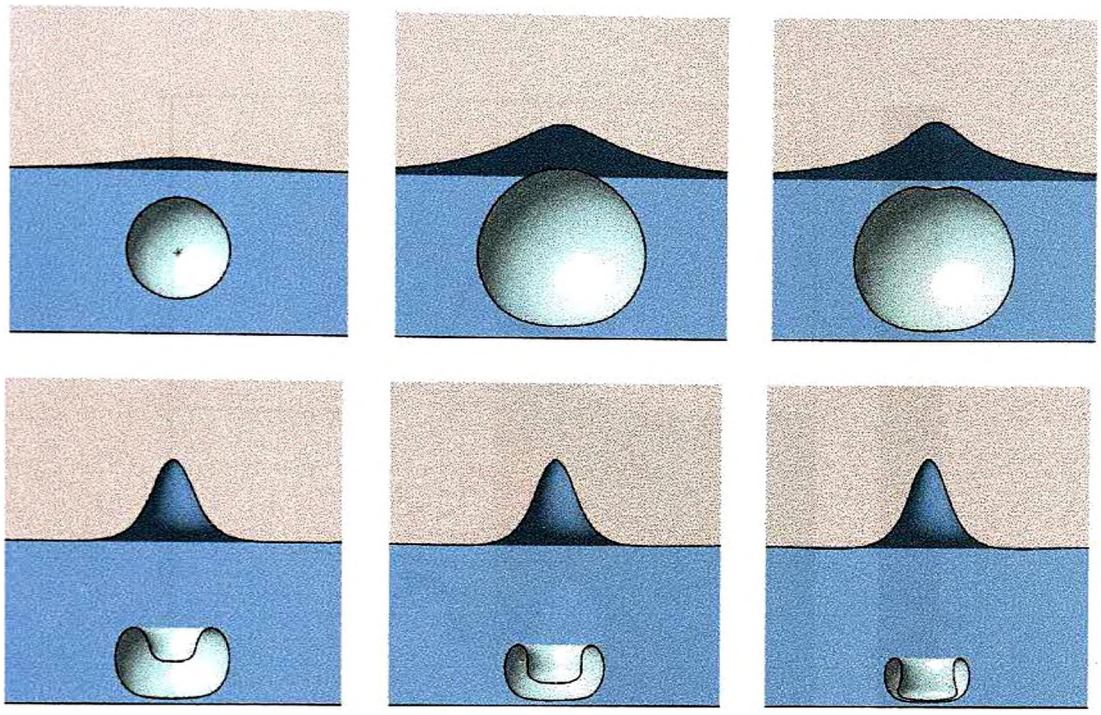

(a) Half-rendered bubble and surface shapes. The rigid boundary is visible at the bottom of each frame. The black star in the first frame denotes the point of bubble initiation. Horizontal and vertical axes are $r \leqslant 2$, $0 \leqslant z \leqslant 4$. Times are 0.1403, 0.7534, 0.9354, 1.4888, 1.5672 and 1.6247 respectively.

Figure 4.25: Motion of a vapour bubble in a shallow layer of fluid for $D = 2.0$, $\gamma_{RB} = 1.0$ ($\gamma_{FS} = -1.0$) up until the time of jet impact.

we show the development of the high-pressure region above the bubble which drives the motion.

We now consider the effects of increasing the depth of the fluid layer whilst maintaining a constant standoff from the free surface of $\gamma_{\mathrm{FS}} = -0.7$. Figure 4.26 shows half-rendered bubble and surface shapes at the time of jet impact over the range of depths $1.4 \leqslant D \leqslant 3.5$. Figure 4.26a shows the bubble previously considered in Figure 4.24, with the flattened underside due to the close proximity of the rigid boundary. As the fluid layer is made deeper and the standoff to the rigid boundary increased, the geometry of the bubble about the lower pole quickly becomes more rounded so for depths greater that $D = 2.0$, increasing depth has little effect.

Similar consideration is given to increasing the fluid depth, but maintaining the stand-

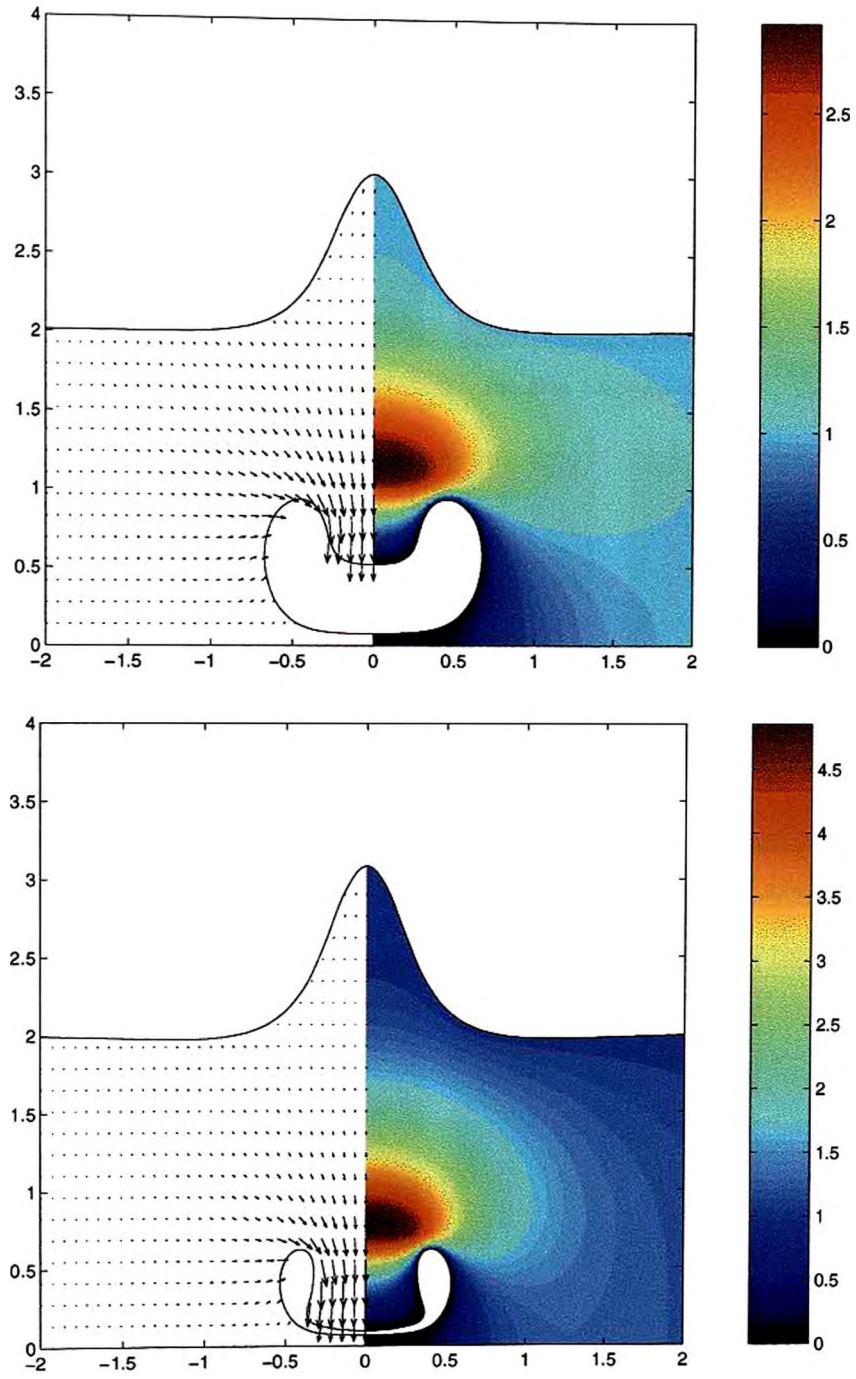

(b) Velocity vectors and pressure contours. Time are 1.4888 and 1.6191.

Figure 4.25 continued: Motion of a vapour bubble in a shallow layer of fluid for $D = 2.0$, $\gamma_{RB} = 1.0$ ($\gamma_{FS} = -1.0$) up until the time of jet impact.

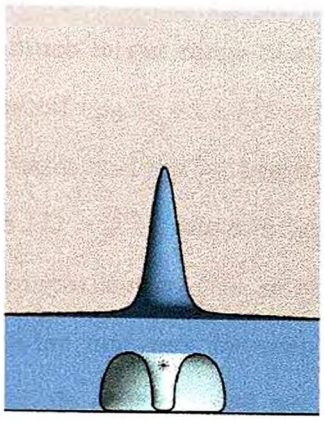

(a) $D = 1.4$, $\gamma_{RB} = 0.7$.

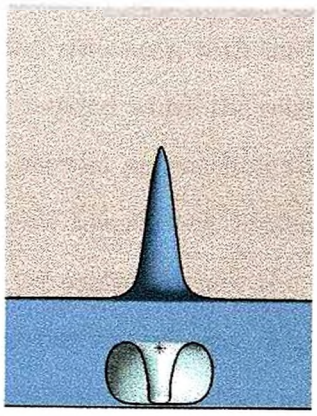

(b) $D = 1.6$, $\gamma_{RB} = 0.9$.

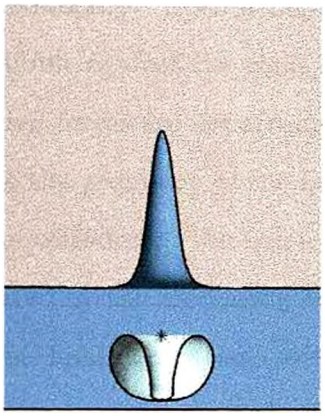

(c) $D = 1.8$, $\gamma_{RB} = 1.1$.

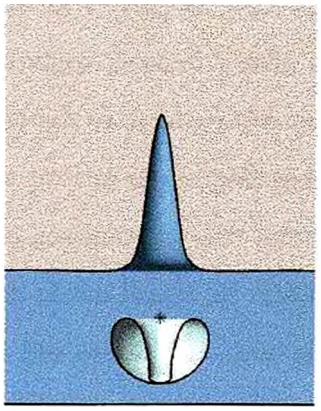

(d) $D = 2.0$, $\gamma_{RB} = 1.3$.

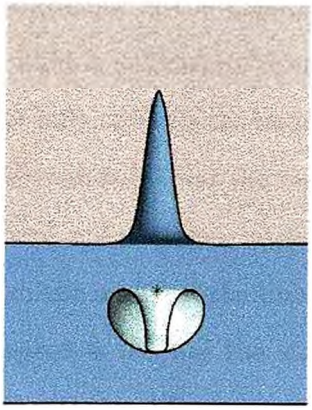

(e) $D = 2.4$, $\gamma_{RB} = 1.7$.

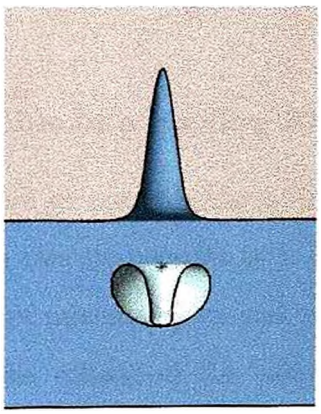

(f) $D = 2.8$, $\gamma_{RB} = 2.1$.

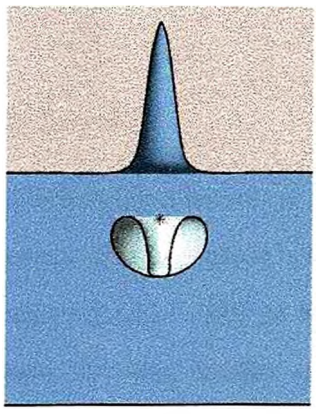

(g) $D = 3.5$, $\gamma_{RB} = 2.8$.

Figure 4.26: Half-rendered bubble and surface shapes showing the geometry of a vapour bubble in a shallow layer of fluid for a range of depths at a constant standoff distance from the free surface ($\gamma_{FS} = -0.7$) at the time of jet impact. The rigid boundary is visible at the bottom of each frame. The black star denotes the point of bubble initiation. Horizontal and vertical axes are $r \leqslant 2.25$, $0 \leqslant z \leqslant 6$.

off to the rigid boundary at $\gamma_{RB} = 0.7$ in Figure 4.27. Here the influence of the free surface may be felt over a much larger range of standoff distances, with the liquid jet becoming broader upto a standoff $\gamma_{FS} = -1.1$ ($D = 1.8$) beyond which the relative influence of the rigid boundary increases and the jet begins to narrow, approaching the semi-infinite fluid limit at $\gamma_{FS} = -2.8$ ($D = 3.5$), wherein negligible free surface displacement is observed.

For our final comparison in this section we again increase the depth of the fluid, but initiate the bubble mid-way between the two boundaries. Figure 4.28 shows the migration of the bubble centroid and jet formation towards the rigid boundary due to the combined repulsion of the bubble from the free surface and attraction towards the rigid boundary. Upto a depth of $D = 2.0$, we note the flattening of the underside of the bubble against the rigid boundary, beyond which, the fluid is sufficiently deep that Bjerknes forces are not strong enough to displace the bubble fully towards the boundary, and so the geometry of the lower pole of the bubble is more rounded. Over the range of depths considered, the motion is governed by the interactions with the free surface, as indicated by the increasing width of the liquid jet relative to the width of the bubble.

One final comparison which has so far not been presented is to vary the standoff distances in a constant depth of fluid. In order to accentuate the differences in fluid pressure as this is done, we consider a bubble with some gaseous content in the following section.

4.3.4 Gas Bubble in a Shallow Fluid Layer

As noted above, here we consider the effects of initiating a bubble at a range of standoff distances from the two boundaries in a constant depth of fluid. We have chosen to consider a bubble of mixed vapour and gas content ($\alpha = 100$) so the influence of the boundaries upon the volume of the bubble may be more readily appreciated through adiabatic compression of gas within the bubble. Figure 4.29a shows half-rendered bubble and surface shapes at the time of jet impact for bubbles generated over the range of standoff distances $0.75 \leqslant \gamma_{RB} \leqslant 4.5$ in a fluid of depth $D = 5.0$. For bubbles formed close to the free surface ($-0.5 \geqslant \gamma_{FS} \geqslant -1.5$), we note the motion is characteristic of bubbles formed in a semi-infinite fluid beneath a free surface, with the liquid jet within

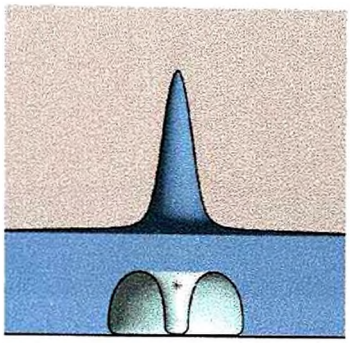

(a) $D = 1.4$, $\gamma_{FS} = -0.7$.

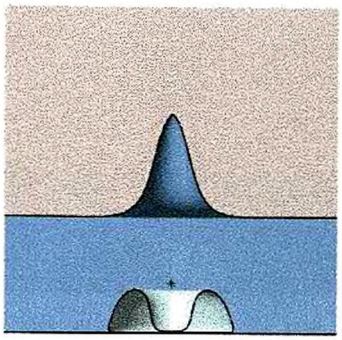

(b) $D = 1.6$, $\gamma_{FS} = -0.9$.

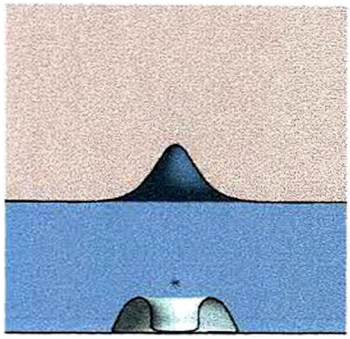

(c) $D = 1.8$, $\gamma_{FS} = -1.1$.

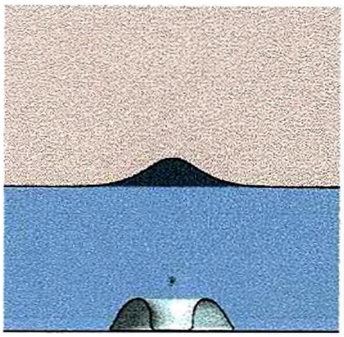

(d) $D = 2.0$, $\gamma_{FS} = -1.3$.

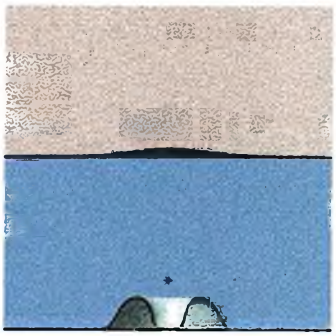

(e) $D = 2.4$, $\gamma_{FS} = -1.7$.

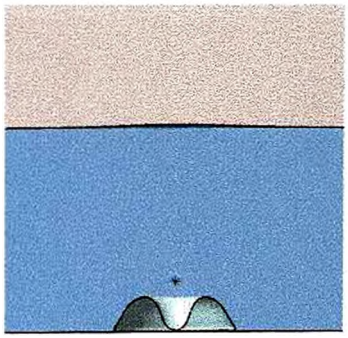

(f) $D = 2.8$, $\gamma_{FS} = -2.1$.

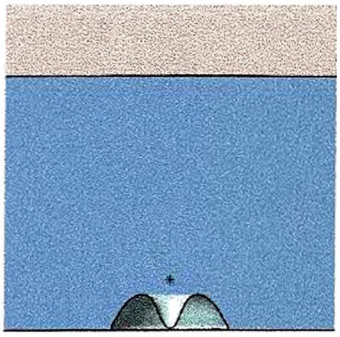

(g) $D = 3.5$, $\gamma_{FS} = -2.8$.

Figure 4.27: Half-rendered bubble and surface shapes showing the geometry of a vapour bubble in a shallow layer of fluid for a range of depths at a constant standoff distance from the rigid boundary ($\gamma_{RB} = 0.7$) at the time of jet impact. The rigid boundary is visible at the bottom of each frame. The black star denotes the point of bubble initiation. Horizontal and vertical axes are $r \leqslant 2.25$, $0 \leqslant z \leqslant 4.5$.

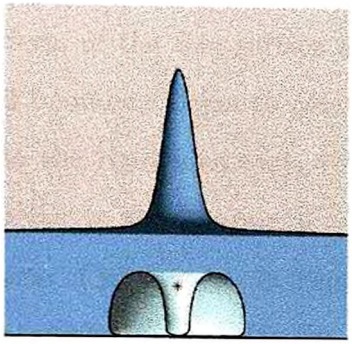

(a) $D = 1.4$, $\gamma_{RB} = 0.7$, $\gamma_{FS} = -0.7$.

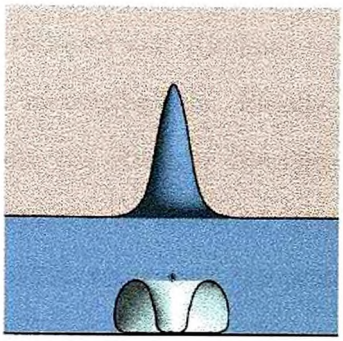

(b) $D = 1.6$, $\gamma_{RB} = 0.8$, $\gamma_{FS} = -0.8$.

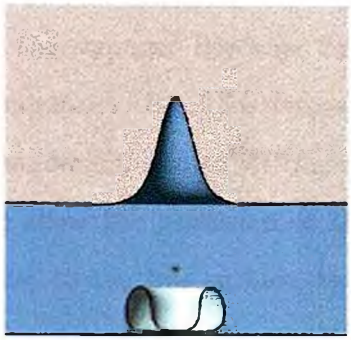

(c) $D = 1.8$, $\gamma_{RB} = 0.9$, $\gamma_{FS} = -0.9$.

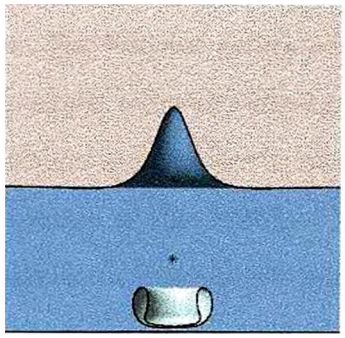

(d) $D = 2.0$, $\gamma_{RB} = 1.0$, $\gamma_{FS} = -1.0$.

(e) $D = 2.4$, $\gamma_{RB} = 1.2$, $\gamma_{FS} = -1.2$.

(f) $D = 2.8$, $\gamma_{RB} = 1.4$, $\gamma_{FS} = -1.4$.

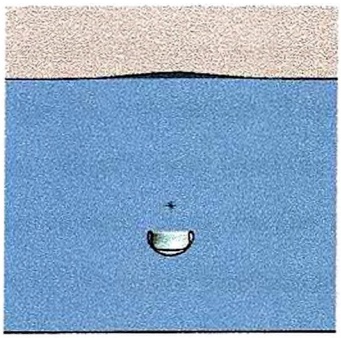

(g) $D = 3.5$, $\gamma_{RB} = 1.75$, $\gamma_{FS} = -1.75$.

Figure 4.28: Half-rendered bubble and surface shapes showing the geometry of a vapour bubble in a shallow layer of fluid for a range of depths at the time of jet impact. The bubble is initiated at a point half-way between the rigid boundary and free surface which is denoted by a black star. The rigid boundary is visible at the bottom of each frame. Horizontal and vertical axes are $r \leqslant 2.25$, $0 \leqslant z \leqslant 4.5$.

the bubble becoming wider and the free surface spike becoming shorter and fatter as the standoff is increased. Beyond this ($\gamma_{FS} = -2.0, -2.5$) we note the liquid jet begins to narrow as the effects of the free surface are reduced and Bjerknes forces of attraction towards the rigid boundary begin to play an increasing rôle. Finally, as the bubble is initiated closer to the rigid boundary, we note the stronger Bjerknes forces initiating collapse much earlier in the lifetime of the bubble, as indicated by the larger bubble volumes at the time of jet impact. In Figure 4.29b we present the pressure and velocity fields around the bubbles just prior to the conclusion of our calculations. Herein we note the much reduced pressures around the bubble for bubbles formed in close proximity to either boundary, as jet impact occurs much earlier in the lifetime of the bubble due to the stronger Bjerknes forces. For bubbles generated roughly mid-way between the boundaries, Bjerknes forces are much reduced (despite the combined influence of the boundaries) and so jet impact occurs much closer to minimum volume. In Figure 4.29c we show the evolution of the volume of the bubbles. We note for bubbles generated close to the free surface, the maximum volumes are much reduced due to the egg-like geometries which form as the bubble becomes entrained in the free surface. The largest maximum volume achieved is for $\gamma_{FS} = -2.5$ due to the more spherical expansion phase of the bubble. The centroid motion for the bubbles is shown in Figure 4.29d. Herein we note the upward migration of bubbles formed close to the free surface during expansion, caused by the entrainment of the bubbles within the free surface. Likewise, for bubbles formed close to the rigid boundary, the bubbles migrate away from the boundary during expansion as this may not be displaced by the bubble. Even for the case $\gamma_{FS} = -2.5$, we note a slight upward movement, indicative of the easier displacement of fluid above the bubble. In Figure 4.29e we show calculations of the Kelvin impulse throughout the lifetime of the bubble, with trends similar to the respective semi-infinite fluid cases considered earlier. Finally in Figure 4.29f, we show the circulations formed at the time of jet impact. We note the gap in the range $3 \leqslant \gamma_{RB} \leqslant 4$ is due to jet impact occurring on a ring about the bubble and not at a singular point. Highest circulations are obtained close to the free surface as the lower pole of the bubble undergoes motion unlike near the rigid boundary.

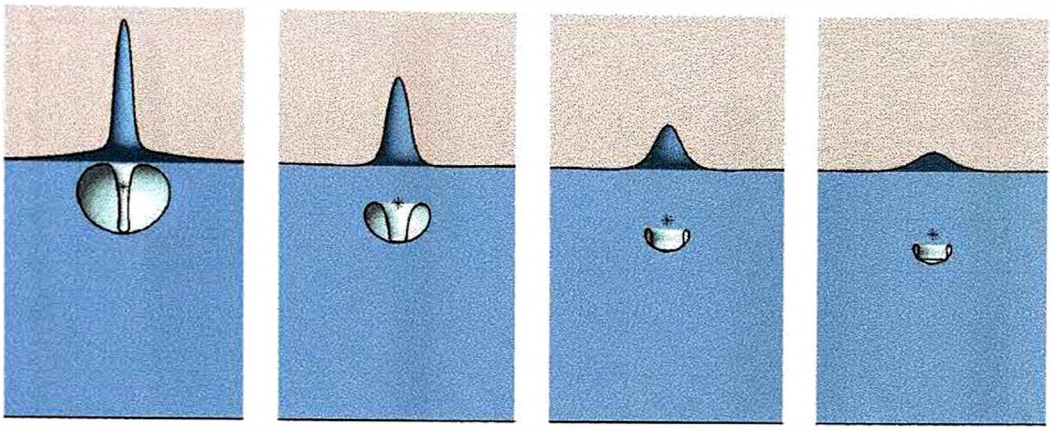

(i) $\gamma_{FS} = -0.5$, $\gamma_{RB} = 4.5$.

(ii) $\gamma_{FS} = -0.75$, $\gamma_{RB} = 4.25$.

(iii) $\gamma_{FS} = -1.0$, $\gamma_{RB} = 4.0$.

(iv) $\gamma_{FS} = -1.25$, $\gamma_{RB} = 3.75$.

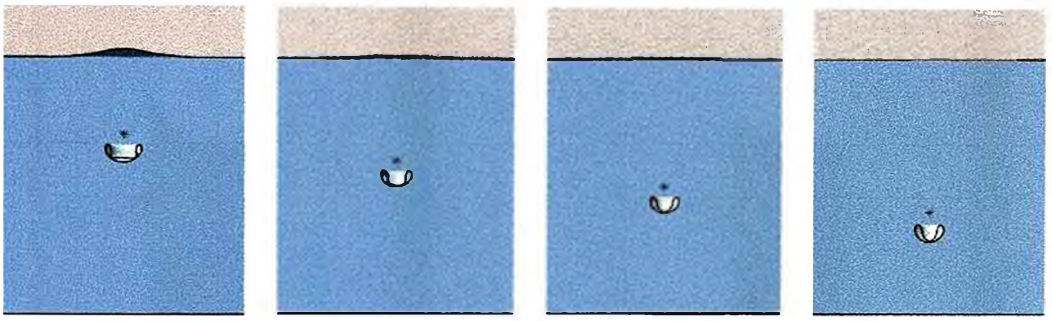

(v) $\gamma_{FS} = -1.5$, $\gamma_{RB} = 3.5$.

(vi) $\gamma_{FS} = -2.0$, $\gamma_{RB} = 3.0$.

(vii) $\gamma_{FS} = -2.5$, $\gamma_{RB} = 2.5$.

(viii) $\gamma_{FS} = -3.0$, $\gamma_{RB} = 2.0$.

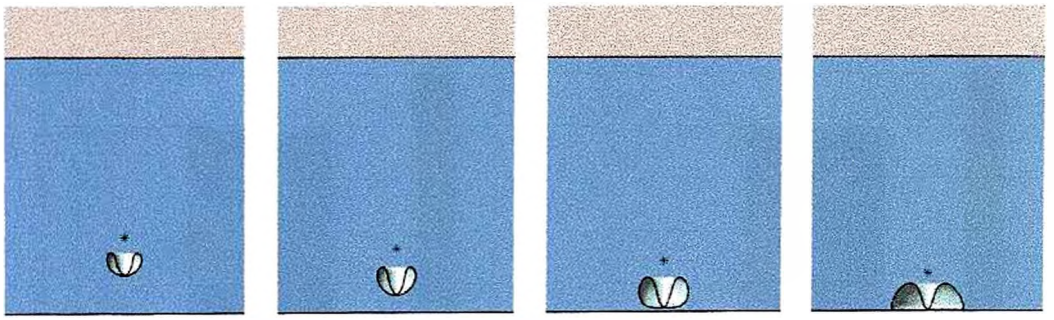

(ix) $\gamma_{FS} = -3.5$, $\gamma_{RB} = 1.5$.

(x) $\gamma_{FS} = -3.75$, $\gamma_{RB} = 1.25$.

(xi) $\gamma_{FS} = -4.0$, $\gamma_{RB} = 1.0$.

(xii) $\gamma_{FS} = -4.25$, $\gamma_{RB} = 0.75$.

(a) Half-rendered bubble and surface shapes at the time of jet impact. The rigid boundary is visible at the bottom of each frame. The black star denotes the point of bubble initiation. Horizontal and vertical axes are: (i) through (iv) $r \leqslant 2.25$, $0 \leqslant z \leqslant 8$, (v) through (xii) $r \leqslant 2.25$, $0 \leqslant z \leqslant 6$.

Figure 4.29: Motion of cavitation bubbles generated in a shallow layer of fluid for $\alpha = 100$, $D = 5$ for a range of standoff distances.

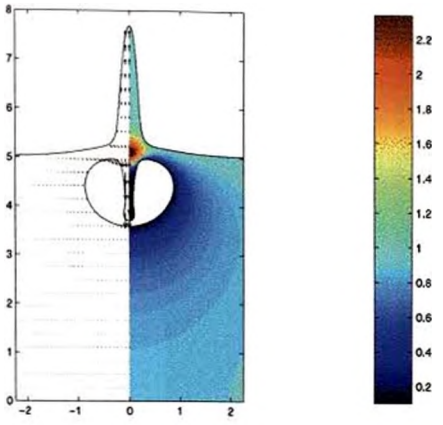

(i) $\gamma_{FS} = -0.5$, $\gamma_{RB} = 4.5$.

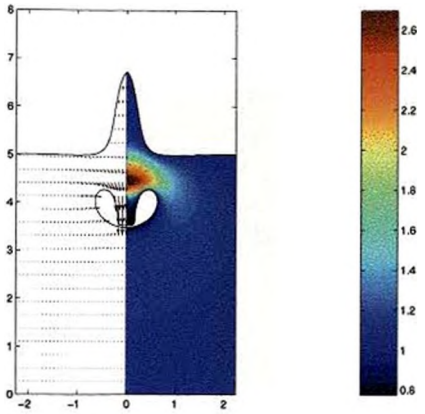

(ii) $\gamma_{FS} = -0.75$, $\gamma_{RB} = 4.25$.

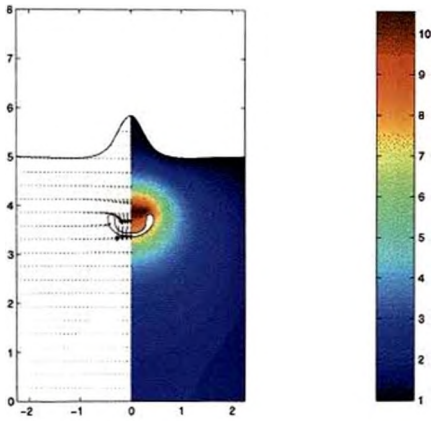

(iii) $\gamma_{FS} = -1.0$, $\gamma_{RB} = 4.0$.

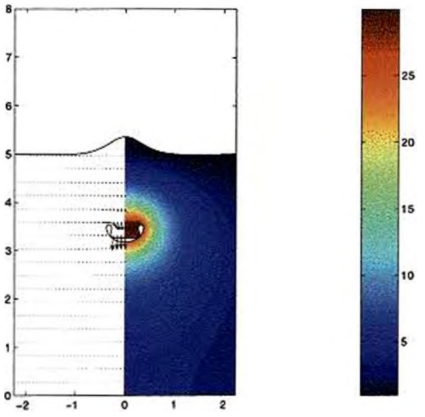

(iv) $\gamma_{FS} = -1.25$, $\gamma_{RB} = 3.75$.

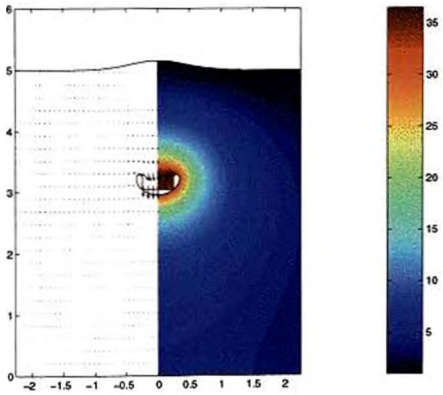

(v) $\gamma_{FS} = -1.5$, $\gamma_{RB} = 3.5$.

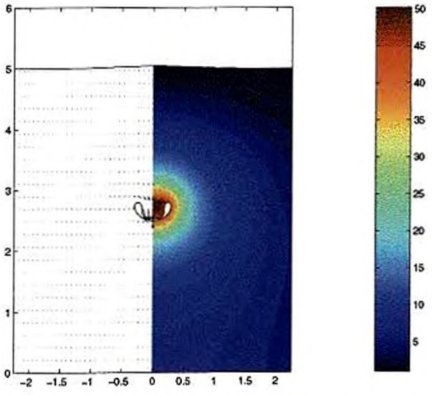

(vi) $\gamma_{FS} = -2.0$, $\gamma_{RB} = 3.0$.

(b) Velocity vectors and pressure contours at the time of jet impact.

Figure 4.29 continued: Motion of cavitation bubbles generated in a shallow layer of fluid for $\alpha = 100$, $D = 5$ for a range of standoff distances.

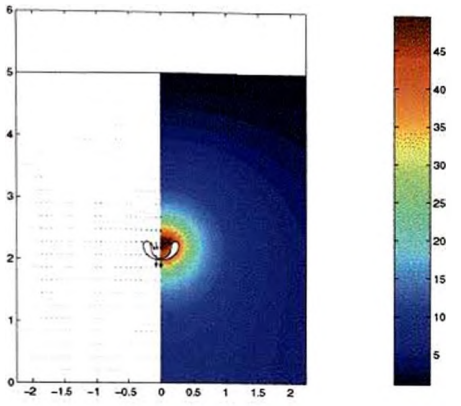

(vii) $\gamma_{FS} = -2.5$, $\gamma_{RB} = 2.5$.

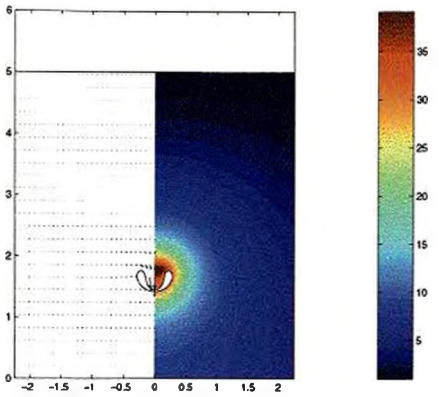

(viii) $\gamma_{FS} = -3.0$, $\gamma_{RB} = 2.0$.

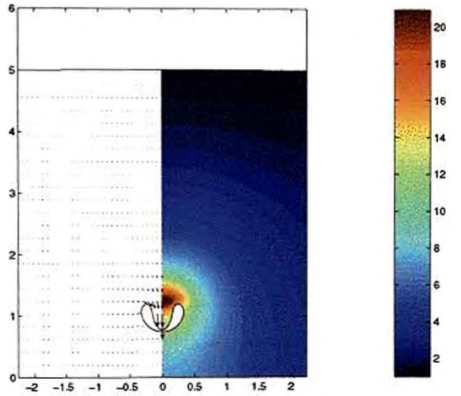

(ix) $\gamma_{FS} = -3.5$, $\gamma_{RB} = 1.5$.

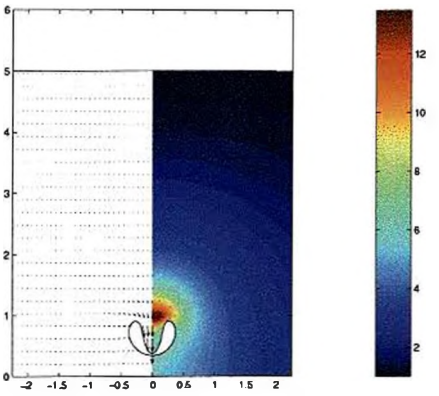

(x) $\gamma_{FS} = -3.75$, $\gamma_{RB} = 1.25$.

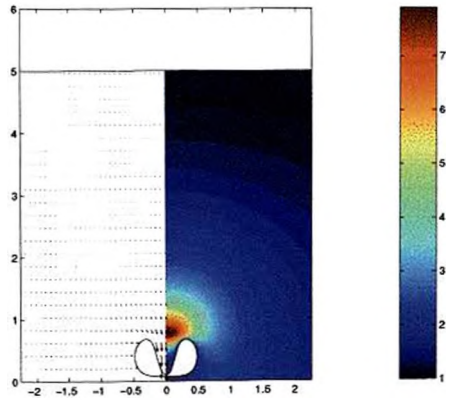

(xi) $\gamma_{FS} = -4.0$, $\gamma_{RB} = 1.0$.

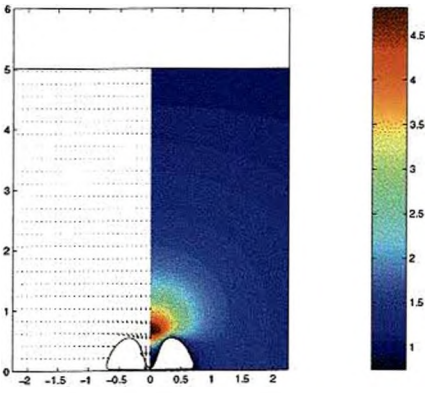

(xii) $\gamma_{FS} = -4.25$, $\gamma_{RB} = 0.75$.

(b continued) Velocity vectors and pressure contours at the time of jet impact.

Figure 4.29 continued: Motion of cavitation bubbles generated in a shallow layer of fluid for $\alpha = 100$, $D = 5$ for a range of standoff distances.

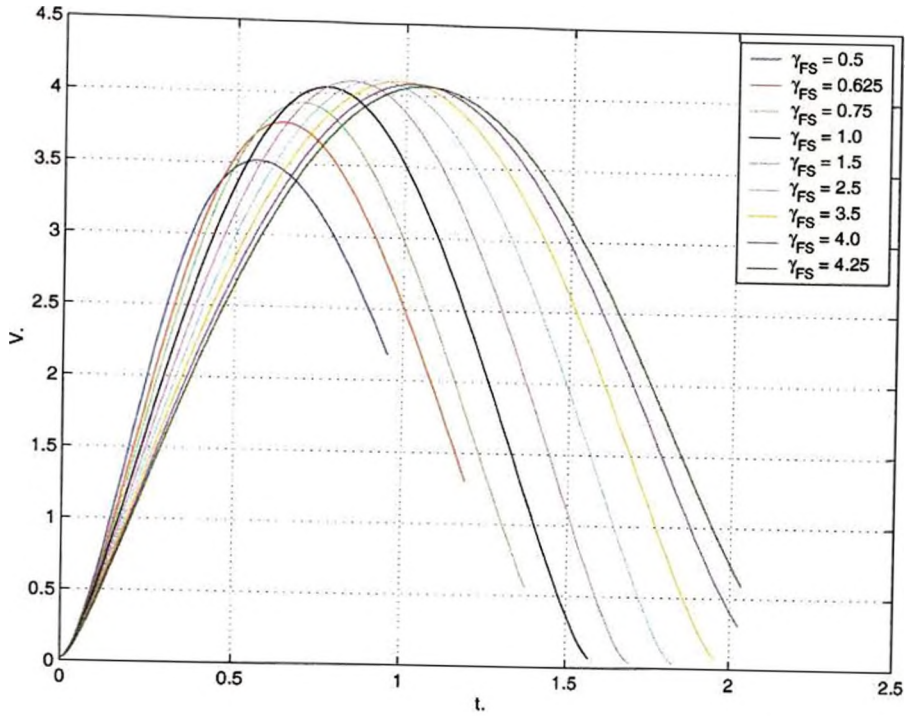

(c) Bubble volumes.

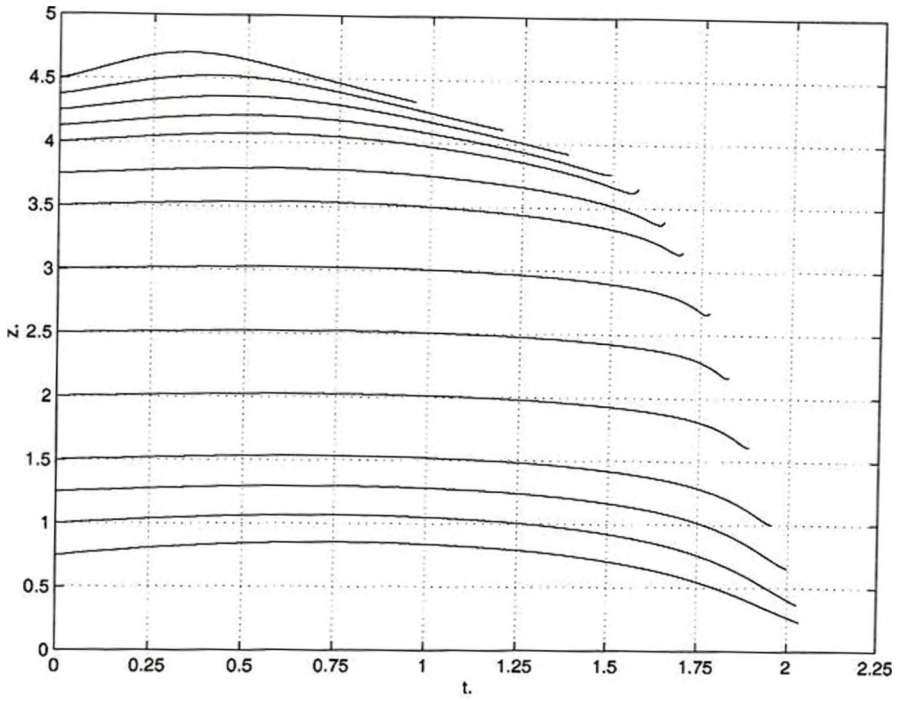

(d) Bubble centroid motions.

Figure 4.29 continued: Motion of cavitation bubbles generated in a shallow layer of fluid for $\alpha = 100$, $D = 5$ for a range of standoff distances.

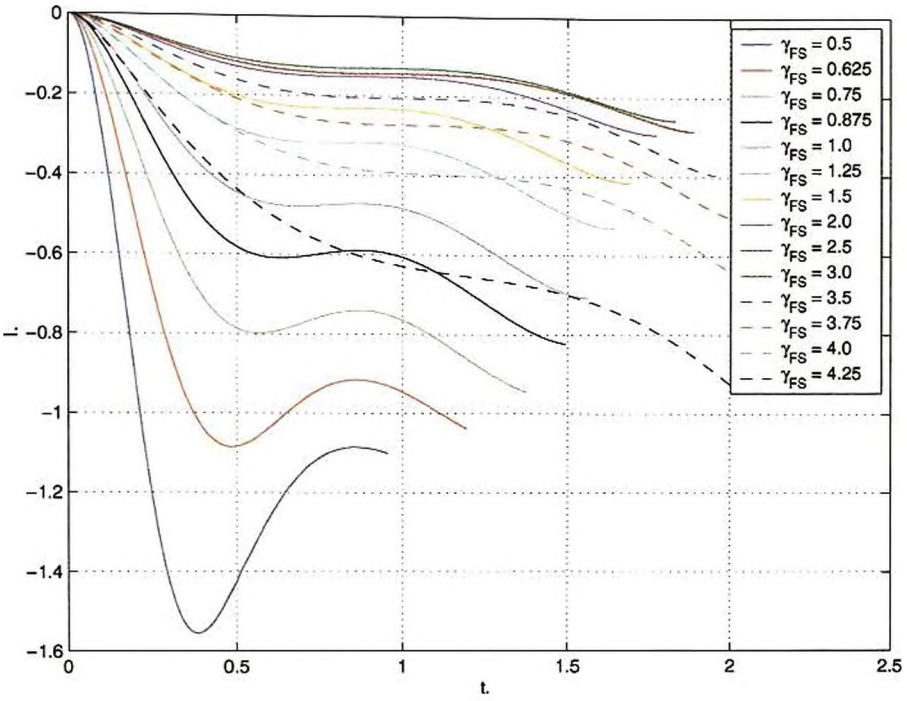

(e) Kelvin impulses of bubbles.

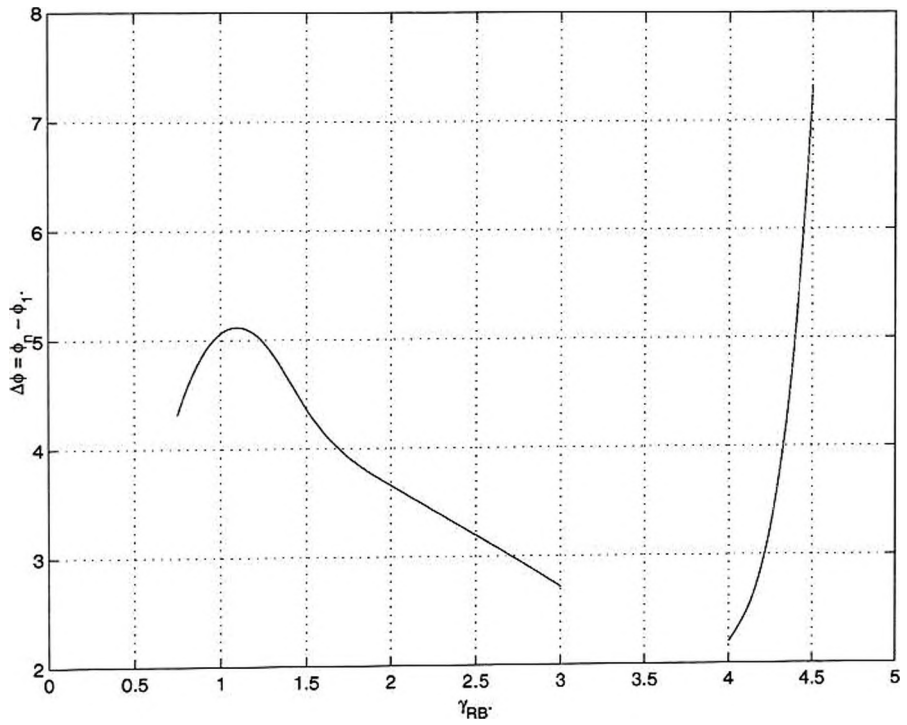

(f) Circulation induced by jet impact in the bubbles.

Figure 4.29 continued: Motion of cavitation bubbles generated in a shallow layer of fluid for $\alpha = 100$, $D = 5$ for a range of standoff distances.

4.4 Summary

In this chapter, we have outlined developments to our single bubble boundary integral scheme (itself presented in Chapter 3) in order to permit the calculation of flows induced by the motion of two or more bubbles; although results presented in the current work concern only two bubbles. In addition to this, our techniques also allow the addition of an infinite free surface which, for bubbles generated near the boundary, cannot be dealt with by means of an image system as done in the previous chapter for the rigid boundary. This has instead, been necessarily evolved as a material surface much in the same manner as the surface of a bubble. The complexity of this task is increased due to the infinite extent of the free surface, though this is readily dealt with by using an analytic form for the variables on the free surface through the assumption of a dipolar far-field. Finally, the image system for the rigid boundary which was used in Chapter 3, has again been employed to permit the calculation of flows in a shallow layer of fluid. This method allows for any finite depth of fluid to be treated equally well, though in order to ensure strong bubble–boundary interactions, results were presented for the motion of a single bubble in a fluid of five maximum bubble radii or less in depth. We note at this stage that methods devised earlier for the calculation of physical quantities relating to the bubble, or fluid which surrounds it, may be employed with little or no modification to the code required; though for brevity, many of these calculations are not presented.

Results presented for the motion of a single bubble near an infinite free surface were shown to compare well with experiments and two and three-dimensional rendering techniques are employed to enhance the presentation of calculated motions. Most worthy of note in this section are: calculations for the motion of a vapour bubble formed at a standoff distance of $\gamma = -0.45$ beneath the free surface, thus showing the ability of our code to cope with such an extreme case; and calculations pertaining to the generation and evolution of the free surface spike, which shows the constant rate of growth of the spike, as in experiments.

Calculations relating to the experimental generation of two cavitation bubbles beneath a free surface show excellent agreement with experiments despite the omission of any gaseous bubble content in our calculations. It was shown however, this agreement

holds true only for bubbles of a similar maximum volume. For bubbles of largely disparate maximum volumes, the adiabatic compression of gasses within the smaller bubble is essential in slowing final collapse so the evolution of the larger bubble is allowed to sufficiently develop.

Though we have no experimental data against which we may compare our calculations in a shallow fluid layer, we may be confident in our results as the code is a trivial amalgamation of our free surface code and rigid boundary integration routines, thus requiring the addition of only three further subroutines: those which deal with the analytic portion of the free surface, to which an image in the rigid boundary must be added. Further, if the bubble is initiated in a sufficiently deep body of water, behaviour near either boundary resembles the appropriate semi-infinite fluid case.

In the following chapter, we further develop our numerical scheme to permit the introduction of bubbles at some time $t > 0$ (where $t = 0$ is taken to be the time of generation of the first bubble). A number of interesting cases are presented.

Chapter 5

BUBBLES GENERATED AT DIFFERENT START TIMES

In the previous chapter, we refined our standard infinite fluid / rigid boundary code (itself described in Chapter 3) to include a free surface of infinite extent. This was necessarily done by integrating over the free surface as a second material surface. Moreover, during the transition from a scheme capable of dealing with only one material surface[1] to one which required two, it was possible to generalise the code to permit a finite number of bubbles with almost no additional effort. Calculations were only limited to two bubbles due to the wealth of controlled experiments provided in the papers by Robinson, Blake, Kodama, Shima & Tomita (2001) and Tomita & Kodama (2001), against which we were able to compare our work. In many physical situations however, such precise generation of bubbles at one instant is highly unlikely. For example bubbles which are formed during extracorporeal shock wave lithotripsy occur due to the reduced pressure front following the shock wave (or by reflected pressure waves within the body) acting on dissolved gases within bodily fluids or tissue. Due to the finite time of passage of this tensile pressure wave, two nearby cavities may be formed, but a split second apart. Such differences in bubble initiation are not solely limited to small scale bubbles. Even in controlled experiments concerning underwater explosion bubbles, slight reactive differences in the charges may lead to two bubbles being formed milliseconds apart. In normal usage where interaction between bubbles may be sought, such differences may be accentuated due to any number of external influences. Whilst it is not fully possible to model such cases due

[1] Here we discount the rigid boundary considered in Chapter 3 which was included through the use of an image system.

to the shocks emitted during initial formation of many of these types of bubble, we are able to provide strong insight into these situations through the use of our incompressible model.

In the remainder of this chapter, we outline the changes to the numerical scheme presented in Chapter 4 which are require in order to permit the introduction of additional bubbles at some time, $t > 0$ where $t = 0$ is taken as the time at which the first bubble is generated. Many of these changes were necessarily implemented at a much earlier stage as requirements for the calculation of several physical quantities and so discussions are limited for brevity. Following this a number of results are presented.

5.1 Changes to the Numerical Scheme

The numerical scheme we employ here is much like that described in Chapter 4 with many of the changes to the code being required in order that we may change the number of material surfaces over which integrations are performed during evolution of the flow field. These changes, although essential and non-trivial, are merely accounting practices and therefore warrant no further discussion herein.

Beyond the internal accounting mechanisms, the number of changes are in fact minimal. Moreover the mechanisms have already been described earlier and are placed in context here. Throughout the thesis, we have assumed an inviscid, incompressible and irrotational flow field (see Chapter 2) governed by some velocity potential, ϕ. In previous chapters, two types of bubble, and hence initial conditions were employed. For gas bubbles, an initially stationary bubble has a zero initial surface potential, the motion being driven by the high internal gas pressures. In some instances, a vapour bubble was considered in order to avoid comparative considerations of several strength parameters. In this case, the motion is governed by some initial velocity imposed over the surface of the bubble. For a single bubble in an infinite fluid, this leads to a constant and non-zero potential over the bubble surface. Where boundaries or additional bubbles are introduced, this initial potential is adjusted slightly as per the techniques discussed in Section 2.5.

Herein we require suitable initial conditions which may be imposed over the surface of the bubble (say bubble j) at time t_{0j} which take into account the motion of the fluid

which is imparted by the expansion or collapse of a bubble (say bubble i) introduced at an earlier time, $t_{0i} = 0$. As the fluid motion is governed by the velocity potential at this time, we appeal to the methodology described in Section 3.7 wherein techniques to calculate the pressure and velocity within the body of the fluid through the calculation of spatial and time derivatives of the potential are detailed. In fact we do not require such complex calculations here and may simply employ these techniques to calculate the fluid potential at the initial location of the nodes used to describe the surface geometry of the bubble being introduced. Moreover we may simplify things further as we are not required to check the proximity of these nodes to already existent material surfaces as, during expansion, the bubble would surely then coalesce with the existing bubble or burst at the free surface. Armed with suitable initial conditions the flow is then advanced further now employing the additional material surface.

Prior to discussion of calculations pertaining to this topic, we pause to discuss the time stepping which is employed. In order that sufficiently small time steps are taken during the initial moments of the introduction of any additional bubbles, we again employ our variable time stepping scheme. However, in many cases the initial bubble has evolved sufficiently that much larger time steps may be taken and as such returning to smaller time stepping would result in a unnecessarily small change in potential. Furthermore, additional iterations will thus be required which necessitates more applications of our smoothing techniques. Both mechanisms introduce additional errors into the calculations. Hence we integrate the bubbles using their respective time steps; adjusted slightly to ensure they are an integer factor different to avoid interpolation difficulties. This ensures additional accuracy during evolution of the flow. For evolutions at the shorter timescale, all bubbles are advanced. Data for surfaces integrated at the longer timescale is then replaced when the time steps once again coincide.

We now proceed to detail several example calculations using this technique.

5.2 Numerical Calculations

Throughout this section, we again limit our calculations to systems which consist of two bubbles. This is primarily in order to avoid the difficulty of coding and testing an

integration scheme which operates on more than two timescales. Nonetheless, the scheme outlined above may readily be extended to permit this. Furthermore, boundaries such as an infinite free surface or rigid boundary are also omitted for brevity.

We begin by considering two identical bubbles introduced at $z = \pm 1$. For consistency, these distances will be denoted by γ, though in the remainder of this section, there are no boundaries present so may not be viewed as standoff distances. If these bubbles are introduced simultaneously, then the two bubble system effectively forms a physical image system for the case of a single bubble near a rigid boundary at a standoff distance $\gamma = 1$; the vapour bubble equivalent case being considered in detail in Chapter 3 (see Figure 3.12). Figure 5.1a shows the bubble geometries at the time of bubble generation (Frame 1), maximum volume (Frame 2) and jet impact (Frame 3), with the expected symmetry in the plane $z = 0$. As the time of introduction is increasingly delayed (Figures 5.1b through 5.1h), the symmetry is quickly lost. Even with a time delay of 0.005 (Figure 5.1b) there is a small but visible discrepancy in Frame 2 which shows the lower bubble at maximum volume. At the time the liquid jet impacts in the upper bubble (Frame 3), the jet in the lower bubble has only transversed approximately two thirds of the bubble height. By increasing this delay, even to only 0.003 (Figure 5.1f), we note the increased asymmetry as the lower bubble reached maximum volume and the lack of any jet formation in the delayed bubble as the liquid jet impacts in the upper bubble.

In order to properly discuss the physical processes which occur during the motion of delayed time bubbles, it is helpful to look at several key physical properties of the motion. Figure 5.2 shows the evolution of the volumes of the two bubbles for two simultaneously released bubbles ($t_{02} = 0$) and a range of delayed times ($t_{02} = 0.005$ through $t_{02} = 0.05$). As the introduction of the lower bubble is delayed, we note the upper, initial bubble reaches a progressively reduced maximum volume, whilst the lower bubble attains greater maximum volumes. Physically, the expansion of the upper bubble quickly forms a cavity of pressure which is below the hydrostatic pressure of the fluid. As the lower bubble expands, it more readily displaces the layer of fluid separating the two bubbles into this region of reduced pressure, slowing the expansion of the lower pole of the bubble and hence reducing the maximum volume which is attained. As the delayed bubble expands

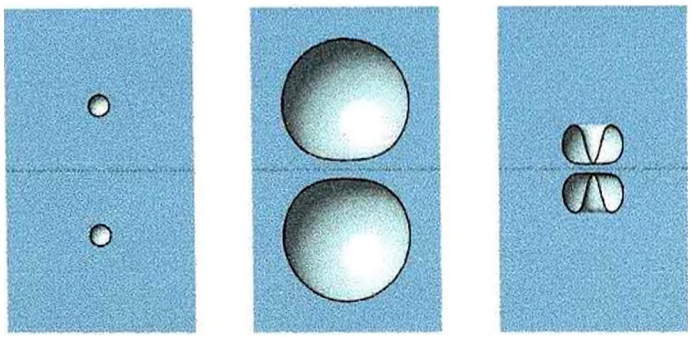

(a) $t_{02} = 0.000$. Times are 0.0000, 1.1349 and 2.2253 respectively.

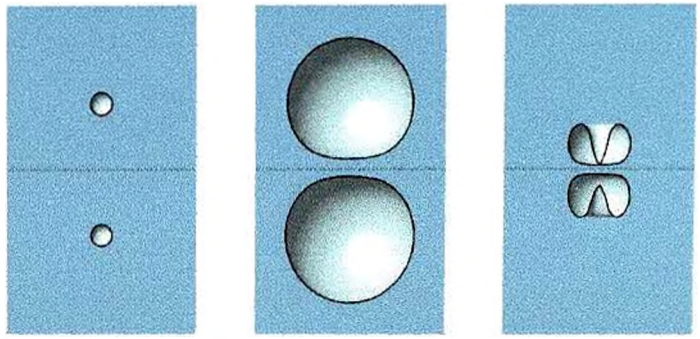

(b) $t_{02} = 0.005$. Times are 0.0050, 1.1947 and 2.2174 respectively.

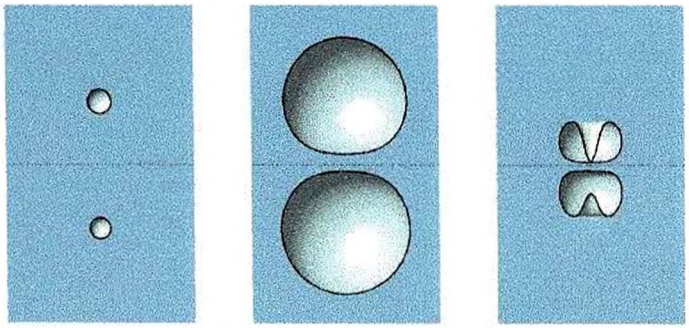

(c) $t_{02} = 0.010$. Times are 0.0100, 1.1542 and 2.2088 respectively.

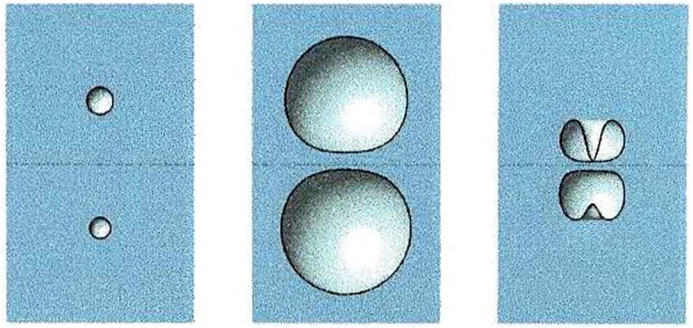

(d) $t_{02} = 0.015$. Times are 0.0150, 1.1687 and 2.1995 respectively.

Figure 5.1: Half-rendered bubble shapes showing the motion of two cavitation bubbles generated at different instants and characterised by $t_{01} = 0$, $\alpha_1 = \alpha_2 = 100$, $\gamma_1 = 1$, $\gamma_2 = -1$, $\delta = 0$ and $\kappa = 1.4$. In each figure, the first frame shows the bubbles at t_{02}, the second frame shows the motion as the lower bubble reaches maximum volume and the final frame at the time of jet impact in the upper bubble. Horizontal and vertical axes are $r \leqslant 1.5$, $-2.5 \leqslant z \leqslant 2.5$. The black dotted line denotes $z = 0$.

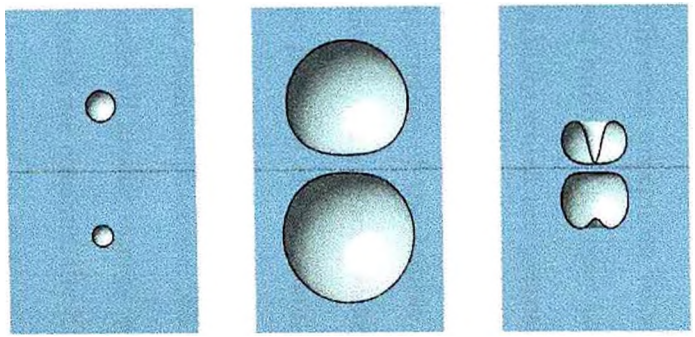

(e) $t_{02} = 0.020$. Times are 0.0020, 1.1729 and 2.1911 respectively.

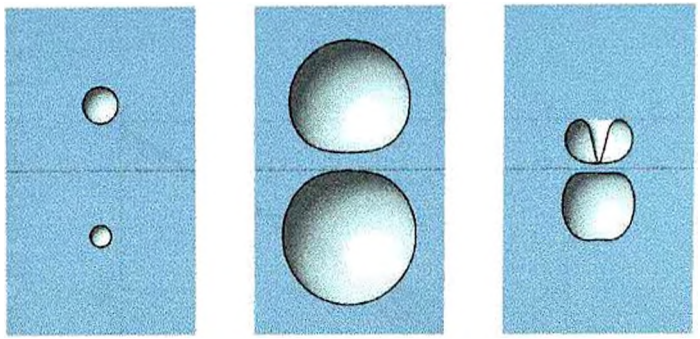

(f) $t_{02} = 0.030$. Times are 0.0030, 1.2007 and 2.1730 respectively.

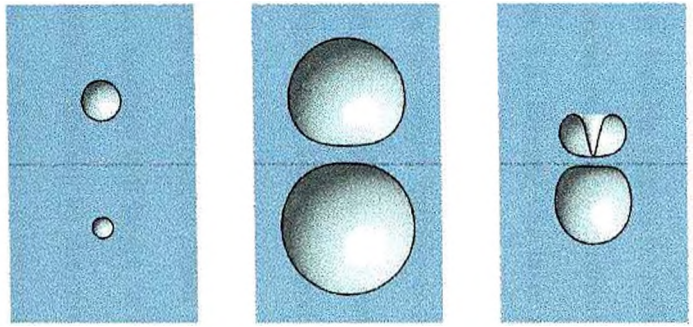

(g) $t_{02} = 0.040$. Times are 0.0040, 1.2241 and 2.1541 respectively.

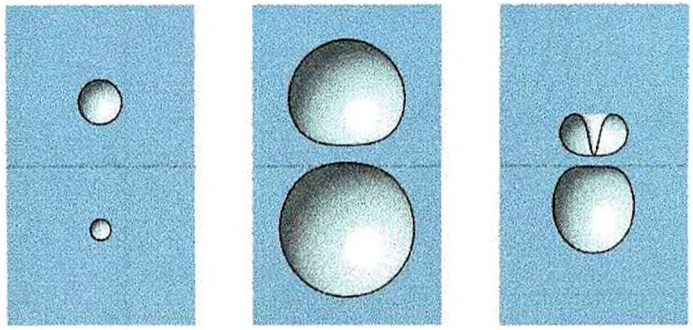

(h) $t_{02} = 0.050$. Times are 0.0050, 1.2346 and 2.1365 respectively.

Figure 5.1 continued: Half-rendered bubble shapes showing the motion of two cavitation bubbles generated at different instants and characterised by $t_{01} = 0$, $\alpha_1 = \alpha_2 = 100$, $\gamma_1 = 1$, $\gamma_2 = -1$, $\delta = 0$ and $\kappa = 1.4$. In each figure, the first frame shows the bubbles at t_{02}, the second frame shows the motion as the lower bubble reaches maximum volume and the final frame at the time of jet impact in the upper bubble. Horizontal and vertical axes are $r \leqslant 1.5$, $-2.5 \leqslant z \leqslant 2.5$. The black dotted line denotes $z = 0$.

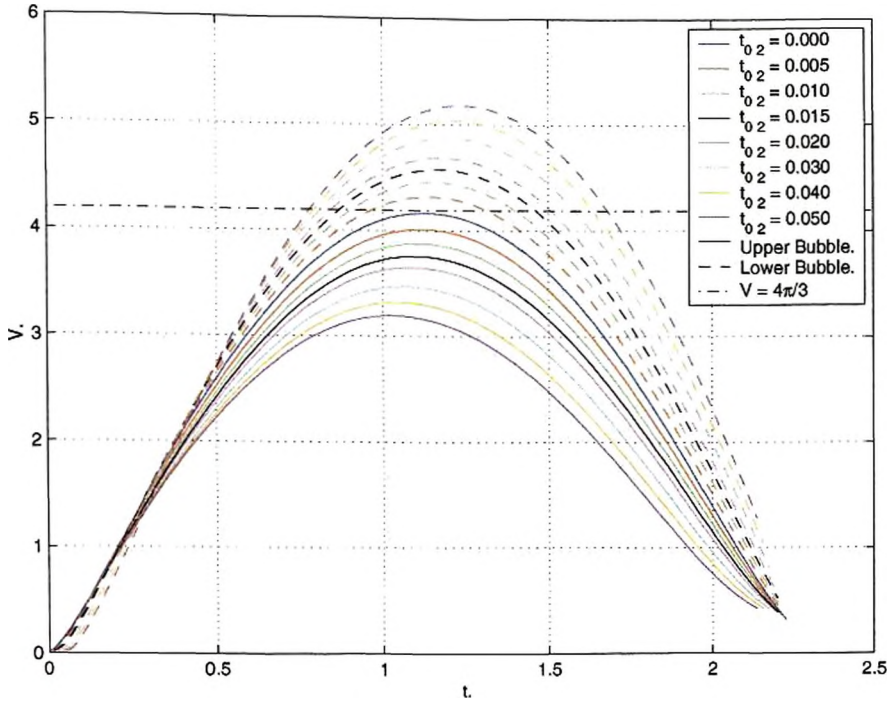

Figure 5.2: Evolution of the volumes of two cavitation bubbles generated at different instants and characterised by $t_{0\,1} = 0$, $\alpha_1 = \alpha_2 = 100$, $\gamma_1 = 1$, $\gamma_2 = -1$, $\delta = 0$ and $\kappa = 1.4$.

more easily than in might in isolation and also for a longer period, so a larger maximum volume is attained.

Following maximum volume the upper bubble begins to collapse prior to the lower, delayed bubble. This may be explained most readily by examining the pressures within the bubbles which are presented in Figure 5.3. During the later stages of expansion, the motion is governed not by a driving pressure within the bubble, but fluid momentum at the surface of the bubble. As such, as the upper bubble is impeded by the delayed bubble, so the surface momentum is reduced, resulting in a smaller bubble and hence higher pressure at maximum volume. Conversely, the increased momentum created by the delayed bubble expanding more readily leads to the larger volume noted above and a further reduced pressure. All these pressures are of course below the hydrostatic pressure and once all kinetic energy is gone, so the bubbles will begin to collapse.

Finally we consider the Kelvin impulses in relation to the motion of the two bubbles. This has proved to be an excellent source of information regarding the physical characteristics of the motion of the bubbles in both previous studies and the earlier chapters

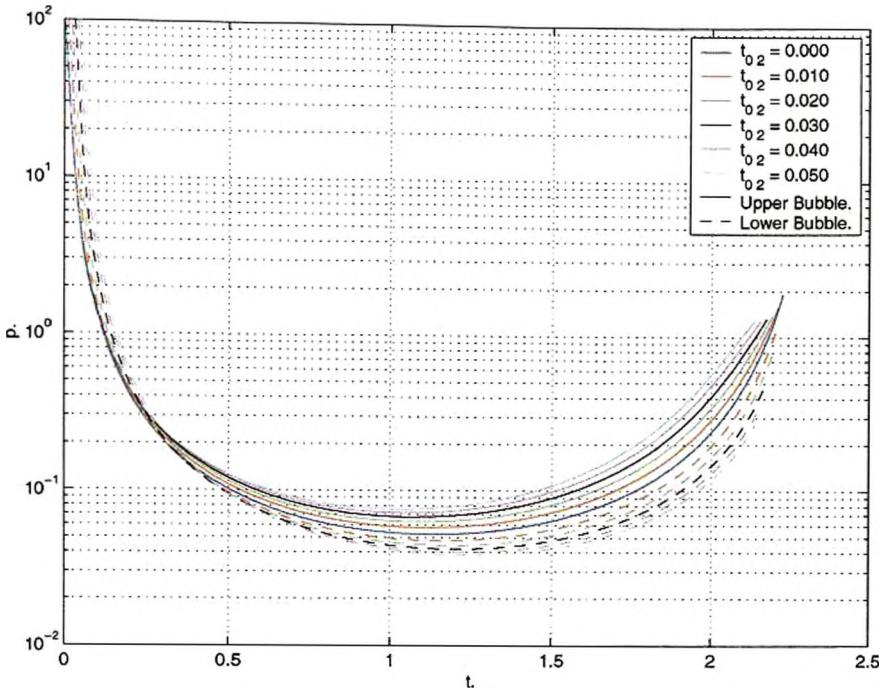

Figure 5.3: Evolution of the pressures of two cavitation bubbles generated at different instants and characterised by $t_{01} = 0$, $\alpha_1 = \alpha_2 = 100$, $\gamma_1 = 1$, $\gamma_2 = -1$, $\delta = 0$ and $\kappa = 1.4$.

of this work. Figure 5.4 shows the strongest attraction between the two bubbles occurs when they are released simultaneously. As the release time of the second bubble is delayed, the forces of attraction start to dwindle as the opposing expansions start to work in tandem to facilitate the motion.

In Figure 5.5, we show the effects of a greatly increased delay time on the motion of two bubbles generated at $\gamma_1 = 0.8$ and $\gamma_2 = -0.8$, i.e. 1.6 maximum bubble radii apart. Frame 1 of Figure 5.5a shows the initial size and future location of the upper bubble, with the location of the lower bubble hinted below. In Frame 2, the lower bubble is introduced and continues to expand rapidly due to the large low pressure cavity above it. As this continues to expand, the upper pole of the delayed bubble is drawn up into the region above it. At the time of jet impact in the upper bubble (Frame 7), the expansion of the delayed bubble continues. Physically we would expect this to be drawn through the upper bubble as time evolves further. However, due to the nature of the cut employed in the current scheme (a flat disc), this would soon transgress the elongated potion of the delayed bubble following which calculations would cease. In such a case we may revert to

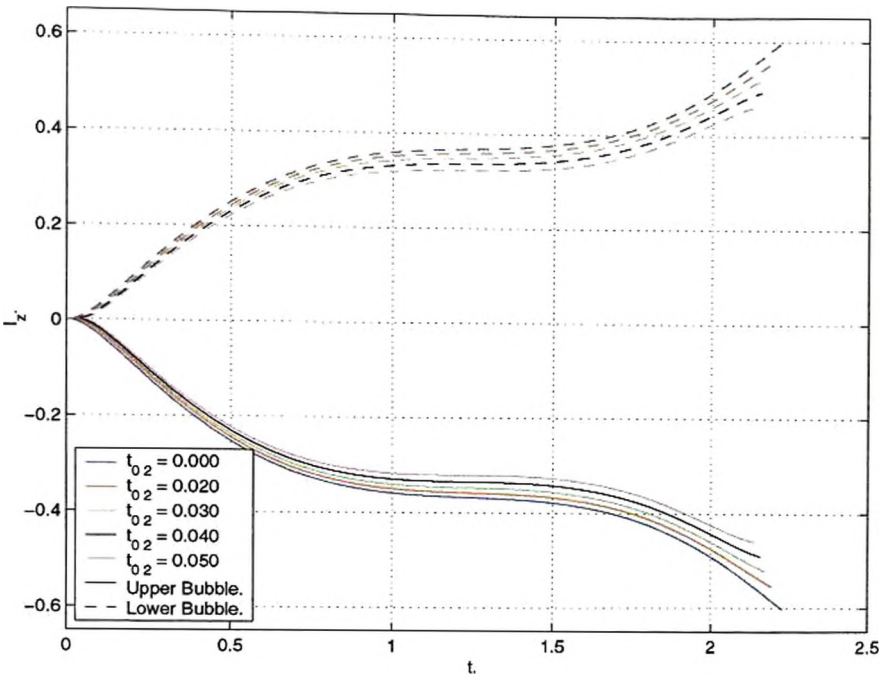

Figure 5.4: Evolution of the Kelvin impulses of two cavitation bubbles generated at different instants and characterised by $t_{01} = 0$, $\alpha_1 = \alpha_2 = 100$, $\gamma_1 = 1$, $\gamma_2 = -1$, $\delta = 0$ and $\kappa = 1.4$.

the numerical scheme employed by Best (1991) which evolves the cut as a material surface which would expand upward and outward with the fluid flow, thus being kept away from the lower bubble. However, due to the limited number of cases where such a scheme may be necessary, this has not been implemented in the revised numerical schemes developed for this work.

In order to provide additional information about the evolution of the flow field in this case, we present a series of pressure contour and velocity vector plots at six instants during the motion. Frame 1 of Figure 5.5b shows the flow field around the bubbles shortly following the initiation of the delayed bubble. Due to the high pressures around the lower bubble, much of the pressure information is disguised, however the velocity vectors show a large downward flow through this location. In Frame 2 we note the rapid expansion of the delayed bubble and initial lack of symmetry in the pressure field, with a thinner region of high pressure above the bubble, into which the bubble more readily expands. As the flow evolves, we note the high pressure region below the bubble which rapidly transitions into the reduced pressure region surrounding the upper bubble (Frame 3).

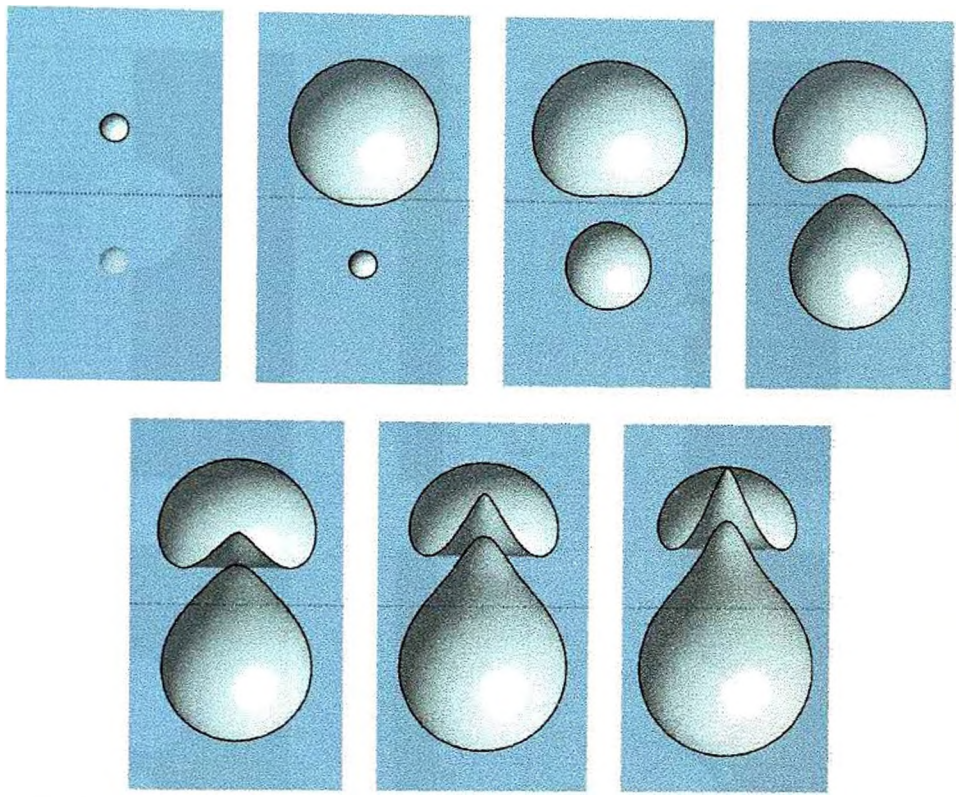

(a) Half-rendered bubble and surface shapes. Horizontal and vertical axes are $r \leqslant 1.25$, $-2.25 \leqslant z \leqslant 2.25$. The black dotted line denotes $z = 0$. Times are 0.0000, 0.0050, 0.6084, 0.7451, 0.8948, 1.0670 and 1.1833 respectively. The semi-transparent bubble in Frame 1 is the future point at which the bubble is introduced.

Figure 5.5: Motion of two cavitation bubbles generated at $t_{0\,1} = 0.0$, $t_{0\,2} = 0.5$ and characterised by$\alpha_1 = \alpha_2 = 100$, $\gamma_1 = 0.8$, $\gamma_2 = -0.8$, $\delta = 0$ and $\kappa = 1.4$.

The bubble then continues to rapidly expand upwards into the low pressure cavity, as shown by the velocity vectors in Frames 4 through 6.

In our final example, we show how even small differences in initial bubble size and time of generation can be further exaggerated as the bubbles are allowed to evolve into toroidal geometries, though ultimately there are, of course, similarities in the characteristic motion of the toroidal bubbles. Figure 5.6 shows the motion of a slightly smaller delayed upper bubble (with equivalent maximum bubble radius $R_{m\,1} = 0.975$) initiated 3 maximum bubble radii away (scaled with respect to the lower bubble, hence $R_{m\,2} = 1.0$). Again Frame 1 shows the initial geometry of the lower bubble and future location of the upper bubble hinted above it. Shortly afterwards ($t_{0\,1} = 0.02$ – Frame 2) the upper bubble is introduced. The bubbles reach maximum volume at similar times and are shown in

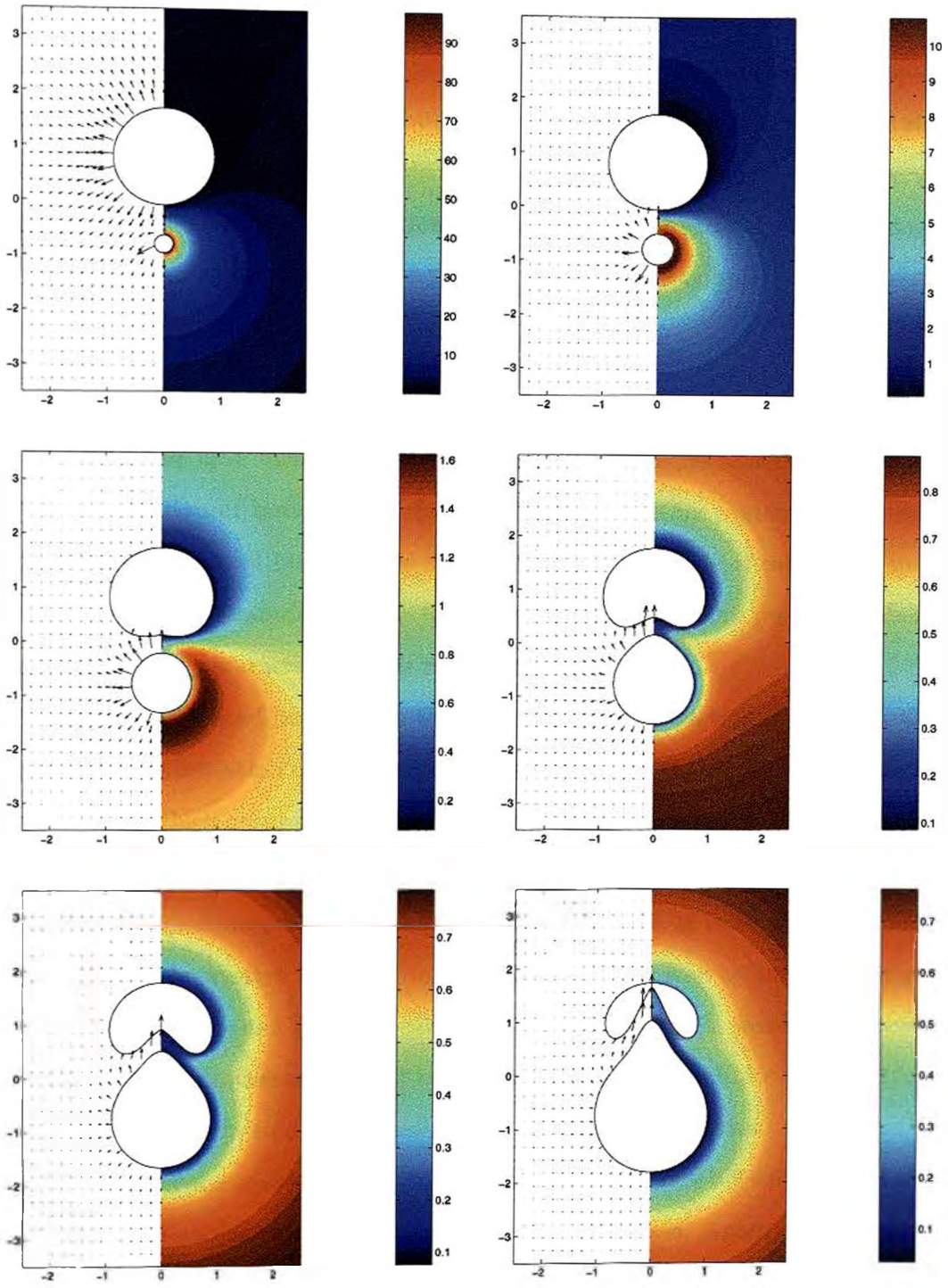

(b) Velocity vectors and pressure contours. Times are 0.5006, 0.5298, 0.6084, 0.7451, 0.8948 and 1.1527 respectively.

Figure 5.5 continued: Motion of two cavitation bubbles generated at $t_{01} = 0.0$, $t_{02} = 0.5$ and characterised by$\alpha_1 = \alpha_2 = 100$, $\gamma_1 = 0.8$, $\gamma_2 = -0.8$, $\delta = 0$ and $\kappa = 1.4$.

Frame 3. Due to the time delay, the upper bubble which would normally collapse just prior to the lower bubble, now reaches a toroidal topology shortly after the lower bubble (Frame 7), by which time the circulation about the lower bubble has generated a splash of liquid which is thrown down into the bubble. Such a splash may also be observed shortly afterwards in the delayed upper bubble. Finally in Frames 9 through 12 we observe the re-expansion of the bubbles. Calculations cease shortly afterwards due to the numerical difficulties as the ring indentations are pinched on the upper bubble.

5.3 Summary

In this chapter, we have further extended our boundary integral scheme to allow for the delayed introduction of bubbles into the flow field. Despite the systems presented only concerning the motion of bubbles, the scheme is equally capable of calculating motions near rigid and/or free boundaries. Due to the number of options this presents, a thorough examination of the parameter space is required.

The results presented have shown the large influence on motion which even a small time delay in the initiation of a second bubble can have on the whole system due to the violent motions which occur during early expansion and final collapse. This is particularly noticeable in Figure 5.1 where the increase in size of the primary bubble at the time the delayed bubble is initiated may be compared. Consideration of basic physical quantities associated with the system (such as volume, pressure and Kelvin impulse) along with more complex velocity and pressure calculations again provide a wealth of information about the physical processes involved in the evolution of the bubbles which could only otherwise be inferred from a large presentation of bubble geometries.

Finally we note the consideration of the two bubbles in Figure 5.6 which also shows the evolution of the bubbles through the toroidal phase of motion. Again, such calculations were omitted from the experimental comparisons in Chapter 4 for brevity and are included as evidence of the possibility of the calculation of toroidal motion in multi-bubble systems.

In the following chapter, we draw together conclusions from the thesis and outline important advances made throughout the research. A number of avenues of possible improvements for the current numerical scheme are also detailed.

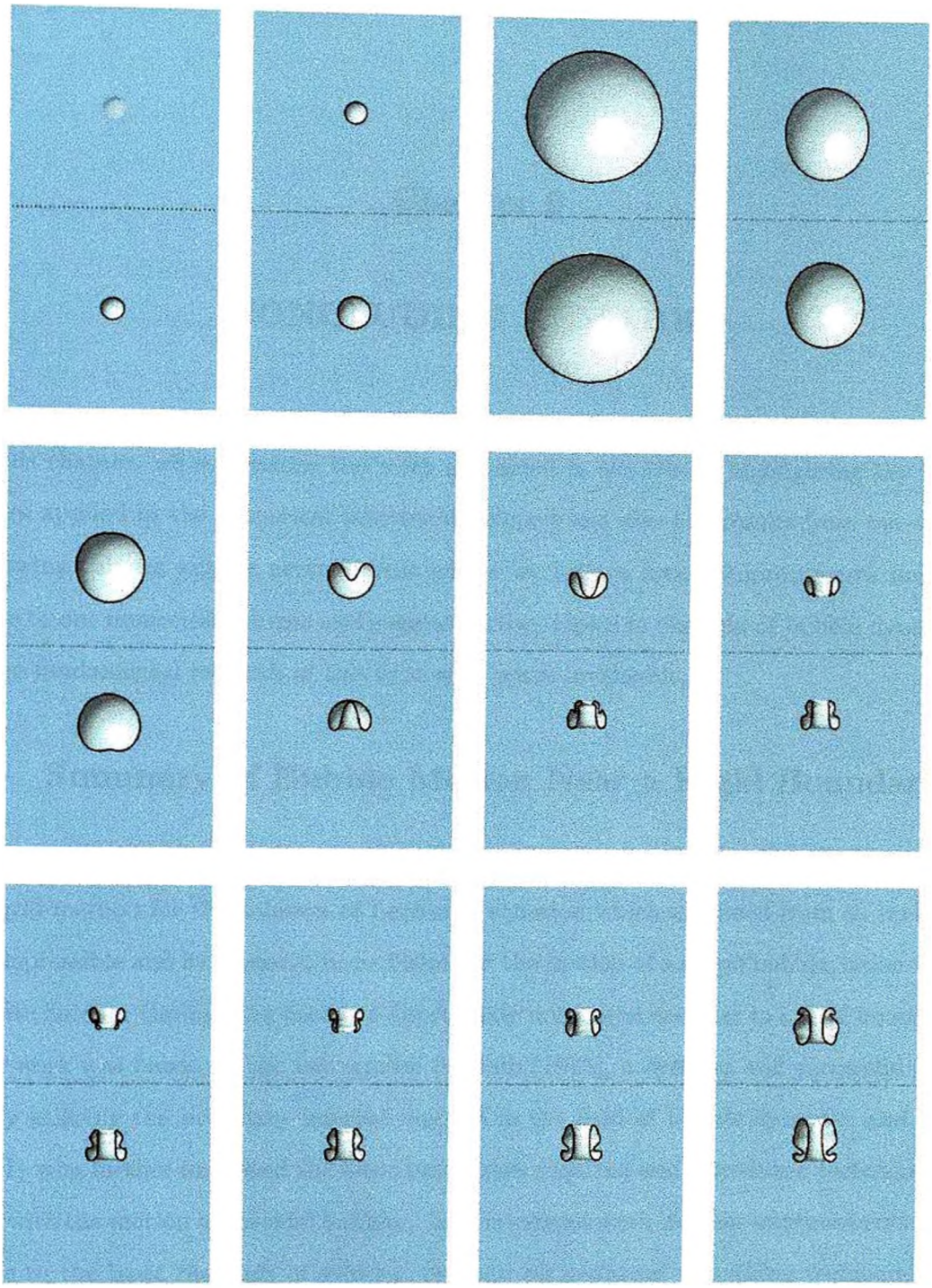

Figure 5.6: Half-rendered bubble shapes showing the motion of two cavitation bubbles generated at $t_{0\,1} = 0.02$ and $t_{0\,2} = 0.00$ and characterised by $R_{\mathrm{m}\,1} = 0.975$, $R_{\mathrm{m}\,2} = 1.0$, $\alpha_1 = \alpha_2 = 100$, $\gamma_1 = 1.5$, $\gamma_2 = -1.5$, $\delta = 0$ and $\kappa = 1.4$. Horizontal and vertical axes are $r \leqslant 1.5$, $-2.5 \leqslant z \leqslant 2.5$. The black dotted line denotes $z = 0$. Times are 0.0000, 0.0212, 1.0857, 1.9568, 2.1425, 2.1653, 2.1751, 2.1793, 2.1854, 2.1969 and 2.2203 respectively. The semi-transparent bubble in Frame 1 is the future point at which the bubble is introduced.

Chapter 6

CONCLUDING REMARKS

In this chapter, we summarise the work contained in the thesis, highlighting key techniques applied in the numerical schemes developed and also key results from our work. Following this we outline several areas where we believe future improvements may be made to our numerical scheme and suggest further topics in the field of bubble dynamics where fundamental research of this type may prove invaluable.

6.1 Summary of Bubble Motion Near a Rigid Boundary

In Chapter 3, we detailed the techniques required to formulate and implement a boundary integral method for the solution of Laplace's equation which stemmed from an inviscid, incompressible and irrotational formulation for the motion of a single bubble, either in an infinite fluid, or through the use of an appropriate image system, near to a rigid boundary. This work was based on the key studies by Taib (1985), a detailed and successful early study utilising the boundary integral method in the field of bubble dynamic; and Best (1991) who further improved the basic techniques required and introduced techniques to deal with the motion of toroidal bubbles. In this current work, further improvements were made to the basic methods of solution through an improved smoothing technique and higher-order time stepping scheme, thus reducing the losses in the numerically calculated energy of the system, signifying an improvement in accuracy over the scheme employed by Best. Furthermore, these energy calculations yield interesting characteristic information, for example the sphericity of expansion near a boundary which may be determined by the total conversion of the kinetic energy attained during expansion to potential energy.

Extensive results for cavitation bubbles generated over a range of standoff distances for two compression ratios, $\alpha = 100$ and 1000 were presented. Included amongst these were comparisons of bubble geometry at the time of jet impact and a range of comparisons for basic physical parameters such as volume, pressure and the Kelvin impulse. Excellent comparisons against the experiments of Lindau (2001) were also obtained.

In addition to the numerical calculations pertaining to the total energy of the motion noted above, techniques were devised to calculate physical quantities associated with the liquid jet, namely the kinetic energy and Kelvin impulse. Such quantities may lead to an understanding of the damping mechanisms involved at the time of jet impact, where energy transferred to a circulation about the bubble is no longer available for compression.

Further information about the physical behaviour of the flow field around the bubble was also gleaned through improved techniques to calculate the pressured and velocity fields. This proved particularly helpful in understanding the behaviour of bubbles near the null Kelvin impulse curve: that which defines a zero impulse and hence force on a buoyant bubble above a rigid boundary. For example the unusual flow observed around an almost spherical bubble at maximum volume in Figure 3.25. We note however, the null impulse states for this work were chosen as those with a zero calculated value at the time of jet impact or bubble splitting. A more suitable comparison with previous spherical bubble studies is made in Brujan, Pearson & Blake (2002) where the centroid motion is examined to determine the null impulse state.

6.2 Summary of Work on Multiple Bubbles and Multiple Boundaries

Exhaustive changes were made to the basic single bubble numerical scheme to permit calculations concerning two (or possibly more) bubbles and an infinite free surface in Chapter 4. Through the addition of a small number of integration routines, the option of adding a rigid boundary along with the infinite free surface permitted calculations of bubble motion in a shallow fluid layer.

Numerical calculations for vapour bubbles generated beneath an infinite free surface

were presented. Amongst these, the ability to calculate motion down to standoff distances of $\gamma = -0.45$ exemplifies the success of the scheme. Extensive calculations including velocity vectors and pressure contours and fully rendered transparent bubble shapes for both the pre-toroidal and toroidal phases of motion show in great detail the evolution of the flow for $\gamma = -0.56$, the often reproduced experimental case from Blake & Gibson (1981). For example the paper by Longuet-Higgins (1983) compares this case against a Dirichlet hyperboloid model for the tip of the free surface spike. Bubble geometries were presented showing the initial formation of this spike when the angle between the tangents to this curve pass the analytically calculated critical angle of 109°. Further, our calculations showing the evolution of the height of the free surface spike corroborate the experimentally observed and theoretically calculated constant growth in height.

Calculations concerning the motion of two vapour bubbles beneath an infinite free surface were shown to compare well with experiments performed by Robinson, Blake, Kodama, Shima & Tomita (2001)[1] and Tomita & Kodama (2001). The primary consideration of this latter paper was of two bubbles of largely disparate maximum radius. Our calculations showed the use of the vapour bubble model to be insufficient and will therefore require calculations concerning bubbles with a gaseous content. Though of course there is a need to obtain suitable strength parameters in order to progress down this route.

Numerical integration routines which allow for an image in the rigid boundary during integration over the analytic portion of the infinite free surface were used to permit consideration of the motion of a bubble in shallow fluid layer. Although our examples consider layers of only a few maximum bubble radii in depth, this may be increased and prove to be a helpful tool in examining the behaviour of an underwater explosion bubble in a finite depth of water such as a harbour through the addition of buoyancy. A number of comparative series of results show how motion varies as the depth of fluid and relative standoff distances from the two boundaries are varied. In a sufficient depth of fluid, motion close to one boundary is much like that which would be observed with only one boundary present. In other instances, the Bjerknes forces of attraction towards the rigid

[1] In which a number of pressure calculations made using our numerical scheme were included.

boundary and repulsion from the free surface combine. Of course beyond a certain depth of fluid this effect may not be so strong as that which would be felt were the bubble moved closer to one boundary.

6.3 Summary of Delayed Bubble Work

In Chapter 5 further modifications to our numerical scheme were made in order to permit the introduction of additional bubbles at some time $t > 0$. Time integration on two timescales was employed to minimise errors. Comparisons showing the significant changes which may occur through only a short time delay in the initiation of one bubble were presented. Physical quantities such as volume and pressure were used to explain the physical behaviour. Further examples were presented showing the unusual effects of a greater time delay and of the influence of a delay on bubbles of slight different maximum bubble radius. This latter example also included the toroidal motion of both bubbles, a feature not demonstrated in the previous chapter but which requires the dynamic cut relocation algorithm to be applied separately to the two bubbles.

6.4 Avenues For Future Work

In recent months, a number of aspects concerning the numerical schemes employed have been earmarked for future improvement. Of most importance is the need to remove the requirement for smoothing during advancement of the flow. As shown in Chapter 3, the application of smoothing is one key source of error in the numerical scheme. Furthermore, as the smoothing acts to remove spikes from the surface, so this will have its predominant effect on the liquid jets which thread the bubble. This will affect calculations which require accuracy at the tip of the jet, such as jet speed calculations. Furthermore, it was noted that for bubble motion near a rigid boundary, there are two critical standoff distances: the first is that at which jet impact occurs at minimum volume; the second where jet impact just occurs during re-expansion of the bubble. Whilst smoothing is required it is pointless to attempt these calculations. One recent publication by Georgescu, Achard & Canot (2002) does not report a need for smoothing and visibly shows node

distributions over the free surface which are non-linear with respect to arclength. Instead these are clustered around points of high curvature which we noted earlier as the location at which high-frequency instabilities most readily occur. This may be attributable to the linear variation with respect to arclength of the normal velocity calculated which will likely vary non-linearly in these regions. We also note the occurrence of many high-curvature regions during the toroidal phase of motion, which at present require more frequent applications of our smoothing techniques. It is likely that large increases in accuracy may be possible here.

As noted above, the resolution of the requirement for smoothing will enable definitive studies of many aspects concerning, primarily, the liquid jet. We also note the current linear distribution of nodes does not permit accurate calculations in which very fine liquid jets occur. In such instances, the tip of the jet becomes blunted as splines are fitted to the nodes. Although observed in experiments, this may be attributed to surface tension effects. Until this can be resolved for bubbles without surface tension effects, it is again futile to attempt any study which attempts to ascertain the effects of surface tension on the geometry of the liquid jet.

As noted in the introduction, many experimental studies are now geared toward determining the effects of flexible boundaries on bubble motion. This is of primary importance due to the large number of applications in the medical field such as in laser eye surgery, extracorporeal shock wave lithotripsy and newer techniques such as in therapeutic ultrasound treatments, or in the use of microbubbles as contrast agents in ultrasound scanning. Of course, such flexible boundaries have complex rheological properties which may be extremely difficult to model. But, given the key need for understanding due to the important nature of medical research, we believe this is a key area worthy of investigation.

Finally, we note the need from an industrial perspective of the need for simplified tools such as spherical bubble models which take into account more physical aspects of the bubble motion than may currently be done. We believe that fundamental works such as this thesis are important in bridging the gap between the current wealth of inviscid, incompressible and irrotational models and those spherical bubble models which

do permit the introduction of some physical aspects such as weakly compressible effects. Key in doing this is the investigation of physical aspects of the motion such as the Kelvin impulse or the kinetic energy of the liquid jet.

Appendix A

POLYNOMIAL APPROXIMATIONS TO ELLIPTIC INTEGRALS

A.1 Revised Polynomial Approximations

Throughout this work, several integrals necessarily require the calculation of elliptic integrals which occur due to the analytic integration over the azimuthal coordinate θ. In order to formulate a workable numerical scheme it is necessary to perform these integrations using polynomial approximations. Throughout much of this work, the coefficients for these polynomial approximations were taken from the excellent reference text by Abramowitz & Stegun (1965), which holds coefficients for fourth-order polynomial approximations of the form

$$K(1-x) = \sum_{i=0}^{n} a_i x^i + \sum_{i=0}^{n} b_i x^i \ln\left(\frac{1}{x}\right) + \text{error}, \tag{A.1.1a}$$

$$E(1-x) = \sum_{i=0}^{n} a_i x^i + \sum_{i=0}^{n} b_i x^i \ln\left(\frac{1}{x}\right) + \text{error}, \tag{A.1.1b}$$

where $K(x)$ and $E(x)$ are elliptic integrals of the first and second-kind respectively.

Recent work by Roumeliotis (2000) gives consideration to many aspects of the boundary integral method with respect to Stokes-flow problems. One aspect is the calculation of improved polynomial approximations to elliptic integrals. Herein we utilise these methods to yield polynomial approximations up to twelfth-order, resulting in improved accuracy. In Figure A.1 we show the absolute value of the errors to the polynomial approximations to the first and second-kind elliptic integrals over the range $[0, 1]$ and note the increasing accuracy as the order of the approximation is increased. The troughs in these curves

a_0	$1.386294361119890619 \times 10^{+0}$
a_1	$9.657359027997265471 \times 10^{-2}$
a_2	$3.088514453248461827 \times 10^{-2}$
a_3	$1.493760036978098688 \times 10^{-2}$
a_4	$8.766312198628351295 \times 10^{-3}$
a_5	$5.754899916512118317 \times 10^{-3}$
a_6	$4.068196489162359578 \times 10^{-3}$
a_7	$3.167134481148401763 \times 10^{-3}$
a_8	$3.859187350434518109 \times 10^{-3}$
a_9	$6.972489272022875537 \times 10^{-3}$
a_{10}	$7.000304984236618735 \times 10^{-3}$
a_{11}	$2.355355762376631333 \times 10^{-3}$
a_{12}	$1.617500382458658709 \times 10^{-4}$

b_0	$5.000000000000000000 \times 10^{-1}$
b_1	$1.250000000000000000 \times 10^{-1}$
b_2	$7.031250000000000000 \times 10^{-2}$
b_3	$4.882812499999999988 \times 10^{-2}$
b_4	$3.738403320299965249 \times 10^{-2}$
b_5	$3.028106526770420434 \times 10^{-2}$
b_6	$2.544378896278751497 \times 10^{-2}$
b_7	$2.189639358590439516 \times 10^{-2}$
b_8	$1.859695172048566289 \times 10^{-2}$
b_9	$1.326644642298080552 \times 10^{-2}$
b_{10}	$5.721506651298451211 \times 10^{-3}$
b_{11}	$9.874948865402974846 \times 10^{-4}$
b_{12}	$3.519107157048046294 \times 10^{-5}$

Table A.1: Polynomial coefficients for elliptic integrals of the first-kind.

denote points near where the sign of the error changes. In some cases, breaks in the curves are observed and show an accurate approximation at that order. The errors for the twelfth-order approximations may be seen to be $< 10^{-15}$ in both cases.

In practice, this has enabled us to remove the requirement for smoothing on the infinite free surface, leading us to believe that deficiencies in lower-order approximations may be one cause of the high-frequency instabilities observed in both previous and the current calculations. The fluctuations between positive and negative errors in these approximations give further confidence to this theory. Coefficients for the twelfth-order approximations to K and E are given in Tables A.1 and A.2 respectively.

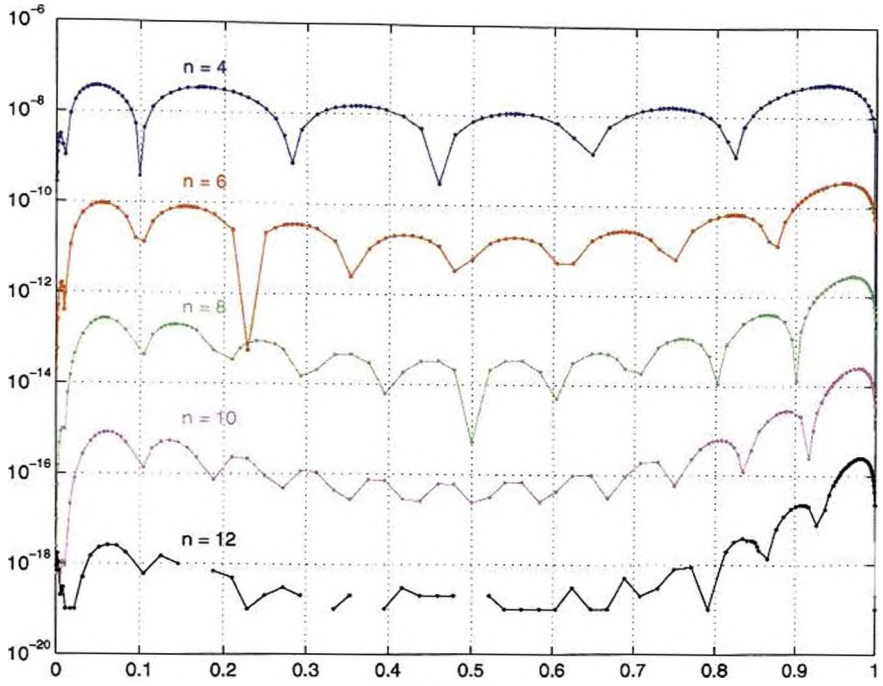

(a) Elliptic integrals of the first kind.

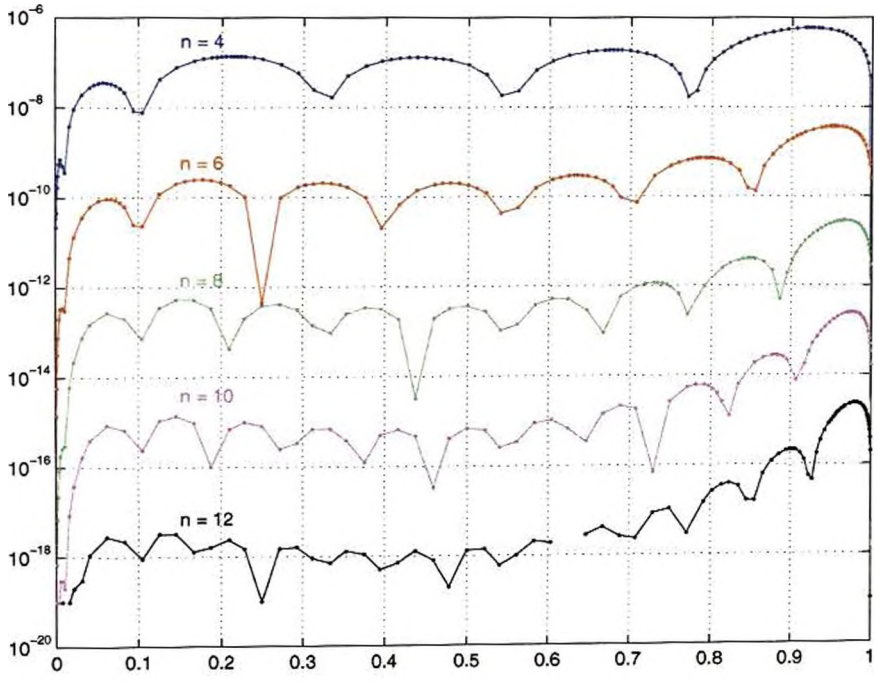

(b) Elliptic integrals of the second kind.

Figure A.1: Errors for polynomial approximations for elliptic integrals of the first and second kinds for n^{th} order polynomial approximations.

a_0	$1.000000000000000000 \times 10^{+0}$
a_1	$4.431471805599453094 \times 10^{-1}$
a_2	$5.680519270997949103 \times 10^{-2}$
a_3	$2.183137044373718190 \times 10^{-2}$
a_4	$1.154452141731604340 \times 10^{-2}$
a_5	$7.142000880629109887 \times 10^{-3}$
a_6	$4.855421383036171293 \times 10^{-3}$
a_7	$3.572564215768735052 \times 10^{-3}$
a_8	$3.631639679361792198 \times 10^{-3}$
a_9	$6.629823709524348552 \times 10^{-3}$
a_{10}	$8.073112000431010522 \times 10^{-3}$
a_{11}	$3.295625172650292327 \times 10^{-3}$
a_{12}	$2.678746225171336572 \times 10^{-4}$

b_0	$0.000000000000000000 \times 10^{+0}$
b_1	$2.500000000000000000 \times 10^{-1}$
b_2	$9.375000000000000000 \times 10^{-2}$
b_3	$5.859375000000000000 \times 10^{-2}$
b_4	$4.272460937499944487 \times 10^{-2}$
b_5	$3.364562982255665144 \times 10^{-2}$
b_6	$2.775753062754274175 \times 10^{-2}$
b_7	$2.361235143679368328 \times 10^{-2}$
b_8	$2.019504255758909479 \times 10^{-2}$
b_9	$1.528924850309902728 \times 10^{-2}$
b_{10}	$7.403836836114060667 \times 10^{-3}$
b_{11}	$1.468180166965393152 \times 10^{-3}$
b_{12}	$6.000736231796714824 \times 10^{-5}$

Table A.2: Polynomial coefficients for elliptic integrals of the second-kind.

REFERENCES

M. Abramowitz & I. A. Stegun (Eds.) (1965). *Handbook of Mathematical Functions.* Dover Publications, New York.

G. R. Baker, D. I. Meiron & S. A. Orszag (1984). Boundary integral methods for axisymmetric and three-dimensional Rayleigh-Taylor instability problems. *Physica* D **12**, 19–31.

G. Batchelor (1996). *The Life and Legacy of G. I. Taylor.* Cambridge University Press.

T. B. Benjamin & A. T. Ellis (1966). The collapse of cavitation bubbles and the pressures thereby produced against solid boundaries. *Phil. Trans. R. Soc.* A **260**, 221–240.

W. H. Besant (1859). *A Treatise on Hydrostatics and Hydrodynamics.* Deighton, Bell and Co., Cambridge.

J. P. Best (1991). *The Dynamics of Underwater Explosions.* PhD thesis, The University of Wollongong.

J. P. Best (1994). The rebound of toroidal bubbles. In Blake, Boulton-Stone & Thomas (1994), pp. 405–412.

J. P. Best & J. R. Blake (1994). An estimate of the Kelvin impulse of a transient cavity. *J. Fluid Mech.* **261**, 75–93.

J. P. Best & A. Kucera (1992). A numerical investigation of non-spherical rebounding bubbles. *J. Fluid Mech.* **245**, 137–154.

J. R. Blake (1988). The Kelvin impulse: Application to cavitation bubble dynamics. *J. Austral. Math. Soc.* B **30**, 127–146.

J. R. Blake, J. M. Boulton-Stone & N. H. Thomas (Eds.) (1994). Volume 23 of *Fluid Mechanics and its Applications.* Kluwer Academic Publishers, Dordrecht.

J. R. Blake, J. M. Boulton-Stone & R. P. Tong (1995). Boundary integral methods for rising, bursting and collapsing bubbles. In Power (1995), pp. 31–71.

J. R. Blake & P. Cerone (1982). A note on the impulse due to a vapour bubble near a boundary. *J. Austral. Math. Soc.* B **23**, 383–393.

J. R. Blake & D. C. Gibson (1981). Growth and collapse of a vapour cavity near a free surface. *J. Fluid Mech.* **111**, 123–140.

J. R. Blake & D. C. Gibson (1987). Cavitation bubbles near boundaries. *Ann. Rev. Fluid Mech.* **19**, 99–123.

J. R. Blake & G. S. Keen (2000). Single cavitation bubble luminescence. In Lauterborn & Kurz (2000), pp. 3–12.

J. R. Blake, G. S. Keen, R. P. Tong & M. Wilson (1999). Acoustic cavitation: the fluid dynamics of non-spherical bubbles. *Phil. Trans. R. Soc. Lond.* A **357**, 251–267.

J. R. Blake, P. B. Robinson, A. Shima & Y. Tomita (1993). Interaction of two cavitation bubbles with a rigid boundary. *J. Fluid Mech.* **255**, 707–721.

J. R. Blake, B. B. Taib & G. Doherty (1986). Transient cavities near boundaries. Part 1. Rigid boudary. *J. Fluid Mech.* **170**, 479–497.

J. R. Blake, B. B. Taib & G. Doherty (1987). Transient cavities near boundaries. Part 2. Free surface. *J. Fluid Mech.* **181**, 197–212.

J. R. Blake, Y. Tomita & R. P. Tong (1998). The art, craft and science of modelling jet impact in a collapsing cavitation bubble. *Appl. Sci. Res* **58**, 77–90.

J. R. Blake, R. P. Tong, G. S. Keen & Y. Tomita (1999). The interaction of a cavitation bubble with a rigid boundary. In Crum, Mason, Reisse & Suslick (1999), pp. 87–96.

J. M. Boulton-Stone (1995). The effect of surfactant on bursting gas-bubbles. *J. Fluid Mech.* **302**, 231–257.

J. M. Boulton-Stone & J. R. Blake (1993). Gas bubbles bursting at a free surface. *J. Fluid Mech.* **254**, 437–466.

C. A. Brebbia (1980). *The Boundary Element Method for Engineers.* Pentech Press, London. Second revised edition.

M. P. Brenner & H. A. Stone (2000, May). Modern classical physics through the work of G. I. Taylor. *Phys. Today*, 30–35.

E. A. Brujan, K. Nahen, P. Schmidt & A. Vogel (2001a). Dynamics of laser-induced cavitation bubbles near an elastic boundary. *J. Fluid Mech.* **433**, 251–281.

E. A. Brujan, K. Nahen, P. Schmidt & A. Vogel (2001b). Dynamics of laser-induced cavitation bubbles near elastic boundaries: influence of the elastic modulus. *J. Fluid Mech.* **433**, 283–314.

E. A. Brujan, A. Pearson & J. R. Blake (2002). On the behaviour of pulsating, buoyant bubbles close to a rigid boundary. Submitted to *J. Fluid Mech.*

A. R. Bryant (1944). Photographic measurements of the size, shape and movement of the bubble produced by 1-oz charges of polar ammon gelignite detonated at an underwater depth of 3 feet. In Hartmann & Hill (1950).

G. L. Chahine (1977). Interaction between an oscillationg bubble and a free surface. *Trans. ASME I: J. Fluids Engng.* **99**, 709–715.

G. L. Chahine (1982). Experimental and asymptotic study of non-spherical bubbles in non-unform flow fields. *Appl. Sci. Res.* **38**, 187–197.

G. L. Chahine & A. Bovis (1980). Oscillation and collapse of a cavitation bubble in the vicinity of a two-liquid interface. In Lauterborn (1980), pp. 23–29.

R. B. Chapman & M. S. Plesset (1972). Nonlinear effects in the collapse of a nearly spherical cavity in a liquid. *Trans. ASME D: J. Basic Engng.* **94**(1), 142–146.

C. G. Chaussy (Ed.) (1986). *Extracorporeal Shock Wave Lithotripsy.* Karger, Basel.

R. H. Cole (1948). *Underwater Explosions.* Princeton University Press.

A. J. Coleman, J. E. Saunders, A. J. Crum & M. Dyson (1987). Acoustic cavitation generated by an extracorporeal shockwave lithotripter. *Ultrasound Med. Biol.* **13**(2), 69–76.

E. Cox (2001). *The Source Signature Due to the Close Interaction of Marine Seismic Airguns.* Master's thesis, The University of Birmingham.

L. A. Crum, T. J. Mason, J. L. Reisse & K. S. Suslick (Eds.) (1999). *Sonochemistry and Sonoluminescence*. Kluwer Academic Publishers, Dordrecht.

C. de Boor (1978). *A Practical Guide to Splines*, Volume 27 of *Applied Mathematical Sciences*. Springer-Verlag, New York.

D. Epstein & J. B. Keller (1972). Expansion and contraction of planar, cylindrical and spherical underwater gas bubbles. *J. Acoust. Soc. Am.* **52**(3), 975–980.

Z. C. Feng & L. G. Leal (1997). Nonlinear bubble dynamics. *Ann. Rev. Fluid Mech.* **29**, 201–243.

S.-C. Georgescu, J. L. Achard & E. Canot (2002). Jet drops ejection in bursting gas bubble processes. *Euro. J. Mech.* B **21**, 265–280.

D. C. Gibson (1968). Cavitation adjacent to plane boundaries. In *Proceedings of the 3rd Australasian Conference on Hydraulic and Fluid Mechanics*, pp. 210–214. Institution of Engineers, Sydney, Australia.

D. C. Gibson & J. R. Blake (1980). Growth and collapse of cavitation bubbles near flexible boundaries. In *Proceedings of the 7th Australasian Conference on Hydraulic and Fluid Mechanics*.

D. C. Gibson & J. R. Blake (1982). The growth and collapse of bubbles near deformable surfaces. *Appl. Sci. Res.* **38**, 215–224.

L. Guerri, G. Lucca & A. Prosperetti (1981). A numerical method for the dynamics of non-spherical cavitation bubbles. In *Proceedings of the 2nd International Colloquium on Drops and Bubbles*, pp. 175–181.

P. Hall & G. Seminara (1980). Nonlinear oscillations of non spherical cavitation bubbles in acoustic fields. *J. Fluid Mech.* **101**, 423–444.

Y. Hao & A. Prosperetti (1999). The effect of viscosity on the spherical stability of oscillating gas bubbles. *Phys. Fluids* **11**(6), 1309–1317.

G. K. Hartmann & E. G. Hill (Eds.) (1950). *Underwater Explosion Research, Vol II.* Office of Naval Research, Washington D.C.

C. Hastings (1955). *Approximations for Digital Computers*. Princeton University Press.

C. Herring (1941). Theory of the pulsations of the gas bubble produced by an underwater explosion. (Revised 1949). In Hartmann & Hill (1950).

M. Holt (1977). Underwater explosions. *Ann. Rev. Fluid Mech.* **9**, 187–214.

M. Hooton (1995). *Explosion Bubble Dynamics.* PhD thesis, The University of Birmingham.

J. B. Keller & I. I. Kolodner (1956). Damping of underwater explosion bubble oscillations. *J. Appl. Phys.* **27**(10), 1152–1161.

J. B. Keller & M. Miksis (1980). Bubble oscillations of large amplitude. *J. Acoust. Soc. Am.* **68**(2), 628–633.

T. Kodama & Y. Tomita (2000). Cavitation bubble behaviour and bubble-shock wave interaction near a gelatin surface as a study of in vivo bubble dynamics. *Appl. Phys. B* **70**, 139–149.

A. Kucera & J. R. Blake (1990). Approximate methods for modelling cavitation bubbles near boundaries. *Bull. Austral. Math. Soc.* **41**, 1–44.

H. Lamb (1923). The early stages of a submarine explosion. *Phil. Mag.* **45**, 257–265.

H. Lamb (1932). *Hydrodynamics.* Cambridge University Press. Sixth edition.

W. Lauterborn (Ed.) (1980). *Cavitation and Inhomogeneities in Underwater Acoustics*, Volume 4 of *Springer Series in Electrophysics.* Springer-Verlag, Berlin.

W. Lauterborn (1982). Cavitation bubble dynamics – new tools for an intricate problem. *Appl. Sci. Res* **38**, 165–178.

W. Lauterborn & H. Bolle (1975). Experimental investigations of cavitation bubble collape in the neighbourhood of a solid boundary. *J. Fluid Mech.* **72**, 391–99.

W. Lauterborn & W. Hentschel (1985). Cavitation bubble dynamics studied by high speed photography and holography: Part I. *Ultrasonics* **23**, 260–268.

W. Lauterborn & T. Kurz (Eds.) (2000). *Nonlinear acoustics at the turn of the millennium*, Volume 524 of *AIP Conference Proceedings.* AIP, New York.

W. Lauterborn & A. Vogel (1984). Modern optical techniques in fluid mechanics. *Ann. Rev. Fluid Mech.* **16**, 223–244.

M. Lenoir (1976). Calcul numérique de l'implosion d'une bulle de cavitation au voisinage d'une paroi ou d'une surface libre. *J. Méc.* **15**(5), 725–751.

A. Lezzi & A. Prosperetti (1987). Bubble dynamics in a compressible liquid. Part 2. Second order theory. *J. Fluid Mech.* **185**, 289–321.

M. J. Lighthill (1990). *An informal introduction to theoretical fluid mechanics.* IMA Monograph Series. Oxford University Press.

O. Lindau (1998). *Dynamik und Lumineszenz lasererzeugter Kavitationsblasen.* Master's thesis, Georg-August-Universität, Göttingen.

O. Lindau (2001). *Untersuchungen zur lasererzeugten Kavitation.* PhD thesis, Georg-August-Universität, Göttingen.

O. Lindau & W. Lauterborn (2003). Cinematographic observation of the collapse and rebound of a laser-produced cavitation bubble near a wall. *J. Fluid Mech.* **479**, 327–348.

M. S. Longuet-Higgins (1983). Bubbles, breaking waves and hyperbolic jets at a free surface. *J. Fluid Mech.* **127**, 103–124.

M. S. Longuet-Higgins & E. D. Cokelet (1976). The deformation of steep surface waves on water I. A numerical method of computation. *Proc. R. Soc. Lond.* A **350**, 1–26.

T. S. Lundgren & N. N. Mansour (1988). Oscillations of drops in zero gravity with weak viscous effects. *J. Fluid Mech.* **194**, 479–510.

C. F. Naude & A. T. Ellis (1961). On the mechanism of cavitation damage by non-hemispherical cavities in contact with a solid boundary. *Trans. ASME D: J. Basic Engng.* **83**, 648–56.

H. N. Oğuz & A. Prosperetti (1990). Bubble entrainment by the impact of drops on liquid surfaces. *J. Fluid Mech.* **219**, 143–179.

H. N. Oğuz & A. Prosperetti (1993). Dynamics of bubble growth and detachment from a needle. *J. Fluid Mech.* **257**, 111–145.

S. Osher & R. P. Fedkiw (2000). Level set methods: an overview and some recent results. In preparation.

S. Osher & J. A. Sethian (1988). Fronts propogating with curvature dependent speed: algorithms based on Hamilton-Jacobi formulations. *J. Comp. Phys.* **79**, 12–49.

A. Osler (1981). *Turbinia.* Tyne and Wear County Council Museums.

A. Pearson (2000). *Hydrodynamics of Jet Impact in a Collapsing Bubble.* Master's thesis, The University of Birmingham.

I. I. Pelekasis, I. I. Tsamopoulos & I. I. Manolis (1992). A hybrid finite-boundary element method for inviscid flows with free-surface. *J. Comp. Phys.* **103**, 90–115.

W. G. Penney & A. T. Price (1942). On the changing form of a nearly spherical submarine bubble. In Hartmann & Hill (1950).

M. S. Plesset & R. B. Chapman (1971). Collapse of an initially spherical vapour cavity in the neighbourhood of a solid boundary. *J. Fluid Mech.* **47**, 283–290.

M. S. Plesset & A. Prosperetti (1977). Bubble dynamics and cavitation. *Ann. Rev. Fluid Mech.* **9**, 145–185.

S. Popinet & S. Zaleski (2000). Bubble collapse near a solid boundary: a numerical study of the influence of viscosity. In preparation.

H. Poritsky (1952). The collapse or growth of a spherical bubble or cavity in a viscous fluid. In *Proc. First U.S. Nat'l Congr. Appl. Mech.*, pp. 813–821. ASME.

H. Power (Ed.) (1995). *B. E. Applications in Fluid Mechanics*, Volume 4 of *Advances in Fluid Mechanics.* Computational Mechanics Publications, Southampton.

A. Prosperetti (1984). Bubble phenomena in sound fields. Part 2. *Ultrasonics* **22**, 115–124.

A. Prosperetti & A. Lezzi (1986). Bubble dynamics in a compressible liquid. Part 1. First order theory. *J. Fluid Mech.* **168**, 457–478.

A. Prosperetti & G. Seminara (1978). Linear stability of a growing or collapsing bubble in a slightly viscous liquid. *Phys. Fluids* **21**, 1465–1470.

C. Ramsauer (1923). Die massenbewegung des wassers bei unterwasserexplosionen. *Ann. d. Physik* **72**, 265.

Lord Rayleigh (1917). On the pressure developed in a liquid during the collapse of a spherical cavity. *Phil. Mag.* **34**, 94–98.

O. Reynolds (1894). Experiments showing the boiling of water in an open tube at ordinary temperature. *Brit. Assoc. Adv. Sci. Rep.* **74**.

P. B. Robinson, J. R. Blake, T. Kodama, A. Shima & Y. Tomita (2001). Interaction of cavitation bubbles with a free surface. *J. Appl. Phys.* **89**(12), 8225–8237.

J. C. W. Rogers & W. G. Szymczak (1997). Computations of violent surface motions: comparisons with theory and experiment. *Phil. Trans. R. Soc. Lond.* A **355**, 649–663.

J. Roumeliotis (2000). *A Boundary Integral Method Applied to Stokes Flow.* PhD thesis, University of New South Wales, Australia.

A. F. Seybert, B. Soenarko, F. J. Rizzo & D. J. Shippy (1985). An advanced computational method for radiation and scattering of acoustic waves in three dimensions. *J. Acoust. Soc. Am.* **77**(2), 362–368.

S. J. Shaw, Y. H. Jin, T. P. Gentry & D. C. Emmony (1999). Experimental observations on the interactions of a laser generated cavitation bubble with a flexible membrane. *Phys. Fluids* **11**(8), 2437–2439.

A. Shima, Y. Tomita, D. C. Gibson & J. R. Blake (1989). The growth and collapse of cavitation bubbles near composite surfaces. *J. Fluid Mech.* **203**, 199–214.

B. D. Storey & A. J. Szeri (2000). Water vapour, sonoluminescence and sonochemistry. *Proc. R. Soc. Lond.* A **456**(1999), 1685–1709.

B. D. Storey & A. J. Szeri (2001). A reduced model of cavitation physics for use in sonochemistry. *Proc. R. Soc. Lond.* A **457**(2011), 1685–1700.

K. Suslick (1989). The chemical effects of ultrasound. *Sci. Am.* **260**(2), 62–68.

M. Sussman & P. Smereka (1997). Axisymmetric free boundary problems. *J. Fluid Mech.* **341**, 269–294.

E. Swift & J. C. Decius (1947). Measurement of bubble pulse phenomena, III, Radius and period studies. In Hartmann & Hill (1950).

A. J. Szeri, B. D. Storey, A. Pearson & J. R. Blake (2002). Heat and mass transfer during the violent collapse of non-spherical bubbles. Submitted to *Phys. Fluids.*

B. B. Taib (1985). *Boundary Integral Method Applied to Cavitation Bubble Dynamics.* PhD thesis, The University of Wollongong.

G. I. Taylor (1942). Vertical motion of a spherical bubble and the pressure surrounding it. In Hartmann & Hill (1950).

G. I. Taylor & R. M. Davies (1943). The motion and shape of the hollow produced by an explosion in a liquid. In Hartmann & Hill (1950).

Y. Tomita, J. R. Blake & P. B. Robinson (1998). Interaction of a cavitation bubble with a curved rigid boundary. In *Third International Symposium on Cavitation, Grenoble, France*, pp. 51–56.

Y. Tomita & T. Kodama (2001). Some aspects of the motion of two laser-produced cavitation bubbles near a free surface. pp. 303–310. Kluwer Academic Publishers.

Y. Tomita & A. Shima (1986). Mechanisms of impulsive pressure generation and damage pit formation by bubble collapse. *J. Fluid Mech.* **169**, 535–564.

R. P. Tong, W. P. Schiffers, S. J. Shaw, J. R. Blake & D. C. Emmony (1999). The rôle of 'splashing' in the collapse of a laser-generated cavity near a rigid boundary. *J. Fluid Mech.* **380**, 339–361.

M. Van Dyke (1982). *An Album of Fluid Motion.* Parabolic Press, Stanford.

L. van Wijngaarden (Ed.) (1982). *Mechanics and Physics of Bubbles in Liquids.* Martinus Nijhoff. Reprinted from Applied Scientific Research volume 38.

A. Vogel (1997). Nonlinear absorbtion: Intraocular microsurgery and laser lithotripsy. *Phys. Med. Biol.* **42**, 895–912.

A. Vogel, R. Engelhardt, U. Behnle & U. Parlitz (1996). Minimization of cavitation effects in pulsed lazer ablation illustrated on laser angioplasty. *Appl. Phys. B* **62**, 173–182.

Y. L. Zhang, K. S. Yeo, B. C. Khoo & W. K. Chong (1998). Three-dimensional computation of bubbles near a free surface. *J. Comp. Phys.* **146**, 105–123.